Magnetic resonance imaging biomarkers of cancer : with applications in high intensity focused ultrasound treatment evaluation

Magnetic Resonance Imaging Biomarkers of Cancer

with applications in High Intensity Focused Ultrasound treatment evaluation

Igor Jacobs

Magnetic Resonance Imaging Biomarkers of Cancer

with applications in High Intensity Focused Ultrasound treatment evaluation

This research was performed within the framework of the Center for Translational Molecular Medicine, project VOLTA (grant 05T-201).

Financial support from Philips Research for printing of this thesis is gratefully acknowledged.

Printing of this thesis was supported by the Wolfram Mathematica distributor CANdiensten (http://www.can.nl). Wolfram Mathematica was used for image analysis in this thesis (via the TU/e campus license).

A catalogue record is available from the Eindhoven University of Technology Library
ISBN: 978-90-386-3843-0

Cover design and lay-out: Igor Jacobs

Cover description: 'By inspecting the tumor tissue in a special way, information can be obtained that would remain invisible otherwise'. The image is a 3D stereogram; an object is hidden inside the image which appears in 3D only when viewed correctly. This is a reference to the MRI methods and image analysis techniques that are presented in this thesis, such as the multiparametric MRI analysis and multi-agent tracer-kinetic modeling approach. With these techniques, valuable information about the tumor tissue could be extracted that could not be obtained with conventional MR imaging techniques. The background pattern of the image is based on a histopathological image of a tumor at 3 days after High Intensity Focused Ultrasound treatment. The 3D object that is hidden in the image can be found at the end of this thesis.

Printed by: Bek.

Magnetic Resonance Imaging Biomarkers of Cancer

with applications in High Intensity Focused Ultrasound treatment evaluation

PROEFSCHRIFT

ter verkrijging van de graad van doctor aan de Technische Universiteit Eindhoven, op gezag van de rector magnificus prof.dr.ir. F.P.T. Baaijens, voor een commissie aangewezen door het College van Promoties, in het openbaar te verdedigen op dinsdag 19 mei 2015 om 16:00 uur

door

Igor Jacobs

geboren te Geldrop

Dit proefschrift is goedgekeurd door de promotoren en de samenstelling van de promotiecommissie is als volgt:

voorzitter:	prof. dr. K. Ito
1e promotor:	prof. dr. K. Nicolay
copromotor:	dr. ir. G.J. Strijkers
leden:	dr. ir. M. Mischi
	prof. dr. C.T.W. Moonen (UMC Utrecht)
	prof. dr. B. Gallez (Université catholique de Louvain)
	dr. J. Fütterer (Radboud UMC)
adviseur:	M.C. Schabel PhD (Oregon Health & Science University)

Contents

Chapter 1

General Introduction

Cancer is one of the leading causes of death, with 14.1 million new cases and 8.2 million cancer deaths worldwide in 2012 (1). Due to this high prevalence, development of new detection and treatment strategies has been a very active field of research for many years. Advances in this field have led to a decreased mortality rate over the past decades. Cancer imaging plays a central role in both everyday clinical practice and preclinical and clinical research. Nowadays, screening programs for particular types of cancer have been established and imaging is involved in cancer detection, staging and grading, as well as in treatment evaluation (2). In addition, in the field of interventional oncology, imaging has a key role in treatment planning, targeting, monitoring and post-treatment evaluation (3). Most cancers are conventionally treated with surgery, chemotherapy, radiation therapy, or a combination of these. Besides conventional therapies, novel minimally invasive cancer treatment strategies are being developed that facilitate treatment with minimal damage to surrounding tissue. An emerging noninvasive treatment strategy is High Intensity Focused Ultrasound (HIFU), which is based on thermal ablation of tumors by local tissue heating (4). It is currently being introduced into clinical practice for treatment of malignant tumors, for which whole tumor coverage is crucial (5).

Oncologic imaging is often based on anatomical and morphological tumor features. The World Health Organization (WHO) has established criteria for treatment response monitoring based on measurement of tumor dimensions, which were further refined by the Response Evaluation Criteria In Solid Tumors (RECIST) (6-8). These criteria provide useful endpoints in clinical trials of cancer therapies. However, even when successful, many treatment strategies do not necessarily induce a direct change in tumor size (9). Therefore, more refined quantitative imaging biomarkers for tumor characterization and early assessment of therapy response have been developed. Imaging-based early response biomarkers can provide insights in treatment mechanisms, aid in therapy optimization and facilitate early adjustment of treatment strategy in case of no response.

In this chapter, medical imaging techniques in cancer care and research will be discussed. An overview of oncologic imaging biomarkers provided by the available imaging modalities will be given. The research presented in this thesis was aimed at the development and evaluation of magnetic resonance imaging (MRI) biomarkers for cancer imaging and early therapy response monitoring. Specific focus was on evaluation of HIFU treatment, which is commonly performed under MRI guidance. Therefore, MRI biomarkers will be more thoroughly covered. Subsequently, the principles of HIFU therapy will be introduced and the suitability of various MRI biomarkers for evaluation of HIFU treatment will be discussed.

1.1. Oncologic imaging biomarkers

Oncologic imaging biomarkers are commonly based on the unique microenvironment of solid tumors, which not only consists of malignant tumor cells but is a complex network of stromal cells, vascular and lymphatic endothelial cells, cancer-associated fibroblasts, infiltrating immune cells and the extracellular matrix (ECM) (10-14). The ECM involves macromolecules such as collagen, polysaccharides, fibrin, fibronectin, and proteoglycans, which provide structural and biochemical support to surrounding

cells. The tumor microenvironment is involved in secretion of growth factors, regulation of the immune response and is characterized by a unique tumor metabolism. As a result, it has a crucial role in tumor development, progression and metastasis.

Growth of solid tumors beyond a size of approximately 1-2 mm^3 requires development of a tumor blood supply, since cancer cells will be located beyond the diffusion distance of nutrients and oxygen (15). As a consequence, angiogenesis is triggered by a combination of factors, including low oxygen pressure, low pH, mechanical and metabolic stress and immune/inflammatory response, resulting in the formation of a vascular bed. Tumors often possess an abnormal vascular network, which is both structurally and functionally different than normal vasculature (15,16). Tumor vasculature may be immature and heterogeneous, with tortuous and hyperpermeable blood vessels (15,17-19). These vascular properties result in heterogeneous perfusion and a tumor microenvironment that may be hypoxic and have a low pH and high interstitial fluid pressure (Figure 1) (15,20,21).

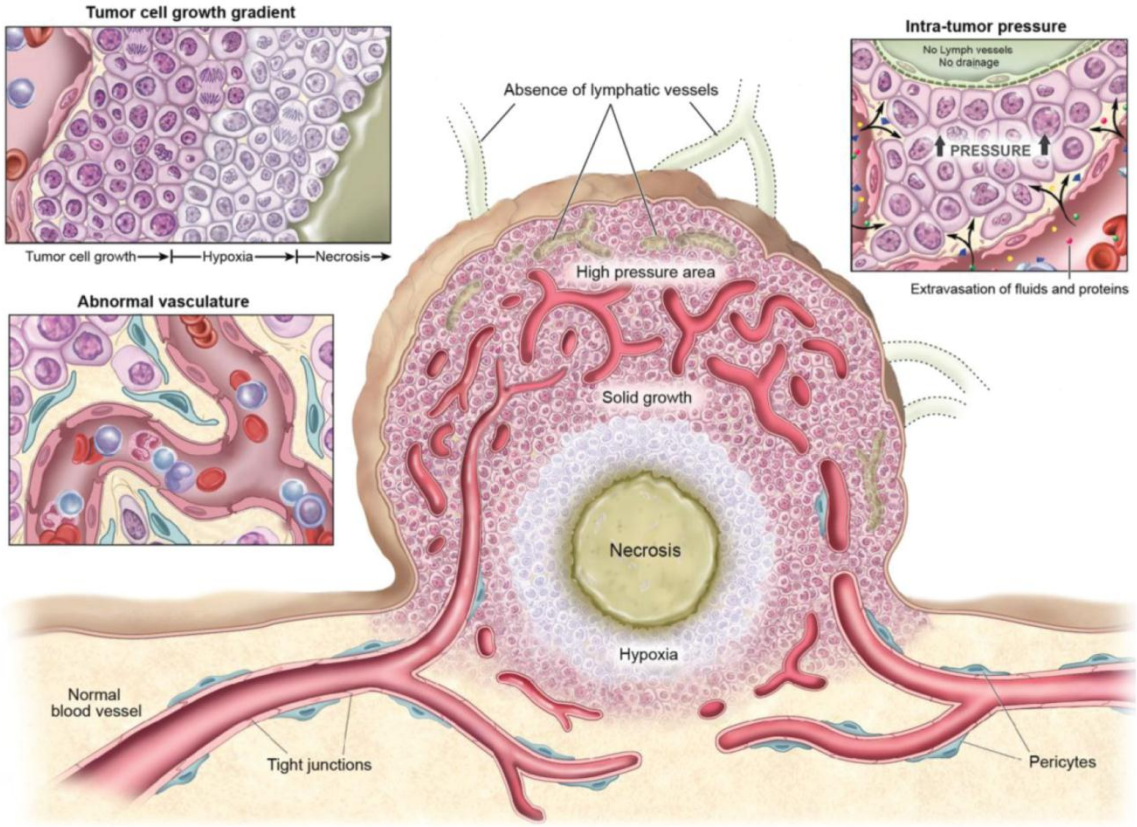

Figure 1. Tumors possess an immature vasculature with heterogeneous perfusion, as well as a poor lymphatic drainage. These characteristics may lead to elevated interstitial pressure and hypoxic conditions. Adapted from Kobayashi et al. (21) with permission. © 2013 by Ivyspring International Publisher.

The distinct tumor properties compared to normal tissue provide potential biomarkers for cancer imaging. In addition, structural, metabolic and functional imaging biomarkers may be used for early evaluation of therapy response. A number of different medical imaging techniques have been exploited to measure these oncologic imaging biomarkers, including computed tomography (CT), MRI and MR spectroscopy

(MRS), positron emission tomography (PET), single photon emission computed tomography (SPECT), ultrasonography (US) and optical imaging. Besides MRI, CT is the most commonly used imaging modality for anatomical tumor imaging (22). It may also be used for functional imaging, by the application of iodine-based CT contrast agents (6). PET is another modality that is commonly used for functional imaging. One of the main applications of PET in oncologic imaging is detection of malignant cells by their increased glucose uptake, which can be measured by administration of the PET tracer ^{18}fluoro-2-deoxy-D-glucose (^{18}FDG). FDG-PET can therefore be used for assessment of tumor aggressiveness and treatment response (23,24). Moreover, PET tracers have been developed that facilitate detection of increased proliferation (^{18}F-FLT) or hypoxia (^{18}F-MISO) (25). In addition to PET, several SPECT tracers are available for tracking therapy-induced apoptosis or changes in tumor metabolism (26). Besides for anatomic imaging, US and more specifically contrast-enhanced US is an imaging modality that is suitable for evaluation of tumor microvascular function (25). It has been shown that dynamic contrast-enhanced US (DCE-US) can be used to assess early response to radiofrequency ablation and antivascular therapies (6,27), as indicated by a lack of contrast-enhancement. In addition, targeted ultrasound bubbles have been developed that allow for assessment of tumor angiogenic activity (25). Another interesting application of ultrasound in medical imaging is US elastography, which has been used for cancer diagnosis based on differences in elasticity between benign and malignant tissue (28). It may be particularly useful for monitoring of thermal ablation therapies, since heat-induced cell necrosis and protein denaturation can result in an elevated elastic modulus of the treated tissue (29). Optical imaging, which involves fluorescent tracers or bioluminescence from genetically modified cells, mainly has preclinical applications due to the limited penetration depth of light. Nevertheless, it can provide useful information by molecular imaging of gene reporters, molecular targets and receptors, or tracking of cells during metastatic progression (30). MRS can be used to assess the tumor energy status, metabolic profile and pH (6,10,13). Whereas different nuclei can be assessed (^{1}H, ^{13}C, ^{19}F, ^{23}Na, ^{31}P), ^{1}H MRS is most commonly applied for evaluation of cancer (6,10). Since ^{1}H nuclei possess slightly different resonance frequencies, dependent on their molecular environment, ^{1}H MRS allows identification of different metabolites. Metabolite levels may be changed in tumors compared to normal tissue, or could be altered as a consequence of treatment. Malignant tumors often possess increased choline levels, related to their proliferative activity (6). In addition, their higher energy metabolism can result in higher creatine and phosphocreatine levels (6). Increased lactate levels, as a consequence of a high glycolytic rate, may also be reflective of tumor metabolism (6). MRS has also been used for treatment evaluation. As an example, reduced choline levels have been reported after chemo- and radiotherapy (6,31). An emerging technique to increase the sensitivity of MRS is hyperpolarized MRS. Hyperpolarization can transiently lead to an approximately 10^4 fold increase in MR signal (32,33). Administration of hyperpolarized ^{13}C-labeled cell substrates facilitates dynamic measurement of metabolic fluxes, such as pyruvate-lactate exchange (as a measure for lactate dehydrogenase activity).

MRI is one of the most commonly used imaging modalities for cancer. It yields excellent soft tissue contrast, relatively high spatial resolution and high versatility. In

addition to its use for anatomical imaging, MRI offers a wide array of structural, metabolic and functional imaging biomarkers. A number of molecular MR imaging approaches have been developed that are aimed at directly targeting specific components of the tumor microenvironment (10-12,34-38). Besides this, MRI offers a number of techniques that may be more generally useful for cancer detection and treatment evaluation. These MRI methods can be either based on endogenous contrast mechanisms or require injection of an MRI contrast agent to enhance the MRI appearance of tumors or extract functional information.

1.2. Endogenous MRI biomarkers of cancer

MRI of the human body is mainly based on the interaction of water proton spins with an externally applied magnetic field. Image contrast in conventional anatomical images is dependent on differences in proton density, spin-lattice or longitudinal relaxation times (T_1) and spin-spin or transversal relaxation times (T_2) between tissues and changes in these properties in diseased tissues. These inherent relaxometric properties of the tissue are influenced by the environment of the nuclei and molecular interactions (39). Most efficient spin-lattice energy transfer occurs when the natural motional frequency of the hydrogen atoms is in the order of the Larmor frequency. Efficient spin-spin relaxation is affected by the distance between hydrogen protons and thereby dependent on tissue structure and density. In addition to spin-spin relaxation, the decay in transverse magnetization may also be affected by static field inhomogeneities. The combination of these effects is described by the T_2^* relaxation time. Different MRI pulse sequences can be exploited to acquire images in which the contrast is dependent on these relaxation times.

1.2.1. Longitudinal and transversal relaxation times

Tumors often have a different appearance on T_1- and T_2-weighted images than healthy surrounding tissue, which could facilitate assessment of tumor size and morphology (40-43). Since many histological grading parameters, such as cellularity, mitotic rate and necrosis, affect their MRI appearance, relaxometric properties of the tumor may inform on tumor grade (44). However, since the relaxation times can be influenced by a variety of factors, their specificity for identification of cancer is low and dependent on tumor type and nature of the surrounding tissue.

Nevertheless, tumor relaxation times can be reflective of underlying tissue characteristics. Rofstad et al. have shown that high fractional water content was correlated with high T_1 and T_2 values in human melanoma xenografts (45). A direct correlation between T_1 values and extracellular water and interstitial water was also observed by Braunschweiger et al. (46). Proton relaxation times can also be affected by treatment-induced tumor necrosis through various mechanisms (45-48). Tumor necrosis may be associated with edema formation, leading to increased T_1 and T_2 values due to an increased fraction of extracellular water. Several other mechanisms could be responsible for a reduction in relaxation times. Necrosis induced microvascular damage may result in erythrocyte extravasation into the extracellular space and hemoglobin denaturation. Increased ferrous deoxyhemoglobin and ferric

hemoglobin concentrations can cause a decrease in T_2 and T_2^* relaxation times. In addition, paramagnetic methemoglobin may reduce T_1 relaxation times by electron-proton dipolar interactions (49). Moreover, changes in blood volume and microvascular perfusion after treatment could potentially lead to a reduced local oxygen concentration and increased levels of deoxyhemoglobin, thereby affecting the relaxation times (50). Furthermore, an increased concentration of freely dissolved paramagnetic ions, that have dissociated from denatured enzymes and proteins, could lower the relaxation times (47,51). In addition, it has been suggested that increased microvascular permeability leads to higher serum levels in the extracellular space, and tissue destruction to higher levels of extracellular macromolecules (48). Association of water with hydrophilic macromolecules slows down the natural motion of water molecules to frequencies closer to the Larmor frequency, shortening T_1 relaxation times. This may be another mechanism of T_1 shortening after cancer treatment.

Other MRI methods have used the dependence of relaxation times on oxygen and deoxyhemoglobin concentrations to specifically assess tumor oxygenation, which affects cancer progression and efficacy of chemotherapy and radiotherapy (52). The ratio of oxygenated and deoxygenated hemoglobin affects the T_2^* relaxation times, which is the basis of blood oxygen level-dependent (BOLD) imaging. By strongly T_2^*-weighted imaging, changes in deoxyhemoglobin concentrations and blood flow can be assessed (10,13,53). Another interesting method to assess tumor oxygenation is Mapping of Oxygen by Imaging Lipids Relaxation Enhancement (MOBILE) (54,55). This technique is based on the higher solubility of oxygen in lipids than in water and evaluates changes in tissue oxygenation by selectively measuring the R_1 of lipids. Colliez et al. have shown that MOBILE enabled measurement of both positive and negative alterations in tumor oxygenation (56). Changes in R_1 of lipid protons correlated with changes in tumor pO_2 and were shown to be more sensitive to tumor oxygenation than changes in the global R_1.

Taken together, tumor relaxometric properties are generally reflective of a wide variety of underlying tissue characteristics, by a complex contribution of water content, tissue integrity and content of paramagnetic ions and macromolecules. Changes in relaxation times may therefore reflect alterations in multiple of these underlying tissue properties and have been used to assess treatment response to e.g. chemotherapy (48,57).

1.2.2. Diffusion MRI

Whereas relaxation times may be indirectly reflective of tissue structure and integrity, water diffusivity within the tissue is more directly related to these properties. Water diffusion is described by random translational or Brownian motion. In the human body, diffusion of water molecules is restricted by physiological barriers such as the microvasculature, cell membranes and components of the ECM. Therefore, the diffusivity of water in vivo is described by the apparent diffusion coefficient (ADC). The ADC can be measured with MRI, by application of diffusion-sensitizing gradients placed on opposite sides of a 180° refocussing pulse (58,59). Nuclear spins will undergo dephasing during application of the first gradient. The second gradient will rephase

static spins, generating an echo. However, mobile spins of randomly moving water will experience differences in local magnetic field and accumulate phase shifts that will not be refocused by the second gradient. This results in a decay of the net magnetization and decreased signal intensity in diffusion-weighted images. The degree of diffusion weighting can be modified based on the amplitude, duration of, and time between the diffusion-sensitizing gradients, and is described by the b-value (s/mm^2).

Diffusion-weighted imaging has been of great interest for cancer diagnostics, tumor grading and evaluation of treatment response. Tumors generally possess low ADC values due to their high cellular density and structural disorganization with tortuous extracellular space, which restricts water diffusion. Therefore, diffusion weighted imaging can facilitate tumor detection and discrimination between benign and malignant lesions (60-62). Blackledge et al. have shown that whole body diffusion-weighted MR imaging is capable of detecting malignancies in different regions of the body (63). Furthermore, ADC values were found to correlate with cellular density in different human melanoma xenografts (64). Whereas diffusion is typically low in solid tumors, natural necrosis can result in higher ADC values due to reduced cellular density (64). The ADC has also been used as an early imaging biomarker for response to cancer therapy (6,13,65-67). It is generally observed that treatment-induced cell lysis and necrosis, accompanied by loss of membrane integrity, reduced cellular density and increased extracellular space, will result in an increased ADC (Figure 2) (67-69).

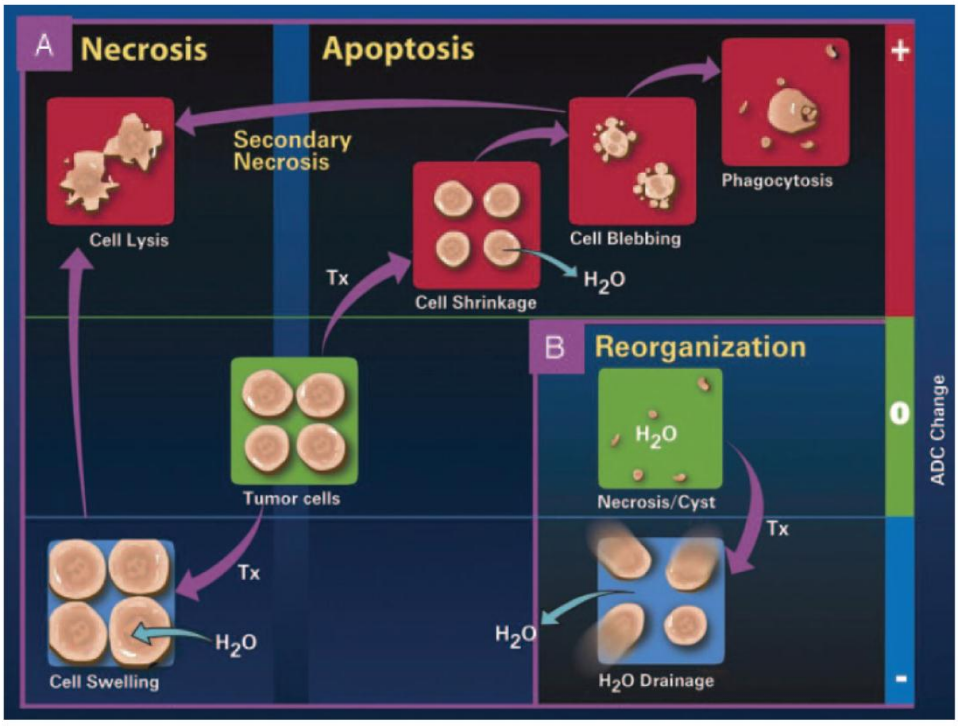

Figure 2. Representation of the different biological processes involved in ADC changes after tumor therapy. A) Death of tumor cells after therapy (through necrosis or apoptosis) generally results in increased ADC values (red). A transiently decreased ADC (blue) may be observed, associated with necrosis-induced transient cell swelling. B) At a later stage after therapy, processes like reorganization or repopulation result in alterations of the ADC. Adapted from Moffat et al. (69) with permission. © 2005 by The National Academy of Sciences of the USA.

Chenevert et al. found a significant correlation between cellular density and mean ADC values at various timepoints after chemotherapy in a rat tumor model (70). Moffat et al. calculated functional diffusion maps of brain tumor patients and observed that increased ADC after chemotherapy and radiotherapy was an early predictor of subsequent volumetric tumor response (69). A transient decrease in ADC, related to cellular swelling, could be observed early after therapy, resulting in more restricted diffusion in the extracellular space (59). Finally, pre-treatment ADC values could potentially also be informative of treatment outcome. High ADC values may be associated with necrotic tumors that are often poorly perfused and hypoxic, which increases their resistance to chemo- and radiotherapy. Dzik-Jurasz et al. have shown that the ADC can predict response to chemoradiation (71). They observed a relatively poor response to chemotherapy and chemoradiation for tumors with high pre-treatment ADC values.
Le Bihan et al. have shown that at low b-values (<100 s/mm^2), signal decay may also be affected by capillary perfusion and suggested that perfusion-related parameters could be separated from pure water diffusion, by intravoxel incoherent motion (IVIM) imaging (58,72). Several studies have shown the potential of IVIM analysis for tumor imaging (73-75) or evaluation of treatment response (76).

1.2.3. Magnetization Transfer imaging

Another method that may be suitable for cancer imaging, is magnetization transfer imaging (77). The tumor extracellular matrix is composed of many macromolecular components that provide structural support to tumor cells. As described, the longitudinal relaxation rate may be increased by dipolar interactions between water protons and macromolecular protons. However, this interaction may also be more specifically measured by magnetization transfer imaging. Magnetization transfer imaging is based on off-resonance irradiation, and saturation of the magnetization of the macromolecular proton pool. Dependent on the extent of the magnetization exchange between macromolecular protons and the bulk water, the signal intensity on the MR images will be decreased (77,78). The magnetization transfer ratio (MTR) is influenced by macromolecular structure, content and concentration. Magnetization transfer contrast can be quantified by image acquisition in presence and absence of the saturation pulse. Tsukushi et al. measured significantly higher MTRs of malignant musculoskeletal tumors compared to benign ones (79). In addition, a significant correlation between the MTR and DNA index, an indicator of tumor malignancy, was observed. Also Bonini et al. showed that the MTR could discriminate between benign and malignant lesions (80). Finally, the MTR has also been used to discriminate post-radiation necrosis from residual tumor after chemoradiotherapy (81).

Whereas classical MT imaging is able to measure exchange between the bulk water and immobile solid-like protons, Zhou and van Zijl et al. have demonstrated selective detection of mobile proteins and peptides by amide proton transfer (APT) imaging. Amide protons resonating at 3.5 ppm downfield of the bulk water can be selectively irradiated to probe the magnetization exchange of these protons with the bulk water. APT contrast is influenced by protein and peptide content and the amide proton exchange rate, which is increased at higher pH. It has been shown that APT imaging

can detect brain tumors, in both the preclinical (82,83) and clinical setting (84-86), mainly based on their increased protein and peptide content. Furthermore, Jia et al. have shown that prostate cancer is associated with significantly higher APT ratios compared to benign tissue (87). Zhou et al. have demonstrated that necrotic lesions possess low APT signal compared to viable tumor after radiotherapy of rat gliomas, which was explained by reduced levels of mobile cytosolic proteins and peptides as a result of loss of cytoplasm (88). Moreover, Dula et al. have shown the potential of APT imaging to assess early response of human breast cancer to chemotherapy (89).

1.2.4. The longitudinal relaxation time in the rotating frame $T_{1\rho}$

A useful endogenous MR parameter that is also related to macromolecular interactions is the longitudinal relaxation time in the rotating frame $T_{1\rho}$. $T_{1\rho}$ imaging involves application of an on-resonance spin-lock pulse after a 90° excitation pulse, that locks the magnetization in the rotating frame. During application of this spin-lock pulse, longitudinal relaxation along the spin-lock field will take place, which is similar to T_1 relaxation at very low field strength. Therefore, $T_{1\rho}$ is sensitive to molecular motion in the low frequency range and predominantly affected by protein-water interactions. It has been shown that $T_{1\rho}$ contrast can be exploited for tumor imaging (90-92). In addition, several studies have shown increased $T_{1\rho}$ after treatment in pre-clinical tumor models, consistent with expected cellular and structural changes during apoptosis or necrosis (93-95).

1.2.5. Additional endogenous MRI biomarkers

Besides these more commonly investigated methods, a number of additional endogenous MRI biomarkers have been explored for cancer imaging. Arterial spin labeling (ASL) is a technique that is able to measure perfusion by magnetically labeling protons in the blood (53,96). Several studies have shown the utility of ASL for imaging tumor perfusion and changes in blood flow after treatment (97,98). Another interesting biomarker is the elastography-derived viscoelasticity. It has long been recognized that mechanical properties of tumors may be different compared to surrounding normal tissues, which is the basis of tumor identification by palpation. It has been described that magnetic resonance elastography (MRE) could discriminate between benign and malignant liver tumors based on their viscoelastic properties (99,100). In addition, Pepin et al. have demonstrated that the elastography-derived shear stiffness was significantly reduced within days of chemotherapy treatment of subcutaneous mouse tumors (101). It was suggested that the observed reduction in stiffness was caused by a decreased cellularity in combination with cell death.

1.3. Contrast-enhanced MRI biomarkers

Oncologic imaging has considerably benefitted from the development of MRI contrast agents. Especially clinically approved low molecular weight paramagnetic contrast agents, such as gadopentetate dimeglumine (Gd-DTPA, Magnevist) and gadoterate meglumine (Gd-DOTA, Dotarem), are widely employed. These contrast agents reduce local tissue relaxation times and provide positive contrast (i.e. generate more signal)

in T_1-weighted images. After intravenous administration, contrast agents will distribute through the body and may leak from the vasculature into the tumor interstitial space.

Tumors generally possess an abnormal vascular structure and physiology, resulting in a different appearance on T_1-weighted images after contrast agent injection. Therefore, contrast-enhanced MRI enables more accurate tumor detection and delineation and improves cancer staging and grading (102-104). Contrast-enhanced MRI scans of different breast tumors are shown in Figure 3, which demonstrates its ability to visualize lesion shape (105).

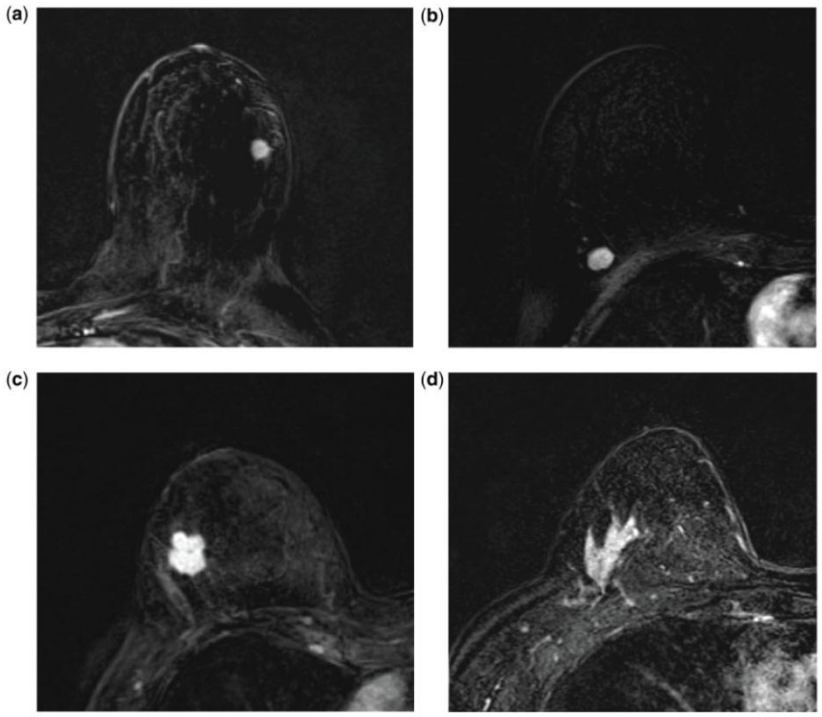

Figure 3. Axial contrast-enhanced images of the breast showing different mass-enhancing lesions, with a (a) round, (b) oval, (c) lobulated, and (d) irregular shape. The pre-contrast image was subtracted from the post-contrast image to highlight regions with signal enhancement. Adapted from Petralia et al. (105) with permission. © 2011 by the International Cancer Imaging Society; Licencee BioMed Central Ltd.

Additional physiological information may be extracted by rapid image acquisition before, during and after contrast agent injection. Mainly two dynamic acquisition approaches have been employed; dynamic susceptibility contrast-enhanced MRI (DSC-MRI) and dynamic contrast-enhanced MRI (DCE-MRI). DSC-MRI is based on rapid acquisition of T_2^*-weighted images and measurement of a rapid decrease in signal intensity upon contrast agent injection, due to an increase in magnetic susceptibility. The main application of DSC-MRI is in assessment of brain perfusion (106). DCE-MRI has been more extensively applied for tumor imaging and involves rapid dynamic acquisition of T_1-weighted images to measure the dynamic signal enhancement upon contrast agent injection (106). The spatial and temporal enhancement pattern in the tumor is affected by underlying pathophysiological properties. Semi-quantitative parameters may be determined that can describe the measured contrast agent uptake

kinetics, including the time to peak, maximum upslope, maximum enhancement and area under the curve (AUC) (107). However, these parameters often do not have a direct physiological interpretation and are dependent on the acquisition protocol. After conversion of the dynamic signal intensity to contrast agent concentration, quantitative analysis by tracer-kinetic modeling can be employed to extract physiological parameters that reflect underlying tumor physiology, such as the blood volume, blood flow, microvascular permeability and volume of the extravascular extracellular space (EES) (106,108). Tracer-kinetic analysis requires assessment of the arterial input function (AIF), which describes the contrast agent concentration in the arterial inlet of the tumor. If the AIF cannot be directly measured, a population averaged AIF may be used (109) or other methods for AIF extraction could be employed, such as reference region models (110) or blind AIF estimation methods (111,112). Contrast agent distribution in the tumor can be modeled by the use of compartmental models that describe the different tissue subspaces over which a contrast agent distributes and the exchange rates between them. The different contrast agent distribution spaces and exchange between them are schematically depicted in Figure 4. Two major distribution compartments can be identified: the capillary vascular plasma space and the EES (113). The transfer rate of the contrast agent to the tumor tissue is influenced by the plasma flow (F_p) and the endothelial permeability surface area product (PS), which describes the microvascular leakage rate and is dependent on the size of the contrast agent that is used.

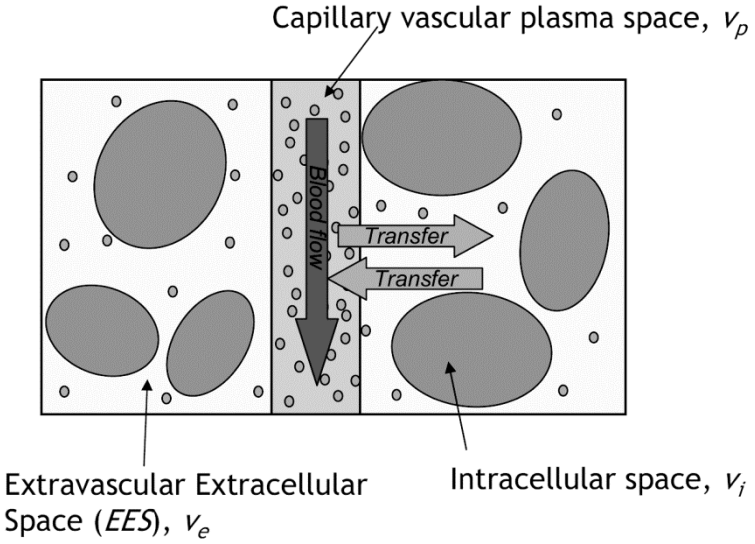

Figure 4. The different compartments involved in the distribution of contrast agents in the tissue and functional variables involved in contrast agent transfer between the compartments. Administered contrast agents enter the tumor tissue via the vascular plasma space v_p, from which they will be distributed into the extravascular extracellular space (EES), followed by washout from the EES. Adapted from Jackson et al. (113) with permission. © 2005 by Springer-Verlag.

A number of tracer-kinetic models have been used to describe contrast agent distribution in the tissue. One of the most widely applied tracer-kinetic models is the Standard Tofts model, which is a one-compartment model that assumes that the tissue is weakly vascularized with a well-mixed EES (106,114,115). It is a two-

parameter model that facilitates estimation of the volume transfer constant K^{trans} (min^{-1}) and washout rate constant k_{ep} (min^{-1}) between the EES and vascular plasma space, in which K^{trans} is a composite measure affected by both the plasma flow and microvascular permeability. The EES volume fraction v_e can be calculated by K^{trans}/k_{ep}. An expansion of this model is the Extended Tofts model, which incorporates a non-negligible vascular contribution by additional assessment of the vascular plasma fraction v_p (115,116). More complex models have been developed, which model the blood plasma and interstitial space both as single compartments, such as the two-compartment exchange (2CX) model (106,117). The 2CX model allows estimation of 4 parameters, including F_p, v_p, PS and v_e, thereby enabling separate estimation of blood flow and permeability (106). A schematic representation of these tracer-kinetic models is shown in Figure 5.

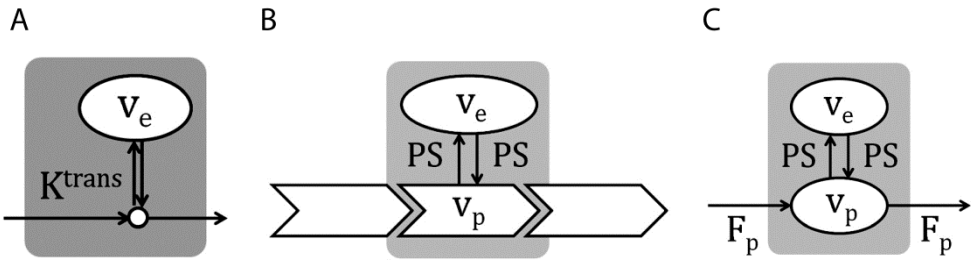

Figure 5. Schematic representation of different tracer-kinetic models. A) Diagram of the standard Tofts model. It assumes a negligible vascular plasma fraction and a well-mixed interstitial space v_e. Contrast agent influx is described by the transfer constant K^{trans}. B) Diagram of the extended Tofts model, which enables estimation of vascular plasma fraction v_p, K^{trans} and v_e. It is valid in weakly vascularized tissues with a well-mixed interstitial space and in highly perfused tissues. K^{trans} is a mixture of the vascular plasma flow F_p and permeability-surface area product (PS). In case of a non-negligible v_p, the tissue must be highly perfused and in that case K^{trans}=PS. C) Diagram of the two-compartment exchange (2CX) model. It models both the vascular plasma space and interstitial space as single compartments and facilitates estimation of F_p, v_p, PS and v_e. Adapted from Sourbron et al. (118) with permission. © 2013 by John Wiley & Sons, Ltd.

Tracer-kinetic parameters provide physiological imaging biomarkers that can aid in cancer detection and treatment evaluation. It has been shown that quantitative DCE-MRI analysis can discriminate between benign and malignant tumors (117,119-121). In addition, DCE-MRI has been widely employed for treatment evaluation. Cancer treatment with chemotherapy, radiotherapy or antivascular therapy generally results in an early decrease in K^{trans}, reflective of a reduced microvascular function (10,122-126). In addition, it has been demonstrated that DCE-MRI parameters may correlate with tumor oxygenation and vascularity and can be used as a predictor for response to radio- or chemotherapy treatment (127,128).

Whereas DCE-MRI utilizing low molecular weight contrast agents, has been widely employed to assess reduced microvascular function by evaluation of changes in K^{trans}, accurate assessment of various treatment induced vascular alterations may require more detailed tracer-kinetic analysis. As an example, antivascular therapies often induce alterations in both the microvascular permeability and tumor blood flow. Antivascular drugs can be divided into two categories: vascular disrupting agents, which are aimed at attacking the established tumor vasculature, and antiangiogenic

agents, focused on inhibiting formation of new blood vessels. Vascular disrupting agents often induce increased microvascular permeability, in conjunction with a decreased microvascular flow (129,130). Similarly, antiangiogenic agents often induce changes in multiple vascular properties (131). In clinical trials of antivascular therapies, often a reduction in K^{trans} is reported as an indicator of tumor treatment response. However, K^{trans} is a composite measure of permeability, capillary surface area and tumor blood flow (132). Separate estimation of these parameters would be of great interest, to obtain a more complete view on the various treatment-induced physiological changes. This may aid in identification of the mechanisms of drug action, dose optimization and treatment selection (126). More advanced tracer-kinetic models, such as the 2CX model, enable differentiation between blood flow and microvascular permeability (118). However, application of these models is limited due to the more stringent requirements on data acquisition (118). Another approach that affords a higher sensitivity to changes in specific tracer-kinetic parameters is the use of macromolecular, high molecular weight contrast agents.

1.3.1. Macromolecular DCE-MRI

Macromolecular contrast agents, also referred to as blood pool agents, provide distinct information on physiological tumor properties in comparison with low molecular weight contrast agents. Since microvascular permeability in tumors is generally high, low molecular weight contrast agents are often readily diffusible across the tumor vasculature (Figure 6A). Therefore, their transfer into the tumor interstitial space is often dominated by blood flow. In contrast, macromolecular agents possess limited transendothelial diffusion and a relatively long intravascular half-life (Figure 6B).

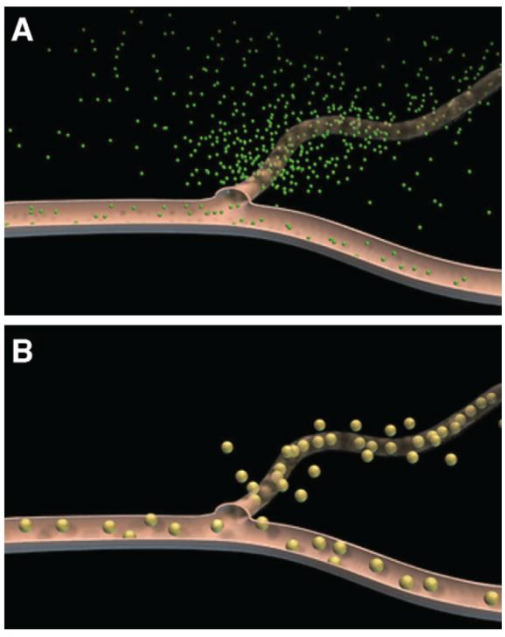

Figure 6. Graphic representation of the transfer of (A) low molecular weight contrast media and (B) high molecular weight contrast media from the tumor vasculature into the interstitial space. Adapted from Barrett et al. (133) with permission. © 2006 by Elsevier Ireland Ltd.

It has been shown that macromolecular contrast agents enable improved assessment of the higher blood volume and microvascular permeability of tumors, which have been associated with angiogenesis and related to tumor grade (53,133-139). In addition, a number of studies have exploited the dependence of tracer-kinetic parameters on contrast agent size to enable an improved evaluation of cancer therapies (140-145). Dendrimer-based contrast agents may be especially suitable for investigation of the dependence of tracer-kinetic parameters on contrast agent molecular weight and to study tumor leakiness to therapeutic agents. Dendrimers are a class of highly branched synthetic polymers with a globular shape, that possess tunable molecular weight and composition (146,147). A wide variety of dendrimer types have been synthesized, including polyamidoamine (PAMAM), poly(propylene imine) (PPI) and poly-L-lysine (PLL) dendrimers (148). Differences in dendrimer core, repeating units and surface functionality between these dendrimers, define their characteristics and in vivo behavior (149-153). Dendrimers are an attractive platform for imaging or drug delivery, because their periphery can be functionalized with various imaging labels or therapeutic agents (147,148,154-157). In addition, their size can be increased proportional to their generation, without altering their chemical composition (147). This facilitates assessment of the effect of molecular size on biodistribution and tumor accumulation, which is an important aspect in drug delivery (148,153,158,159). With respect to their application in imaging, dendrimer-based contrast agents have been used for both MR angiography (160,161) and for quantitative DCE-MRI involving tracer-kinetic modeling (139), exploiting their increased relaxivity, prolonged intravascular retention, and suitability of high molecular weight agents to assess tumor microvascular permeability and blood volume.

An alternative type of blood pool agents is represented by low molecular weight contrast media that reversibly bind to serum albumin, of which the most common example is gadofosveset trisodium (MS-325) (162-164). Reversible albumin-binding results in decreased contrast agent extravasation and a prolonged circulation half-life. Its main application is in MR angiography, which exploits the limited extravasation and prolonged intravascular life-time of blood pool agents to visualize the tumor vasculature. This facilitates high quality image acquisition without stringent requirements on temporal resolution. Goyen et al. have demonstrated that gadofosveset has several promising application areas, including diagnosis of vascular stenosis and overall characterization of vascular disease (165). Gadofosveset has also been explored for tumor imaging (166), nodal staging (167,168) and therapy evaluation (169).

1.4. Imaging biomarkers for the evaluation of HIFU treatment

A number of MRI biomarkers may have applications in the evaluation of HIFU treatment. The following sections will focus on the principles of HIFU, the role of MRI in guidance of HIFU therapy, and the potential sensitivity of MRI biomarkers to HIFU-induced tumor changes.

1.4.1. The principles of HIFU treatment

HIFU treatment is an emerging noninvasive cancer treatment strategy (170-172). In contrast to diagnostic ultrasound, using relatively high frequency (1-20 MHz) ultrasound waves with low acoustic power, HIFU employs focused ultrasound waves of relatively low frequency (~0.8-3.5 MHz) but high acoustic power (4). In the MHz frequency range, ultrasound waves have relatively short wavelengths, which allows them to be focused into a very small treatment volume.

Local absorption of focused ultrasound energy induces high temperature elevations in the tumor, whereas healthy surrounding tissue is minimally affected (Figure 7A). Local tissue heating to temperatures of about 60 °C induces coagulative necrosis and facilitates thermal tumor ablation (4). Volumetric ablation can be performed by mechanical or electronic steering of the ellipsoidal ablation volume (Figure 7B).

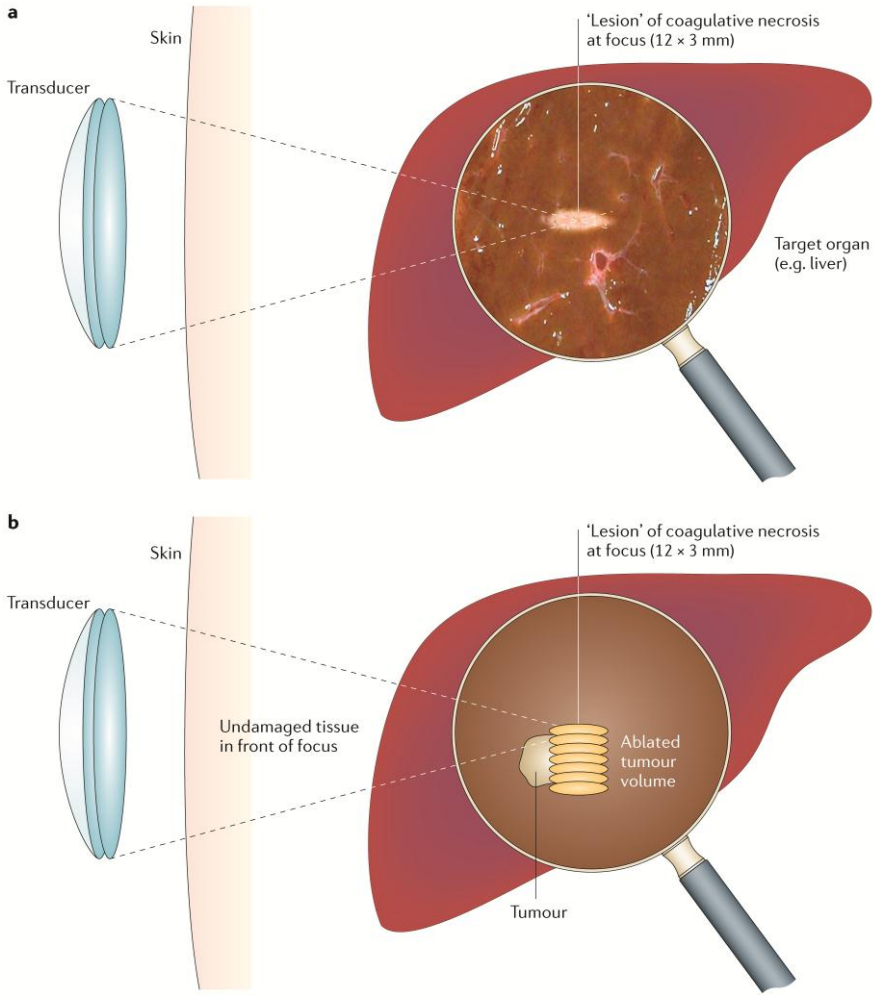

Figure 7. Schematic drawing showing the principle of HIFU treatment. (A) An extracorporeal HIFU transducer generates an ultrasound beam, which is focused deep within the body. Deposition of ultrasound energy in the target tissue (liver in this case), results in focal heating of the tissue and a cigar-shaped lesion is formed due to coagulative necrosis. (B) By placement of multiple ablation cells in the tumor, thermal ablation of the entire tumor can be performed with no damage to the surrounding tissue. Adapted from Kennedy et al. (4) with permission. © 2005 by Nature Publishing Group.

Besides induction of temperatures that are directly cytotoxic, HIFU can be employed to induce mild temperature elevations (40-42 °C) that increase microvascular permeability and facilitate hyperthermia-mediated drug delivery (173-175). Dependent on the applied treatment settings, HIFU may also induce tissue damage by mechanical effects (170,173). The oscillating acoustic pressure during propagation of ultrasound waves through the tissue may result in generation, growth and oscillation of small gas bubbles, which is called cavitation (4). Collapse of cavitation bubbles (inertial cavitation) can induce both irreversible cell damage and induce a reversible increase in membrane permeability. In addition, stable oscillations may induce local mechanical stress in blood vessel walls. Besides cavitation, high amplitude sonications may induce a transfer of momentum to the tissue, generating a unidirectional force called a radiation force (173). Radiation forces could lead to structural changes to the tissue, by induction of local tissue displacements and acoustic streaming. Acoustic cavitation and induction of radiation forces may be exploited to enhance the delivery of therapeutic agents to the tumor (173).

1.4.2. MR-guided HIFU

Clinical application of HIFU for tumor treatment is expanding from benign uterine fibroids (176,177) to malignant lesions (5), including prostate (178-181), liver (182-184), breast (185,186), pancreatic (187) and bone tumors (188). For treatment of malignant tumors, accurate treatment planning, monitoring and evaluation are of critical importance to ensure whole tumor coverage. Therefore, HIFU therapy is often performed in conjunction with MR image guidance. MR thermometry based on the linear dependence of the proton resonance frequency (PRF) on changes in tissue temperature, allows for accurate temperature monitoring during treatment (189,190). MR-HIFU systems, in which the HIFU transducer is integrated in the patient bed of the MRI scanner, provide real-time temperature feedback control. Knowledge of the temperature history of the tissue allows for calculation of the locally applied thermal dose.

A thermal dose of 240 equivalent minutes (EM) at 43 °C is generally used as a threshold for predicting cell death (191-193). However, it has been shown that the thermal sensitivity may be tissue and species dependent (192,193). Furthermore, whereas high temperatures of approximately 60 °C can immediately result in coagulative necrosis, sublethal temperature elevations may potentially result in delayed cell death (194). To verify that the induced temperature elevations have indeed resulted in tumor cell death and assess the extent of successfully treated tumor, accurate treatment evaluation is of crucial importance. Clinical MRI evaluation of HIFU therapy has been mainly restricted to T_2-weighted and contrast-enhanced T_1-weighted imaging (5,178,181,195-198). HIFU-treated tumor generally has a heterogeneous appearance on T_2-weighted images, whereas contrast-enhanced T_1-weighted images show a lack of contrast-enhancement. Although these methods provide useful information about treatment response, a number of MRI biomarkers potentially have a higher specificity or sensitivity for the early identification of successfully treated tumor.

1.4.3. MRI biomarkers for the evaluation of HIFU treatment

In order to identify suitable imaging biomarkers for evaluation of HIFU treatment, insight in HIFU-induced tumor changes is required. After focal HIFU treatment, the ablated lesion may be divided into three zones (Figure 8): the central ablation zone with lethal temperature elevations to approximately 60 °C, the peripheral or transitional zone with sublethal and potentially reversible thermal damage at temperatures between 41-45 °C and the unaffected surrounding tissue (194).

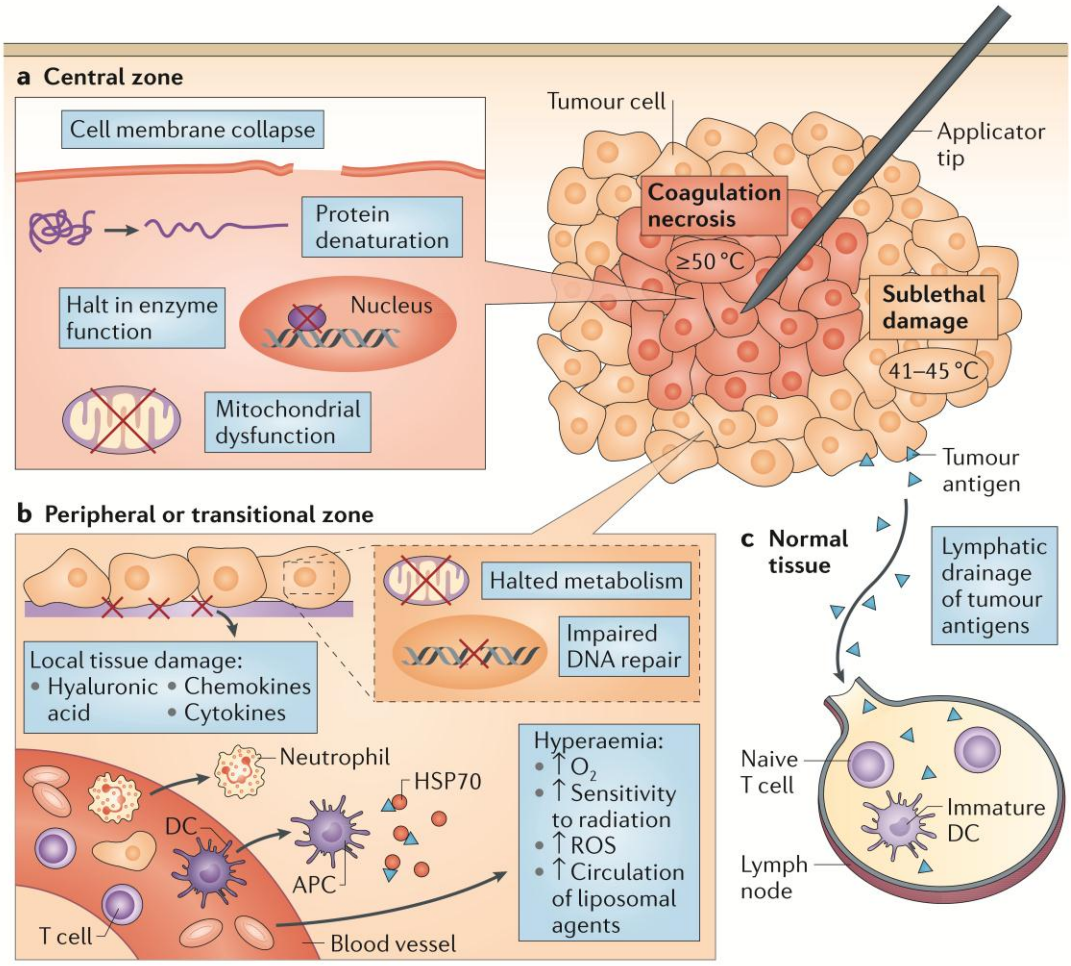

Figure 8. Schematic overview of the zones of hyperthermic ablation. The location of heat application is surrounded by three zones. (A) The central zone, in which temperatures exceeding 50 °C upon HIFU treatment will result in coagulative necrosis. (B) The peripheral or transitional zone, in which temperatures between 41-45 °C can still induce heat-induced injury, but this may be reversible and recovery from this injury could occur. On the other hand, metabolic function may be impaired and cells in this zone may be susceptible to further injury. C) The normal surrounding tissues, in which blood vessels cause a heat-sink effect, which dissipates the thermal energy and decreases ablation efficacy. The different tissue changes in the three zones are summarized in the insets. Adapted from Chu et al. (194) with permission. © 2014 by Nature Publishing Group.

In the central ablation zone, temperatures of approximately 60 °C will result in rapid denaturation of proteins, which is cytotoxic and leads to coagulative necrosis. In addition, heat-induced damage to cellular membranes will lead to impairment of facilitated diffusion, energy-dependent transport across the cell membrane, and other critically important membrane functions. Other mechanisms of cell death include

inactivation of crucial enzymes, such as DNA polymerase, and mitochondrial dysfunction. Furthermore, vascular disruption and vascular occlusion may be observed after treatment (194,199).
The transitional zone can also be characterized by halted metabolism and impaired DNA repair, which could result in induction of apoptosis (194). Further delayed cell death could be caused by ischemia as a consequence of vascular damage, or ischemia-reperfusion injury by formation of reactive oxygen species (ROS). Other tissue changes involve increased release of chemokines and cytokines that could stimulate the immune response. Hyperthermic conditions in the peripheral zone might also result in increased blood flow and enhanced microvascular permeability (174,175,200,201). In the normal surrounding tissues, blood vessels cause heat dissipation and decrease the ablation efficacy. Tumor antigens that are released after necrosis could stimulate an immune response.

MR imaging biomarkers that are sensitive to these HIFU-induced tissue changes could facilitate early evaluation of HIFU therapy and identification of the successfully treated tumor. These imaging biomarkers may either be directly related to a loss of cell viability, or be reflective of structural, functional or metabolic changes that can result in delayed cell death.
A number of acute treatment effects may be directly detectable with MRI. The ADC is a promising biomarker to detect structural disruption, damage to cellular membranes and cell shrinkage due to coagulative necrosis in the central ablation zone. The MTR, APT and $T_{1\rho}$ are potentially suitable for assessment of changes in macromolecular structure, dynamics and content in this area. These properties can be directly altered by high temperature elevations or change as a consequence of structural disruption and a loss of viability. The APT and $T_{1\rho}$ potentially possess increased sensitivity and specificity to protein denaturation and aggregation. Relaxation times may also be altered, due to changes in water content, water access to macromolecules or paramagnetic sites, or changes in tissue structure and rigidity. Structural changes may also be evaluated by MR elastography. Besides these structural alterations, tumor function and metabolism are directly altered after HIFU. HIFU-induced reduced microvascular function due to vascular disruption and congestion could be evaluated with DCE-MRI and MRS may be employed to assess direct changes in energy status and metabolism.
Mild temperature elevations in the peripheral zone may result in decreased microvascular function, or hyperemia and increased permeability, dependent on the temperature elevation (174). These effects may be investigated with macromolecular DCE-MRI, including MR angiography to investigate potential microvascular occlusion or tracer-kinetic modeling to assess changes in microvascular permeability.
Delayed cell death may occur in the transitional zone, as a consequence of vascular damage, tumor hypoxia and halted metabolism. These functional changes, that often precede cell death, may be assessed with DCE-MRI and MRS. ADC measurements may be employed to assess delayed cell death.

1.4.4. Multiparametric MRI evaluation of HIFU treatment

It has been discussed that HIFU treatment may induce alterations in multiple MRI parameters. These parameters could be affected by various underlying tumor changes and may be heterogeneous and time dependent. Therefore, the ability of a single MRI parameter to identify the successfully treated tumor after HIFU is likely to be limited. However, combining the different MR parameters into a multiparametric MRI protocol may facilitate more robust assessment of the treated tissue. Previous non-HIFU studies have shown that a multiparametric MRI analysis enables improved tumor detection, classification and treatment response evaluation, compared to analysis of a single parameter (202-210). Clustering algorithms, that divide the tumor into groups of pixels with similar MR parameter values, can be employed for automatic segmentation of tumor tissue populations. The combination of multiparametric MRI with cluster analysis offers promising approaches to discriminate between viable and non-viable tumor tissue (211-213). Quantification of these distinct tumor populations not only enables assessment of early therapy response, but also offers opportunities to evaluate changes in functional MRI biomarkers specifically in the viable tumor regions, which is often the tissue of therapeutic interest (214,215).

1.5. Aim and outline of this thesis

The aim of this thesis was the development and evaluation of endogenous and contrast-enhanced MRI methods for tumor imaging and early therapy assessment, with a specific focus on HIFU treatment. To this aim, various studies were performed in a preclinical setting.
The studies in the first part of this thesis were focused on the characterization and in vivo application of macromolecular contrast agents for vascular imaging and evaluation of tumor microvascular function.

Chapter 2 describes the characterization and in vivo evaluation of albumin-binding dendrimer-based MRI contrast agents. Contrast agent efficacy and albumin-binding capability were assessed using relaxometry measurements. Subsequently, the blood-kinetics and biodistribution of the agents were determined in tumor-bearing mice. The utility of the agents for blood pool imaging was evaluated using whole-body MR angiography.

Related to chapter 2, **chapter 3** is aimed at characterization and in vivo evaluation of dendrimer-based MRI contrast agents of various molecular weight. Relaxometric properties of the agents and their blood-kinetics and biodistribution were determined in tumor-bearing mice. The potential value of the highest molecular weight dendrimer for macromolecular contrast-enhanced MRI was examined by whole-body MR angiography.

The study in **chapter 4** demonstrates a novel tracer-kinetic modeling approach for macromolecular DCE-MRI, which facilitated a more detailed assessment of tumor vascular status. The multi-agent modeling approach involved sequential injection of

contrast agents of various molecular weight and simultaneous modeling of the multi-agent data.

The remaining part of this thesis describes studies aimed at assessing the suitability of various MRI biomarkers for the evaluation of HIFU treatment. In the work of **chapter 5 and 6**, HIFU treatment was performed outside the MRI scanner and MRI measurements were done at high field strength.

The study in **chapter 5** describes the application of a multiparametric MRI protocol for the evaluation of HIFU treatment of subcutaneous mouse tumors. Mice underwent MRI before, directly after and 3 days after HIFU, and cluster analysis of the multiparametric MRI data (consisting of T_1, T_2, ADC and MTR) was performed to identify the successfully treated tumor regions. Quantitative comparison between MRI-derived and histology-derived non-viable tumor fractions enabled selection of the optimal set of MRI parameters for evaluation of HIFU treatment.

Chapter 6 describes a cluster analysis of tracer-kinetic parameters derived from DCE-MRI, to identify regional tracer-kinetic changes after HIFU treatment of subcutaneous tumors in mice. DCE-MRI was performed before, directly after and 3 days after HIFU. Non-perfused tumor fractions were quantitatively compared with histology-derived non-viable tumor fractions. Moreover, changes in contrast agent uptake-kinetics in the region outside the non-perfused tumor were assessed.

Whereas HIFU treatment was performed outside the MRI scanner in chapter 5 and 6, HIFU treatment was performed under MRI guidance in the study described in **chapter 7**, in which a clinical 3 T MR-HIFU system was used as a step towards clinical translation. This study focused on evaluation of HIFU treatment using a multiparametric MRI protocol, consisting of quantitative assessment of T_1, T_2, ADC, $T_{1\rho}$, APT and tracer-kinetic parameters derived from DCE-MRI. HIFU treatment was performed on subcutaneous rat tumors and MRI was performed before, directly after and 3 days after treatment. HIFU-induced changes in the different MRI parameters were extensively investigated. In addition, the optimal set of MRI parameters to identify successfully treated tumor was determined by cluster analysis of the multiparametric MRI data and quantitative comparison between MRI-derived and histology-derived non-viable tumor fractions. Furthermore, the performance of multiparametric MRI for HIFU therapy evaluation was compared with contrast-enhanced MRI and temperature mapping data.

In **chapter 8**, a general discussion reflecting upon the work presented in this thesis and future perspectives of the different MRI methods are given.

1.6. References

1. Ferlay J, Soerjomataram I, Dikshit R, Eser S, Mathers C, Rebelo M, Parkin DM, Forman D, Bray F. Cancer incidence and mortality worldwide: Sources, methods and major patterns in GLOBOCAN 2012. Int J Cancer 2015;136(5):E359-386.

2. Eberhardt SC, Johnson JA, Parsons RB. Oncology imaging in the abdomen and pelvis: where cancer hides. Abdom Imaging 2013;38(4):647-671.
3. Solomon SB, Silverman SG. Imaging in interventional oncology. Radiology 2010;257(3):624-640.
4. Kennedy JE. High-intensity focused ultrasound in the treatment of solid tumours. Nat Rev Cancer 2005;5(4):321-327.
5. Zhou YF. High intensity focused ultrasound in clinical tumor ablation. World J Clin Oncol 2011;2(1):8-27.
6. Marcus CD, Ladam-Marcus V, Cucu C, Bouche O, Lucas L, Hoeffel C. Imaging techniques to evaluate the response to treatment in oncology: current standards and perspectives. Crit Rev Oncol Hematol 2009;72(3):217-238.
7. Rezai P, Pisaneschi MJ, Feng C, Yaghmai V. A radiologist's guide to treatment response criteria in oncologic imaging: anatomic imaging biomarkers. AJR Am J Roentgenol 2013;201(2):237-245.
8. Eisenhauer EA, Therasse P, Bogaerts J, Schwartz LH, Sargent D, Ford R, Dancey J, Arbuck S, Gwyther S, Mooney M, Rubinstein L, Shankar L, Dodd L, Kaplan R, Lacombe D, Verweij J. New response evaluation criteria in solid tumours: revised RECIST guideline (version 1.1). Eur J Cancer 2009;45(2):228-247.
9. Desar IM, van Herpen CM, van Laarhoven HW, Barentsz JO, Oyen WJ, van der Graaf WT. Beyond RECIST: molecular and functional imaging techniques for evaluation of response to targeted therapy. Cancer Treat Rev 2009;35(4):309-321.
10. Bell LK, Ainsworth NL, Lee SH, Griffiths JR. MRI & MRS assessment of the role of the tumour microenvironment in response to therapy. NMR Biomed 2011;24(6):612-635.
11. Penet MF, Glunde K, Jacobs MA, Pathak AP, Bhujwalla ZM. Molecular and functional MRI of the tumor microenvironment. J Nucl Med 2008;49(5):687-690.
12. Penet MF, Artemov D, Farahani K, Bhujwalla ZM. MR - eyes for cancer: looking within an impenetrable disease. NMR Biomed 2013;26(7):745-755.
13. Gillies RJ, Raghunand N, Karczmar GS, Bhujwalla ZM. MRI of the tumor microenvironment. J Magn Reson Imaging 2002;16(4):430-450.
14. Stasinopoulos I, Penet MF, Chen Z, Kakkad S, Glunde K, Bhujwalla ZM. Exploiting the tumor microenvironment for theranostic imaging. NMR Biomed 2011;24(6):636-647.
15. Carmeliet P, Jain RK. Angiogenesis in cancer and other diseases. Nature 2000;407(6801):249-257.
16. Jain RK. Determinants of tumor blood flow: a review. Cancer Res 1988;48(10):2641-2658.
17. Jain RK. Transport of molecules across tumor vasculature. Cancer Metastasis Rev 1987;6(4):559-593.
18. Hobbs SK, Monsky WL, Yuan F, Roberts WG, Griffith L, Torchilin VP, Jain RK. Regulation of transport pathways in tumor vessels: role of tumor type and microenvironment. Proc Natl Acad Sci U S A 1998;95(8):4607-4612.
19. Dvorak HF, Nagy JA, Dvorak JT, Dvorak AM. Identification and characterization of the blood vessels of solid tumors that are leaky to circulating macromolecules. Am J Pathol 1988;133(1):95-109.

20. Gillies RJ, Schornack PA, Secomb TW, Raghunand N. Causes and effects of heterogeneous perfusion in tumors. Neoplasia 1999;1(3):197-207.
21. Kobayashi H, Watanabe R, Choyke PL. Improving conventional enhanced permeability and retention (EPR) effects; what is the appropriate target? Theranostics 2013;4(1):81-89.
22. Bernsen MR, Ruggiero A, van Straten M, Kotek G, Haeck JC, Wielopolski PA, Krestin GP. Computed tomography and magnetic resonance imaging. Recent Results Cancer Res 2013;187:3-63.
23. Kapoor V, Fukui MB, McCook BM. Role of 18FFDG PET/CT in the treatment of head and neck cancers: principles, technique, normal distribution, and initial staging. AJR Am J Roentgenol 2005;184(2):579-587.
24. Ben-Haim S, Ell P. 18F-FDG PET and PET/CT in the evaluation of cancer treatment response. J Nucl Med 2009;50(1):88-99.
25. Cyran CC, Paprottka PM, Eisenblatter M, Clevert DA, Rist C, Nikolaou K, Lauber K, Wenz F, Hausmann D, Reiser MF, Belka C, Niyazi M. Visualization, imaging and new preclinical diagnostics in radiation oncology. Radiat Oncol 2014;9:3.
26. Cai J, Li F. Single-photon emission computed tomography tracers for predicting and monitoring cancer therapy. Curr Pharm Biotechnol 2013;14(7):693-707.
27. Cosgrove D, Lassau N. Imaging of perfusion using ultrasound. Eur J Nucl Med Mol Imaging 2010;37 Suppl 1:S65-85.
28. Dewall RJ. Ultrasound elastography: principles, techniques, and clinical applications. Crit Rev Biomed Eng 2013;41(1):1-19.
29. Zhou Z, Wu W, Wu S, Xia J, Wang CY, Yang C, Lin CC, Tsui PH. A survey of ultrasound elastography approaches to percutaneous ablation monitoring. Proc Inst Mech Eng H 2014;228(10):1069-1082.
30. Penet MF, Mikhaylova M, Li C, Krishnamachary B, Glunde K, Pathak AP, Bhujwalla ZM. Applications of molecular MRI and optical imaging in cancer. Future Med Chem 2010;2(6):975-988.
31. Begley JK, Redpath TW, Bolan PJ, Gilbert FJ. In vivo proton magnetic resonance spectroscopy of breast cancer: a review of the literature. Breast Cancer Res 2012;14(2):207.
32. Brindle KM, Bohndiek SE, Gallagher FA, Kettunen MI. Tumor imaging using hyperpolarized 13C magnetic resonance spectroscopy. Magn Reson Med 2011;66(2):505-519.
33. Brindle K. New approaches for imaging tumour responses to treatment. Nat Rev Cancer 2008;8(2):94-107.
34. Pathak AP, Penet MF, Bhujwalla ZM. MR molecular imaging of tumor vasculature and vascular targets. Adv Genet 2010;69:1-30.
35. Penet MF, Chen Z, Bhujwalla ZM. MRI of metastasis-permissive microenvironments. Future Oncol 2011;7(11):1269-1284.
36. Narunsky L, Oren R, Bochner F, Neeman M. Imaging aspects of the tumor stroma with therapeutic implications. Pharmacol Ther 2014;141(2):192-208.
37. Strijkers GJ, Kluza E, Van Tilborg GA, van der Schaft DW, Griffioen AW, Mulder WJ, Nicolay K. Paramagnetic and fluorescent liposomes for target-specific imaging and therapy of tumor angiogenesis. Angiogenesis 2010;13(2):161-173.

38. Mulder WJ, Strijkers GJ, Habets JW, Bleeker EJ, van der Schaft DW, Storm G, Koning GA, Griffioen AW, Nicolay K. MR molecular imaging and fluorescence microscopy for identification of activated tumor endothelium using a bimodal lipidic nanoparticle. FASEB J 2005;19(14):2008-2010.
39. Haacke EM. Magnetic resonance imaging: physical principles and sequence design. New York: Wiley; 1999.
40. De Schepper AM, De Beuckeleer L, Vandevenne J, Somville J. Magnetic resonance imaging of soft tissue tumors. Eur Radiol 2000;10(2):213-223.
41. De Schepper AM, Bloem JL. Soft tissue tumors: grading, staging, and tissue-specific diagnosis. Top Magn Reson Imaging 2007;18(6):431-444.
42. Aydin H, Kizilgoz V, Tatar IG, Damar C, Ugan AR, Paker I, Hekimoglu B. Detection of prostate cancer with magnetic resonance imaging: optimization of T1-weighted, T2-weighted, dynamic-enhanced T1-weighted, diffusion-weighted imaging apparent diffusion coefficient mapping sequences and MR spectroscopy, correlated with biopsy and histopathological findings. J Comput Assist Tomogr 2012;36(1):30-45.
43. Davis PL, McCarty KS, Jr. Magnetic resonance imaging in breast cancer staging. Top Magn Reson Imaging 1998;9(1):60-75.
44. Hasegawa S, Semelka RC, Noone TC, Woosley JT, Marcos HB, Kenney PJ, Siegelman ES. Gastric stromal sarcomas: correlation of MR imaging and histopathologic findings in nine patients. Radiology 1998;208(3):591-595.
45. Rofstad EK, Steinsland E, Kaalhus O, Chang YB, Hovik B, Lyng H. Magnetic resonance imaging of human melanoma xenografts in vivo: proton spin-lattice and spin-spin relaxation times versus fractional tumour water content and fraction of necrotic tumour tissue. Int J Radiat Biol 1994;65(3):387-401.
46. Braunschweiger PG, Schiffer LM, Furmanski P. 1H-NMR relaxation times and water compartmentalization in experimental tumor models. Magn Reson Imaging 1986;4(4):335-342.
47. Jakobsen I, Kaalhus O, Lyng H, Rofstad EK. Detection of necrosis in human tumour xenografts by proton magnetic resonance imaging. Br J Cancer 1995;71(3):456-461.
48. McSheehy PM, Weidensteiner C, Cannet C, Ferretti S, Laurent D, Ruetz S, Stumm M, Allegrini PR. Quantified tumor t1 is a generic early-response imaging biomarker for chemotherapy reflecting cell viability. Clin Cancer Res 2010;16(1):212-225.
49. Janick PA, Hackney DB, Grossman RI, Asakura T. MR imaging of various oxidation states of intracellular and extracellular hemoglobin. AJNR Am J Neuroradiol 1991;12(5):891-897.
50. O'Connor JP, Naish JH, Jackson A, Waterton JC, Watson Y, Cheung S, Buckley DL, McGrath DM, Buonaccorsi GA, Mills SJ, Roberts C, Jayson GC, Parker GJ. Comparison of normal tissue R1 and R2* modulation by oxygen and carbogen. Magn Reson Med 2009;61(1):75-83.
51. Negendank W, Corbett T, Crowley M, Kellogg C. Evidence for a contribution of paramagnetic ions to water proton spin-lattice relaxation in normal and malignant mouse tissues. Magn Reson Med 1991;18(2):280-293.

52. Walsh JC, Lebedev A, Aten E, Madsen K, Marciano L, Kolb HC. The clinical importance of assessing tumor hypoxia: relationship of tumor hypoxia to prognosis and therapeutic opportunities. Antioxid Redox Signal 2014;21(10):1516-1554.
53. Barrett T, Brechbiel M, Bernardo M, Choyke PL. MRI of tumor angiogenesis. J Magn Reson Imaging 2007;26(2):235-249.
54. Jordan BF, Magat J, Colliez F, Ozel E, Fruytier AC, Marchand V, Mignion L, Bouzin C, Cani PD, Vandeputte C, Feron O, Delzenne N, Himmelreich U, Denolin V, Duprez T, Gallez B. Mapping of oxygen by imaging lipids relaxation enhancement: A potential sensitive endogenous MRI contrast to map variations in tissue oxygenation. Magn Reson Med 2012.
55. Jordan BF, Magat J, Colliez F, Ozel E, Fruytier AC, Marchand V, Mignion L, Gallez B. Application of MOBILE (mapping of oxygen by imaging lipids relaxation enhancement) to study variations in tumor oxygenation. Adv Exp Med Biol 2013;789:281-288.
56. Colliez F, Neveu MA, Magat J, Cao Pham TT, Gallez B, Jordan BF. Qualification of a noninvasive magnetic resonance imaging biomarker to assess tumor oxygenation. Clin Cancer Res 2014;20(21):5403-5411.
57. Weidensteiner C, Allegrini PR, Sticker-Jantscheff M, Romanet V, Ferretti S, McSheehy PM. Tumour T1 changes in vivo are highly predictive of response to chemotherapy and reflect the number of viable tumour cells--a preclinical MR study in mice. BMC Cancer 2014;14:88.
58. Le Bihan D, Turner R, Moonen CT, Pekar J. Imaging of diffusion and microcirculation with gradient sensitization: design, strategy, and significance. J Magn Reson Imaging 1991;1(1):7-28.
59. Patterson DM, Padhani AR, Collins DJ. Technology insight: water diffusion MRI--a potential new biomarker of response to cancer therapy. Nat Clin Pract Oncol 2008;5(4):220-233.
60. Guo Y, Cai YQ, Cai ZL, Gao YG, An NY, Ma L, Mahankali S, Gao JH. Differentiation of clinically benign and malignant breast lesions using diffusion-weighted imaging. J Magn Reson Imaging 2002;16(2):172-178.
61. Sinha S, Lucas-Quesada FA, Sinha U, DeBruhl N, Bassett LW. In vivo diffusion-weighted MRI of the breast: potential for lesion characterization. J Magn Reson Imaging 2002;15(6):693-704.
62. Woodhams R, Matsunaga K, Iwabuchi K, Kan S, Hata H, Kuranami M, Watanabe M, Hayakawa K. Diffusion-weighted imaging of malignant breast tumors: the usefulness of apparent diffusion coefficient (ADC) value and ADC map for the detection of malignant breast tumors and evaluation of cancer extension. J Comput Assist Tomogr 2005;29(5):644-649.
63. Blackledge MD, Leach MO, Collins DJ, Koh DM. Computed diffusion-weighted MR imaging may improve tumor detection. Radiology 2011;261(2):573-581.
64. Lyng H, Haraldseth O, Rofstad EK. Measurement of cell density and necrotic fraction in human melanoma xenografts by diffusion weighted magnetic resonance imaging. Magn Reson Med 2000;43(6):828-836.
65. Padhani AR, Liu G, Koh DM, Chenevert TL, Thoeny HC, Takahara T, Dzik-Jurasz A, Ross BD, Van Cauteren M, Collins D, Hammoud DA, Rustin GJ, Taouli B, Choyke PL.

Diffusion-weighted magnetic resonance imaging as a cancer biomarker: consensus and recommendations. Neoplasia 2009;11(2):102-125.
66. Thoeny HC, Ross BD. Predicting and monitoring cancer treatment response with diffusion-weighted MRI. J Magn Reson Imaging 2010;32(1):2-16.
67. Moffat BA, Hall DE, Stojanovska J, McConville PJ, Moody JB, Chenevert TL, Rehemtulla A, Ross BD. Diffusion imaging for evaluation of tumor therapies in preclinical animal models. MAGMA 2004;17(3-6):249-259.
68. Ross BD, Moffat BA, Lawrence TS, Mukherji SK, Gebarski SS, Quint DJ, Johnson TD, Junck L, Robertson PL, Muraszko KM, Dong Q, Meyer CR, Bland PH, McConville P, Geng HR, Rehemtulla A, Chenevert TL. Evaluation of cancer therapy using diffusion magnetic resonance imaging. Mol Cancer Ther 2003;2(6):581-587.
69. Moffat BA, Chenevert TL, Lawrence TS, Meyer CR, Johnson TD, Dong Q, Tsien C, Mukherji S, Quint DJ, Gebarski SS, Robertson PL, Junck LR, Rehemtulla A, Ross BD. Functional diffusion map: a noninvasive MRI biomarker for early stratification of clinical brain tumor response. Proc Natl Acad Sci U S A 2005;102(15):5524-5529.
70. Chenevert TL, Stegman LD, Taylor JM, Robertson PL, Greenberg HS, Rehemtulla A, Ross BD. Diffusion magnetic resonance imaging: an early surrogate marker of therapeutic efficacy in brain tumors. J Natl Cancer Inst 2000;92(24):2029-2036.
71. Dzik-Jurasz A, Domenig C, George M, Wolber J, Padhani A, Brown G, Doran S. Diffusion MRI for prediction of response of rectal cancer to chemoradiation. Lancet 2002;360(9329):307-308.
72. Le Bihan D, Breton E, Lallemand D, Aubin ML, Vignaud J, Laval-Jeantet M. Separation of diffusion and perfusion in intravoxel incoherent motion MR imaging. Radiology 1988;168(2):497-505.
73. Lee HJ, Rha SY, Chung YE, Shim HS, Kim YJ, Hur J, Hong YJ, Choi BW. Tumor perfusion-related parameter of diffusion-weighted magnetic resonance imaging: correlation with histological microvessel density. Magn Reson Med 2014;71(4):1554-1558.
74. Woo S, Lee JM, Yoon JH, Joo I, Han JK, Choi BI. Intravoxel incoherent motion diffusion-weighted MR imaging of hepatocellular carcinoma: correlation with enhancement degree and histologic grade. Radiology 2014;270(3):758-767.
75. Fujima N, Yoshida D, Sakashita T, Homma A, Tsukahara A, Tha KK, Kudo K, Shirato H. Intravoxel incoherent motion diffusion-weighted imaging in head and neck squamous cell carcinoma: assessment of perfusion-related parameters compared to dynamic contrast-enhanced MRI. Magn Reson Imaging 2014;32(10):1206-1213.
76. Joo I, Lee JM, Han JK, Choi BI. Intravoxel incoherent motion diffusion-weighted MR imaging for monitoring the therapeutic efficacy of the vascular disrupting agent CKD-516 in rabbit VX2 liver tumors. Radiology 2014;272(2):417-426.
77. Wolff SD, Balaban RS. Magnetization transfer imaging: practical aspects and clinical applications. Radiology 1994;192(3):593-599.
78. Henkelman RM, Stanisz GJ, Graham SJ. Magnetization transfer in MRI: a review. NMR Biomed 2001;14(2):57-64.
79. Tsukushi S, Takahashi M, Miyagi N, Matsushima S, Andoh M, Kinosada Y. Magnetization transfer ratios of musculoskeletal tumors. J Orthop Sci 2002;7(5):524-527.

80. Bonini RH, Zeotti D, Saraiva LA, Trad CS, Filho JM, Carrara HH, de Andrade JM, Santos AC, Muglia VF. Magnetization transfer ratio as a predictor of malignancy in breast lesions: preliminary results. Magn Reson Med 2008;59(5):1030-1034.
81. Martens MH, Lambregts DM, Papanikolaou N, Heijnen LA, Riedl RG, zur Hausen A, Maas M, Beets GL, Beets-Tan RG. Magnetization transfer ratio: a potential biomarker for the assessment of postradiation fibrosis in patients with rectal cancer. Invest Radiol 2014;49(1):29-34.
82. Zhou J, Lal B, Wilson DA, Laterra J, van Zijl PC. Amide proton transfer (APT) contrast for imaging of brain tumors. Magn Reson Med 2003;50(6):1120-1126.
83. Salhotra A, Lal B, Laterra J, Sun PZ, van Zijl PC, Zhou J. Amide proton transfer imaging of 9L gliosarcoma and human glioblastoma xenografts. NMR Biomed 2008;21(5):489-497.
84. Jones CK, Schlosser MJ, van Zijl PC, Pomper MG, Golay X, Zhou J. Amide proton transfer imaging of human brain tumors at 3T. Magn Reson Med 2006;56(3):585-592.
85. Zhou J, Blakeley JO, Hua J, Kim M, Laterra J, Pomper MG, van Zijl PC. Practical data acquisition method for human brain tumor amide proton transfer (APT) imaging. Magn Reson Med 2008;60(4):842-849.
86. Zhou J. Amide proton transfer imaging of the human brain. Methods Mol Biol 2011;711:227-237.
87. Jia G, Abaza R, Williams JD, Zynger DL, Zhou J, Shah ZK, Patel M, Sammet S, Wei L, Bahnson RR, Knopp MV. Amide proton transfer MR imaging of prostate cancer: a preliminary study. J Magn Reson Imaging 2011;33(3):647-654.
88. Zhou JY, Tryggestad E, Wen ZB, Lal B, Zhou TT, Grossman R, Wang SL, Yan K, Fu DX, Ford E, Tyler B, Blakeley J, Laterra J, van Zijl PCM. Differentiation between glioma and radiation necrosis using molecular magnetic resonance imaging of endogenous proteins and peptides. Nature Medicine 2011;17(1):130-U308.
89. Dula AN, Arlinghaus LR, Dortch RD, Dewey BE, Whisenant JG, Ayers GD, Yankeelov TE, Smith SA. Amide proton transfer imaging of the breast at 3 T: establishing reproducibility and possible feasibility assessing chemotherapy response. Magn Reson Med 2013;70(1):216-224.
90. Santyr GE, Henkelman RM, Bronskill MJ. Spin locking for magnetic resonance imaging with application to human breast. Magn Reson Med 1989;12(1):25-37.
91. Markkola AT, Aronen HJ, Lukkarinen S, Ramadan UA, Tanttu JI, Sepponen RE. Multiple-slice spin lock imaging of head and neck tumors at 0.1 Tesla: exploring appropriate imaging parameters with reference to T2-weighted spin-echo technique. Invest Radiol 2001;36(9):531-538.
92. Poptani H, Duvvuri U, Miller CG, Mancuso A, Charagundla S, Fraser NW, Glickson JD, Leigh JS, Reddy R. T1rho imaging of murine brain tumors at 4 T. Acad Radiol 2001;8(1):42-47.
93. Kettunen MI, Sierra A, Narvainen MJ, Valonen PK, Yla-Herttuala S, Kauppinen RA, Grohn OH. Low spin-lock field T1 relaxation in the rotating frame as a sensitive MR imaging marker for gene therapy treatment response in rat glioma. Radiology 2007;243(3):796-803.
94. Duvvuri U, Poptani H, Feldman M, Nadal-Desbarats L, Gee MS, Lee WM, Reddy R, Leigh JS, Glickson JD. Quantitative T1rho magnetic resonance imaging of RIF-1

tumors in vivo: detection of early response to cyclophosphamide therapy. Cancer Res 2001;61(21):7747-7753.
95. Sierra A, Michaeli S, Niskanen JP, Valonen PK, Grohn HI, Yla-Herttuala S, Garwood M, Grohn OH. Water spin dynamics during apoptotic cell death in glioma gene therapy probed by T1rho and T2rho. Magn Reson Med 2008;59(6):1311-1319.
96. Williams DS, Detre JA, Leigh JS, Koretsky AP. Magnetic-Resonance-Imaging of Perfusion Using Spin Inversion of Arterial Water. P Natl Acad Sci USA 1992;89(1):212-216.
97. Cai W, Li F, Wang J, Du H, Wang X, Zhang J, Fang J, Jiang X. A comparison of arterial spin labeling perfusion MRI and DCE-MRI in human prostate cancer. NMR Biomed 2014;27(7):817-825.
98. Fujima N, Kudo K, Yoshida D, Homma A, Sakashita T, Tsukahara A, Khin Khin T, Yuri Z, Satoshi T, Hiroki S. Arterial spin labeling to determine tumor viability in head and neck cancer before and after treatment. J Magn Reson Imaging 2014;40(4):920-928.
99. Venkatesh SK, Yin M, Glockner JF, Takahashi N, Araoz PA, Talwalkar JA, Ehman RL. MR elastography of liver tumors: preliminary results. AJR Am J Roentgenol 2008;190(6):1534-1540.
100. Garteiser P, Doblas S, Daire JL, Wagner M, Leitao H, Vilgrain V, Sinkus R, Van Beers BE. MR elastography of liver tumours: value of viscoelastic properties for tumour characterisation. Eur Radiol 2012;22(10):2169-2177.
101. Pepin KM, Chen J, Glaser KJ, Mariappan YK, Reuland B, Ziesmer S, Carter R, Ansell SM, Ehman RL, McGee KP. MR elastography derived shear stiffness--a new imaging biomarker for the assessment of early tumor response to chemotherapy. Magn Reson Med 2014;71(5):1834-1840.
102. Morana G, Cugini C, Scatto G, Zanato R, Fusaro M, Dorigo A. Use of contrast agents in oncological imaging: magnetic resonance imaging. Cancer Imaging 2013;13(3):350-359.
103. Padhani AR, Husband JE. Dynamic contrast-enhanced MRI studies in oncology with an emphasis on quantification, validation and human studies. Clin Radiol 2001;56(8):607-620.
104. Knopp MV, Giesel FL, Marcos H, von Tengg-Kobligk H, Choyke P. Dynamic contrast-enhanced magnetic resonance imaging in oncology. Top Magn Reson Imaging 2001;12(4):301-308.
105. Petralia G, Bonello L, Priolo F, Summers P, Bellomi M. Breast MR with special focus on DW-MRI and DCE-MRI. Cancer Imaging 2011;11:76-90.
106. Sourbron SP, Buckley DL. Classic models for dynamic contrast-enhanced MRI. NMR Biomed;26(8):1004-1027.
107. Sourbron S. Technical aspects of MR perfusion. Eur J Radiol 2010;76(3):304-313.
108. Sourbron SP, Buckley DL. Tracer kinetic modelling in MRI: estimating perfusion and capillary permeability. Phys Med Biol 2012;57(2):R1-33.
109. Parker GJ, Roberts C, Macdonald A, Buonaccorsi GA, Cheung S, Buckley DL, Jackson A, Watson Y, Davies K, Jayson GC. Experimentally-derived functional form for a population-averaged high-temporal-resolution arterial input function for dynamic contrast-enhanced MRI. Magn Reson Med 2006;56(5):993-1000.

110. Yankeelov TE, Luci JJ, Lepage M, Li R, Debusk L, Lin PC, Price RR, Gore JC. Quantitative pharmacokinetic analysis of DCE-MRI data without an arterial input function: a reference region model. Magn Reson Imaging 2005;23(4):519-529.
111. Schabel MC, Fluckiger JU, DiBella EV. A model-constrained Monte Carlo method for blind arterial input function estimation in dynamic contrast-enhanced MRI: I. Simulations. Phys Med Biol;55(16):4783-4806.
112. Schabel MC, DiBella EV, Jensen RL, Salzman KL. A model-constrained Monte Carlo method for blind arterial input function estimation in dynamic contrast-enhanced MRI: II. In vivo results. Phys Med Biol;55(16):4807-4823.
113. Jackson A, Buckley D, Parker GJM. Dynamic contrast-enhanced magnetic resonance imaging in oncology. Berlin ; New York: Springer; 2005. xii, 311 p. p.
114. Tofts PS, Kermode AG. Measurement of the blood-brain barrier permeability and leakage space using dynamic MR imaging. 1. Fundamental concepts. Magn Reson Med 1991;17(2):357-367.
115. Tofts PS, Brix G, Buckley DL, Evelhoch JL, Henderson E, Knopp MV, Larsson HB, Lee TY, Mayr NA, Parker GJ, Port RE, Taylor J, Weisskoff RM. Estimating kinetic parameters from dynamic contrast-enhanced T1-weighted MRI of a diffusable tracer: standardized quantities and symbols. J Magn Reson Imaging 1999;10(3):223-232.
116. Tofts PS. Modeling tracer kinetics in dynamic Gd-DTPA MR imaging. J Magn Reson Imaging 1997;7(1):91-101.
117. Brix G, Kiessling F, Lucht R, Darai S, Wasser K, Delorme S, Griebel J. Microcirculation and microvasculature in breast tumors: pharmacokinetic analysis of dynamic MR image series. Magn Reson Med 2004;52(2):420-429.
118. Sourbron SP, Buckley DL. Classic models for dynamic contrast-enhanced MRI. NMR Biomed 2013;26(8):1004-1027.
119. Schabel MC, Morrell GR, Oh KY, Walczak CA, Barlow RB, Neumayer LA. Pharmacokinetic mapping for lesion classification in dynamic breast MRI. J Magn Reson Imaging 2010;31(6):1371-1378.
120. El Khouli RH, Macura KJ, Kamel IR, Jacobs MA, Bluemke DA. 3-T dynamic contrast-enhanced MRI of the breast: pharmacokinetic parameters versus conventional kinetic curve analysis. AJR Am J Roentgenol 2011;197(6):1498-1505.
121. Jain R. Measurements of tumor vascular leakiness using DCE in brain tumors: clinical applications. NMR Biomed 2013;26(8):1042-1049.
122. O'Connor JP, Jackson A, Parker GJ, Jayson GC. DCE-MRI biomarkers in the clinical evaluation of antiangiogenic and vascular disrupting agents. Br J Cancer 2007;96(2):189-195.
123. Zweifel M, Padhani AR. Perfusion MRI in the early clinical development of antivascular drugs: decorations or decision making tools? Eur J Nucl Med Mol Imaging 2010;37 Suppl 1:S164-182.
124. Jackson A. Imaging microvascular structure with contrast enhanced MRI. Br J Radiol 2003;76 Spec No 2:S159-173.
125. Koh TS, Thng CH, Hartono S, Tai BC, Rumpel H, Ong AB, Sukri N, Soo RA, Wong CI, Low AS, Humerickhouse RA, Goh BC. A comparative study of dynamic contrast-enhanced MRI parameters as biomarkers for anti-angiogenic drug therapy. NMR Biomed 2011;24(9):1169-1180.

126. O'Connor JP, Jackson A, Parker GJ, Roberts C, Jayson GC. Dynamic contrast-enhanced MRI in clinical trials of antivascular therapies. Nat Rev Clin Oncol 2012;9(3):167-177.
127. Zahra MA, Hollingsworth KG, Sala E, Lomas DJ, Tan LT. Dynamic contrast-enhanced MRI as a predictor of tumour response to radiotherapy. Lancet Oncology 2007;8(1):63-74.
128. Jensen RL, Mumert ML, Gillespie DL, Kinney AY, Schabel MC, Salzman KL. Preoperative dynamic contrast-enhanced MRI correlates with molecular markers of hypoxia and vascularity in specific areas of intratumoral microenvironment and is predictive of patient outcome. Neuro Oncol 2014;16(2):280-291.
129. Tozer GM, Prise VE, Wilson J, Cemazar M, Shan S, Dewhirst MW, Barber PR, Vojnovic B, Chaplin DJ. Mechanisms associated with tumor vascular shut-down induced by combretastatin A-4 phosphate: intravital microscopy and measurement of vascular permeability. Cancer Res 2001;61(17):6413-6422.
130. Zhao L, Ching LM, Kestell P, Kelland LR, Baguley BC. Mechanisms of tumor vascular shutdown induced by 5,6-dimethylxanthenone-4-acetic acid (DMXAA): Increased tumor vascular permeability. Int J Cancer 2005;116(2):322-326.
131. Jain RK. Normalization of tumor vasculature: an emerging concept in antiangiogenic therapy. Science 2005;307(5706):58-62.
132. Sourbron SP, Buckley DL. On the scope and interpretation of the Tofts models for DCE-MRI. Magn Reson Med 2011;66(3):735-745.
133. Barrett T, Kobayashi H, Brechbiel M, Choyke PL. Macromolecular MRI contrast agents for imaging tumor angiogenesis. Eur J Radiol 2006;60(3):353-366.
134. vanDijke CF, Brasch RC, Roberts TPL, Weidner N, Mathur A, Shames DM, Mann JS, Demsar F, Lang P, Schwickert HC. Mammary carcinoma model: Correlation of macromolecular contrast-enhanced MR imaging characterizations of tumor microvasculature and histologic capillary density. Radiology 1996;198(3):813-818.
135. Brasch R, Pham C, Shames D, Roberts T, vanDijke K, vanBruggen N, Mann J, Ostrowitzki S, Melnyk O. Assessing tumor angiogenesis using macromolecular MR imaging contrast media. J Magn Reson Imaging 1997;7(1):68-74.
136. Brasch R, Turetschek K. MRI characterization of tumors and grading angiogenesis using macromolecular contrast media: status report. Eur J Radiol 2000;34(3):148-155.
137. Delrue LJ, Casneuf V, Van Damme N, Blanckaert P, Peeters M, Ceelen WP, Duyck PC. Assessment of neovascular permeability in a pancreatic tumor model using dynamic contrast-enhanced (DCE) MRI with contrast agents of different molecular weights. MAGMA 2011;24(4):225-232.
138. Ivanusa T, Beravs K, Medic J, Sersa I, Sersa G, Jevtic V, Demsar F, Mikac U. Dynamic contrast enhanced MRI of mouse fibrosarcoma using small-molecular and novel macromolecular contrast agents. Phys Med 2007;23(3-4):85-90.
139. de Lussanet QG, Langereis S, Beets-Tan RG, van Genderen MH, Griffioen AW, van Engelshoven JM, Backes WH. Dynamic contrast-enhanced MR imaging kinetic parameters and molecular weight of dendritic contrast agents in tumor angiogenesis in mice. Radiology 2005;235(1):65-72.
140. Bradley DP, Tessier JL, Checkley D, Kuribayashi H, Waterton JC, Kendrew J, Wedge SR. Effects of AZD2171 and vandetanib (ZD6474, Zactima) on haemodynamic

variables in an SW620 human colon tumour model: an investigation using dynamic contrast-enhanced MRI and the rapid clearance blood pool contrast agent, P792 NMR Biomed 2008;21(3):302-302.
141. Fruytier AC, Magat J, Neveu MA, Karroum O, Bouzin C, Feron O, Jordan B, Cron GO, Gallez B. Dynamic contrast-enhanced MRI in mouse tumors at 11.7 T: comparison of three contrast agents with different molecular weights to assess the early effects of combretastatin A4. NMR Biomed 2014;27(11):1403-1412.
142. Preda A, Novikov V, Moglich M, Turetschek K, Shames DM, Brasch RC, Cavagna FM, Roberts TP. MRI monitoring of Avastin antiangiogenesis therapy using B22956/1, a new blood pool contrast agent, in an experimental model of human cancer. J Magn Reson Imaging 2004;20(5):865-873.
143. Roberts TP, Turetschek K, Preda A, Novikov V, Moeglich M, Shames DM, Brasch RC, Weinmann HJ. Tumor microvascular changes to anti-angiogenic treatment assessed by MR contrast media of different molecular weights. Acad Radiol 2002;9 Suppl 2:S511-513.
144. Turetschek K, Preda A, Novikov V, Brasch RC, Weinmann HJ, Wunderbaldinger P, Roberts TP. Tumor microvascular changes in antiangiogenic treatment: assessment by magnetic resonance contrast media of different molecular weights. J Magn Reson Imaging 2004;20(1):138-144.
145. Dafni H, Kim SJ, Bankson JA, Sankaranarayanapillai M, Ronen SM. Macromolecular dynamic contrast-enhanced (DCE)-MRI detects reduced vascular permeability in a prostate cancer bone metastasis model following anti-platelet-derived growth factor receptor (PDGFR) therapy, indicating a drop in vascular endothelial growth factor receptor (VEGFR) activation. Magn Reson Med 2008;60(4):822-833.
146. Boas U, Heegaard PM. Dendrimers in drug research. Chem Soc Rev 2004;33(1):43-63.
147. Barrett T, Ravizzini G, Choyke PL, Kobayashi H. Dendrimers in medical nanotechnology. IEEE Eng Med Biol Mag 2009;28(1):12-22.
148. Agarwal A, Asthana A, Gupta U, Jain NK. Tumour and dendrimers: a review on drug delivery aspects. J Pharm Pharmacol 2008;60(6):671-688.
149. Bosman AW, Janssen HM, Meijer EW. About Dendrimers: Structure, Physical Properties, and Applications. Chem Rev 1999;99(7):1665-1688.
150. Bumb A, Brechbiel MW, Choyke P. Macromolecular and dendrimer-based magnetic resonance contrast agents. Acta Radiol 2010;51(7):751-767.
151. Kojima C, Turkbey B, Ogawa M, Bernardo M, Regino CA, Bryant LH, Jr., Choyke PL, Kono K, Kobayashi H. Dendrimer-based MRI contrast agents: the effects of PEGylation on relaxivity and pharmacokinetics. Nanomedicine 2011;7(6):1001-1008.
152. Kobayashi H, Brechbiel MW. Nano-sized MRI contrast agents with dendrimer cores. Adv Drug Deliv Rev 2005;57(15):2271-2286.
153. Kobayashi H, Brechbiel MW. Dendrimer-based macromolecular MRI contrast agents: characteristics and application. Mol Imaging 2003;2(1):1-10.
154. Cloninger MJ. Biological applications of dendrimers. Curr Opin Chem Biol 2002;6(6):742-748.
155. Lee CC, MacKay JA, Frechet JM, Szoka FC. Designing dendrimers for biological applications. Nat Biotechnol 2005;23(12):1517-1526.

156. Longmire MR, Ogawa M, Choyke PL, Kobayashi H. Biologically optimized nanosized molecules and particles: more than just size. Bioconjug Chem 2011;22(6):993-1000.
157. Langereis S, Dirksen A, Hackeng TM, van Genderen MHP, Meijer EW. Dendrimers and magnetic resonance imaging. New Journal of Chemistry 2007;31(7):1152-1160.
158. Langereis S, de Lussanet QG, van Genderen MH, Meijer EW, Beets-Tan RG, Griffioen AW, van Engelshoven JM, Backes WH. Evaluation of Gd(III)DTPA-terminated poly(propylene imine) dendrimers as contrast agents for MR imaging. NMR Biomed 2006;19(1):133-141.
159. Margerum LD, Campion BK, Koo M, Shargill N, Lai JJ, Marumoto A, Sontum PC. Gadolinium(III) DO3A macrocycles and polyethylene glycol coupled to dendrimers - Effect of molecular weight on physical and biological properties of macromolecular magnetic resonance imaging contrast agents. J Alloy Compd 1997;249(1-2):185-190.
160. Kobayashi H, Sato N, Hiraga A, Saga T, Nakamoto Y, Ueda H, Konishi J, Togashi K, Brechbiel MW. 3D-micro-MR angiography of mice using macromolecular MR contrast agents with polyamidoamine dendrimer core with reference to their pharmacokinetic properties. Magn Reson Med 2001;45(3):454-460.
161. Sato N, Kobayashi H, Hiraga A, Saga T, Togashi K, Konishi J, Brechbiel MW. Pharmacokinetics and enhancement patterns of macromolecular MR contrast agents with various sizes of polyamidoamine dendrimer cores. Magn Reson Med 2001;46(6):1169-1173.
162. Lauffer RB, Parmelee DJ, Ouellet HS, Dolan RP, Sajiki H, Scott DM, Bernard PJ, Buchanan EM, Ong KY, Tyeklar Z, Midelfort KS, McMurry TJ, Walovitch RC. MS-325: a small-molecule vascular imaging agent for magnetic resonance imaging. Acad Radiol 1996;3 Suppl 2:S356-358.
163. Parmelee DJ, Walovitch RC, Ouellet HS, Lauffer RB. Preclinical evaluation of the pharmacokinetics, biodistribution, and elimination of MS-325, a blood pool agent for magnetic resonance imaging. Invest Radiol 1997;32(12):741-747.
164. Lauffer RB, Parmelee DJ, Dunham SU, Ouellet HS, Dolan RP, Witte S, McMurry TJ, Walovitch RC. MS-325: albumin-targeted contrast agent for MR angiography. Radiology 1998;207(2):529-538.
165. Goyen M. Gadofosveset-enhanced magnetic resonance angiography. Vasc Health Risk Manag 2008;4(1):1-9.
166. Puig J, Blasco G, Essig M, Daunis IEJ, Laguillo G, Quiles AM, Remollo S, Bergmann K, Joly C, Bernado L, Sanchez-Gonzalez J, Pedraza S. Albumin-binding MR blood pool contrast agent improves diagnostic performance in human brain tumour: comparison of two contrast agents for glioblastoma. Eur Radiol 2013;23(4):1093-1101.
167. Schipper RJ, Smidt ML, van Roozendaal LM, Castro CJ, de Vries B, Heuts EM, Keymeulen KB, Wildberger JE, Lobbes MB, Beets-Tan RG. Noninvasive nodal staging in patients with breast cancer using gadofosveset-enhanced magnetic resonance imaging: a feasibility study. Invest Radiol 2013;48(3):134-139.
168. Heijnen LA, Lambregts DM, Martens MH, Maas M, Bakers FC, Cappendijk VC, Oliveira P, Lammering G, Riedl RG, Beets GL, Beets-Tan RG. Performance of

gadofosveset-enhanced MRI for staging rectal cancer nodes: can the initial promising results be reproduced? Eur Radiol 2014;24(2):371-379.
169. Seshadri M, Sacadura NT, Coulthard T. Monitoring antivascular therapy in head and neck cancer xenografts using contrast-enhanced MR and US imaging. Angiogenesis 2011;14(4):491-501.
170. ter Haar G. Therapeutic applications of ultrasound. Prog Biophys Mol Biol 2007;93(1-3):111-129.
171. Hynynen K. MRI-guided focused ultrasound treatments. Ultrasonics 2010;50(2):221-229.
172. Tempany CM, McDannold NJ, Hynynen K, Jolesz FA. Focused ultrasound surgery in oncology: overview and principles. Radiology 2011;259(1):39-56.
173. Frenkel V. Ultrasound mediated delivery of drugs and genes to solid tumors. Adv Drug Deliv Rev 2008;60(10):1193-1208.
174. Kong G, Braun RD, Dewhirst MW. Characterization of the effect of hyperthermia on nanoparticle extravasation from tumor vasculature. Cancer Res 2001;61(7):3027-3032.
175. Kong G, Braun RD, Dewhirst MW. Hyperthermia enables tumor-specific nanoparticle delivery: effect of particle size. Cancer Res 2000;60(16):4440-4445.
176. Tempany CM, Stewart EA, McDannold N, Quade BJ, Jolesz FA, Hynynen K. MR imaging-guided focused ultrasound surgery of uterine leiomyomas: a feasibility study. Radiology 2003;226(3):897-905.
177. Hesley GK, Gorny KR, Woodrum DA. MR-guided focused ultrasound for the treatment of uterine fibroids. Cardiovasc Intervent Radiol 2013;36(1):5-13.
178. Kirkham AP, Emberton M, Hoh IM, Illing RO, Freeman AA, Allen C. MR imaging of prostate after treatment with high-intensity focused ultrasound. Radiology 2008;246(3):833-844.
179. Murat FJ, Poissonnier L, Pasticier G, Gelet A. High-intensity focused ultrasound (HIFU) for prostate cancer. Cancer Control 2007;14(3):244-249.
180. Gelet A, Chapelon JY, Bouvier R, Rouviere O, Lasne Y, Lyonnet D, Dubernard JM. Transrectal high-intensity focused ultrasound: minimally invasive therapy of localized prostate cancer. J Endourol 2000;14(6):519-528.
181. Rouviere O, Gelet A, Crouzet S, Chapelon JY. Prostate focused ultrasound focal therapy--imaging for the future. Nat Rev Clin Oncol 2012;9(12):721-727.
182. Leslie TA, Kennedy JE, Illing RO, Ter Haar GR, Wu F, Phillips RR, Friend PJ, Roberts IS, Cranston DW, Middleton MR. High-intensity focused ultrasound ablation of liver tumours: can radiological assessment predict the histological response? Br J Radiol 2008;81(967):564-571.
183. Leslie T, Ritchie R, Illing R, Ter Haar G, Phillips R, Middleton M, Bch B, Wu F, Cranston D. High-intensity focused ultrasound treatment of liver tumours: post-treatment MRI correlates well with intra-operative estimates of treatment volume. Br J Radiol 2012;85(1018):1363-1370.
184. Wijlemans JW, Bartels LW, Deckers R, Ries M, Mali WP, Moonen CT, van den Bosch MA. Magnetic resonance-guided high-intensity focused ultrasound (MR-HIFU) ablation of liver tumours. Cancer Imaging 2012;12:387-394.
185. Merckel LG, Bartels LW, Kohler MO, van den Bongard HJ, Deckers R, Mali WP, Binkert CA, Moonen CT, Gilhuijs KG, van den Bosch MA. MR-guided high-intensity

focused ultrasound ablation of breast cancer with a dedicated breast platform. Cardiovasc Intervent Radiol 2013;36(2):292-301.
186. Schmitz AC, Gianfelice D, Daniel BL, Mali WP, van den Bosch MA. Image-guided focused ultrasound ablation of breast cancer: current status, challenges, and future directions. Eur Radiol 2008;18(7):1431-1441.
187. Wu F. High intensity focused ultrasound: A noninvasive therapy for locally advanced pancreatic cancer. World J Gastroenterol 2014;20(44):16480-16488.
188. Gianfelice D, Gupta C, Kucharczyk W, Bret P, Havill D, Clemons M. Palliative treatment of painful bone metastases with MR imaging--guided focused ultrasound. Radiology 2008;249(1):355-363.
189. Rieke V, Butts Pauly K. MR thermometry. J Magn Reson Imaging 2008;27(2):376-390.
190. Ishihara Y, Calderon A, Watanabe H, Okamoto K, Suzuki Y, Kuroda K, Suzuki Y. A precise and fast temperature mapping using water proton chemical shift. Magn Reson Med 1995;34(6):814-823.
191. Sapareto SA, Dewey WC. Thermal dose determination in cancer therapy. Int J Radiat Oncol Biol Phys 1984;10(6):787-800.
192. Dewhirst MW, Viglianti BL, Lora-Michiels M, Hanson M, Hoopes PJ. Basic principles of thermal dosimetry and thermal thresholds for tissue damage from hyperthermia. Int J Hyperthermia 2003;19(3):267-294.
193. Yarmolenko PS, Moon EJ, Landon C, Manzoor A, Hochman DW, Viglianti BL, Dewhirst MW. Thresholds for thermal damage to normal tissues: an update. Int J Hyperthermia 2011;27(4):320-343.
194. Chu KF, Dupuy DE. Thermal ablation of tumours: biological mechanisms and advances in therapy. Nat Rev Cancer 2014;14(3):199-208.
195. Postma EL, van Hillegersberg R, Daniel BL, Merckel LG, Verkooijen HM, van den Bosch MA. MRI-guided ablation of breast cancer: where do we stand today? J Magn Reson Imaging 2011;34(2):254-261.
196. Rouviere O, Girouin N, Glas L, Ben Cheikh A, Gelet A, Mege-Lechevallier F, Rabilloud M, Chapelon JY, Lyonnet D. Prostate cancer transrectal HIFU ablation: detection of local recurrences using T2-weighted and dynamic contrast-enhanced MRI. Eur Radiol 2010;20(1):48-55.
197. Rouviere O, Souchon R, Salomir R, Gelet A, Chapelon JY, Lyonnet D. Transrectal high-intensity focused ultrasound ablation of prostate cancer: effective treatment requiring accurate imaging. Eur J Radiol 2007;63(3):317-327.
198. Rouviere O, Lyonnet D, Raudrant A, Colin-Pangaud C, Chapelon JY, Bouvier R, Dubernard JM, Gelet A. MRI appearance of prostate following transrectal HIFU ablation of localized cancer. Eur Urol 2001;40(3):265-274.
199. Wu F, Chen WZ, Bai J, Zou JZ, Wang ZL, Zhu H, Wang ZB. Tumor vessel destruction resulting from high-intensity focused ultrasound in patients with solid malignancies. Ultrasound Med Biol 2002;28(4):535-542.
200. Vaupel PW, Kelleher DK. Pathophysiological and vascular characteristics of tumours and their importance for hyperthermia: heterogeneity is the key issue. Int J Hyperthermia 2010;26(3):211-223.
201. Huang SK, Stauffer PR, Hong K, Guo JW, Phillips TL, Huang A, Papahadjopoulos D. Liposomes and hyperthermia in mice: increased tumor uptake and therapeutic

efficacy of doxorubicin in sterically stabilized liposomes. Cancer Res 1994;54(8):2186-2191.
202. Vos PC, Barentsz JO, Karssemeijer N, Huisman HJ. Automatic computer-aided detection of prostate cancer based on multiparametric magnetic resonance image analysis. Phys Med Biol 2012;57(6):1527-1542.
203. Mouthuy N, Cosnard G, Abarca-Quinones J, Michoux N. Multiparametric magnetic resonance imaging to differentiate high-grade gliomas and brain metastases. J Neuroradiol 2012;39(5):301-307.
204. Hoeks CM, Barentsz JO, Hambrock T, Yakar D, Somford DM, Heijmink SW, Scheenen TW, Vos PC, Huisman H, van Oort IM, Witjes JA, Heerschap A, Futterer JJ. Prostate cancer: multiparametric MR imaging for detection, localization, and staging. Radiology 2011;261(1):46-66.
205. Bhooshan N, Giger M, Lan L, Li H, Marquez A, Shimauchi A, Newstead GM. Combined use of T2-weighted MRI and T1-weighted dynamic contrast-enhanced MRI in the automated analysis of breast lesions. Magn Reson Med 2011;66(2):555-564.
206. Jacobs MA. Multiparametric magnetic resonance imaging of breast cancer. J Am Coll Radiol 2009;6(7):523-526.
207. Macura KJ. Multiparametric magnetic resonance imaging of the prostate: current status in prostate cancer detection, localization, and staging. Semin Roentgenol 2008;43(4):303-313.
208. Verma R, Zacharaki EI, Ou Y, Cai H, Chawla S, Lee SK, Melhem ER, Wolf R, Davatzikos C. Multiparametric tissue characterization of brain neoplasms and their recurrence using pattern classification of MR images. Acad Radiol 2008;15(8):966-977.
209. Jacobs MA, Barker PB, Bluemke DA, Maranto C, Arnold C, Herskovits EH, Bhujwalla Z. Benign and malignant breast lesions: diagnosis with multiparametric MR imaging. Radiology 2003;229(1):225-232.
210. Padhani AR, Miles KA. Multiparametric imaging of tumor response to therapy. Radiology 2010;256(2):348-364.
211. Carano RA, Ross AL, Ross J, Williams SP, Koeppen H, Schwall RH, Van Bruggen N. Quantification of tumor tissue populations by multispectral analysis. Magn Reson Med 2004;51(3):542-551.
212. Barck KH, Willis B, Ross J, French DM, Filvaroff EH, Carano RA. Viable tumor tissue detection in murine metastatic breast cancer by whole-body MRI and multispectral analysis. Magn Reson Med 2009;62(6):1423-1430.
213. Henning EC, Azuma C, Sotak CH, Helmer KG. Multispectral quantification of tissue types in a RIF-1 tumor model with histological validation. Part I. Magn Reson Med 2007;57(3):501-512.
214. Berry LR, Barck KH, Go MA, Ross J, Wu X, Williams SP, Gogineni A, Cole MJ, Van Bruggen N, Fuh G, Peale F, Ferrara N, Ross S, Schwall RH, Carano RA. Quantification of viable tumor microvascular characteristics by multispectral analysis. Magn Reson Med 2008;60(1):64-72.
215. Shi Y, Oeh J, Eastham-Anderson J, Yee S, Finkle D, Peale FV, Jr., Ross J, Hedehus M, van Bruggen N, Venook R, Ross S, Sampath D, Carano RA. Mapping in vivo tumor oxygenation within viable tumor by 19F-MRI and multispectral analysis. Neoplasia 2013;15(11):1241-1250.

Chapter 2

Synthesis and characterization of palmitoylated poly(propylene imine) dendrimer-based albumin-binding magnetic resonance imaging contrast agents

Igor Jacobs[1], Siem J Wouters[1], Henk M Keizer[2], Henk M Janssen[2], Eliana Gianolio[3], Francesca Arena[3], Silvio Aime[3], Gustav J Strijkers[1,4], Klaas Nicolay[1]

[1] Biomedical NMR, Department of Biomedical Engineering, Eindhoven University of Technology, Eindhoven, The Netherlands
[2] SyMO-Chem BV, Eindhoven, The Netherlands
[3] Department of Molecular Biotechnology and Health Sciences & Molecular Imaging Center, University of Turin, Italy
[4] Biomedical Engineering and Physics, Academic Medical Center, University of Amsterdam, Amsterdam, The Netherlands

In preparation

Abstract

Purpose

This work focused on the characterization of poly(propylene imine) (PPI) dendrimer-based albumin-binding magnetic resonance imaging (MRI) contrast agents, as well as evaluation of their blood-kinetics, biodistribution and utility for blood pool imaging.

Experimental

Various lower generations of PPI dendrimers, functionalized with a variable number of Gd-DOTA moieties and a palmitoyl moiety to facilitate reversible albumin binding, were synthesized by SyMO-Chem BV. The agents were primarily intended for preclinical imaging studies in mice. Relaxometric properties and aggregation behavior of the agents were characterized by relaxivity measurements at 60 MHz in phosphate buffered saline (PBS) and mouse plasma, and by nuclear magnetic relaxation dispersion (NMRD) measurements in presence and absence of mouse serum albumin (MSA) at physiological concentration. MSA binding affinity was assessed using proton relaxation enhancement (PRE) measurements at 20 MHz. Blood-kinetics and biodistribution of the agents were determined in CT26 colon carcinoma bearing Balb/c mice. The utility of the agents for blood pool imaging was evaluated in tumor-bearing Balb/c mice, by whole-body MR angiography with a 1 T MRI Bruker Icon^{TM} system.

Results and discussion

The agents palmitoylputrescine-DOTA-Gd (**1**), G_1-PPI-GdDOTA$_3$-Palm$_1$ (**2(G1)**) and G_2-PPI-GdDOTA$_7$-Palm$_1$ (**3(G2)**) were successfully synthesized by SyMO-Chem BV. Relaxivity measurements in PBS at 60 MHz demonstrated that these agents possessed a higher relaxivity compared to gadoterate meglumine (Gd-DOTA). Moreover, a critical aggregation concentration (CAC) was observed for the different agents, above which they formed aggregates, resulting in an enhanced relaxivity. Relaxivities were generally higher in mouse plasma than in PBS. PRE measurements showed a high albumin-binding strength for **1**, whereas the affinity of **2(G1)** and **3(G2)** for MSA was less and comparable to the commercially available human serum albumin-binding MS-325. Whereas **1** possessed the highest albumin-binding affinity, it appeared to be toxic in vivo. Nevertheless, the albumin-binding capabilities and macromolecular structure of **2(G1)** and **3(G2)** resulted in a relatively long half-life compared to Gd-DOTA. Accumulation of **2(G1)** and **3(G2)** in various organs was higher than of Gd-DOTA, with the highest accumulation for **3(G2)** in the tumor and most organs. Whole-body MR angiography showed prolonged visualization of the vasculature after administration of **3(G2)**. Vascular enhancement after **2(G1)** injection diminished after 10 min post-contrast, but was more pronounced compared to Gd-DOTA.

Conclusion

Differences in structure of the palmitoylated agents resulted in different relaxometric properties, aggregation behavior and affinity for MSA. Whereas albumin-binding affinity was highest for **1**, this agent appeared to be toxic in vivo. Nevertheless, **2(G1)** and **3(G2)** possessed prolonged circulation times and enabled MR angiographic imaging. The most persistent vascular enhancement was observed for **3(G2)**.

2.1. Introduction

Contrast agents are widely used to improve the sensitivity and specificity of magnetic resonance imaging (MRI) for detection of a broad range of pathologies. Paramagnetic gadolinium chelates can enhance the relaxation rates of diseased tissues and thereby improve the contrast with healthy tissue in an MR image (1,2). Commercially available low molecular weight contrast agents are routinely used in clinical diagnostic imaging and have been extensively applied in preclinical and clinical studies for evaluation of new treatment strategies (3,4). Considerable effort has been made to increase the efficacy of these agents by enhancing their relaxivity and increasing their blood circulation times (5,6). Macromolecular contrast agents have been developed, which possess a reduced clearance rate and higher relaxivity at clinically relevant field strengths due to their increased rotational correlation time (1,7). In addition, contrast agents have been developed that are able to reversibly bind to serum albumin, which decreases their leakage rate from the intravascular space, prolongs their blood circulation half-life and enhances their relaxivity (8). These characteristics make these agents especially suitable for use as blood pool agents for vascular imaging. The most widely studied albumin-binding agent is MS-325, which possesses a hydrophobic diphenylcyclohexyl moiety that facilitates reversible binding to human serum albumin (HSA) (9-11). Several other studies have explored the use of other albumin-binding moieties, such as alkyl chains (12-14) or benzyloxymethyl substituents (15-17) and investigated their albumin-binding and relaxation enhancement capabilities (18). Macromolecular contrast agents have been used for tumor imaging, exploiting the enhanced permeability of tumor vessels in comparison with normal vasculature (19). It has been shown that macromolecular agents may be suitable for imaging tumor angiogenesis (20,21), could detect alterations of tumor vessel permeability after radiation therapy (22) and can be used for evaluation of vascular disrupting and antiangiogenic therapies (23).

A particular type of platform for macromolecular contrast agents are dendrimers, which are a class of highly branched synthetic polymers with a well-defined structure that can be functionalized with various ligands or imaging labels (24). A major advantage of dendrimer-based contrast agents is that they can possess a wide range of tunable molecular weights whilst having a very similar chemical composition (25). In the present research, different lower generations of poly(propylene imine) (PPI) dendrimers, which have been functionalized with a variable number of Gd-DOTA moieties and a palmitoyl moiety to facilitate reversible albumin binding, were characterized in vitro and in vivo. A higher number of Gd-DOTA moieties per dendrimer and thereby higher molecular weight increases the payload of gadolinium and may amplify the relaxivity. In addition, a higher molecular weight may result in longer circulation times of the albumin-binding agents, also in unbound form, which would be advantageous for their use as a blood pool agent. However, an increased size of the headgroup could also potentially interfere with albumin-binding capabilities. The consequences of the differences in structure between the dendrimer-based contrast agents for their relaxivity was investigated with relaxivity measurements in phosphate buffered saline (PBS) and mouse plasma and by nuclear magnetic relaxation dispersion (NMRD) measurements in presence and absence of albumin at

physiological concentration. In addition, the consequences of their size differences for their albumin-binding capabilities were further investigated using proton relaxation enhancement (PRE) measurements (15,26). Since the used PPI dendrimers were primarily intended for preclinical tumor imaging, albumin-binding was studied using mouse serum albumin (MSA). Subsequently the albumin-binding dendrimers were applied in vivo in tumor-bearing mice to assess their blood-kinetics, biodistribution, and utility for angiographic imaging. This provided further insight in their suitability for in vivo imaging purposes.

2.2. Experimental

2.2.1. In vitro characterization

2.2.1.1. Contrast agents

An overview of the different albumin-binding dendrimers-based contrast agents, as well as of gadoterate meglumine (Gd-DOTA, Dotarem®, Guerbet, Villepente, France) and gadofosveset trisodium (MS-325) is given in Figure 1 and Table 1. Synthesis of the palmitoylated contrast agents and manufacturer information of Gd-DOTA and MS-325 is described Supporting information 1.

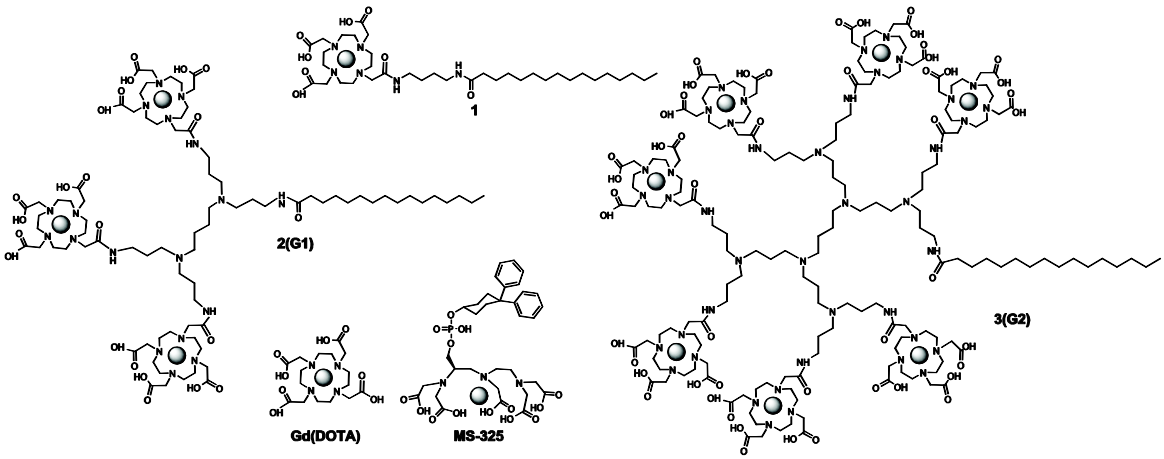

Figure 1. Schematic representation of Gd-DOTA, the palmitoylated (PPI dendrimer-based) contrast agents and MS-325.

Table 1. Overview of the used contrast agents: gadoterate meglumine, the palmitoylated contrast agents and MS-325.

Full name	Short name	Chemical formula	MW (kDa)
Gadoterate meglumine	Gd-DOTA	$C_{23}H_{42}GdN_5O_{13}$	0.754
Palmitoylputrescine-DOTA-Gd	**1**	$C_{36}H_{65}GdN_6O_8$	0.867
G1-PPI-GdDOTA$_3$-Palm$_1$	**2(G1)**	$C_{80}H_{139}Gd_3N_{18}O_{22}$	2.178
G2-PPI-GdDOTA$_7$-Palm$_1$	**3(G2)**	$C_{168}H_{287}Gd_7N_{42}O_{50}$	4.798
Gadofosveset trisodium	MS-325	$C_{33}H_{40}GdN_3Na_3O_{15}P$	0.976

2.2.1.2. Relaxivity measurements in PBS and mouse plasma

The longitudinal (r_1) and transverse (r_2) relaxivity of the palmitoylated contrast agents and the commercially available Gd-DOTA and MS-325 were measured on a 60 MHz (1.41 T) Bruker Minispec MQ60 (Bruker, Germany) spectrometer at 37 °C. Relaxivities were determined in PBS (Sigma-Aldrich, St. Louis, MO, USA) and Balb/c mouse plasma with Na Heparin as anticoagulant (Innovative Research, Novi, MI, USA). For each contrast agent, relaxation times of eight samples with varying gadolinium concentration ($[Gd^{3+}]$, ~0.01-1.0 mM Gd^{3+}) were determined using an inversion recovery sequence for T_1 and a Carr-Purcell-Meiboom-Gill (CPMG) sequence for T_2 measurements. At least four samples below and four samples above the CAC were used for the palmitoylated contrast agents. Relaxivities were determined by fitting the data with $R_i=R_{i,0}+r_i*[Gd^{3+}]$, with $i \in \{1,2\}$ and $R_i=1/T_i$. The critical aggregation concentration (CAC) of the palmitoylated agents was determined by assessment of the point of intersection between the fits to the $R_{1,2}$ data in the low and high relaxivity regime (14).

2.2.1.3. PRE measurements

PRE measurements were performed to investigate the interaction of the palmitoylated dendrimer-based contrast agents and MS-325 with MSA. The PRE method has been previously described (15,26). In short, it relies on assessment of the enhancement factor ε^* at increasing albumin concentrations (E-titration), according to:

$$\varepsilon^* = \frac{R^*_{1,obs-}R^*_{1,d}}{R_{1,obs-}R_{1,d}}$$

in which $R_{1,obs}$ is the measured longitudinal relaxation rate of the gadolinium containing solution, R_1 is the measured relaxation rate of the diamagnetic solvent and the asterisk indicates the presence of MSA in solution. These relaxation rates were measured on a Stelar spinmaster spectrometer (Stelar, Mede, Pavia, Italy) operating at 20 MHz (0.47 T) at 37 °C using an inversion recovery sequence. For the palmitoylated agents, PRE measurements were performed at concentrations below (~0.025 mM Gd^{3+}) and above the CAC (~1 mM Gd^{3+}). The gadolinium concentration of the palmitoylated contrast agents solutions used for the PRE measurements were determined by mineralizing a given quantity of the solutions by addition of 37% hydrochloric acid (HCl) at 120 °C overnight, as previously described (27). By measuring the relaxation rates of the obtained solutions and with the known relaxivity of the Gd^{3+} aqua ion in acidic solutions (13.5 $mM^{-1}s^{-1}$), the $[Gd^{3+}]$ could be determined (this method was calibrated using standard ICP solutions). The dendrimer concentration was subsequently determined based on the gadolinium content of the dendrimers as determined with Inductively Coupled Plasma-Atomic Emission Spectrometry (ICP-AES) (Philips Innovation Services, Eindhoven, The Netherlands).

MSA (dissolved lyophilized powder, fatted) (Equitech Bio, Kerrville, USA) was weighed using a microbalance and dissolved in PBS at increasing concentrations of 0-1.5 mM MSA, assuming a molecular weight of 67 kDa. By nonlinear fitting of the ε^* data as previously described (15,26), the binding parameter $n*K_A$ (with n the number of binding sites and K_A the association constant) and maximum enhancement factor ε_b could be determined. The parameter $n*K_A$ was only determined for PRE measurements

performed at concentrations below the CAC, since above this concentration the aggregation number of the agents was not known. The maximum bound relaxivity $r_{1,b}$ was assessed by multiplication of the measured relaxivity at 20 MHz with the maximum enhancement factor ε_b.

2.2.1.4. NMRD measurements

The dependence of the longitudinal relaxivity (r_1) of the palmitoylated contrast agents on the applied magnetic field strength was assessed with NMRD measurements. Longitudinal water proton relaxation rates were measured using a Stelar field-cycling relaxometer (Stelar, Mede, Pavia, Italy) operating at proton Larmor frequencies between 0.01 MHz and 20 MHz, corresponding to field strengths between 0.0024 and 0.47 T. The relaxometer works under complete computer control with an absolute uncertainty in R_1 of 1%. Relaxation rates at field strengths from 20-70 MHz (0.47-1.7 T) were determined using a Stelar Spinmaster spectrometer (Stelar, Mede, Pavia, Italy) working at variable field. The gadolinium concentration of the palmitoylated contrast agents solutions used for the NMRD measurements were determined as previously described (27). NMRD profiles were acquired in PBS solutions, in absence and in presence of 0.6 mM MSA (dissolved lyophilized powder, fatted) (Equitech Bio, Kerrville, USA).

2.2.2. In vivo characterization

2.2.2.1. Ethics Statement

All animal experiments were performed according to the Directive 2010/63/EU of the European Commission and approved by the Animal Care and Use Committee of Maastricht University (protocol: 2010-132).

2.2.2.2. Tumor model

10-12 week-old Balb/c mice (Charles River, Maastricht, The Netherlands) were inoculated with $2x10^6$ CT26.WT murine colon carcinoma cells (American Type Culture Collection (ATCC; CRL-2638), Manassas, VA, USA) subcutaneously in the right hind limb. Approximately 10 days after inoculation, tumors became palpable in all animals and mice were subjected to the blood clearance kinetics and biodistribution experiments (n=3-4 per contrast agent).

2.2.2.3. Blood-kinetics and biodistribution

Mice were intravenously injected with a dose of 0.1 mmol/kg Gd ([Gd]=25 mM) of one of the palmitoylated dendrimer-based contrast agents (**1**, **2(G1)**, or **3(G2)**) or Gd-DOTA (Dotarem®), followed by a saline flush, via the tail vain in 5 seconds using an infusion pump (Chemyx Fusion 100, Stafford, TX, USA) under general anesthesia (2% isoflurane in medical air). Blood samples (20 µL) were collected via the saphenous vein before and at 8 time points after contrast agent injection (at 2, 15, 30, 45 min and 1, 4, 8, 24 h after injection) and immediately mixed with 20 µL of heparinized physiological saline solution to prevent coagulation of the blood. 24 h after contrast agent administration, mice were sacrificed by cervical dislocation and the tumor, hind limb muscle, liver, spleen, kidneys, heart and lungs were excised to determine the

biodistribution of the contrast agents. Mice injected with **1** had to be sacrificed prematurely due to contrast agent toxicity.
After destruction of the samples with nitric acid, Gd^{3+} content of the blood samples and organs was assessed by means of ICP-AES or ICP Mass Spectrometry (ICP-MS) (Philips Innovation Services, Eindhoven, The Netherlands).
To determine the circulation half-lives of the agents, a biexponential function was fit to the combined [Gd^{3+}]-time curves of all mice:

$$C_b(t) = C_\alpha \cdot e^{-\alpha t} + C_\beta \cdot e^{-\beta t}, \text{ with } \alpha = \frac{\ln(2)}{t_{1/2,\alpha}} \text{ and } \beta = \frac{\ln(2)}{t_{1/2,\beta}}$$

in which C_α and C_β represent concentration contributions from the distribution and elimination phase, respectively, to the total blood concentration $C_b(t)$. α and β are the corresponding decay constants and $t_{1/2,\alpha}$ and $t_{1/2,\beta}$ are the distribution and elimination half-lives.

2.2.3. Whole body MR-Angiography

2.2.3.1. Tumor model
Studies were approved by the local ethics committee of the University of Turin and carried out in accordance with the guidelines of the European Commission. Male BALB/c mice (Charles River Laboratories, Calco, Italy) were inoculated with $1x10^6$ CT26 colon carcinoma cells (ATCC; CRL-2638, Manassas, VA, USA), subcutaneously in their hind limb. Tumors reached a size of approximately 0.4–0.6 cm in diameter 10-12 days after cell inoculation.

2.2.3.2. MR Angiography in tumor-bearing mice
MR angiography was performed in tumor-bearing mice using **2(G1)**, **3(G2)** and Gd-DOTA (n=1 per agent). Mice were anesthetized with isofluorane and placed supine in a solenoid Tx/Rx coil with an inner diameter of 3.5 cm for the MRI experiment. During measurements, respiration was monitored with a sensor connected to an ECG/respiratory unit. The contrast agents were injected via the tail vein at a dose of 0.1 mmol Gd/kg.

MR images were acquired before and at 10, 20 and 30 min post-injection of the contrast agents on a 1 T MRI Bruker Icon™ system (Bruker BioSpin MRI, Ettlingen, Germany). A 35 mm Tx/Rx mouse solenoid whole body coil was used for both RF excitation and reception of MR signal. A 3D gradient-echo (GRE) fast low angle shot (FLASH) pulse sequence (TR = 10 ms, TE = 4.1 ms, flip angle = 30°, field of view (FOV) = 80x40x40 mm^3, matrix size = 192x96x96, number of averages = 2, temporal resolution = 3 min 4 s per image) with an isotropic spatial resolution of 417 µm was used for image acquisition. Pre-contrast data were subtracted from post-contrast data using Mathematica 8.0 (Wolfram Research, Champaign, IL, USA) and 3D maximum intensity projection (MIP) images were reconstructed using OsiriX-Lite (Pixmeo, Switzerland).

2.3. Results and Discussion

2.3.1. In vitro characterization

2.3.1.1. Synthesis of the albumin-binding contrast agents

Palmitoylputrescine **4**, a natural antibiotic product, was prepared according to an alternative synthetic procedure to that reported in literature (Figure 2) (28,29).

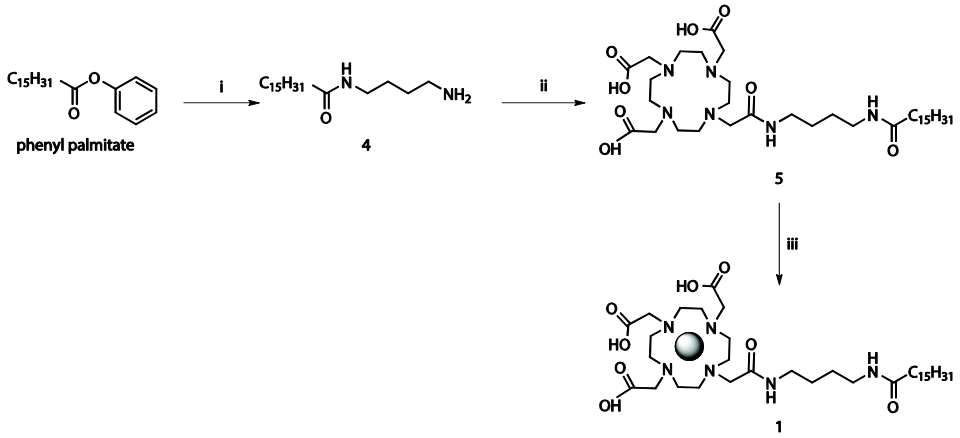

Figure 2. The synthesis of Palmitoyl-putrescine-DOTA-Gd. (i) 1,4-diaminobutane, triethanolamine (TEA), cholorform ($CHCl_3$), 50 °C; (ii) DOTA-NHS ester, $CHCl_3$/DMF, 40 °C; (iii) $Gd(OAc)_3$, pyridine, $CHCl_3$/MeOH/H_2O, room temperature.

Phenylpalmitate was reacted with an excess (5 equivalents (eq)) of 1,4-diaminobutane (DAB) in chloroform resulting in a precipitate, which was filtered off, washed with water and re-precipitated into acetonitrile. The palmitoylputrescine **4** was suspended in a mixture of dimethylformamide (DMF) / chloroform and reacted with an excess of DOTA-NHS with di-isopropylethylamine (DIPEA) as a base at 50 °C. After either precipitation in tetrahydrofuraan (THF) / acetonitrile (ACN) or an RP-C18 column the ligand **5** could be isolated in nearly quantitative yield. The complex **1** was formed by dissolving **5** in a mixture of water / methanol (MeOH) / chloroform (1/6/10 v/v/v) and adding pyridine and subsequently $Gd(OAc_3)$ at neutral pH.

The first step towards **2(G1)** and **3(G2)** was the synthesis of **6, 7** PPI dendrimers with only one palmitoyl chain (Figure 3).

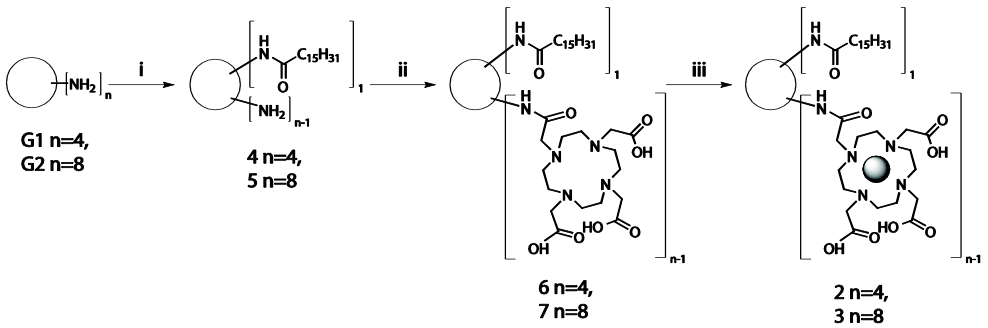

Figure 3. The synthesis of **G1(2)** and **G2(3)**. (i) Phenyl palmitate, ACN / $CHCl_3$, 0 °C; (ii) DOTA-NHS ester, TEA, $CHCl_3$ / MeOH, room temperature; (iii) $Gd(OAc)_3$, H_2O pH~7, room temperature.

The approach was to avoid the formation of PPI dendrimers with two or more palmitoyl chains, since those appeared hard to separate from the PPI dendrimers with one palmitoyl chain. Thus, a less reactive phenylpalmitate was used as the limiting reactant (0.3 - 0.5 eq) and added drop wise to a dilute solution of PPI dendrimer at low temperature 0 °C. In case of **2(G1)** only ~8% of PPI dendrimers with two palmitoyl chains were formed, while for **3(G2)** ~14% with 2 and ~2 % with 3 palmitoyl chains were found. The excess of PPI dendrimer was easily removed by extraction with either water or brine. The number of palmityol chains per PPI dendrimer could be determined with high performance liquid chromatography-evaporative light scattering detection (HPLC-ELSD). The next step was the reaction of the remaining amine end-groups of the PPI dendrimer with an excess of DOTA-NHS in presence of a base triethylamine (Et_3N). Finally, the Gd complexes **2(G1), 3(G2)** were formed by reacting the ligands **6, 7** with an excess of $Gd(OAc)_3$ at pH ~7 in water.

2.3.1.2. Relaxivity measurements in PBS and mouse plasma

The longitudinal (r_1) and transverse (r_2) relaxivities of Gd-DOTA, the palmitoylated contrast agents and MS-325 at 60 MHz and 37 °C in both PBS and mouse plasma are displayed in Table 2.

Table 2. Relaxivities of Gd-DOTA, the palmitoylated contrast agents and MS-325 in PBS and mouse plasma, measured at 60 MHz and 37 °C. * Since no CAC was observed only a single $r_{1,2}$ is reported. # Since Eldredge et al. reported a decrease in albumin-bound fraction of MS-325 at concentrations >0.1 mM and flattening of the $R_{1,2}$ curve was observed at higher concentrations (8), only concentrations <0.1 mM were used for calculation of the relaxivity.

Agent	**Relaxivity in PBS ($mM^{-1}s^{-1}$) below CAC**		**Relaxivity in PBS ($mM^{-1}s^{-1}$) above CAC**		**CAC (mM agent)**	**Relaxivity in mouse plasma ($mM^{-1}s^{-1}$)**	
	r_1	**r_2**	**r_1**	**r_2**		**r_1**	**r_2**
Gd-DOTA	3.0 *	3.7 *	n.a.	n.a.	n.a.	3.6	4.5
1	3.2	4.1	14.2	18.3	0.08	12.2	18.5
2(G1)	3.5	4.3	5.5	6.9	0.04	9.0	12.6
3(G2)	6.5	7.4	10.5	13.0	0.01	14.4	20.4
MS-325	5.5 *	6.4 *	n.a.	n.a.	n.a.	14.5 #	26.5 #

As shown in Figure 4, the increase in relaxivity above a threshold concentration indicates the presence of a critical aggregation concentration (CAC) for the palmitoylated agents in PBS. Therefore, the relaxivities of these agents in PBS were separately determined for concentrations below and above the CAC. As expected, this aggregation behavior could neither be observed for Gd-DOTA nor for MS-325. Below the CAC, the relaxivity of the palmitoylated agents increased with their molecular weight.

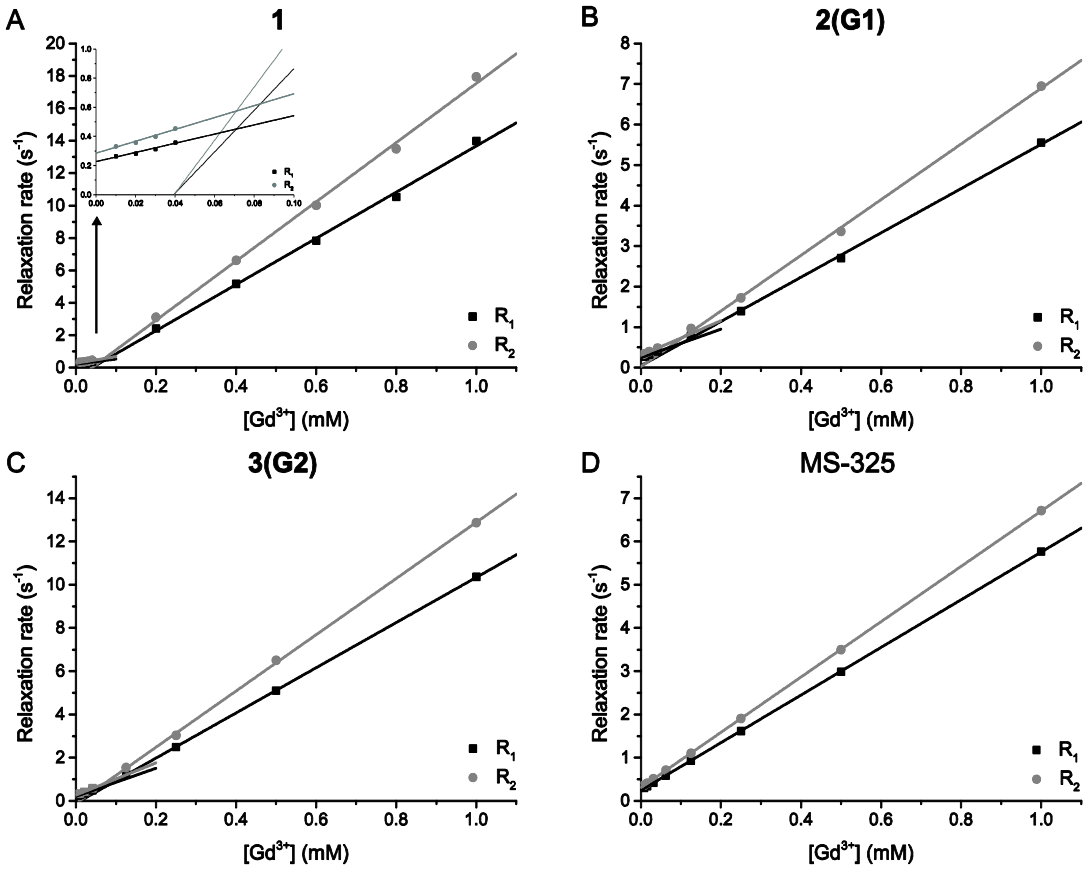

Figure 4. Longitudinal (R_1) and transverse (R_2) relaxation rates in PBS, measured at 60 MHz and 37 °C, versus the concentration of Gd^{3+} for A) **1**, B) **2(G1)**, C) **3(G2)** and D) MS-325. The solid lines represent the fits through the data. The inset in Figure 4A is a zoomed image of the low concentration range.

Above the CAC, the strongest increase in relaxivity compared to below the CAC was observed for **1** (4.5-fold increase in r_1 and r_2), whereas this increase was less pronounced for **2(G1)** (1.6-fold increase in r_1 and r_2) and **3(G2)** (1.6-fold and 1.7-fold increase in r_1 and r_2, respectively). The increase in relaxivity can be explained by an increase in complex size, resulting in an increased rotational correlation time (1,30). Differences in the extent of the increase in relaxivity between the different agents are indicative of differences in aggregation type and aggregation number. Most likely, micellar aggregates were formed above the CAC for **1**. Nicolle et al. described a proportionate increase in relaxivity upon micellization for similar Gd-DOTA complexes with an aliphatic side chain, at approximately the same CAC as for **1** (31). The increased headgroup size due to the higher number of Gd-DOTA moieties of **2(G1)** and **3(G2)** per dendrimer is expected to result in formation of smaller aggregates with a lower aggregation number.

Relaxivity measurements in mouse plasma demonstrated that for all contrast agents the relaxivity was higher in plasma than in PBS, except for **1** above the CAC (Table 2). For Gd-DOTA, which is known to possess no specific interaction with plasma albumin, only a minor increase in relaxivity could be observed in mouse plasma compared to PBS. However, the relaxivity of **1**, the palmitoylated dendrimer-based contrast agents

2(G1), **3(G2)** and MS-325 were strongly increased in mouse plasma compared to PBS. This is likely caused by an increased rotational correlation time of the macromolecular adduct upon binding to albumin, which is reported to be the main mechanism of relaxivity enhancement for MS-325 (11,15).

1 possessed the strongest increase in relaxivity in mouse plasma compared to its relaxivity in PBS below the CAC (3.8-fold increase in r_1). A slightly lower increase in relaxivity was observed for **2(G1)** (2.6-fold increase in r_1), **3(G2)** (2.2-fold increase in r_1) and MS-325 (2.6-fold increase in r_1). Remarkably, the relaxivity of **1** was lower in mouse plasma than in PBS at concentrations above the CAC. This suggests that a transfer occurs of monomeric **1** complex from the micellar aggregates to albumin. Importantly, due to noncovalent binding of the agents to albumin, no CAC was found in mouse plasma for the different agents (Figure 5).

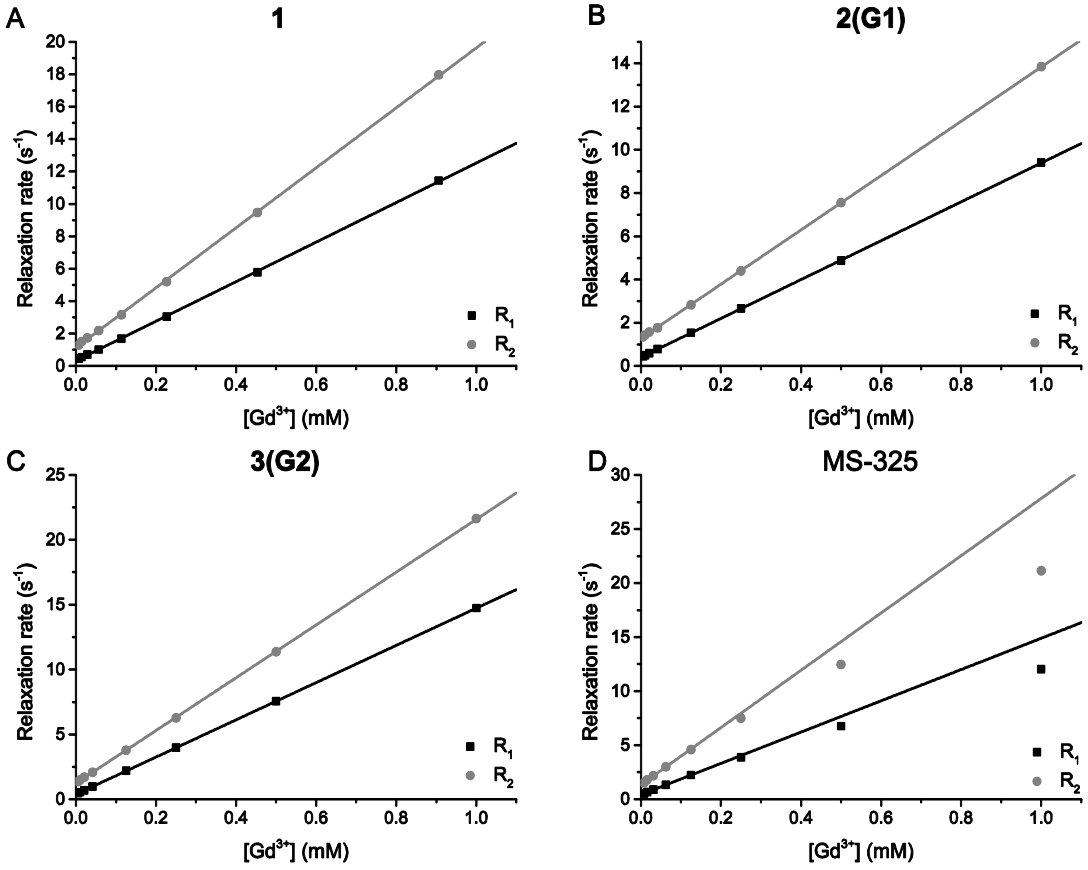

Figure 5. Longitudinal (R_1) and transverse (R_2) relaxation rates in mouse plasma, measured at 60 MHz and 37 °C, versus the concentration of Gd^{3+} for A) **1**, B) **2(G1)**, C) **3(G2)** and D) MS-325. The fit in Figure 5D resulted from fitting the 4 data points with the lowest Gd^{3+} concentration.

This is in agreement with findings by Richieri et al., who observed that fatty acid aggregates do not form in the presence of albumin and reported that association of the fatty acids with albumin exceeded association between the fatty acids (32). For MS-325, a decrease in slope of the $R_{1,2}$ curves was observed with increasing contrast agent concentration (Figure 5D), which is in agreement with the decrease in albumin-bound fraction of MS-325 at concentrations higher than 0.1 mM described by Eldredge et al. (8). This was explained by a higher fraction of unbound MS-325, which has a

lower relaxivity than the bound form. Such decrease in slope of the $R_{1,2}$ curves was not observed for the palmitoylated dendrimer-based contrast agents. This may be caused by the occurrence of a higher number of high affinity binding sites for the palmitoylated agents compared to the diphenylcyclohexyl functionalized MS-325. The existence of two or three high affinity binding sites for fatty acids such as palmitate has been reported for albumins of various species (14,33). Furthermore, the presence of multiple high-affinity stepwise association constants has been reported for palmitate and mouse albumin (32). Although as many as thirty MS-325 can bind to one single human albumin molecule (20), the binding affinity of MS-325 is moderate (11) and secondary binding events could have a substantially lower association constant than the primary one (11). However, Eldredge et al. did not report substantial differences in the primary and secondary stepwise association constants of MS-325 to mouse albumin (8).

2.3.1.3. PRE measurements

The interaction of the palmitoylated agents and MS-325 was further investigated with PRE measurements. Because of the observed aggregation behavior of the palmitoylated dendrimers, PRE measurements were performed at contrast agent concentrations both below and above the CAC for these agents. Figure 6A shows the results of the E-titrations of the different albumin-binding contrast agents below the CAC, displaying the enhancement factor (ε^*) at increasing MSA concentrations.

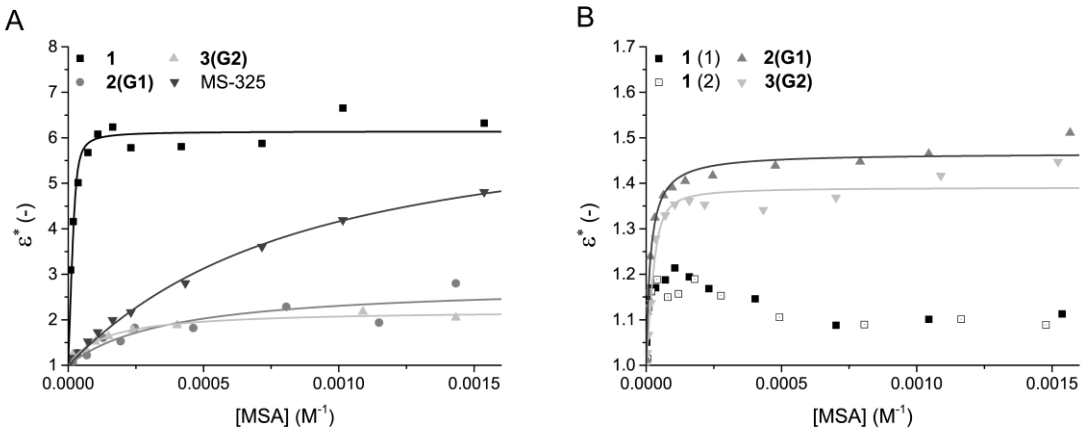

Figure 6. PRE curves of the palmitoylated PPI dendrimer-based contrast agents and MS-325, measured at 20 MHz and 37 °C at a concentration A) below and B) above the CAC. The solid lines represent the PRE fits trough the data. The PRE measurements of **1** at a concentration above the CAC were performed in duplicate, as indicated with the numbers (1) and (2).

At concentrations below the CAC, a strong and rapid increase in ε^* was observed for **1**. The increase in ε^* was slower and less marked for **2(G1)**, **3(G2)** and MS-325. Modeling of the PRE data facilitated assessment of the maximum enhancement factor ε_b and number of binding sites times the association constant $n*K_A$. Since the number of binding sites for each agent was not known, this parameter was fixed at one. The binding parameters of the different agents are shown in Table 3.

Table 3. Results of the PRE measurements of the palmitoylated contrast agents and MS-325 performed at 20 MHz and 37 °C at concentrations below and above the CAC. * Above the CAC, $n*K_A$ was not determined since the aggregation number at these concentrations was not known. # The PRE data of **1** above the CAC could not be accurately modeled by the PRE equations. & Since no CAC was observed for MS-325, PRE measurements were only performed at one concentration.

Agent	$n*K_A$ (10^4 M^{-1})		ε_b (-)		$r_{1,b}$ ($mM^{-1}s^{-1}$)	
	Below	Above CAC	Below	Above	Below	Above
1	38.3 ±20.5	- *	6.1±0.1	- #	18.7	- #
2(G1)	0.27± 0.13	- *	2.8±0.3	1.5±0.01	12.6	10.1
3(G2)	0.76± 0.13	- *	2.2±0.1	1.4±0.01	20.1	15.3
MS-325	0.15± 0.02	- *	6.6±0.3	- &	32.1	- &

1 possessed the highest $n*K_A$ ($38.3\pm20.5*10^4$ M^{-1}), which reflects its relatively strong interaction with mouse albumin compared to the other palmitoylated agents ($0.27\pm0.13*10^4$ M^{-1} and $0.76\pm0.13*10^4$ M^{-1} for **2(G1)** and **3(G2)**, respectively). In addition, **1** had a high ε_b of 6.1±0.1 in comparison with **2(G1)** (2.8±0.3) and **3(G2)** (2.2±0.3). It has been previously shown that complexes of smaller size, with the same number of hydrophobic groups and charge, bind more tightly to human serum albumin than larger complexes (34,35). Although MS-325 possessed a comparable ε_b of 6.6±0.3 to **1**, its binding strength ($n*K_A=0.15\pm0.02*10^4$ M^{-1}) to MSA was considerably lower. This finding is in agreement with previous investigations (8) in which it was demonstrated that the binding of MS-325 to plasma proteins depends on the species. The order found for plasma protein binding was human > pig ~ rabbit > dog ~ rat ~ mouse. In contrast, several examples of fatty acid or fatty acid analogs were shown to have high affinity to different domains on serum albumin (12,14,32-34).

The results of the E-titrations above the CAC are displayed in Figure 6B. Remarkably, the enhancement factor of **1** did not consistently increase with the concentration of MSA. Instead, after an initial peak the enhancement factor ε^* decreased again to a value close to one. This may be due to alterations in the equilibrium between monomeric **1**, micellar **1** and albumin-bound **1** during the titration. Gianolio et al. reported the formation of a supramolecular adduct between preformed Gd-AAZTAC17 micelles and HSA (14). This association was driven by electrostatic interactions among the negative charges of the micelles and positively charged residues on the albumin surface. Binding of the micellar aggregates of **1** is less feasible since the palmitoyl moieties will be located at the interior of the micellar aggregates and the net neutral charge of the Gd-DOTA moieties makes electrostatic interactions less likely. However, Gianolio et al. also indicated that translocation of Gd-AAZTAC17 to the protein binding sites could occur, which may also occur here. Since the PRE data of **1** above the CAC could not be fitted by the PRE equations, the binding parameters of **1** at concentrations above the CAC could not be determined. For **2(G1)** and **3(G2)** at concentrations above the CAC, a gradual increase in ε^* could be observed for increasing MSA concentrations. The maximum enhancement factor ε_b of **2(G1)** and **3(G2)** above the CAC was lower than for concentrations below the CAC, which may also be due to the fact that the aggregate form of **2(G1)** and **3(G3)** could be in competition with their monomeric form bound to albumin. The binding parameter $n*K_A$

was not assessed at concentrations above the CAC, since the aggregation number at these concentrations was not known. The $n*K_A$ values of **1** below the CAC ($n*K_A=38.3\pm20.5*10^4$ M^{-1}) were higher than for Gd-AAZTAC17 below the CMC, reported by Gianolio et al. (14) for fatted HSA at 25 °C ($n*K_A=7.1\pm1.8*10^4$ M^{-1}) and also slightly higher than the $n*K_A$ values of MS-325 ($n*K_A=3.0\pm0.2*10^4$ M^{-1}) and $[Gd(BOM)_3DTPA(H_2O)]^{-2}$ ($n*K_A=4.0\pm0.3*10^4$ M^{-1}) with HSA at 25 °C (15). However, $n*K_A$ values of **2(G1)** and **3(G2)** were lower than these previously reported association constants with HSA. This might be due to the higher number of Gd-DOTA moieties and thus a larger headgroup with respect to the albumin-binding palmitoyl moiety, which could result in a less tight albumin binding (34,35). The $n*K_A$ value of MS-325 and mouse albumin was lower than previously reported by Aime et al. for human albumin (15). This could be due to the lower binding affinity of MS-325 to mouse albumin in comparison with human albumin (8).
Further insight in albumin properties of the palmitoylated dendrimer-based contrast agents could be obtained by a titration with a fixed albumin concentration and variable amounts of the albumin-binding contrast agent (26), which facilitates separate assessment of the number of binding sites. However, this titration would be complicated by the presence of a CAC at a relatively low concentration for the used agents and was not carried out.

2.3.1.4. NMRD measurements

To further investigate the effect of aggregation of the palmitoylated contrast agents on their relaxivity, NMRD measurements were performed at a concentration above the CAC of the agents. Figure 7A shows the relaxivity of the palmitoylated agents in PBS as a function of the applied field strength.

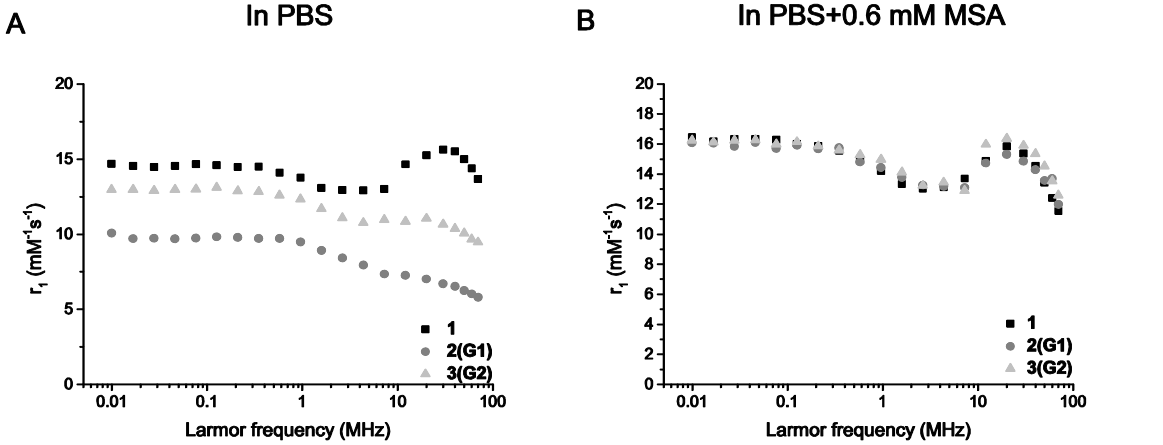

Figure 7. NMRD profiles of the palmitoylated contrast agents acquired at proton Larmor frequencies of 0.01-70 MHz (0.0024-1.7 T) measured at 37 °C. The graphs represent the longitudinal relaxivity r_1 ($mM^{-1}s^{-1}$) as a function of the Larmor frequency, measured in A) PBS and B) in PBS+0.6 mM MSA.

For **1** a peak in longitudinal relaxivity was measured at approximately 30 MHz, which is typically observed in NMRD profiles of micellar aggregates (14,30). It was described that the larger size of the micellar complex probably results in an increased global rotational correlation time, thereby increasing the contrast agent relaxivity. This behavior was not seen for **2(G1)** and **3(G2)**, which indicates that these agents indeed form smaller aggregates. However, a minor peak was observed around 20 MHz for **3(G2)**, which is likely due to its macromolecular structure. In addition, NMRD measurements of the palmitoylated agents at concentrations above the CAC were performed in the presence of MSA at physiological concentration (Figure 7B). Albumin binding led to an increased relaxivity for **2(G1)** and **3(G2)**, whereas the relaxivity of **1** was not evidently increased due the relatively high relaxivity of the micellar **1** aggregates. NMRD profiles of the different agents had a very similar appearance due to their noncovalent binding to albumin, which resulted in the presence of a macromolecular peak at approximately 20 MHz in agreement with literature (12,14). This may be reflective of the association of the monomeric palmitoylated agents with mouse albumin.
The effect of aggregation and albumin binding of the contrast agents on their relaxivity was only investigated qualitatively. Quantitative modeling of the NMRD data would provide additional insight in the relaxometric parameters of the different agents (11,12,15). However, to obtain a robust assessment of the relaxometric parameters, variable temperature ^{17}O transverse relaxation rate measurements should be included in the analyses.

2.3.2. In vivo characterization

2.3.2.1. Blood-kinetics and biodistribution

Application of the different palmitoylated contrast agents and Gd-DOTA in tumor-bearing mice showed differences in circulation half-lives and biodistribution between these agents. After administration of **1**, this agent appeared to be toxic and the mice had to be sacrificed prematurely. Therefore, no blood-kinetics and biodistribution data of these mice could be shown. **1** toxicity may be due to changes in erythrocyte morphology and membrane fluidity, resulting from interaction of the palmitoyl moieties with the cell membrane. This may induce erythrocyte aggregation and hemolysis (36). In addition, it has been reported that fatty-acid infusion induces thrombosis through activation of the Hageman factor (37). The blood-kinetics data of the other agents are shown in Figure 8. Rapid clearance of the low molecular weight Gd-DOTA could be observed, whereas the elimination rate was lower for the albumin-binding **2(G1)** and **3(G2)** after an initial phase of rapid clearance. This rapid clearance may be due to the presence of a relatively high fraction of unbound contrast agent early after injection. After this period, an equilibrium is reached between free and albumin-bound **2(G1)** and **3(G2)**.

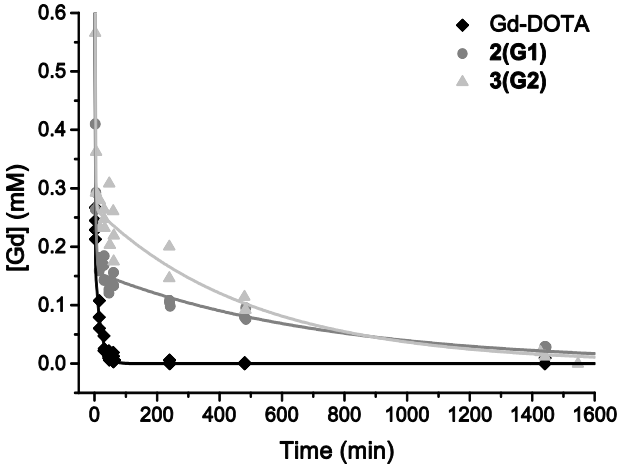

Figure 8. Blood-kinetics data of all mice injected with Gd-DOTA (n=4), **2(G1)** (n=3) and **3(G2)** (n=3) and biexponential fits to the data. Data of **1** could not be obtained due to contrast agent toxicity.

Table 4 shows that indeed elimination half-lives of **2(G1)** (499.5±103.7 min) and **3(G2)** (350.8±68.8 min) were longer than of Gd-DOTA (11.9±1.7 min). In addition, these elimination half-lives are substantially longer than reported for MS-325 in rats at an equal dose (23.1±2.88 min) (38). Since the combined data of all mice were fit for the different agents, these half-lives could not be statistically compared.

Table 4. Distribution ($t_{1/2,\alpha}$) and elimination ($t_{1/2,\beta}$) half-lives of Gd-DOTA, **2(G1)** and **3(G2)**, obtained by biexponential fitting of the combined data of all mice. Data of **1** could not be determined due to contrast agent toxicity. The error represents the standard error on the biexponential fits.

Agent	$t_{1/2,\alpha}$ (min)	$t_{1/2,\beta}$ (min)
Gd-DOTA	0.3±0.1	11.9± 1.7
2(G1)	2.1±0.8	499.5±103.7
3(G2)	1.1±0.3	350.8± 68.8

The biodistribution data obtained from tissue samples collected 24 h after contrast agent injection are shown in Figure 9 and Table 5.

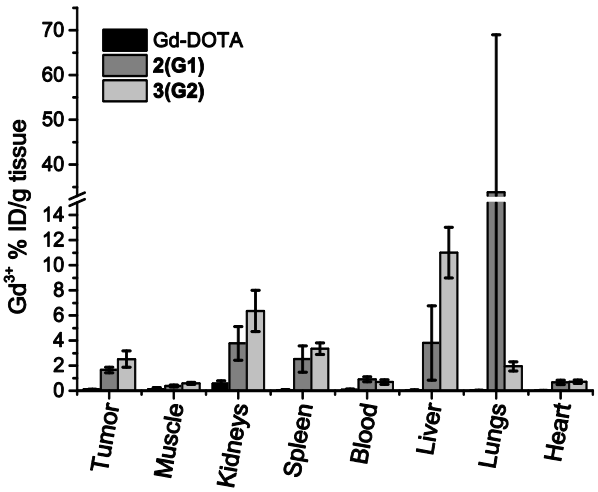

Figure 9. Biodistribution data of Gd-DOTA (n=4), **2(G1)** (n=3) and **3(G2)** (n=4). Data of **1** could not be determined due to contrast agent toxicity. Data are presented as mean±standard deviation (SD) of all mice.

Table 5. Biodistribution of Gd-DOTA (n=4), **2(G1)** (n=3) and **3(G2)** (n=4) in tumor-bearing mice, expressed as Gd^{3+} % injected dose (ID)/g tissue. Data are presented as mean±standard deviation (SD) of all mice.

	Gd^{3+} % ID/g tissue		
Organ	Gd-DOTA	**2(G1)**	**3(G2)**
Tumor	0.10±0.03	1.66± 0.22	2.52±0.65
Muscle	0.11±0.15	0.38± 0.08	0.59±0.08
Kidneys	0.57±0.23	3.76± 1.35	6.36±1.64
Spleen	0.06±0.03	2.52± 1.05	3.35±0.46
Blood	0.07±0.07	0.91± 0.20	0.69±0.18
Liver	0.05±0.02	3.80± 2.96	11.01±2.02
Lungs	0.04±0.02	33.84±35.19	1.94±0.36
Heart	0.02±0.01	0.67± 0.17	0.72±0.14

Accumulation of **2(G1)** and **3(G2)** in the different organs was high compared to Gd-DOTA and could predominantly be observed in the kidneys (3.76±1.35 and 6.36±1.64% ID/g of tissue for **2(G1)** and **3(G2)**, respectively), spleen (2.52±1.05 and 3.35±0.46% ID/g of tissue for **2(G1)** and **3(G2)**, respectively) and liver (3.80±2.96 and 11.01±2.02% ID/g of tissue for **2(G1)** and **3(G2)**, respectively). Langereis et al. reported clearance of a Gd-DTPA-terminated PPI dendrimer of comparable molecular weight (3.1 kDa) as **2(G1)** and **3(G2)** via the renal collecting system (39). The high liver accumulation may be caused by the apolar palmitoyl moiety on the albumin-binding dendrimers, of which the apolar nature could result in hepatocellular uptake (40). Remarkably, a high gadolinium accumulation in the lungs was observed for **2(G1)** (33.84±35.19% ID/g of tissue). Tumor accumulation of **2(G1)** and **3(G2)** (1.66±0.22 and 2.52±0.65% ID/g of tissue) was also substantially higher than of Gd-DOTA (0.10±0.03% ID/g of tissue), which may be caused by their higher molecular weight and prolonged tumor accumulation due to the relatively long circulation half-lives of **2(G1)** and **3(G2)** compared to Gd-DOTA, which is also reflected by the relatively high amount of **2(G1)** and **3(G2)** (0.67±0.17 and 0.72±0.14% ID/g of tissue, respectively) in the blood at 24 h after injection compared to Gd-DOTA (0.07±0.07 ID/g of tissue) (41).

2.3.3. Magnetic Resonance Angiography

Figure 10 shows three-dimensional maximum intensity projection (MIP) contrast enhanced images of mice injected with **2(G1)**, **3(G2)** or Gd-DOTA at 10, 20 and 30 min post-injection. The investigated contrast agents showed different contrast enhancement properties, in terms of persistence or localization of the contrast. After injection of **3(G2),** stronger and more prolonged contrast enhancement was observed compared to **2(G1)** and Gd-DOTA in the heart and blood vessels. The vasculature remained well enhanced up to at least 30 min post-injection. Administration of **2(G1)** resulted in less pronounced blood pool enhancement, which was primarily visible in the jugular veins at 10 min post injection, after which the signal gradually faded away due to the clearance of the agent from the blood. This resulted in a strong enhancement inside the bladder, which gradually increased over time. For Gd-DOTA, no clear visualization of the vasculature was observed at the evaluated time points.

The tumor vasculature could not be clearly visualized, which likely requires a higher spatial resolution (42).

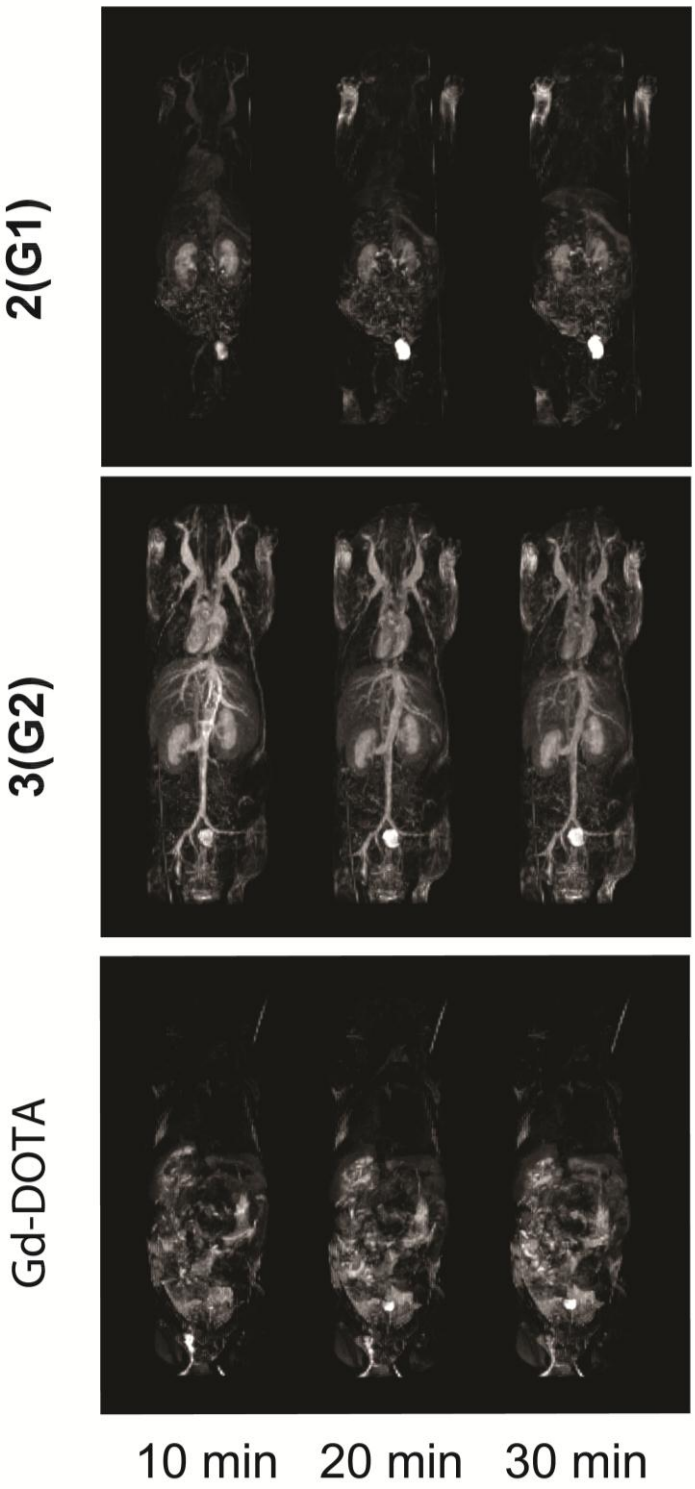

Figure 10. Whole-body MR angiography. Coronal maximum intensity projection (MIP) of the 3D FLASH images obtained from the mice after intravenous administration of **2(G1)**, **3(G2)** or Gd-DOTA at a dose of 0.1 mmol Gd/kg. Post-contrast images at 10, 20 and 30 min are shown after the subtraction of the corresponding pre-contrast images.

2.4. Conclusion

PPI dendrimer-based MRI contrast agents, functionalized with a palmitoyl moiety to facilitate albumin binding, were characterized in vitro and in vivo in tumor-bearing mice. It was shown that the dendrimer-based contrast agents possessed a higher relaxivity than the low molecular weight Gd-DOTA and could potentially form aggregates in PBS, which enhanced their relaxivity. The effect of structural differences between the dendrimer-based contrast agents and their aggregation behavior on albumin-binding capabilities was investigated in vitro. A high albumin-binding strength was found for **1**, whereas the albumin-binding ability of **2(G1)** and **3(G2)** was less and comparable to the commercially available MS-325. Although in vitro properties of **1** were favorable in terms of albumin binding, this agent appeared to be toxic in vivo. Nevertheless, **2(G1)** and **3(G2)** possessed a long elimination half-life, mainly due to their albumin-binding capabilities and macromolecular nature. Whole-body MR angiography showed prolonged visualization of the vasculature after administration of **3(G2)**, compared to **2(G1)** and Gd-DOTA, which demonstrated its utility as a blood pool imaging agent.

2.5. Acknowledgements

This research was performed within the framework of CTMM, the Center for Translational Molecular Medicine (www.ctmm.nl), project VOLTA (grant 05T-201).

2.6. References

1. Toth E, Helm L, Merbach AE. Relaxivity of MRI contrast agents. Contrast Agents I 2002;221:61-101.
2. Burtea C, Laurent S, Vander Elst L, Muller RN. Contrast agents: magnetic resonance. Handb Exp Pharmacol 2008(185 Pt 1):135-165.
3. Lauffer RB. Paramagnetic Metal-Complexes as Water Proton Relaxation Agents for Nmr Imaging - Theory and Design. Chemical Reviews 1987;87(5):901-927.
4. Caravan P, Ellison JJ, McMurry TJ, Lauffer RB. Gadolinium(III) chelates as MRI contrast agents: Structure, dynamics, and applications. Chemical Reviews 1999;99(9):2293-2352.
5. Caravan P. Strategies for increasing the sensitivity of gadolinium based MRI contrast agents. Chem Soc Rev 2006;35(6):512-523.
6. Aime S, Botta M, Fasano M, Crich SG, Terreno E. H-1 and O-17-NMR relaxometric investigations of paramagnetic contrast agents for MRI. Clues for higher relaxivities. Coordin Chem Rev 1999;185-6:321-333.
7. Bumb A, Brechbiel MW, Choyke P. Macromolecular and dendrimer-based magnetic resonance contrast agents. Acta Radiol 2010;51(7):751-767.
8. Eldredge HB, Spiller M, Chasse JM, Greenwood MT, Caravan P. Species dependence on plasma protein binding and relaxivity of the gadolinium-based MRI contrast agent MS-325. Invest Radiol 2006;41(3):229-243.
9. Lauffer RB, Parmelee DJ, Ouellet HS, Dolan RP, Sajiki H, Scott DM, Bernard PJ, Buchanan EM, Ong KY, Tyeklar Z, Midelfort KS, McMurry TJ, Walovitch RC. MS-325: a

small-molecule vascular imaging agent for magnetic resonance imaging. Acad Radiol 1996;3 Suppl 2:S356-358.
10. Lauffer RB, Parmelee DJ, Dunham SU, Ouellet HS, Dolan RP, Witte S, McMurry TJ, Walovitch RC. MS-325: albumin-targeted contrast agent for MR angiography. Radiology 1998;207(2):529-538.
11. Caravan P, Cloutier NJ, Greenfield MT, McDermid SA, Dunham SU, Bulte JW, Amedio JC, Jr., Looby RJ, Supkowski RM, Horrocks WD, Jr., McMurry TJ, Lauffer RB. The interaction of MS-325 with human serum albumin and its effect on proton relaxation rates. J Am Chem Soc 2002;124(12):3152-3162.
12. Caravan P, Greenfield MT, Li X, Sherry AD. The Gd(3+) complex of a fatty acid analogue of DOTP binds to multiple albumin sites with variable water relaxivities. Inorg Chem 2001;40(26):6580-6587.
13. Laurent S, Vander Elst L, Henrotte V, Muller RN. Noncovalent binding of some new lipophilic gadolinium DTPA complexes to human serum albumin. A structure-affinity relationship. Chem Biodivers 2010;7(12):2846-2855.
14. Gianolio E, Giovenzana GB, Longo D, Longo I, Menegotto I, Aime S. Relaxometric and modelling studies of the binding of a lipophilic Gd-AAZTA complex to fatted and defatted human serum albumin. Chemistry 2007;13(20):5785-5797.
15. Aime S, Chiaussa M, Digilio G, Gianolio E, Terreno E. Contrast agents for magnetic resonance angiographic applications: 1H and 17O NMR relaxometric investigations on two gadolinium(III) DTPA-like chelates endowed with high binding affinity to human serum albumin. J Biol Inorg Chem 1999;4(6):766-774.
16. Johansson L, Kirchin MA, Ahlstrom H. Gadobenate dimeglumine (MultiHance) in MR angiography: an in-vitro phantom comparison with gadopentetate dimeglumine (Magnevist) at different concentrations. Acta Radiol 2012;53(10):1112-1117.
17. La Ferla R, Dapra M, Hentrich HR, Pirovano G, Kirchin MA. Gadobenate dimeglumine (Multihance) in contrast-enhanced magnetic resonance angiography. Acad Radiol 2002;9 Suppl 2:S409-411.
18. Henrotte V, Vander Elst L, Laurent S, Muller RN. Comprehensive investigation of the non-covalent binding of MRI contrast agents with human serum albumin. J Biol Inorg Chem 2007;12(6):929-937.
19. Zhou Z, Lu ZR. Gadolinium-based contrast agents for magnetic resonance cancer imaging. Wiley Interdiscip Rev Nanomed Nanobiotechnol 2013;5(1):1-18.
20. Barrett T, Kobayashi H, Brechbiel M, Choyke PL. Macromolecular MRI contrast agents for imaging tumor angiogenesis. Eur J Radiol 2006;60(3):353-366.
21. Brasch R, Turetschek K. MRI characterization of tumors and grading angiogenesis using macromolecular contrast media: status report. Eur J Radiol 2000;34(3):148-155.
22. Kobayashi H, Reijnders K, English S, Yordanov AT, Milenic DE, Sowers AL, Citrin D, Krishna MC, Waldmann TA, Mitchell JB, Brechbiel MW. Application of a macromolecular contrast agent for detection of alterations of tumor vessel permeability induced by radiation. Clin Cancer Res 2004;10(22):7712-7720.
23. Turetschek K, Preda A, Novikov V, Brasch RC, Weinmann HJ, Wunderbaldinger P, Roberts TP. Tumor microvascular changes in antiangiogenic treatment: assessment by magnetic resonance contrast media of different molecular weights. J Magn Reson Imaging 2004;20(1):138-144.

24. Kobayashi H, Brechbiel MW. Dendrimer-based macromolecular MRI contrast agents: characteristics and application. Mol Imaging 2003;2(1):1-10.
25. Kobayashi H, Brechbiel MW. Nano-sized MRI contrast agents with dendrimer cores. Adv Drug Deliv Rev 2005;57(15):2271-2286.
26. Aime S, Botta M, Fasano M, Crich SG, Terreno E. Gd(III) complexes as contrast agents for magnetic resonance imaging: A proton relaxation enhancement study of the interaction with human serum albumin. J Biol Inorg Chem 1996;1(4):312-319.
27. Gianolio E, Porto S, Napolitano R, Baroni S, Giovenzana GB, Aime S. Relaxometric investigations and MRI evaluation of a liposome-loaded pH-responsive gadolinium(III) complex. Inorg Chem 2012;51(13):7210-7217.
28. Brady SF, Clardy J. Palmitoylputrescine, an antibiotic isolated from the heterologous expression of DNA extracted from bromeliad tank water. J Nat Prod 2004;67(8):1283-1286.
29. Cuthbertson A, Eriksen M, Frigstad S, Oestensen J, Rongved P, Skurtveit R, Tolleshaug H, inventors; Nycomed Imaging As, assignee. Improvements in or relating to contrast agents. Patent WO1999053963 A1. October 28, 1999.
30. Andre JP, Toth E, Fischer H, Seelig A, Macke HR, Merbach AE. High relaxivity for monomeric Gd(DOTA)-based MRI contrast agents, thanks to micellar self-organization. Chem-Eur J 1999;5(10):2977-2983.
31. Nicolle GM, Toth E, Eisenwiener KP, Macke HR, Merbach AE. From monomers to micelles: investigation of the parameters influencing proton relaxivity. J Biol Inorg Chem 2002;7(7-8):757-769.
32. Richieri GV, Anel A, Kleinfeld AM. Interactions of long-chain fatty acids and albumin: determination of free fatty acid levels using the fluorescent probe ADIFAB. Biochemistry 1993;32(29):7574-7580.
33. Curry S, Brick P, Franks NP. Fatty acid binding to human serum albumin: new insights from crystallographic studies. Biochim Biophys Acta 1999;1441(2-3):131-140.
34. Fasano M, Curry S, Terreno E, Galliano M, Fanali G, Narciso P, Notari S, Ascenzi P. The extraordinary ligand binding properties of human serum albumin. IUBMB Life 2005;57(12):787-796.
35. Aime S, Anelli L, Botta M, Brocchetta M, Canton S, Fedeli F, Gianolio E, Terreno E. Relaxometric evaluation of novel manganese(II) complexes for application as contrast agents in magnetic resonance imaging. J Biol Inorg Chem 2002;7(1-2):58-67.
36. Zavodnik IB, Zaborowski A, Niekurzak A, Bryszewska M. Effect of free fatty acids on erythrocyte morphology and membrane fluidity. Biochem Mol Biol Int 1997;42(1):123-133.
37. Connor WE, Hoak JC, Warner ED. Massive thrombosis produced by fatty acid infusion. J Clin Invest 1963;42:860-866.
38. Parmelee DJ, Walovitch RC, Ouellet HS, Lauffer RB. Preclinical evaluation of the pharmacokinetics, biodistribution, and elimination of MS-325, a blood pool agent for magnetic resonance imaging. Invest Radiol 1997;32(12):741-747.
39. Langereis S, de Lussanet QG, van Genderen MH, Meijer EW, Beets-Tan RG, Griffioen AW, van Engelshoven JM, Backes WH. Evaluation of Gd(III)DTPA-terminated poly(propylene imine) dendrimers as contrast agents for MR imaging. NMR Biomed 2006;19(1):133-141.

40. D'Onofrio M, Gianolio E, Ceccon A, Arena F, Zanzoni S, Fushman D, Aime S, Molinari H, Assfalg M. High relaxivity supramolecular adducts between human-liver fatty-acid-binding protein and amphiphilic Gd(III) complexes: structural basis for the design of intracellular targeting MRI probes. Chemistry 2012;18(32):9919-9928.
41. Torchilin V. Tumor delivery of macromolecular drugs based on the EPR effect. Adv Drug Deliv Rev 2011;63(3):131-135.
42. Zhu W, Kato Y, Artemov D. Heterogeneity of tumor vasculature and antiangiogenic intervention: insights from MR angiography and DCE-MRI. PLoS One 2014;9(1):e86583.

Supporting Information

Materials

Reagents, chemicals, materials and solvents were obtained from commercial sources, and were used as received: Biosolve, Merck for solvents, Cambridge Isotope Laboratories for deuterated solvents, and Aldrich, Acros, ABCR, Merck, Fluka and MacroCyclics (for DOTA-NHS ester) for chemicals, materials and reagents. All solvents were of AR quality. Moisture or oxygen-sensitive reactions were performed under an atmosphere of dry N_2 or argon. Analytical thin layer chromatography (TLC) was performed on Kieselgel F-254 precoated silica plates. Sephadex G-10, G15, G-25 were obtained from GE Healthcare.

Methods

^{1}H-NMR, ^{13}C-NMR spectra were recorded on a Varian Mercury (400 MHz for ^{1}H-NMR and 100 MHz for ^{13}C-NMR) spectrometer at 298 K. Chemical shifts are reported in ppm downfield from TMS at room temperature (RT) using deuterated chloroform ($CDCl_3$) as a solvent and internal standard unless otherwise indicated. Abbreviations used for splitting patterns are s = singlet, t = triplet, q = quartet, m = multiplet, dd = double doublet, br = broad. Infrared (IR) spectra were recorded on a Perkin Elmer 1600 FT-IR (UATR). Preparative size exclusion chromatography was performed using Sephadex G-10, G-15, G-25. MALDI-TOF mass spectrometry (MS) was measured on a Bruker Autoflex Speed using α-cyano-4-hydroxycinnamic acid (CHCA) as the matrix. Liquid chromatography-MS (LC-MS) was performed using a Shimadzu LC-10 AD VP series HPLC coupled to a diode array detector (Finnigan Surveyor PDA Plus detector, Thermo Electron Corporation) and an Ion-Trap (LCQ Fleet, Thermo Scientific) where ions were created via electrospray ionization (ESI). Analyses were performed using an Alltech Alltima HP C_{18} 3μ column using an injection volume of 1-4 μL, a flow rate of 0.2 mL min^{-1} and typically a gradient (5% to 100% in 10 min, held at 100% for a further 3 min) of CH_3CN in H_2O (both containing 0.1% formic acid) at 298 K. Reversed phase (RP) chromatography was performed on the Biotage Isolera One applying a SNAP KP-C18-HS cartridge. The HPLC system (Shimadzu LC-10 AD) was coupled to an evaporative light scattering detector (ELSD), Alltech ELSD 2000 (Nicholasville, UK). Analyses were executed at RT using an Intersil ODS-3, 5 micrometer particles, 3.0 x 150 mm column (GL Sciences Inc.) using an injection volume of 20 μL, a flow rate of 0.2 mL per min. and a THF in H_2O gradient (from 5% to 70% THF in 27 minutes), where both THF and H_2O contain 0.1% TFA. An aqueous sample solution at a concentration of 0.2 mg/mL was used. Elemental analyses were performed on a Perkin Elmer Series II CHNS/O Analyser 2400. The gadolinium content of the dendrimers was measured with Inductively Coupled Plasma-Atomic Emission Spectrometry (ICP-AES) (Philips Innovation Services, Eindhoven, The Netherlands).

Synthesis

*Palmitoylputrescine **(4)***
Palmitoylputrescine, a natural product antibiotic, was prepared according to an alternative synthetic procedure to that reported in patent literature; analytical data on the isolated material were in line with reported values (1,2). Briefly, equimolar amounts of palmitoyl chloride and phenol were converted to phenyl palmitate using 2 molar equivalents of TEA as base and chloroform as the solvent. The isolated phenyl palmitate (3.9 g; 11.8 mmol) was reacted overnight with 1,4-diaminobutane (DAB, 5.2 g; 59.0 mmol) in chloroform (50 mL) at 50 °C. The formed precipitate was removed by filtration, the filtrate was washed with water (3 times 50 mL), was concentrated and then precipitated into MeCN, giving a white powder product.
^{1}H NMR ($CDCl_3$): δ = 5.8 (bs, 1H), 3.25 (m, 2H), 2.7 (t, 2H), 2.1 (t, 2H), 1.7-1.3 (multiple signals, 8H), 1.3-1.1 (multiple signals, 24H), 0.9 (t, 3H). ^{13}C NMR ($CDCl_3$): δ = 173.2, 41.6, 39.2, 36.9, 31.9, 30.7, 30-29 (multiple peaks), 27.1, 25.8, 22.7, 14.0. MALDI-TOF-MS: *m/z* = 327.2 $[M+H]^+$, (calcd 326.57 for $C_{20}H_{42}N_2O$).

*Palmitoylputrescine-DOTA **(5)***
Next, palmitoylputrescine **4** (412 mg; 1.26 mmol) was suspended in DMF (4 mL) and $CHCl_3$ (4 mL), also containing DIPEA (1.34 g; 10.4 mmol) base. DOTA-NHS·TFA·$NaPF_6$ (1.05 g; 1.37 mmol) was added as a solid to the suspension that was heated to 50 °C on a water bath. Within ca. 10 minutes an almost clear reaction mixture had developed. After half an hour, an extra portion of DOTA-NHS ester was added (188 mg; 0.23 mmol), and after 5 hours of further stirring at 40 °C (water bath), the mixture was concentrated, and co-evaporated repeatedly with toluene to remove the DMF. The residue was stirred in MeCN/THF (5/1), centrifuged and the residue was washed with MeCN and centrifuged (twice). Drying of the residue gave a first crop of product. All supernatants were collected, concentrated, and the residue was stirred in MeCN and centrifuged to give a second crop of product. Finally, the supernatant was concentrated and was eluted on a RP-C18 column (Biotage), applying an isopropanol/water 10% to 80% isopropanol gradient. TLC plate analysis, using a 10% KI solution in water also containing some I_2 as staining agent, was used to assess which fractions contained product for pooling and concentration to give a third crop of product. The total yield was nearly quantitative.
^{1}H NMR ($CDCl_3$): δ = 5.0-2.8 (br., 33H), 2.2-2.0 (br. signal, 2H), 1.7-1.4 (br., 4H), 1.4-1.1 (br., 26H), 0.85 (t, 3H). ^{13}C NMR ($CDCl_3$): δ = 174 (br.), 170 (br.), 62-40 (br.), 39 (br.), 36 (br.), 31.9, 31-28 (multiple br.), 27 (br.), 26 (br.), 22.7, 14.1. ELSD-HPLC: one peak eluting at t = 23 min. MALDI-TOF-MS: *m/z* = 713.4 $[M+H]^+$, 735.4 $[M+Na]^+$, 751.4 $[M+K]^+$, 773.4 $[M+Na+K-H]^+$ (calcd 712.97 for $C_{36}H_{68}N_6O_8$). Elemental analysis: calcd (C=59.89; H=9.63; N=11.64), found (C=59.95; H=9.36; N=10.99) for $C_{36}H_{68}N_6O_8 \cdot 1/2 \cdot H_2O$. ATR-FT-IR: 3280, 3075, 2920, 2851, 1717, 1629, 1552 cm^{-1}.

Palmitoylputrescine-DOTA-Gd ***(1)***

Palmitoylputrescine-DOTA **5** (875 mg; 1.23 mmol) and pyridine (300 mg) were stirred in a mixture of $CHCl_3$, MeOH and water (10/6/1, v/v/v) to give a slightly turbid solution. In several portions, $Gd(OAc)_3 \cdot 3.88\ H_2O$ (780 mg; 1.94 mmol) was added, and the mixture was stirred overnight at RT. The pH of the mixture was ca. neutral as assessed by using pH-paper. Concentration of the reaction mixture was followed by dissolution of the residue in $CHCl_3$ and centrifugation to remove insolubles. This treatment was repeated using first isopropanol/water 3/2 (v/v) and thereafter $CHCl_3$/hexane 3/1 (v/v), where for both solvents the insolubles were removed by centrifugation. Finally, evaporation of the $CHCl_3$/hexane gave 855 mg (80%) of product as a white powder.

ELSD-HPLC: one peak eluting at t = 22.5 min. MALDI-TOF-MS: *m/z* = 868-cluster $[M+H]^+$, 890-cluster $[M+Na]^+$, 912-cluster $[M+2Na-H]^+$, 1735-cluster $[2M+H]^+$, 1757-cluster $[2M+Na]^+$, 1779-cluster $[2M+2Na-H]^+$, 1801-cluster $[2M+3Na-2H]^+$, (calcd 867.20 for $C_{36}H_{65}N_6O_8Gd$). Elemental analysis: calcd (C=45.04; H=6.74; N=8.52), found (C=44.78; H=6.74; N=8.32) for $C_{36}H_{65}N_6O_8Gd \cdot CHCl_3$. ICP-MS Gd: calcd wt%= 18.1%, found wt% = 15.3%.

G1-PPI-palm$_1$ ***(6)***

G1-PPI dendrimer (500 mg, 1,58 mmol) was dissolved in acetonitrile (6 mL) and cooled to 0 ^oC, followed by the drop wise addition of phenylpalmitate (158 mg, 0.474 mmol) dissolved in chloroform (6 mL). The reaction mixture was kept at 0 ^oC for another 30 minutes, after which it was allowed to warm-up to room temperature and kept stirring overnight. The reaction mixture was diluted with 30 mL of chloroform and washed two times with 20 mL water. The organic phase was dried over Na_2SO_4 and evaporated under reduced pressure, resulting in G1-PPI-palm$_1$ as an off-white solid (270 mg, 31% yield)

^1H NMR (399 MHz, Chloroform-*d*) δ 3.30 (q, *J* = 6.1 Hz, 2H), 2.74 (q, *J* = 6.6 Hz, 6H), 2.57 – 2.31 (multiple signals, 12H), 2.21 – 2.05 (t, 2H), 1.70 – 1.52 (multiple signals, 10H), 1.43 (dd, *J* = 7.3, 3.6 Hz, 4H), 1.25 (multiple signals, 24H), 0.94 – 0.81 (t, 3H). ^{13}C NMR (100 MHz, $cdcl_3$) δ 173.70, 53.98, 52.30, 40.67, 38.81, 38.19, 36.87, 31.93, 29.72, 29.67, 29.58, 29.45, 29.37, 25.92, 25.01, 22.70, 14.13. Based on integrals the average number of palmitoyl groups can be calculated: palm$_1$, 96%; palm$_2$, 4%. FT-IR (ATR): *υ* (cm^{-1}) = 3288, 2922, 2852, 1643, 1549, 1465, 1377, 1260, 1122, 1080, 754, 721, 694. MALDI-TOF MS m/z calcd ($C_{32}H_{70}N_6O$) 554 g/mol; found 555 g/mol. HPLC R_t= G1-PPI-palm$_1$ 17.8 min (92%), G1-PPI-palm$_2$ 20.3 min (8%).

G1-PPI-Palm$_1$-DOTA$_3$ ***(8)***

G1-PPI-palm$_1$ **6** (270 mg, 0.487 mmol) and triethylamine (0.814 mL, 5.84 mmol) were dissolved in chloroform (6 mL)/ MeOH (12 mL). DOTA-NHS·TFA·$NaPF_6$ (1.46 g, 1.91 mmol) was added as a solid. The reaction mixture was stirred for 16h under an argon atmosphere. Then, the reaction mixture was evaporated under reduced pressure and re-dissolved in water. A Sephadex G15 (MWCO 1500 g/mol) column with demi-water as eluent was used for further purification. After freeze-drying, G1-PPI-palm$_1$-DOTA$_3$ **8** was obtained as an off-white solid (580 mg, 70%).

^{1}H NMR (399 MHz, Deuterium Oxide) δ 4.19 – 2.38 (multiple signals br, 92H), 2.24 (s, 2H), 2.11 – 1.67 (br, 12H), 1.66 – 1.52 (br, 2H), 1.29 (br, 24H), 0.89 (t, *J* = 7.0 Hz, 3H). FT-IR (ATR): *υ* (cm^{-1}) = 3289, 2921, 2852, 1732, 1588, 1456, 1383, 1325, 1216, 1160, 1088, 995, 917, 697. MALDI-TOF MS m/z calcd ($C_{80}H_{148}N_{18}O22$) 1713 g/mol; found 1714 $[M+H]^+$ and 1328 $[M\text{-}DOTA_1+H]^+$ g/mol. HPLC R_t= G1-PPI-palm$_1$DOTA$_3$ 16.6 min (92%), G1-PPI-palm$_2$DOTA$_2$ 19.1 min (8%).

G1-PPI-Palm$_1$-GdDOTA$_3$ ***(2)***

After, dissolving G1-PPI-Palm$_1$-DOTA$_3$ **8** (520 mg, 0.303 mmol) in water (10 mL), the pH was corrected with 1 M NaOH to pH = 7. A solution of Gd(OAc)$_3$ x H2O (x=3.88, 552 mg, 1.365 mmol) in water (5 mL) was added followed by pH correction to 7 with 1 M NaOH. This solution was stirred overnight at room temperature under Argon. The reaction volume was reduced under vacuum. A Sephadex G15 (MWCO 1500 g/mol) column with demi-water as eluent was used for further purification. After freeze-drying, G1-PPI-palm$_1$-GdDOTA$_3$ **2** was obtained as an off-white solid (580 mg, 70%). Xylenol orange test was negative; G1-PPI-palm$_1$-GdDOTA$_3$ ~0.5 mg was dissolved in 1 mL of 1,6*10^{-5} M in acetic acid buffer pH 5.8 and no colour change from orange to purple was observed.

MALDI-TOF m/z calcd ($C_{80}H_{139}Gd_3N_{18}O_{22}$) 2178 g/mol; found 2178 M g/mol. ICP-MS Gd: calcd wt%= 21.7%, found wt% = 19.6%. FT-IR (ATR): *υ* (cm^{-1}) = 3264, 2921, 2852, 1595, 1459, 1429, 1388, 1318, 1242, 1158, 1085, 1003, 936, 904, 801, 717. HPLC R_t= G1-PPI-palm$_1$-GdDOTA$_3$ 16.5 min (92%), G1-PPI-palm$_2$-GdDOTA$_2$ 19.2 min (8%).

G2-PPI-palm$_1$ ***(7)***

G2-PPI dendrimer (500 mg, 0647 mmol) was dissolved in acetonitrile (10 mL) and cooled to 0 °C, followed by the drop wise addition of phenylpalmitate (120 mg, 0.361 mmol) dissolved in chloroform (5 mL). The reaction mixture was kept at 0 °C for another 30 minutes, after which it was allowed to warm-up to room temperature and kept stirring overnight. The reaction mixture was diluted with 30 mL of chloroform and washed with 20 mL brine. The organic phase was dried over Na_2SO_4 and evaporated under reduced pressure, resulting in G2-PPI-palm$_1$ **7** as an off-white solid (327 mg, 50% yield).

^{1}H NMR (399 MHz, Chloroform-*d*) δ 3.28 (q, *J* = 6.2 Hz, 2H), 2.73 (q, *J* = 6.8 Hz, 14H), 2.43 (dt, *J* = 36, 7.2 Hz, 36H), 2.13 (t, *J* = 7.7 Hz, 2H), 1.60 (multiple siganls, *J* = 14.4, 6.9 Hz, 26H), 1.39 (br, 4H), 1.27 (br, *J* = 10.7 Hz, 24H), 0.94 – 0.83 (t, 3H). Based on integrals the average number of palmitoyl groups can be calculated: palm$_1$ 87% palm$_2$ 13%. FT-IR (ATR): *υ* (cm^{-1}) = 3299, 3073, 2920, 2851, 1639, 1552, 1467, 1378, 1249, 1120, 755, 721, 694. MALDI-TOF MS m/z calcd ($C_{56}H_{126}N_{14}O$) 1011 g/mol; found 1012 $[M+H]^+$ g/mol. HPLC R_t= G2-PPI-palm$_1$ 17.3 min (84%), G2-PPI-palm$_2$ 18.8 min (14%), G2-PPI-palm$_3$ 20.7 min (2%).

G2-PPI-Palm$_1$-DOTA$_7$ ***(9)***

G2-PPI-palm$_1$ **7** (320 mg, 0.316 mmol) and triethylamine (0.882 mL, 6.33 mmol) were dissolved in chloroform (6 mL)/ MeOH (12 mL). DOTA-NHS·TFA·$NaPF_6$ (2.22 g, 2.88 mmol) was added as a solid. The reaction mixture was stirred for 16h under an

argon atmosphere. Then, the reaction mixture was evaporated under reduced pressure and re-dissolved in water. A Sephadex G15 (MWCO 1500 g/mol) column with demi-water as eluent was used for further purification. After freeze-drying, G2-PPI-palm$_1$-DOTA$_7$ **9** was obtained as an off-white solid (550 mg, 47%).
^{1}H NMR (399 MHz, Deuterium Oxide) δ 4.2 – 2.5 (multiple signals br, 220H), 2.4 – 1.5 (multiple signals br, 30H), 1.4 – 1.0 (br, 24H), 0.9 - 0.8 (s, 3H). FT-IR (ATR): *υ* (cm^{-1}) = 3267, 2925, 2852, 1720, 1607, 1458, 1391, 1326, 1285, 1220, 1092, 1010, 918, 789, 716, 614. MALDI-TOF MS m/z calcd ($C_{168}H_{306}N_{42}O_{50}$) 3714 g/mol; found 3712 $[M]^+$ and 3270 $[M\text{-}DOTA_1+H]^+$ g/mol. HPLC R_t= G2-PPI-palm$_1$-DOTA$_7$ 16.1 min (84%), G2-PPI-palm$_2$-DOTA$_6$ 17.7 min (14%) and G2-PPI-palm$_3$-DOTA$_5$ 19.1 min (2%).

G2-PPI-Palm$_1$-GdDOTA$_7$ ***(3)***
After, dissolving G2-PPI-Palm$_1$-DOTA$_7$ **9** (250 mg, 0.067 mmol) in water (5 mL), the pH was corrected with 1 M NaOH to pH = 7. A solution of Gd(OAc)$_3$ x H_2O (x=3.88, 286 mg, 0.706 mmol) in water (5 mL) was added followed by pH correction to 7 with 1M NaOH. This solution was stirred overnight at room temperature under Argon. The reaction volume was reduced under vacuum. A Sephadex G15 (MWCO 1500 g/mol) column with demi-water as eluent was used for further purification. After freeze-drying, G2-PPI-palm$_1$-GdDOTA$_7$ **3** was obtained as an off-white solid (230 mg, 71%). Xylenol orange test was negative; G2-PPI-palm$_1$-GdDOTA$_7$ **3**~0.5 mg was dissolved in 1 mL of 1,6 *10^{-5} M in acetic acid buffer pH 5.8 and no colour change from orange to purple was observed.
MALDI-TOF m/z calcd ($C_{168}H_{287}N_{42}O_{50}Gd_7$) 4798 g/mol; found 4795 M g/mol. ICP-MS Gd: calcd wt%= 23%, found wt% = 17.9%. FT-IR (ATR): *υ* (cm^{-1}) = 3241, 2921, 2852, 1615, 1457, 1433, 1364, 1313, 1240, 1159, 1086, 1002, 979, 932, 903, 839, 801, 714, 614, 567, 495. HPLC R_t = G2-PPI-palm$_1$-GdDOTA$_7$ 15.9 min (84%), G2-PPI-palm$_2$-GdDOTA$_6$ 17.7 min (14%) and G2-PPI-palm$_3$-GdDOTA$_5$ 19.1 min (2%).

References

1. Brady SF, Clardy J. Palmitoylputrescine, an antibiotic isolated from the heterologous expression of DNA extracted from bromeliad tank water. J Nat Prod 2004;67(8):1283-1286.
2. Cuthbertson A, Eriksen M, Frigstad S, Oestensen J, Rongved P, Skurtveit R, Tolleshaug H, inventors; Nycomed Imaging As, assignee. Improvements in or relating to contrast agents. Patent WO1999053963 A1. October 28, 1999.

Chapter 3

Synthesis and characterization of poly(propylene imine) dendrimer-based magnetic resonance imaging contrast agents of various molecular weight

Igor Jacobs[1], Siem J Wouters[1], Henk M Keizer[2], Henk M Janssen[2], Eliana Gianolio[3], Francesca Arena[3], Silvio Aime[3], Gustav J Strijkers[1,4], Klaas Nicolay[1]

[1] Biomedical NMR, Department of Biomedical Engineering, Eindhoven University of Technology, Eindhoven, The Netherlands
[2] SyMO-Chem BV, Eindhoven, The Netherlands
[3] Department of Molecular Biotechnology and Health Sciences & Molecular Imaging Center, University of Turin, Italy
[4] Biomedical Engineering and Physics, Academic Medical Center, University of Amsterdam, Amsterdam, The Netherlands

In preparation

Abstract

Purpose
The purpose of this study was to synthesize poly(propylene imine) (PPI) dendrimer-based magnetic resonance imaging (MRI) contrast agents of various molecular weight and to evaluate their in vitro and in vivo characteristics.

Experimental
Different molecular weight PPI dendrimers of generation 2, 3 and 5, functionalized with a variable number of Gd-DOTA moieties, polyethylene glycol (PEG) and the fluorescent label Rhodamine B (RhoB), were synthesized by SyMO-Chem BV. The relaxivity of the agents in phosphate buffered saline (PBS) and mouse plasma was determined at 60 MHz. Relaxometric properties were further investigated by nuclear magnetic relaxation dispersion (NMRD) measurements. To investigate the influence of contrast agent size on in vivo characteristics, blood-kinetics and biodistribution of the agents were determined in CT26 colon carcinoma bearing Balb/c mice (subcutaneous, in the hind limb). The suitability of the agents for macromolecular contrast-enhanced MRI was evaluated by whole-body MR angiographic imaging for the highest molecular weight dendrimer, using a 1 T MRI Bruker Icon^{TM} system.

Results and discussion
The agents G2-PPI-RhoB$_1$-PEG$_3$-GdDOTA$_4$ (**1(G2)**), G3-PPI-RhoB$_1$-PEG$_7$-GdDOTA$_8$ (**2(G3)**) and G5-PPI-RhoB$_3$-PEG$_{30}$-GdDOTA$_{31}$ (**3(G5)**) were successfully synthesized. Relaxivity measurements at 60 MHz demonstrated that the dendrimer-based contrast agents possessed an increased relaxivity compared to the low molecular weight gadoterate meglumine (Gd-DOTA). No differences could be observed between their relaxivity in PBS compared to in mouse plasma. Fitting of the NMRD data using the Lipari-Szabo approach for macromolecules with internal flexibility showed that global rotational correlation times increased with molecular weight of the agent, demonstrating that this is the main mechanism for the observed enhanced relaxivity. The circulation half-lives of the dendrimers increased with their molecular weight and the elimination half-life of the highest molecular weight **3(G5)** was 5 times higher than of Gd-DOTA. The accumulation of the contrast agents in the different organs generally increased with the molecular weight of the agents, although the uptake of **1(G2)** was higher than of **2(G3)** in all tissues except for the tumor and liver. Whole-body MR angiography demonstrated sustained vascular enhancement for **3(G5)** until at least 30 min after contrast agent administration, whereas for Gd-DOTA no visualization of the vasculature could be observed within the sampled time frame.

Conclusion
The evaluated dendrimers possessed different relaxometric and physiological properties, related to their molecular weight. Differences in blood-kinetics and tumor accumulation implied that these agents possess a range of tumor wash-in and wash-out rates. Whole-body MR angiography demonstrated the utility of the highest molecular weight dendrimer-based contrast agent as a blood pool imaging agent.

3.1. Introduction

Dynamic contrast-enhanced magnetic resonance imaging (DCE-MRI) is a widely applied method for tumor characterization and evaluation of tumor therapies (1-3). The dynamic contrast enhancement pattern is affected by contrast agent uptake kinetics and may therefore provide insight in underlying vascular characteristics. Tracer-kinetic modeling of DCE-MRI data facilitates assessment of specific microvascular properties, such as the tumor blood flow, blood volume and microvascular permeability, which may aid in the assessment of tumor aggressiveness or response to therapy (4-6). Especially for antivascular therapies, which are aimed at destruction of the existing tumor vasculature or inhibition of angiogenesis, DCE-MRI is a commonly applied evaluation method (7). In many clinical trials of antivascular therapies a reduction in the transfer constant K^{trans}, which is defined as the volume transfer constant between the blood plasma and extracellular extravascular space, has been reported as a measure for treatment efficacy (8-10). This parameter is a composite measure of the blood flow, microvascular permeability and capillary surface area, of which the interpretation is dependent on the perfusion regime of the tumor. These parameters cannot be separately quantified with the clinically used low molecular weight contrast agents and conventional tracer-kinetic modeling and the interpretation of K^{trans} is dependent on the perfusion regime of the tumor (11). To overcome this problem, macromolecular contrast agents have been introduced that have a limited extravasation from the healthy microvasculature and prolonged circulation half-life (12). Therefore, macromolecular contrast agents are more sensitive to changes in blood volume and microvascular permeability, whereas low molecular weight contrast agents are mainly suitable for assessment of changes in blood flow due to their high first pass extraction fraction (13-15). It has been shown that macromolecular DCE-MRI could give an improved tumor characterization and may be favorable for assessment of specific changes in the microvascular architecture after tumor treatment (16-29). Furthermore, high molecular weight contrast agents can be employed for angiographic imaging, enabling detailed visualization of the vasculature (30-32). In addition, macromolecular contrast agents have a higher relaxivity than low molecular weight contrast agents due to their decreased tumbling rate and can be functionalized with multiple MR imaging moieties, which is favorable for in vivo detection (33).

A specific platform for macromolecular contrast agents are dendrimers, which represent a class of highly branched synthetic polymers, of which the terminal groups can be functionalized with imaging labels or drugs (34-36). Because of their tunable molecular weight yet similar chemical composition, dendrimer-based contrast agents are especially suitable for the assessment of the dependency of various tracer-kinetic parameters on the contrast agent molecular weight. Langereis et al. have shown the potential of Gd-DTPA based poly(propylene imine) (PPI) dendrimers for MR imaging of the tumor microvasculature. They reported differences in tumor wash-in and wash-out rates dependent on the molecular weight of the agents and found that the higher generation dendrimers have a lower detection limit and stronger and prolonged signal enhancement in the vascular compartment than the low molecular weight agents (37).

DCE-MRI experiments in tumor-bearing mice using these dendrimer-based contrast agents confirmed that high molecular weight agents may indeed be more suitable to assess the blood volume and microvascular permeability in comparison with low molecular weight contrast agents (14).
In the present study, the synthesis, in vitro characterization, blood-kinetics and biodistribution of PPI dendrimer-based MRI contrast agents of various molecular weight (Figure 1) are reported.

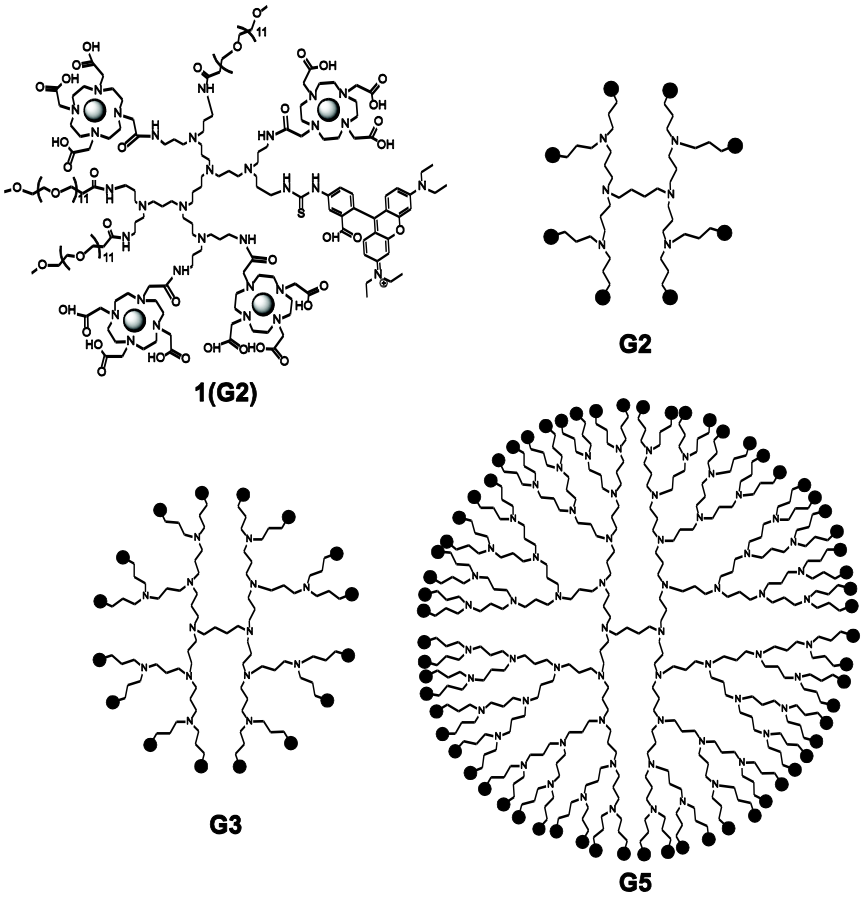

Figure 1. Schematic representation of the PPI dendrimer-based contrast agents. The black dots represent the different functionalized end-groups.

Generation 2, 3 and 5 dendrimers were functionalized with Gd-DOTA, which has a higher in vitro stability than noncyclic complexes (38). The dendrimers were conjugated with poly(ethylene) glycol (PEG), which reduces nanoparticle toxicity and recognition by the reticuloendothelial system and thereby results in a decreased clearance rate (39,40). In addition, the fluorescent imaging label rhodamine B (RhoB) was incorporated in the dendrimers, which could facilitate in vivo fluorescence imaging or ex vivo high-resolution microscopic analysis to validate differences in extravasation between the dendrimers (41). The characteristics and suitability of the dendrimers for in vivo imaging were assessed by relaxivity measurements in phosphate buffered saline (PBS) and mouse plasma, nuclear magnetic relaxation dispersion (NMRD) measurements and evaluation of their blood-kinetics and biodistribution in tumor-bearing mice. The low molecular weight Gd-DOTA was used as a control. The utility of

the dendrimers for in vivo MR imaging purposes was demonstrated by MR angiography using the highest molecular weight generation 5 dendrimer.

3.2. Experimental

3.2.1. Synthesis

3.2.1.1. Materials

All reagents, chemicals, materials and solvents were obtained from commercial sources, and were used as received: Biosolve, Merck and Cambridge Isotope Laboratories for (deuterated) solvents; Aldrich, Acros, ABCR, Merck and Fluka for chemicals, materials and reagents. All solvents were of AR quality. Moisture or oxygen-sensitive reactions were performed under an Ar atmosphere. Spectra/por 6 standard RC dialysis tubing with molecular weight cut-off (MWCO) 1000 was obtained from Spectrumlabs. Gadoterate meglumine (Gd-DOTA, Dotarem®) was purchased from Guerbet (Villepinte, France).

3.2.1.2. Methods

^{1}H-NMR, ^{13}C-NMR spectra were recorded on a Varian Mercury (400 MHz for ^{1}H-NMR and 100 MHz for ^{13}C-NMR) spectrometer at 298 K. Chemical shifts are reported in parts per million (ppm) downfield from TMS at room temperature (r.t.) using deuterated chloroform ($CDCl_3$) as a solvent and internal standard unless otherwise indicated. Abbreviations used for splitting patterns are s = singlet, t = triplet, q = quartet, m = multiplet and br = broad. Infrared (IR) spectra were recorded on a Perkin Elmer 1600 FT-IR (UATR). MALDI-TOF mass spectrometry (MS) was measured on a Bruker Autoflex Speed. Liquid chromatography (LC)-MS was performed using a Shimadzu LC-10 AD VP series HPLC coupled to a diode array detector (Finnigan Surveyor PDA Plus detector, Thermo Electron Corporation) and an Ion-Trap (LCQ Fleet, Thermo Scientific) where ions were created via electrospray ionization (ESI). Analyses were performed using a Alltech Alltima HP C_{18} 3µ column using an injection volume of 1-4 µL, a flow rate of 0.2 mL min^{-1} and typically a gradient (5% to 100% in 10 min, held at 100% for a further 3 min) of CH_3CN in H_2O (both containing 0.1% formic acid) at 298 K. Ultraviolet-visible (UV-vis) absorbance spectra were recorded on a Jasco V-650 UV-vis spectrometer. The gadolinium content of the dendrimers was determined by inductively coupled plasma-atomic emission spectrometry (ICP-AES) (Philips Innovation Services, Eindhoven, The Netherlands).

3.2.1.3. Synthesis

G2-PPI-RhoB$_1$-PEG$_3$-DOTA$_4$ ***(4)***

G2-PPI (160 mg, 0168 mmol) was dissolved in 3 mL MeOH, TEA (47 µL) was added, followed by dropwise addition of Rhodamine B isothiocyanate (99 mg, 0.185 mmol) dissolved in 2 mL MeOH. After one hour TEA (141 µL) and PEG-FTP (372 mg, 0.504 mmol) were added and this mixture was stirred for 16h. Then, TEA 0.23 mL was added, followed by DOTA-NHS·TFA·HPF_6 (674 mg, 0.879 mmol) and this was further stirred for 16 h. Subsequently, the solvent was removed under reduced vacuum. The

remaining mixture was dissolved in water and dialyzed (MWCO 1000) against MeOH/TEA/water 0.1/0.02/0.88 v/v/v (3x 1L) and water (3x 1L). The solution in the dialysis tube was freeze-dried, resulting in G2-PPI-RhoB$_1$-PEG$_3$-DOTA$_4$ **4** as a purple powder (505 mg).
^{1}H NMR (D_2O): δ = ^{1}H-NMR: δ = 8.0-6.5 (m, 9H, Ar RhoB), 4.0-2.6 ppm (m, 304H, DOTA(COCH_2N, NCH_2CH_2N), PEG(COCH_2, CH_2O, CH_3O), PPI(CH_2NHCO, CH_2NCH_2), 2.6-2.5 (br, 6H CH_2CONH), 1.97 (bm, 28H, NCH$_2$CH_2CH$_2$N, NCH$_2$CH_2CH_2CH$_2$N), 1.4-1.1 (br, 12H N*CH2CH3*). FT-IR (ATR): υ (cm^{-1}) = 3402, 2871, 1715, 1588, 1466, 1398, 1347, 1327, 1277, 1246, 1197, 1182, 1104, 984, 937, 846, 824, 702, 683. MALDI-TOF MS m/z calcd ($C_{211}H_{380}N_{33}O_{70}S$) 4531 g/mol; found 3964 (average) g/mol.

G2-PPI-RhoB$_1$-PEG$_3$-GdDOTA$_4$ ***(1)***
After dissolving G2-PPI-RhoB$_1$-PEG$_3$-DOTA$_4$ (480 mg, 0.106 mmol) in water (6 mL), the pH was corrected with 1 M NaOH to pH = 7. A solution of Gd(OAc)$_3$ x H_2O (x=3.88, 257 mg, 0.636 mmol) in water (4 mL) was added followed by pH correction to 7 with 1 M NaOH. This solution was stirred overnight at room temperature under Argon. The reaction mixture was dialyzed (MWCO 1000) against water (6x 1L). The solution in the dialysis tube was freeze-dried, resulting in G2-PPI-RhoB$_1$-PEG$_3$-GdDOTA$_4$ **1** as a purple powder (418 mg, yield 77%).
MALDI-TOF m/z calcd ($C_{211}H_{380}N_{33}O_{70}S_1Gd_4$) 5148 g/mol; found 5216 M, 4677 M-GdDOTA, 4232 M-(GdDOTA)$_2$ g/mol. LC-MS(ESI) R_t= 3.10-6.0 min, m/z calcd ($C_{211}H_{380}N_{33}O_{70}S_1Gd_4$) 5148; found 1038 $[M+2Na+3H]^{5+}$, 1305 $[M+3Na+1H]^{4+}$. Inductively Coupled Plasma-Mass Spectrometry (ICP-MS) Gd: calcd wt%= 12.2%, found wt% = 9.1%. FT-IR (ATR): υ (cm^{-1}) = 3251, 2867, 1590, 1462, 1350, 1316, 1272, 1243, 1199, 1181, 1084, 1002, 935, 838, 800, 716, 683. UV-vis in MeOH λ_{max} = 552 nm.

G3-PPI-RhoB$_1$-PEG$_7$-DOTA$_8$ ***(5)***
A similar synthetic procedure was used as for the G2 dendrimer.

^{1}H NMR (D_2O): δ = ^{1}H-NMR: δ = 8.0-6.5 (m, 9H, Ar RhoB), 4.0-2.6 ppm (m, 660H, DOTA(COCH_2N, NCH_2CH_2N), PEG(COCH_2, CH_2O, CH_3O), PPI(CH_2NHCO, CH_2NCH_2), 2.6-2.5 (br, 14H CH_2CONH), 1.97 (br, 60H, NCH$_2$CH_2CH$_2$N, NCH$_2$CH_2CH_2CH$_2$N), 1.4-1.1 (br, 12H N*CH2CH3*). Based on integrals an average number of (peripheral) groups was found: Rhodamine B 0.7 (1), PEG 7.1 (7) and DOTA 7.2 (8), the number between brackets denotes the theoretical number. FT-IR (ATR): υ (cm^{-1}) = 3265, 2866, 1717, 1630, 1454, 1378, 1324, 1239, 1090, 951, 920, 849, 786, 696. MALDI-TOF MS m/z calcd ($C_{427}H_{796}N_{65}O_{150}S$) 9273 g/mol; found 8394 (average) g/mol.

G3-PPI-RhoB$_1$-PEG$_7$-GdDOTA$_8$ ***(2)***
A similar synthetic procedure was used as for the G2 dendrimer.

MALDI-TOF m/z calcd ($C_{427}H_{772}N_{65}O_{150}S_1Gd_8$) 10507 g/mol; found 9997 (average) g/mol. ICP-MS Gd: calcd wt%= 12.0%, found wt% = 9.3%. FT-IR (ATR): υ (cm^{-1}) = 3261, 2865, 1602, 1468, 1382, 1366, 1315, 1241, 1200, 1088, 1002, 982, 939, 903, 886, 839, 807, 713. UV-vis in MeOH λ_{max} = 552 nm.

G5-PPI-RhoB$_3$-PEG$_{30}$-DOTA$_{31}$ ***(6)***
A similar synthetic procedure was used as for the G2 dendrimer.

^{1}H NMR (D_2O): δ = ^{1}H-NMR: δ = 8.0-6.5 (m, 27H, Ar RhoB), 4.5-2.5 ppm (m, 2741H, DOTA(COC*H*$_2$N, NC*H*$_2$C*H*$_2$N), PEG(COC*H*$_2$, C*H*$_2$O, *CH*$_3$O), PPI(C*H*$_2$NHCO, C*H*$_2$NC*H*$_2$), 2.6-2.5 (br, 60H *CH*$_2$CONH), 1.97 (br, 252H, NCH$_2$C*H*$_2$CH$_2$N, NCH$_2$C*H*$_2$C*H*$_2$CH$_2$N), 1.4-1.1 (br, 36H N*CH2CH3*). Based on integrals an average number of (peripheral) groups was found: Rhodamine B 2.1 (3), PEG 30.0 (30) and DOTA 26.4 (31), the number between brackets denotes the theoretical number. FT-IR (ATR): *υ* (cm^{-1}) = 3280, 2866, 1717, 1629, 1455, 1380, 1325, 1239, 1088, 950, 918, 849, 785, 697.

G5-PPI-RhoB$_3$-PEG$_{30}$-GdDOTA$_{31}$ ***(3)***
A similar synthetic procedure was used as for the G2 dendrimer.

ICP-MS Gd: calcd wt%= 11.5%, found wt% = 11.0%. FT-IR (ATR): *υ* (cm^{-1}) = 3260, 2866, 1602, 1458, 1382, 1366, 1315, 1242, 1085, 1002, 933, 903, 839, 801, 713. UV-vis in MeOH λ_{max} = 553 nm.

3.2.2. In vitro characterization

3.2.2.1. Relaxivity measurements in PBS and mouse plasma
The longitudinal (r_1) and transverse (r_2) relaxivities of the PPI dendrimer-based contrast agents and Gd-DOTA were measured on a 60 MHz (1.41 T) Bruker Minispec MQ60 (Bruker, Germany) spectrometer at 37 °C. Relaxivities were determined in PBS (Sigma-Aldrich, St. Louis, MO, USA) and Balb/c mouse plasma with Na Heparin as anticoagulant (Innovative Research, Novi, MI, USA). For each contrast agent, relaxation times of 8 samples with varying [Gd^{3+}] (~0.01-1.5 mM Gd^{3+}) were determined using an inversion recovery sequence for T_1 and a Carr-Purcell-Meiboom-Gill (CPMG) sequence for T_2 measurements. Relaxivities were determined by fitting the data with $R_i=R_{i,0}+r_i*[Gd^{3+}]$, with $i \in \{1,2\}$ and $R_i=1/T_i$.

3.2.2.2. NMRD measurements
The dependence of the longitudinal relaxivity (r_1) of the dendrimer-based contrast agents on the applied magnetic field strength was assessed with NMRD measurements. Longitudinal water proton relaxation rates were measured in PBS at 37 °C using a Stelar field-cycling relaxometer (Stelar, Mede, Pavia, Italy) operating at proton Larmor frequencies between 0.01 MHz and 20 Mhz, corresponding to field strengths between 0.0024 and 0.47 T. The relaxometer works under complete computer control with an absolute uncertainty in R_1 of 1%. Relaxation rates at field strengths from 0.47-1.7 T (20-70 MHz) were determined using a Stelar Spinmaster spectrometer (Stelar, Mede, Pavia, Italy) working at variable field. The gadolinium concentration of the contrast agent solutions used for the NMRD measurements were determined by mineralizing a given quantity of the used solutions by addition of 37% hydrochloric acid (HCl) at 120 °C overnight. By measuring the relaxation rates of the obtained solutions and with the known relaxivity of the Gd^{3+} aqua ion in acidic

solutions (13.5 $mM^{-1}s^{-1}$), the exact [Gd^{3+}] could be determined (this method was calibrated using standard ICP solutions).

NMRD data in the high field range (2.6-70 MHz) were fit using the Lipari-Szabo approach, which discriminates between local (τ_l) and global (τ_g) correlation times (42,43). The order parameter S^2 describes the order of restriction of local motion. The fitted parameters were the rotational correlation times τ_l and τ_g, the order of restriction (S^2), the mean square of the transient zero field-splitting energy (Δ^2) and the associated relaxation time τ_v. Since quantitative modeling of NMRD data using the Lipari-Szabo approach is relatively uncertain without additional variable temperature ^{17}O transverse relaxation rate measurements (44,45), a number of parameters was fixed to reduce the degrees of freedom during fitting of the NMRD data in our analysis. The water residential lifetime (τ_m^{310} = 400 ps) was calculated from the τ_m^{298} measured through ^{17}O-NMR vs R_{2p} data for a DOTA-monoamide derivative, to which the structure of the Gd-DOTA groups of the dendrimers closely corresponded (46). Other fixed parameters were the distance between the paramagnetic center and coordination inner- and outer sphere water protons (r = 3.1 Å and a=3.8 Å, respectively), the water diffusion constant at 37 °C (D = $3.2*10^{-3}$ mm^2/s), the hyperfine coupling constant (A/ħ = 0 rad/s) and the number of coordinated water molecules (q = 1).

3.2.3. In vivo characterization

3.2.3.1. Ethics Statement

All animal experiments were performed according to the Directive 2010/63/EU of the European Commission and approved by the Animal Care and Use Committee of Maastricht University (protocol: 2010-132).

3.2.3.2. Tumor model

10-12 week-old Balb/c mice (Charles River, Maastricht, The Netherlands) were inoculated with $2x10^6$ CT26.WT murine colon carcinoma cells (American Type Culture Collection (ATCC; CRL-2638), Manassas, VA, USA) subcutaneously in the right hind limb. Approximately 10 days after inoculation, tumors became palpable in all animals and mice were subjected to the blood clearance kinetics and biodistribution experiments (n=3-4 per contrast agent).

3.2.3.3. Blood-kinetics and biodistribution

Mice were intravenously injected with a dose of 0.1 mmol/kg Gd ([Gd]=25 mM) of one of the PPI dendrimer-based contrast agents (**1(G2)**, **2(G3)**, or **3(G5)** or Gd-DOTA (Dotarem®), followed by a saline flush, via the tail vain in 5 seconds using an infusion pump (Chemyx Fusion 100, Stafford, TX, USA) under general anesthesia (2% isoflurane in medical air). Blood sampling was performed before and up to 24 h after contrast agent injection. Blood samples (20 µL) were collected via the saphenous vein before and at 8 time points after contrast agent injection (before and at 2, 15, 30, 45 min and 1, 4, 8, 24 h after injection) and immediately mixed with 20 µL of heparinized physiological saline solution to prevent coagulation of the blood. 24 h after contrast agent administration, mice were sacrificed by cervical dislocation and tumor, hind limb

muscle, liver, spleen, kidneys, heart and lungs were excised to determine the biodistribution of the contrast agents. After destruction of the samples with nitric acid, Gd^{3+} content of the samples was assessed by means of Inductively Coupled Plasma-Atomic Emission Spectrometry (ICP-AES) or ICP-MS (Philips Innovation Services, Eindhoven, The Netherlands). Tumor to muscle uptake ratios of the different agents were compared using a one-way ANOVA with post-hoc Games-Howell test. The level of statistical significance was set at α=0.05.

The longitudinal relaxation rate R_1 (s^{-1}) of the heparinized blood samples was determined with a 6.3 T horizontal bore Bruker scanner (Bruker BioSpin, Ettlingen, Germany), equipped with a 3.2-cm-diameter quadrature birdcage RF coil (Rapid Biomedical, Rimpar, Germany). R_1 relaxation rates of all blood samples were measured at room temperature, using a segmented inversion recovery fast low angle shot (FLASH) sequence (repetition time (TR) = 15 s, echo time (TE) = 2 ms, flip angle (FA) = 8°, inversion times (TI) between 72.51 and 4792.51 ms in 60 steps, one slice planned through the blood samples, slice thickness = 1 mm, field of view (FOV) = 3x3 cm^2, matrix size = 128x128, number of averages = 4). The ΔR_1 at each time point was determined by subtraction of the pre-contrast R_1 from R_1 (t). With the assumption that the ΔR_1 is proportional to the contrast agent concentration in the blood, circulation half-lives were determined by fitting a biexponential decay model to the ΔR_1 data of all mice:

$$\Delta R_1(t) = A \cdot e^{-\alpha t} + B \cdot e^{-\beta t}, \text{ with } \alpha = \frac{\ln(2)}{t_{1/2,\alpha}} \text{ and } \beta = \frac{\ln(2)}{t_{1/2,\beta}}$$

in which A and B represent the contributions from the distribution and elimination phase, respectively. α and β are the corresponding decay constants and $t_{1/2,\alpha}$ and $t_{1/2,\beta}$ are the distribution and elimination half-lives.

3.2.4. Whole-body MR angiography

3.2.4.1. Tumor model

Studies were approved by the local ethics committee of the University of Turin and carried out in accordance with the guidelines of the European Commission. Male BALB/c mice (Charles River Laboratories, Calco, Italy) were inoculated with $1x10^6$ CT26 colon carcinoma cells (ATCC; CRL-2638, Manassas, VA, USA) subcutaneously in their hind limb. Tumors reached a size of approximately 0.4-0.6 cm in diameter at 10-12 days after cell inoculation.

3.2.4.2. MR angiography in tumor-bearing mice

MR angiography was performed in tumor-bearing mice using **3(G5)**, with Gd-DOTA as a control (n=1 per agent). Mice were anesthetized with isofluorane and placed supine in a solenoid Tx/Rx coil with an inner diameter of 3.5 cm for the MRI experiment. During measurements, respiration was monitored with a sensor connected to an ECG/respiratory unit. The contrast agents were injected via a tail vein at a dose of 0.1 mmol Gd/kg.

MR images were acquired before and at 10, 20 and 30 min post-injection of the contrast agents on a 1 T MRI Bruker Icon™ system (Bruker BioSpin MRI, Ettlingen, Germany). A 35 mm Tx/Rx mouse solenoid whole body coil was used for both RF excitation and reception of MR signal. A 3D gradient-echo (GRE) fast low angle shot (FLASH) pulse sequence (TR = 10 ms, TE = 4.1 ms, flip angle = 30°, field of view (FOV) = 80x40x40 mm^3, matrix size = 192x96x96, number of averages = 2, temporal resolution = 3 min 4 s per image) with an isotropic spatial resolution of 417 µm was used for image acquisition. Pre-contrast data were subtracted from post-contrast data using Mathematica 8.0 (Wolfram Research, Champaign, IL, USA) and 3D maximum intensity projection (MIP) images were reconstructed using OsiriX-Lite (Pixmeo, Switzerland).

3.3. Results and Discussion

3.3.1. Synthesis

Synthesis of the PPI dendrimer-based contrast agents is shown in Figure 2.

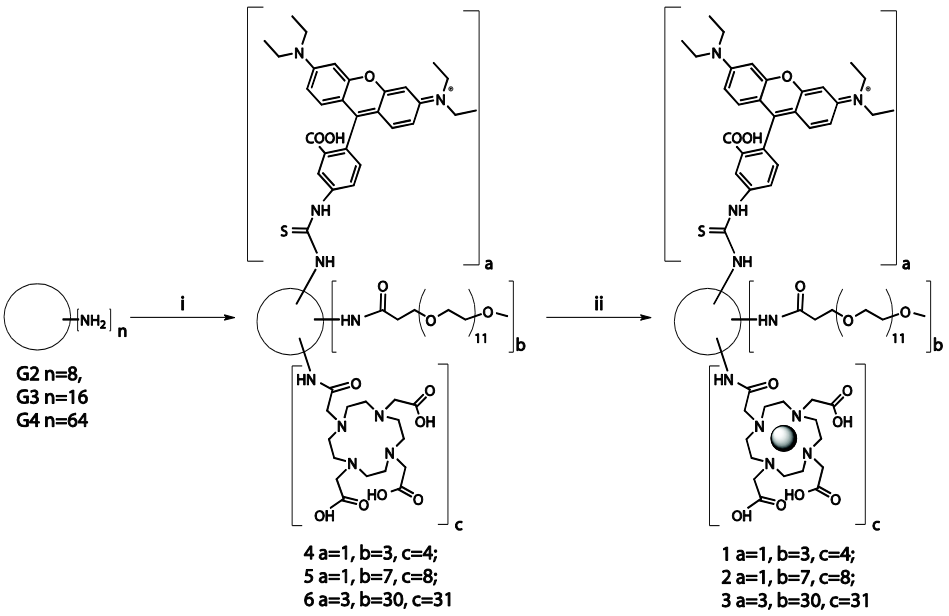

Figure 2. The synthesis of **1(G2)**, **2(G3)** and **3(G5)**. (i) 1.Rhodamine B isothiocyanate, TEA, MeOH, RT; 2. Poly(ethyleneglycol) tetrafluorophenol ester, TEA, MeOH, RT; 3. DOTA-NHS ester, TEA, MeOH, RT; (ii) $Gd(OAc)_3$, H_2O pH~7, RT.

The amine end-groups of the PPI dendrimers were reacted with three different reactive groups: the isothiocyanate of Rhodamine B, the tetrafluorophenol ester of PEG and the succinimidyl ester of DOTA. In a 'one-pot' approach the reactants were added sequentially, while purification followed afterwards. Purification was performed by dialysis first against a mixture of MeOH/TEA/water 0.1/0.02/0.88 v/v/v and against demi-water, followed by lyophilization. Due to this synthetic approach there is an expected distribution in the number of the three end-groups (Rhodamine B, PEG, and DOTA) per PPI dendrimer. The ratio between the end-groups per PPI dendrimer was determined by ^{1}H-NMR and UV-vis spectroscopy (Table 1). In the next step, complexation with an excess of $Gd(OAc)_3$ in water at pH~7 was performed, followed

by dialysis and lyophilization. ICP-MS was performed to determine the number of Gd per PPI dendrimer (Table 1). The measured numbers of conjugates were slightly lower than the theoretically expected numbers, although these amounts were generally in good agreement.

Table 1. Characteristics of Gd-DOTA and the PPI dendrimer-based contrast agents. For every type of end-group the left column denotes the theoretical and the right column the measured average number per PPI dendrimer. The measured average number of end-groups per PPI dendrimer was used to determine the average molecular weights. * UV-vis, † ^{1}H-NMR, ‡ ICP-MS, # MW after Gd complexation (g/mol).

	RhoB		**PEG**		**Dota**		**Gd**		**MW** #	
	Theo	Meas*	Theo	Meas†	Theo	Meas†	Theo	Meas‡	Theo	Meas
Gd-DOTA	-	-	-	-	1	-	1	-	754	-
1(G2)	1	0.7	3	3.2	4	3.2	4	2.7	5148	4621
2(G3)	1	0.7	7	7.1	8	7.2	8	5.6	10507	9556
3(G5)	3	2.1	30	30.0	31	26.4	31	28.5	42550	40757

3.3.2. In vitro characterization

3.3.2.1. Relaxivity measurements

The longitudinal (R_1) and transverse (R_2) relaxation rates of Gd-DOTA and the dendrimer-based contrast agents in PBS and mouse plasma versus their concentration, measured at 60 MHz and 37 °C, are shown in Figure 3.

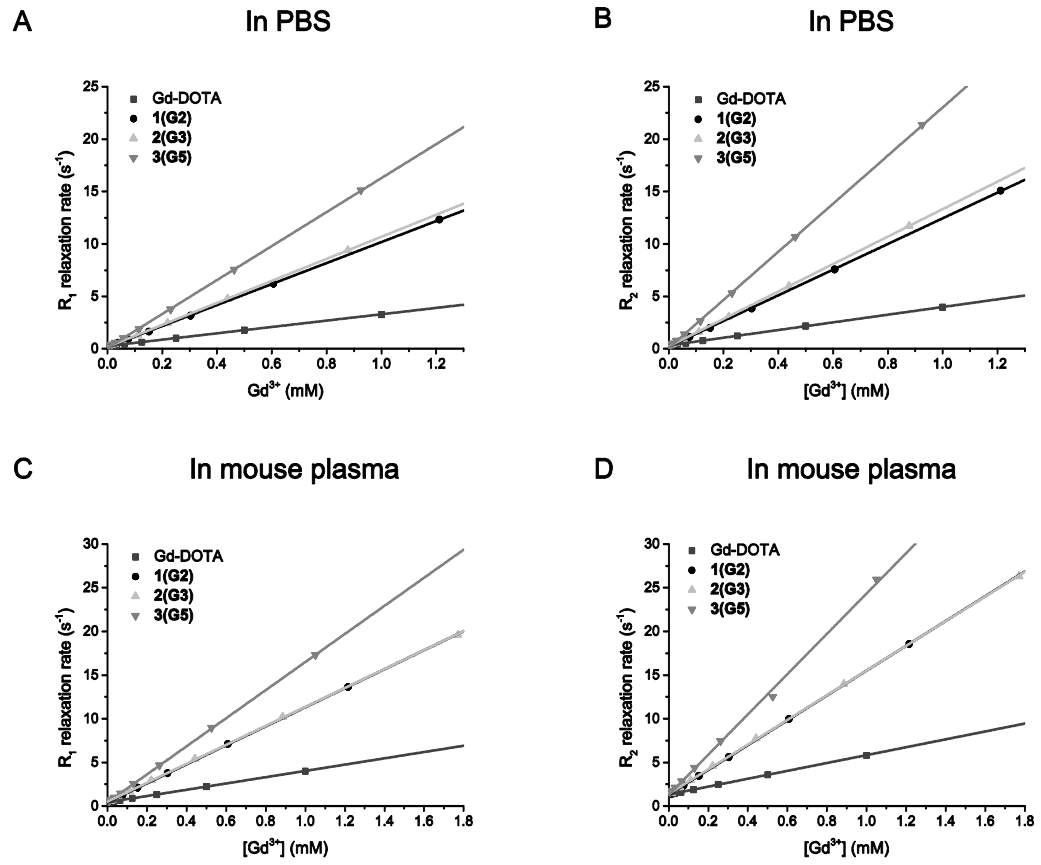

Figure 3. A,B) Longitudinal (R_1) and transverse (R_2) relaxation rates in PBS and C,D) in mouse plasma, measured at 60 MHz and 37 °C, versus the concentration of Gd^{3+} for Gd-DOTA and the PPI dendrimer-based contrast agents. The solid lines represent the linear fits through the data.

The relaxation rates increased linearly with the contrast agent concentration. The longitudinal (r_1) and transverse (r_2) relaxivities are shown in Table 2.

Table 2. Relaxivities of Gd-DOTA and the PPI dendrimer-based contrast agents, measured at 60 MHz and 37 °C, in PBS and mouse plasma.

Agent	Relaxivity in PBS ($mM^{-1}s^{-1}$)			Relaxivity in mouse plasma ($mM^{-1}s^{-1}$)		
	r_1	r_2	r_2/r_1	r_1	r_2	r_2/r_1
Gd-DOTA	3.0	3.7	1.2	3.6	4.5	1.3
1(G2)	10.0	12.2	1.2	10.9	14.2	1.3
2(G3)	10.5	13.1	1.2	10.8	14.1	1.3
3(G5)	16.2	22.9	1.4	16.1	23.1	1.4

Both in PBS and in mouse plasma, the relaxivities of the dendrimer-based contrast agents were higher than those of Gd-DOTA. **3(G5)** possessed the highest relaxivity in PBS and mouse plasma in comparison with **1(G2)** and **2(G3)**, of which the relaxivities were approximately equal. Relaxivities in PBS and mouse plasma were similar, which is advantageous since association of the agents with plasma proteins may result in unpredictable in vivo behavior. Although it has been described that rhodamine B possesses albumin binding properties (47), potential binding of rhodamine B to albumin may be hampered by the presence of the PEG and Gd-DOTA moieties.

3.3.2.2. NMRD measurements

NMRD measurements were performed in PBS at 37 °C to gain further insight in the relaxometric properties of the PPI dendrimer-based contrast agents, of which the results are shown in Figure 4. A macromolecular peak at approximately 20 MHz was most predominantly observed for **3(G5)**, whereas a less pronounced peak was detected around 30 MHz for **1(G2)** and **2(G3)**. For the low molecular weight Gd-DOTA, such peak is known to be absent (48).

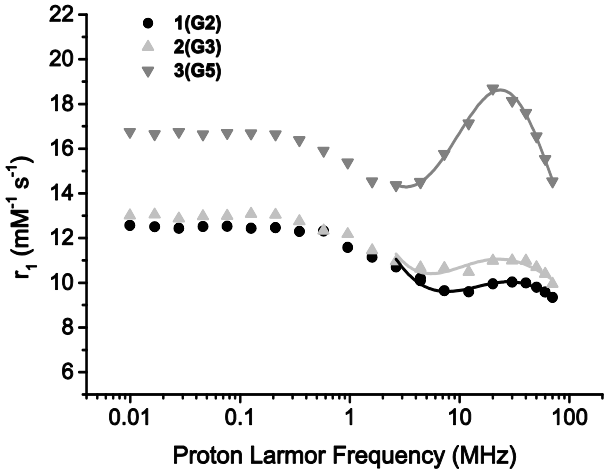

Figure 4. NMRD profiles of the PPI dendrimer-based contrast agents acquired at proton Larmor frequencies of 0.01-70 MHz (0.0024-1.7 T) measured in PBS at 37 °C. The graphs represent the measured longitudinal relaxivity r_1 ($mM^{-1}s^{-1}$) as a function of the Larmor frequency. The solid lines were obtained by fitting the 2.63-70 MHz NMRD data with the Lipari-Szabo model.

The results from quantitative fitting of the NMRD data using the Lipari-Szabo approach, a model-free approach for interpretation of NMRD data of macromolecules with internal flexibility (42,43), are shown in Table 3.

Table 3. Parameters obtained from fitting the NMRD data of the PPI dendrimer-based contrast agents measured at 37 °C in PBS with the Lipari-Szabo model. The error represents the standard error on the Lipari-Szabo fits.

Agent	Δ^2 (10^{18} s^{-2})	τ_v (ps)	τ_l (ps)	τ_g (ps)	S^2 (-)
1(G2)	7.1±1.0	16.2±0.3	301± 42	1830± 105	0.245±0.07
2(G3)	5.8±0.6	24.7±0.6	357± 41	2100± 283	0.222±0.05
3(G5)	4.3±0.5	23.6±0.3	504±209	2990±1033	0.498±0.12

The global rotational correlation time τ_g increased with the molecular weight of the dendrimer-based agents, which is known to be the main mechanism for the increase in relaxivity with increasing molecular weight (33). Such increase in rotational correlation time has been previously reported for linear polymers (τ_g = 2300±100 and 3100±300 ps at 36 °C for [Gd(DTPA-BA)-$(CH_2)_{10}]_x$ of 10.3 kDa and [Gd(DTPA-BA)-$(CH_2)_{12}]_x$ of 15.7 kDa, respectively) (49) and polyamidoamine (PAMAM) dendrimer-based contrast agents (τ_R = 580±10, 700±20 and 870±20 ps at 25 °C for G_3Gd_{23}, G_4Gd_{30} and G_5Gd_{52} of 22.1, 37.4 and 61.8 kDa, respectively) (50). The local rotational correlation times were considerably lower than the global correlation times, which indicates the presence of relatively rapid local motion compared to the slower global motion of the dendrimer-based contrast agents. Dendrimers are known to possess internal flexibility of the linker between the gadolinium chelate and dendrimer (33). This was also suggested by the order of restriction S^2, which was slightly lower for the lower molecular weight **1(G2)** and **2(G3)** (S^2 ~ 0.2) compared to the higher molecular weight **3(G5)** (S^2 ~ 0.5). These values were comparable to those observed for various PAMAM conjugates (S^2 ~ 0.3) and the commercially available poly-lysine-based Gadomer-17 (S^2 = 0.5) (51).

3.3.2.3. Blood-kinetics and biodistribution

The blood-kinetics of Gd-DOTA and the PPI dendrimer-based contrast agents were determined in tumor-bearing mice in order to assess their suitability for in vivo DCE-MRI studies. The blood-kinetics data are displayed in Figure 5 and the distribution and elimination half-lives are shown in Table 4.

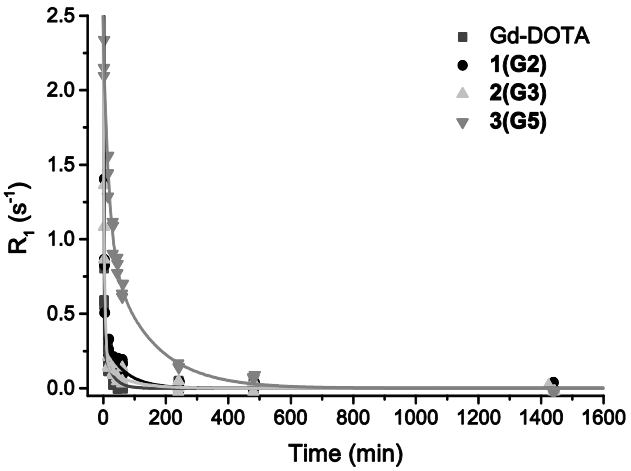

Figure 5. Blood-kinetics data of all mice injected with Gd-DOTA (n=4), **1(G2)** (n=4), **2(G3)** (n=3) and **3(G5)** (n=3) and biexponential fit to the data.

Table 4. Distribution ($t_{1/2,\alpha}$) and elimination ($t_{1/2,\beta}$) half-lives of Gd-DOTA and the PPI dendrimer-based contrast agents, obtained by biexponential fitting of the combined data of all mice. The error represents the standard error on the biexponential fits.

Agent	$t_{1/2,\alpha}$ (min)	$t_{1/2,\beta}$ (min)
Gd-DOTA	0.3±0.1	18.8± 6.8
1(G2)	0.7±0.1	44.6±11.0
2(G3)	2.8±0.9	52.5±60.5
3(G5)	12.2±2.6	95.4±22.8

Both the distribution and elimination half-lives increased with the molecular weight of the contrast agents. A five-fold increase in the elimination half-life was observed for **3(G5)** compared to Gd-DOTA, in correspondence with the finding that dendrimers larger than ~40 kDa had longer circulation half-lives compared to lower molecular weight dendrimers (52). In addition, Langereis et al. reported molecular weight dependent differences in blood plasma clearance and tumor accumulation of Gd-DTPA-based PPI dendrimers with a similar range of molecular weights. They observed that accumulation of relatively low molecular weight dendrimers in the tumor periphery reflected the blood plasma clearance profile, whereas a gradual and sustained tumor accumulation of the dendrimers was measured for the higher molecular weight agents (37).

The biodistribution of Gd-DOTA and the PPI dendrimer-based contrast agents in tumor-bearing mice at 24 h after injection is shown in Figure 6 and Table 5.

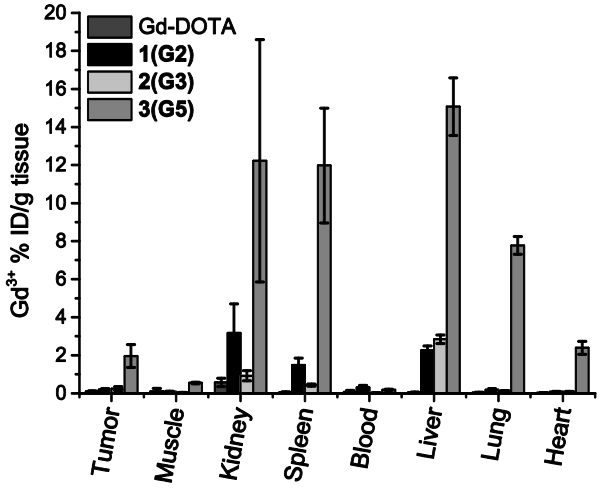

Figure 6. Biodistribution data of Gd-DOTA (n=4), **1(G2)** (n=4), **2(G3)** (n=3) and **3(G5)** (n=3). For **1(G2)**, **2(G3)** and **3(G5)** the blood samples were obtained with n=2 and for **2(G3)** the blood and liver samples were obtained with n=2. Data are presented as mean±standard deviation (SD) of all mice.

Table 5. Biodistribution of Gd-DOTA and the PPI dendrimer-based contrast agents in tumor-bearing mice. Data are presented as mean±standard deviation (SD) of all mice.

	Gd^{3+} % ID/g tissue			
Organ	Gd-DOTA	**1(G2)**	**2(G3)**	**3(G5)**
Tumor	0.10±0.03	0.20±0.04	0.24±0.10	1.96±0.61
Muscle	0.11±0.15	0.08±0.04	0.04±0.00	0.54±0.04
Kidney	0.57±0.22	3.18±1.53	0.92±0.27	12.23±6.37
Spleen	0.06±0.03	1.49±0.37	0.43±0.06	11.97±3.02
Blood	0.07±0.07	0.31±0.10	0.02±0.01	0.18±0.03
Liver	0.05±0.02	2.26±0.23	2.84±0.23	15.07±1.51
Lung	0.04±0.02	0.18±0.07	0.13±0.01	7.78±0.47
Heart	0.02±0.01	0.08±0.02	0.09±0.01	2.39±0.34

The accumulation of the contrast agents in the different organs increased with the molecular weight of the agents, although the uptake of **1(G2)** was higher than of **2(G3)** in all tissues except for the tumor and liver. The lower uptake of **2(G3)** than **1(G2)** in most tissues may be due to the lower concentration of **2(G3)** in the blood (0.02±0.01% ID/g tissue) in comparison with **1(G2)** (0.31±0.10% ID/g tissue) at 24 h after injection. A generally size-dependent accumulation of the agents in the tumor was observed, which may be caused by the higher molecular weight of the dendrimers and prolonged tumor accumulation due to their longer circulation times in comparison with Gd-DOTA (53). No significant differences in tumor to muscle uptake ratio were observed between the agents. Gd-DOTA was predominantly cleared by the kidneys, whereas for the PPI dendrimers also accumulation in the spleen and liver was observed. These findings are in agreement with the results of Langereis et al., who observed that non-PEGylated Gd-DTPA-based PPI dendrimers of 0.7-3.1 KDa were

predominantly cleared via the renal collecting system, whereas also accumulation in the liver and spleen was observed for dendrimers of 12.7 and 51.2 kDa at early time points after injection (37). The relatively high uptake of **3(G5)** in the liver is in agreement with the reported size limit of 30-40 kDa for renal clearance of polyethylene oxides (54). A size-dependent accumulation of poly(propylene imine) diaminobutyl (DAB) G2-G4 dendrimers of 12-51 kDa in the liver at 15 min after injection has also previously been reported by Kobayashi et al. (55). Accumulation in the lungs and heart was relatively high for **3(G5)** in comparison with the other agents, which requires further investigation.

3.3.3. Whole body MR angiography

MR angiography was performed using **3(G5)** to demonstrate its utility as a blood pool agent. In Figure 7, the 3D maximum intensity projection (MIP) contrast enhanced images of mice injected with **3(G5)** at 10, 20 and 30 min post-injection are shown, with Gd-DOTA as a control.

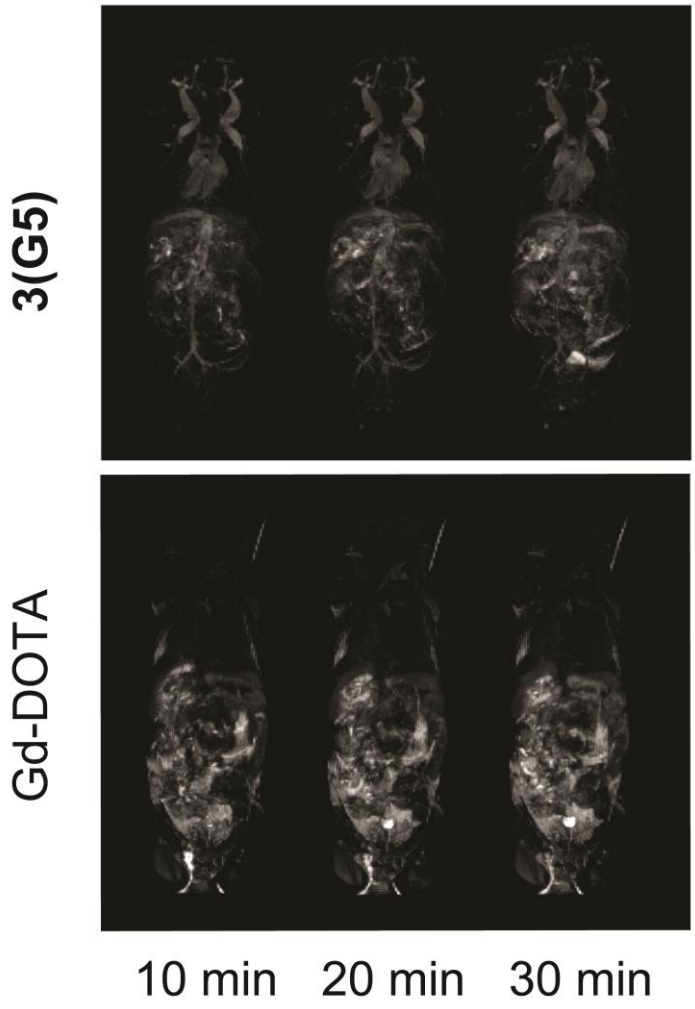

Figure 7. Whole-body MR angiography. Coronal maximum intensity projection (MIP) of the 3D FLASH images obtained from the mice after intravenous administration of **3(G5)** or Gd-DOTA at a dose of 0.1 mmol Gd/kg. Post-contrast images at 10, 20 and 30 min are shown after the subtraction of the corresponding pre-contrast images. The data of Gd-DOTA are the same as shown in chapter 2 of this thesis.

Clear visualization of the heart and vasculature - primarily the jugular veins - was obtained for **3(G5)**. Enhancement of the vasculature was most pronounced at 10 min after contrast agent administration, although it persisted until at least 30 min post-injection. Administration of the low molecular weight Gd-DOTA did not result in visualization of the vasculature at the evaluated time points. These findings were in line with those of Kobayashi et al., who demonstrated the suitability of a high molecular weight (43 kDa) polyamidoamine for whole-body angiographic imaging in mice, whereas vascular enhancement was less pronounced for lower molecular weight agents. In the present study, the tumor vasculature could not be visualized, which may be due to a relatively coarse spatial resolution used for the whole-body angiography. Reducing the FOV could improve tumor-specific angiographic imaging (31). Zhu et al. have shown that high molecular weight contrast agents can be employed for a combined angiography and DCE-MRI approach (31).

3.4. Conclusion

PPI dendrimer-based MRI contrast agents of various molecular weight were characterized in vitro and their blood-kinetics and biodistribution were evaluated in tumor-bearing mice. The dendrimers possessed an increased relaxivity compared to the low molecular weight Gd-DOTA, related to their increased rotational correlation times. The circulation half-lives of the dendrimers increased with their molecular weight and the elimination half-life of the G5 dendrimer was 5 times higher than that of Gd-DOTA. These physiological properties enabled visualization of the vasculature by MR angiography using the G5 dendrimer. Differences in circulation times and tumor accumulation imply that these agents likely possess a range of tumor wash-in and wash-out rates. Besides for angiographic imaging, these agents could find their use in a macromolecular DCE-MRI approach, in which the size-dependent sensitivity of these agents to different tracer-kinetic parameters is exploited for better characterization of microvascular function.

3.5. Acknowledgements

This research was performed within the framework of CTMM, the Center for Translational Molecular Medicine (www.ctmm.nl), project VOLTA (grant 05T-201).

3.6. References

1. Jackson A. Imaging microvascular structure with contrast enhanced MRI. Br J Radiol 2003;76 Spec No 2:S159-173.
2. Barrett T, Brechbiel M, Bernardo M, Choyke PL. MRI of tumor angiogenesis. J Magn Reson Imaging 2007;26(2):235-249.
3. Li SP, Padhani AR. Tumor response assessments with diffusion and perfusion MRI. J Magn Reson Imaging 2012;35(4):745-763.
4. Tofts PS, Kermode AG. Measurement of the blood-brain barrier permeability and leakage space using dynamic MR imaging. 1. Fundamental concepts. Magn Reson Med 1991;17(2):357-367.

5. Tofts PS, Brix G, Buckley DL, Evelhoch JL, Henderson E, Knopp MV, Larsson HB, Lee TY, Mayr NA, Parker GJ, Port RE, Taylor J, Weisskoff RM. Estimating kinetic parameters from dynamic contrast-enhanced T1-weighted MRI of a diffusable tracer: standardized quantities and symbols. J Magn Reson Imaging 1999;10(3):223-232.
6. Hylton N. Dynamic contrast-enhanced magnetic resonance imaging as an imaging biomarker. J Clin Oncol 2006;24(20):3293-3298.
7. Ferl GZ, Port RE. Quantification of antiangiogenic and antivascular drug activity by kinetic analysis of DCE-MRI data. Clin Pharmacol Ther 2012;92(1):118-124.
8. O'Connor JP, Jackson A, Parker GJ, Jayson GC. DCE-MRI biomarkers in the clinical evaluation of antiangiogenic and vascular disrupting agents. Br J Cancer 2007;96(2):189-195.
9. O'Connor JP, Jackson A, Asselin MC, Buckley DL, Parker GJ, Jayson GC. Quantitative imaging biomarkers in the clinical development of targeted therapeutics: current and future perspectives. Lancet Oncol 2008;9(8):766-776.
10. O'Connor JP, Jackson A, Parker GJ, Roberts C, Jayson GC. Dynamic contrast-enhanced MRI in clinical trials of antivascular therapies. Nat Rev Clin Oncol 2012;9(3):167-177.
11. Sourbron SP, Buckley DL. On the scope and interpretation of the Tofts models for DCE-MRI. Magn Reson Med 2011;66(3):735-745.
12. Barrett T, Kobayashi H, Brechbiel M, Choyke PL. Macromolecular MRI contrast agents for imaging tumor angiogenesis. Eur J Radiol 2006;60(3):353-366.
13. Padhani AR. MRI for assessing antivascular cancer treatments. Br J Radiol 2003;76 Spec No 1:S60-80.
14. de Lussanet QG, Langereis S, Beets-Tan RG, van Genderen MH, Griffioen AW, van Engelshoven JM, Backes WH. Dynamic contrast-enhanced MR imaging kinetic parameters and molecular weight of dendritic contrast agents in tumor angiogenesis in mice. Radiology 2005;235(1):65-72.
15. Jaspers K, Aerts HJ, Leiner T, Oostendorp M, van Riel NA, Post MJ, Backes WH. Reliability of pharmacokinetic parameters: small vs. medium-sized contrast agents. Magn Reson Med 2009;62(3):779-787.
16. Daldrup H, Shames DM, Wendland M, Okuhata Y, Link TM, Rosenau W, Lu Y, Brasch RC. Correlation of dynamic contrast-enhanced MR imaging with histologic tumor grade: comparison of macromolecular and small-molecular contrast media. AJR Am J Roentgenol 1998;171(4):941-949.
17. Brasch R, Turetschek K. MRI characterization of tumors and grading angiogenesis using macromolecular contrast media: status report. Eur J Radiol 2000;34(3):148-155.
18. Roberts TP, Turetschek K, Preda A, Novikov V, Moeglich M, Shames DM, Brasch RC, Weinmann HJ. Tumor microvascular changes to anti-angiogenic treatment assessed by MR contrast media of different molecular weights. Acad Radiol 2002;9 Suppl 2:S511-513.
19. Turetschek K, Preda A, Novikov V, Brasch RC, Weinmann HJ, Wunderbaldinger P, Roberts TP. Tumor microvascular changes in antiangiogenic treatment: assessment by magnetic resonance contrast media of different molecular weights. J Magn Reson Imaging 2004;20(1):138-144.

20. Pike MM, Stoops CN, Langford CP, Akella NS, Nabors LB, Gillespie GY. High-resolution longitudinal assessment of flow and permeability in mouse glioma vasculature: Sequential small molecule and SPIO dynamic contrast agent MRI. Magn Reson Med 2009;61(3):615-625.
21. Orth RC, Bankson J, Price R, Jackson EF. Comparison of single- and dual-tracer pharmacokinetic modeling of dynamic contrast-enhanced MRI data using low, medium, and high molecular weight contrast agents. Magn Reson Med 2007;58(4):705-716.
22. Weidensteiner C, Rausch M, McSheehy PM, Allegrini PR. Quantitative dynamic contrast-enhanced MRI in tumor-bearing rats and mice with inversion recovery TrueFISP and two contrast agents at 4.7 T. J Magn Reson Imaging 2006;24(3):646-656.
23. Delrue LJ, Casneuf V, Van Damme N, Blanckaert P, Peeters M, Ceelen WP, Duyck PC. Assessment of neovascular permeability in a pancreatic tumor model using dynamic contrast-enhanced (DCE) MRI with contrast agents of different molecular weights. MAGMA 2011;24(4):225-232.
24. Ivanusa T, Beravs K, Medic J, Sersa I, Sersa G, Jevtic V, Demsar F, Mikac U. Dynamic contrast enhanced MRI of mouse fibrosarcoma using small-molecular and novel macromolecular contrast agents. Phys Med 2007;23(3-4):85-90.
25. Henderson E, Sykes J, Drost D, Weinmann HJ, Rutt BK, Lee TY. Simultaneous MRI measurement of blood flow, blood volume, and capillary permeability in mammary tumors using two different contrast agents. J Magn Reson Imaging 2000;12(6):991-1003.
26. Fries P, Runge VM, Bucker A, Schurholz H, Reith W, Robert P, Jackson C, Lanz T, Schneider G. Brain Tumor Enhancement in Magnetic Resonance Imaging at 3 Tesla Intraindividual Comparison of Two High Relaxivity Macromolecular Contrast Media With a Standard Extracellular Gd-Chelate in a Rat Brain Tumor Model. Invest Radiol 2009;44(4):200-206.
27. Preda A, Novikov V, Moglich M, Turetschek K, Shames DM, Brasch RC, Cavagna FM, Roberts TP. MRI monitoring of Avastin antiangiogenesis therapy using B22956/1, a new blood pool contrast agent, in an experimental model of human cancer. J Magn Reson Imaging 2004;20(5):865-873.
28. Bradley DP, Tessier JL, Checkley D, Kuribayashi H, Waterton JC, Kendrew J, Wedge SR. Effects of AZD2171 and vandetanib (ZD6474, Zactima) on haemodynamic variables in an SW620 human colon tumour model: an investigation using dynamic contrast-enhanced MRI and the rapid clearance blood pool contrast agent, P792 NMR Biomed 2008;21(3):302-302.
29. Bentzen L, Vestergaard-Poulsen P, Nielsen T, Overgaard J, Bjornerud A, Briley-Saebo K, Horsman MR, Ostergaard L. Intravascular contrast agent-enhanced MRI measuring contrast clearance and tumor blood volume and the effects of vascular modifiers in an experimental tumor. Int J Radiat Oncol Biol Phys 2005;61(4):1208-1215.
30. Kobayashi H, Sato N, Hiraga A, Saga T, Nakamoto Y, Ueda H, Konishi J, Togashi K, Brechbiel MW. 3D-micro-MR angiography of mice using macromolecular MR contrast agents with polyamidoamine dendrimer core with reference to their pharmacokinetic properties. Magn Reson Med 2001;45(3):454-460.

31. Zhu W, Kato Y, Artemov D. Heterogeneity of tumor vasculature and antiangiogenic intervention: insights from MR angiography and DCE-MRI. PLoS One 2014;9(1):e86583.
32. Fink C, Kiessling F, Bock M, Lichy MP, Misselwitz B, Peschke P, Fusenig NE, Grobholz R, Delorme S. High-resolution three-dimensional MR angiography of rodent tumors: morphologic characterization of intratumoral vasculature. J Magn Reson Imaging 2003;18(1):59-65.
33. Toth E, Helm L, Merbach AE. Relaxivity of MRI contrast agents. Contrast Agents I; Top Curr Chem 2002;221:61-101.
34. Kobayashi H, Brechbiel MW. Dendrimer-based macromolecular MRI contrast agents: characteristics and application. Mol Imaging 2003;2(1):1-10.
35. Kobayashi H, Brechbiel MW. Nano-sized MRI contrast agents with dendrimer cores. Adv Drug Deliv Rev 2005;57(15):2271-2286.
36. Lee CC, MacKay JA, Frechet JM, Szoka FC. Designing dendrimers for biological applications. Nat Biotechnol 2005;23(12):1517-1526.
37. Langereis S, de Lussanet QG, van Genderen MH, Meijer EW, Beets-Tan RG, Griffioen AW, van Engelshoven JM, Backes WH. Evaluation of Gd(III)DTPA-terminated poly(propylene imine) dendrimers as contrast agents for MR imaging. NMR Biomed 2006;19(1):133-141.
38. Bousquet JC, Saini S, Stark DD, Hahn PF, Nigam M, Wittenberg J, Ferrucci JT, Jr. Gd-DOTA: characterization of a new paramagnetic complex. Radiology 1988;166(3):693-698.
39. Margerum LD, Campion BK, Koo M, Shargill N, Lai JJ, Marumoto A, Sontum PC. Gadolinium(III) DO3A macrocycles and polyethylene glycol coupled to dendrimers - Effect of molecular weight on physical and biological properties of macromolecular magnetic resonance imaging contrast agents. J Alloy Compd 1997;249(1-2):185-190.
40. Kojima C, Turkbey B, Ogawa M, Bernardo M, Regino CA, Bryant LH, Jr., Choyke PL, Kono K, Kobayashi H. Dendrimer-based MRI contrast agents: the effects of PEGylation on relaxivity and pharmacokinetics. Nanomedicine 2011;7(6):1001-1008.
41. Dreher MR, Liu W, Michelich CR, Dewhirst MW, Yuan F, Chilkoti A. Tumor vascular permeability, accumulation, and penetration of macromolecular drug carriers. J Natl Cancer Inst 2006;98(5):335-344.
42. Lipari G, Szabo A. Model-Free Approach to the Interpretation of Nuclear Magnetic-Resonance Relaxation in Macromolecules. 1. Theory and Range of Validity. J Am Chem Soc 1982;104(17):4546-4559.
43. Lipari G, Szabo A. Model-Free Approach to the Interpretation of Nuclear Magnetic-Resonance Relaxation in Macromolecules. 2. Analysis of Experimental Results. J Am Chem Soc 1982;104(17):4559-4570.
44. Laus S, Sour A, Ruloff R, Toth E, Merbach AE. Rotational dynamics account for pH-dependent relaxivities of PAMAM dendrimeric, Gd-based potential MRI contrast agents. Chemistry 2005;11(10):3064-3076.
45. Powell DH, NiDhubhghaill OM, Pubanz D, Helm L, Lebedev YS, Schlaepfer W, Merbach AE. Structural and dynamic parameters obtained from O-17 NMR, EPR, and NMRD studies of monomeric and dimeric Gd3+ complexes of interest in magnetic resonance imaging: An integrated and theoretically self consistent approach. J Am Chem Soc 1996;118(39):9333-9346.

46. Rojas-Quijano FA, Tircso G, Tircsone Benyo E, Baranyai Z, Tran Hoang H, Kalman FK, Gulaka PK, Kodibagkar VD, Aime S, Kovacs Z, Sherry AD. Synthesis and characterization of a hypoxia-sensitive MRI probe. Chemistry 2012;18(31):9669-9676.
47. Cai HH, Zhong X, Yang PH, Wei W, Chen JN, Cai JY. Probing site-selective binding of rhodamine B to bovine serum albumin. Colloid Surface A 2010;372(1-3):35-40.
48. Laurent S, Elst LV, Muller RN. Comparative study of the physicochemical properties of six clinical low molecular weight gadolinium contrast agents. Contrast Media Mol Imaging 2006;1(3):128-137.
49. Toth E, Helm L, Kellar KE, Merbach AE. Gd(DTPA-bisamide)alkyl copolymers: A hint for the formation of MRI contrast agents with very high relaxivity. Chem-Eur J 1999;5(4):1202-1211.
50. Toth E, Pubanz D, Vauthey S, Helm L, Merbach AE. The role of water exchange in attaining maximum relaxivities for dendrimeric MRI contrast agents. Chem-Eur J 1996;2(12):1607-1615.
51. Polasek M, Hermann P, Peters JA, Geraldes CF, Lukes I. PAMAM dendrimers conjugated with an uncharged gadolinium(III) chelate with a fast water exchange: the influence of chelate charge on rotational dynamics. Bioconjug Chem 2009;20(11):2142-2153.
52. Gillies ER, Dy E, Frechet JM, Szoka FC. Biological evaluation of polyester dendrimer: poly(ethylene oxide) "bow-tie" hybrids with tunable molecular weight and architecture. Mol Pharm 2005;2(2):129-138.
53. Torchilin V. Tumor delivery of macromolecular drugs based on the EPR effect. Adv Drug Deliv Rev 2011;63(3):131-135.
54. Yamaoka T, Tabata Y, Ikada Y. Distribution and tissue uptake of poly(ethylene glycol) with different molecular weights after intravenous administration to mice. J Pharm Sci 1994;83(4):601-606.
55. Kobayashi H, Kawamoto S, Jo SK, Bryant HL, Jr., Brechbiel MW, Star RA. Macromolecular MRI contrast agents with small dendrimers: pharmacokinetic differences between sizes and cores. Bioconjug Chem 2003;14(2):388-394.

Chapter 4

A novel approach to tracer-kinetic modeling for (macromolecular) dynamic contrast-enhanced magnetic resonance imaging

Igor Jacobs[1], Gustav J Strijkers[1,2], Henk M Keizer[3], Henk M Janssen[3], Klaas Nicolay[1], Matthias C Schabel[4,5]

[1] Biomedical NMR, Department of Biomedical Engineering, Eindhoven University of Technology, Eindhoven, The Netherlands
[2] Biomedical Engineering and Physics, Academic Medical Center, University of Amsterdam, Amsterdam, The Netherlands
[3] SyMO-Chem BV, Eindhoven, The Netherlands
[4] Advanced Imaging Research Center, Oregon Health & Science University, Portland, Oregon, USA
[5] Utah Center for Advanced Imaging Research, University of Utah, Salt Lake City, Utah, USA

In press, Magn Reson Med 2015; DOI 10.1002/mrm.25704

Abstract

Purpose:
To develop a novel tracer-kinetic modeling approach for multi-agent dynamic contrast-enhanced magnetic resonance imaging (DCE-MRI), that facilitates separate estimation of parameters characterizing blood flow and microvascular permeability within one individual.

Methods:
Monte Carlo simulations were performed to investigate the performance of the constrained multi-agent model. Subsequently, multi-agent DCE-MRI was performed on tumor-bearing mice (n=5) on a 7T Bruker scanner on three measurement days, in which two dendrimer-based contrast agents having high and intermediate molecular weight, respectively, along with gadoterate meglumine, were sequentially injected within one imaging session. Multi-agent data were simultaneously fit with the gamma capillary transit time (GCTT) model. Blood flow, mean capillary transit time and bolus arrival time were constrained to be identical between the boluses, while extraction fractions and washout rate constants were separately determined for each agent.

Results:
Simulations showed that constrained multi-agent model regressions led to less uncertainty and bias in estimated tracer-kinetic parameters compared with single-bolus modeling. The approach was successfully applied in vivo and significant differences in the extraction fraction and washout rate constant between the agents, dependent on their molecular weight, were consistently observed.

Conclusion:
A novel multi-agent tracer-kinetic modeling approach that enforces self-consistency of model parameters and can robustly characterize tumor vascular status was demonstrated.

4.1. Introduction

Accurate evaluation of antivascular tumor therapy requires a detailed assessment of the induced vascular changes (1). Dynamic contrast-enhanced magnetic resonance imaging (DCE-MRI) has been widely employed for characterization of tumor microvasculature (2) and evaluation of antivascular therapies (3-5). Tracer-kinetic modeling of DCE-MRI data can be applied to identify vascular biomarkers that could be used for accurate treatment assessment and optimization (6-8). The most commonly applied pharmacokinetic models that have been used in the evaluation of antivascular tumor therapies are the standard and extended Tofts models (9,10). One of the parameters that can be determined with these models is the transfer constant K^{trans}, which is influenced by tumor blood flow, microvascular surface area, and capillary permeability (11). In many of the clinical trials of antivascular agents in which DCE-MRI has been used for treatment evaluation, a reduction in K^{trans} has been reported as evidence for drug efficacy (5-7). This reduction may be associated with a decrease in blood flow and/or microvascular permeability, but these parameters cannot be separately resolved since the interpretation of K^{trans} is dependent on the perfusion regime of the tumor (11). Separate determination of blood flow and microvascular permeability would be of great value. Vascular targeting agents, aimed at destruction of the existing tumor vasculature, can induce an early increase in microvascular permeability and subsequent reduction in blood flow, having counteracting effects on K^{trans} (12,13). Furthermore, antiangiogenic therapy may induce (transient) blood vessel normalization, resulting in alterations in multiple vascular parameters (14,15). The ability to non-invasively identify the different vascular alterations induced by antivascular therapy may provide an improved understanding of the mechanisms of drug action and aid in accurate assessment and optimization of antivascular therapies.

Different strategies have been suggested to improve the precision with which these vascular alterations may be characterized. More advanced tracer-kinetic models have been developed that facilitate separate assessment of e.g. blood flow, capillary transit time, vascular heterogeneity, microvascular permeability, and blood volume (16-18). However, application of these models is limited due to the more stringent requirements on data acquisition (18-20). It has been proposed that the use of macromolecular contrast agents may facilitate better assessment of specific tracer-kinetic parameters; low molecular weight contrast agents have high transendothelial diffusion and are therefore more sensitive to blood flow changes, whereas the limited transendothelial diffusion and long intravascular half-life of macromolecular agents make them more sensitive to permeability and blood volume changes (21,22). Several studies have shown that combining low molecular weight contrast agents with macromolecular contrast agents can facilitate improved assessment of tracer-kinetic parameters and changes therein after treatment (23-28). In most of these studies, DCE-MRI with the various contrast agents was performed in separate animals or at different experimental time points, whereas others have shown that contrast agents of various molecular weight can be combined in one imaging protocol (29-33). In these studies, often the different boluses were separately analyzed and accurate assessment of the diverse vascular changes induced by antivascular therapies could benefit from

modeling contrast agent uptake in more detail.
Therefore, the aim of the present study was to develop a novel tracer-kinetic modeling approach that facilitates separate estimation of the parameters characterizing blood flow and microvascular permeability within one individual. To this aim a multi-agent DCE-MRI approach was developed, in which contrast agents of various molecular weights were sequentially injected under identical circumstances within one imaging session (34). A novel tracer-kinetic modeling strategy for multi-agent DCE-MRI was developed, in which a number of tracer-kinetic parameters were constrained to be identical between the different agents based on physiological grounds, while other parameters were separately determined for each contrast agent bolus. The performance of the multi-agent tracer-kinetic modeling approach was demonstrated with simulations and the method was applied in vivo in a mouse tumor model. It is hypothesized that this approach, based on simultaneous fitting of the multi-agent data, is suitable to robustly assess the tumor vascular status and it is expected that the presented method can be applied to accurately evaluate treatment effects on different vascular biomarkers.

4.2. Methods

4.2.1. Tracer-kinetic modeling

Our multi-agent tracer-kinetic modeling approach was based on the gamma capillary transit time (GCTT) model (35). This model can be expressed as:

$$C_t(t) = F(R_v(t) + R_p(t)) \star C_a(t) \quad [1]$$

where $C_t(t)$ is the measured total tissue contrast agent concentration, $R_v(t)$ is the vascular impulse response function, $R_p(t)$ is the parenchymal impulse response function, $C_a(t)$ is the contrast agent concentration in the arterial blood and F is the blood flow. The asterisk represents the convolution operator.

For the GCTT model the vascular and parenchymal impulse response functions are described by the following equations:

$$R_v(t) = 1 - \int_0^t D(u)du \quad [2]$$

$$R_p(t) = E \int_0^t D(u)e^{-k_{ep}(t-u)}du \quad [3]$$

where D(u) is the distribution of capillary transit times, E is the extraction fraction and k_{ep} is the washout rate constant. In the GCTT model the transit time distribution is described by a gamma distribution on the mean capillary transit time (t_c) and capillary transit time heterogeneity (σ_c):

$$D(t; t_c, \sigma_c) = \frac{t^{\alpha-1}e^{-t/\tau}}{\tau^{\alpha}\Gamma(\alpha)} \quad [4]$$

where $\alpha = \sqrt{t_c/\sigma_c}$, $\tau = \sigma_c^2/t_c$ and $\Gamma(\alpha)$ is the gamma-variate function.

Therefore, the GCTT model can be fully specified by a total of six parameters: the blood flow F (min^{-1}), extraction fraction E, washout rate constant k_{ep} (min^{-1}), mean capillary transit time t_c (min), vascular heterogeneity index α^{-1}, and a delay time t_d (min) between contrast agent injection and bolus arrival in the tumor. A number of tracer-kinetic parameters can be derived from this model: the transfer constant $K^{trans}=E*F$ (min^{-1}), extravascular extracellular volume fraction $v_e=E*F/k_{ep}$ and fractional blood volume $v_b=F*t_c$. The Renkin-Crone equation can then be used to estimate the permeability surface area product $PS=-F*\log(1-E)$ (min^{-1}) (36,37).

4.2.1.1. Constrained multi-agent tracer-kinetic modeling

The multi-agent modeling approach is based on the assumption that a number of tracer-kinetic parameters can be constrained to be identical between the different boluses based on physiological grounds. For N different contrast agent boluses, the unconstrained GCTT model is defined by a total number of 6N free parameters. However, the cardiac output and tumor hemodynamics are relatively constant over the time-scale of the multi-agent DCE-MRI experiment and therefore the blood flow, mean capillary transit time, capillary transit time dispersion and delay time are not expected to be significantly different between the different contrast agent boluses. When these parameters are constrained to be identical between the sequentially injected boluses, the number of free parameters in the multi-agent modeling is reduced to 6+2(N-1). Only the extraction fractions and washout rate constants (which are dependent on the molecular dimensions of the contrast agents) are now varied between the different contrast agent boluses. Initial modeling revealed large uncertainty in estimates of the vascular heterogeneity index (α^{-1}) for these data, so this parameter was fixed to a value of 1 which is appropriate for tumor tissues where vascular heterogeneity is known to be large, as is typical in malignant tumors (38).

4.2.1.2. Bootstrapping initialization of the non-linear optimization algorithm

Bootstrapping initialization was applied to minimize the chance of becoming trapped in a local minimum during model regression; initial parameter values for the extended Tofts model were determined by using a fast linearized tracer-kinetic modeling algorithm. The limiting mathematical relationship between the extended Tofts model and GCTT model for $lim_{t_c \to 1}$ and $lim_{\sigma \to 0}$ was then used to obtain initial parameter estimates for the GCTT model. Subsequently, nonlinear regression was performed separately for each bolus injection by sequential fitting of the individual boluses, using the "lsqcurvefit" function in MATLAB (Natick MA, USA). Constrained parameters were then initialized by taking the median of the estimates obtained from the separate fits of the different injections. Unconstrained parameters were directly initialized from the unconstrained regressions. All parameters were constrained to be positive in the model regressions.

4.2.2. Simulations

Monte Carlo simulations were performed to investigate the performance of the constrained multi-agent model. In vivo DCE-MRI data were acquired from a human glioblastoma patient with a temporal resolution of 3.2 s per frame and a standard bolus injection of a low molecular weight contrast agent (gadobenate dimeglumine, Multihance, 0.1 mmol/kg) (35,38). Pre-contrast T_1-values were determined with a variable flip angle approach (39). Measured signal changes were converted to contrast agent concentration (40), the arterial input function (AIF) was determined using a blind estimation algorithm (41,42) and the DCE-MRI data were fit with the GCTT model (35). Model parameters that were selected from a region of interest (ROI) placed in a relatively homogeneous, enhancing tumor region were averaged to obtain the following simulated tissue uptake curve parameters: $F=0.256$ min^{-1}, $v_e=0.570$, $t_c=15.5$ s, and $\alpha^{-1}=0.5$ ($v_b=0.066$). A multi-agent experiment was subsequently simulated as follows: three contrast agent injections were simulated, starting with high molecular weight (HMW, E=0.05), followed by medium molecular weight (MMW, E=0.27) and finally low molecular weight (LMW, E=0.54), determined as above from the measured data. Contrast-agent injections were spaced by 6 minutes, with 30 seconds of baseline acquisition prior to injection of the first agent. Gaussian noise with a standard deviation (SD) of 0.04 mM (equal to the noise level in the original human study, which corresponds to a signal-to-noise ratio of approximately 7) was added to generate 1000 random realizations of the tissue contrast agent uptake curve. Each realization was fit with the constrained model, simultaneously fitting all three superimposed uptake curves. Individual uptake curves for each agent were also fit separately with the unconstrained model. Estimated model parameters were subsequently compared with the known starting values to determine the bias and uncertainty in the estimated parameters for both the constrained and the unconstrained modeling approach.

4.2.3. Contrast agents for in vivo multi-agent DCE-MRI

Multi-agent experiments in tumor-bearing mice were performed with contrast agents with a range of molecular weights but an equal composition. Modified poly(propylene imine) (PPI) dendrimers, functionalized with Gd-DOTA moieties through a polyethylene glycol (PEG) spacer (Figure 1), were synthesized by SyMO-Chem BV (Eindhoven, The Netherlands). An intermediate molecular weight dendrimer of generation 2 (G2-PPI-$(PEG_6$-$GdDOTA)_8$), high molecular weight dendrimer of generation 5 (G5-PPI-$(PEG_6$-$GdDOTA)_{64}$), and a low molecular weight agent gadoterate meglumine (Gd-DOTA, Dotarem, Guerbet, Villepente, France) were used in the in vivo multi-agent experiments. Synthesis of the dendrimers according to their theoretical structure was confirmed using ^{1}H-NMR (prior to Gd-complexation).

Additional information on synthesis and further characterization of the dendrimers (after Gd-complexation), including gel permeation chromatography (GPC), dynamic light scattering (DLS) and Inductively Coupled Plasma-Atomic Emission Spectrometry (ICP-AES), is given in Supporting information 1. The molecular weight, diameter and plasma relaxivity measured at 7 T at 37 °C of the contrast agents are listed in Table 1.

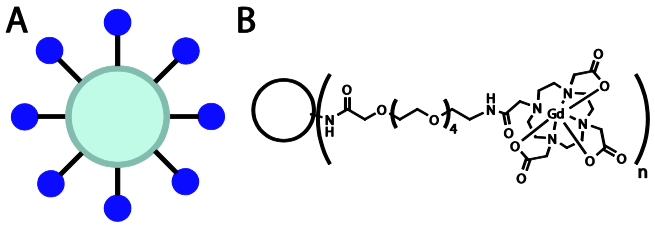

Figure 1. Representation of the dendrimer-based contrast agents.
Figure 1A) Schematic drawing of the G2 dendrimer, in which the dendrimer core is represented by the large circle, to which multiple Gd-DOTA moieties (blue circles) are attached via a PEG-spacer (black lines). Figure 1B) The general dendrimer structure, consisting of a dendrimer core (represented by the large circle) and a variable number (n) Gd-DOTA moieties attached via the PEG linkers, dependent on the dendrimer generation.

Table 1. General characteristics of the different contrast agents.
The molecular weight (MW), expressed in Dalton (Da), is the theoretical molecular weight of the different contrast agents. The hydrodynamic diameter and distribution widths of the dendrimers were determined in PBS of pH 7.4 (Supporting Information 1). * The diameter of gadoterate meglumine was obtained from literature (43). The longitudinal (r_1) and transverse (r_2) relaxivities of the agents were measured in Balb/c mouse plasma at 7 T at 37 °C.

Contrast agent	MW (Da)	Diameter (nm)	r_1 ($mM^{-1}*s^{-1}$)	r_2 ($mM^{-1}*s^{-1}$)	r_2/r_1 (-)
Gadoterate meglumine	754	0.9 *	3.6	4.0	1.12
G2-PPI-$(PEG_6$-GdDOTA$)_8$	7317	4.3±1.1	5.5	6.6	1.19
G5-PPI-$(PEG_6$-GdDOTA$)_{64}$	59517	10.0±3.6	7.2	10.0	1.39

For the in vivo multi-agent experiments an infusion line was filled with equal volumes of the generation 5 (G5) and generation 2 (G2) dendrimer and gadoterate meglumine (at a concentration of 125 mM Gd, ~ 0.1 mmol Gd/kg), separated by equal volumes of saline. A small air bubble between all volumes prevented mixing of the different solutions.

4.2.4. Ethics Statement

All animal experiments were performed according to the Directive 2010/63/EU of the European Commission and approved by the Animal Care and Use Committee of Maastricht University (protocol: 2010-132).

4.2.5. Animal model

CT26.WT murine colon carcinoma cells (American Type Culture Collection (ATCC; CRL-2638)) were cultured as a monolayer at 37 °C and 5% CO_2 in RPMI-1640 medium (Invitrogen, Breda, The Netherlands), supplemented with 10% fetal bovine serum (Greiner Bio-One, Alphen a/d Rijn, The Netherlands) and 50 U/ml penicillin/streptomycin (Lonza Bioscience, Basel, Switzerland). Early passages (5-10) of the original ATCC batch were used for inoculation.
10-12 week-old Balb/c mice (Charles River, Maastricht, The Netherlands) were inoculated with $1x10^6$ CT26.WT cells subcutaneously in the right hind limb. Approximately 10 days after inoculation, tumors became palpable in all animals.

4.2.6. In vivo multi-agent DCE-MRI in tumor-bearing mice

Multi-agent DCE-MRI experiments were performed on a 7T Bruker BioSpec 70/30 USR equipped with a 1H 59/35 (outer/inner diameter in mm) circular polarized MRI transceiver volume coil. All mice underwent MRI 3 times with 2 days of recovery in between, to investigate if differences in extraction fraction and washout rate constant between the agents can consistently be observed. For the MRI measurements, mice were anesthetized with isoflurane (3% for induction, 1-2% for maintenance) in medical air (flow rate of 0.4 L/min). During the measurements mice were positioned in a custom made cradle, equipped with a mask for anesthetic gas. Respiration rate was monitored with a balloon sensor and body temperature was monitored and maintained with a warm water pad. To minimize susceptibility artifacts at air-tissue interfaces, the tumor was covered with a small layer of degassed ultrasound gel (Aquasonic® 100, Parker Laboratories, Inc, Fairfield, NJ, USA) and artifacts were further reduced by local shimming of the tumor-bearing paw.

A three-dimensional T_2-weighted (effective echo time (TE) = 34 ms) turbo rapid acquisition with relaxation enhancement (RARE) acquisition was performed for anatomical reference. B_1-mapping was performed based on the 180° signal-null method (44). Pre-contrast T_1 mapping was performed using a three-dimensional variable flip angle gradient-spoiled (5 ms duration) and radiofrequency (RF)-spoiled three-dimensional fast low-angle shot (FLASH) sequence with the following sequence parameters: repetition time (TR) = 20 ms, TE = 3.23 ms, acquisition matrix = 52x72x14 (reconstructed to 96x96x16), field of view (FOV) = 30x30x24 mm^3, flip angle (FA) = 2, 3, 5, 7, 10, 13, 20° (39,45,46). T_1 values were determined using a DESPOT1 (driven equilibrium single-pulse observation of T_1) analysis (39). For the multi-agent DCE-MRI measurements a three-dimensional gradient-spoiled (5 ms duration) and RF-spoiled three-dimensional FLASH sequence (covering the tumor) was used with the following sequence parameters: TR = 2.5 ms, TE = 0.84 ms, FA = 6°, acquisition matrix = 52x72x14 (reconstructed to 96x96x16), FOV = 30x30x24 mm^3, temporal resolution = 1.89 s, total scan time = 47 min. Phantom measurements for validation of the variable flip angle and dynamic T_1 mapping method are shown in Supporting information 2. Contrast injections were performed at 2 (G5 dendrimer), 17 (G2 dendrimer) and 32 (gadoterate meglumine) min after start of the acquisition, using an infusion pump (Chemyx Fusion 100, Stafford, TX, USA) at a rate of 2 mL/min. B_1-corrected ΔR_1 ($=1/\Delta T_1$) values were calculated on a pixel-pixel basis based on the standard signal-equation for a spoiled gradient-echo sequence (40), using the pre-contrast T_1 values and the post-contrast dynamic signal intensities. Regions of interest delineating the tumor tissue were manually drawn on the anatomic images.

4.2.7. In vivo multi-agent modeling

AIFs, composed of one bolus for each of the three injected agents, were determined for each agent separately using the Monte Carlo Blind Estimation (MCBE) algorithm applied to the ΔR_1 curves of enhancing tumor voxels (41,42). Each individual bolus within the AIF was modeled by a gamma-variate function with recirculation and a sigmoid representing contrast at quasi-equilibrium in the blood pool (41). During the blind AIF estimation, tissue curves were modeled using the GCTT model with vascular heterogeneity index (α^{-1}) fixed to a value of 1. The algorithm was initialized using a population averaged AIF from previous measurements made in the left ventricular lumen of mice that were injected with gadopentetic acid (Gd-DTPA) with a similar injection protocol (47). MCBE estimation of the AIF of the first injected agent (G5 dendrimer) was performed by truncating the tissue curves before injection of the second agent (G2 dendrimer). The resulting AIF for the G5 dendrimer bolus was then used to generate model curve fits to the tissue curves and these fits were subtracted from the measured tissue data to remove the effect of uptake of G5 dendrimer. This procedure was then repeated for the G2 dendrimer and gadoterate meglumine injections to provide separate AIF estimates for each agent. Differences in relaxivities between the different agents were compensated by rescaling each bolus to an equivalent dose of gadoterate meglumine, using measured relaxivities for the different agents. Exemplary AIFs of the dendrimers and gadoterate, as determined with the MCBE algorithm, are shown in Supporting information 3. The tracer-kinetic model described by equation [1] is invariant under the simultaneous transformation $C_p(t) \rightarrow \gamma C_p(t), F \rightarrow F/\gamma$ and $v_b \rightarrow v_b/\gamma$ for any scalar value of γ. Therefore, the global AIF scale factor γ remains indeterminate, as is common for blind AIF estimation methods. This scale factor could be obtained from a secondary reference measurement of the true contrast agent concentration in the blood, which has not been employed in the present study. As a result, absolute values for F and v_b could not be derived and these parameter estimates are scaled by the amplitude of the initial population-averaged AIF provided to the MCBE algorithm as a starting guess.

Multi-agent data were simultaneously fit with the GCTT model with vascular heterogeneity index (α^{-1}) fixed to a value of 1. Blood flow (F), mean capillary transit time (t_c), and bolus arrival time (t_d) were constrained to be identical between the different boluses, while extraction fractions (E) and washout rate constants (k_{ep}) were separately determined for each contrast agent. Blood volume fractions (v_b) were calculated by $F*t_c$. Median pharmacokinetic parameters were calculated in all tumor pixels with statistically significant blood flow and low uncertainty in blood flow, relative to the estimated blood flow value. Median tumor parameter values for each measurement day were determined by taking the median of the median parameter values of all perfused tumor pixels of all mice.

4.2.8. Statistics

Data are reported as median ± median absolute deviation (MAD) of the five mice for each measurement day. Differences in the perfused tumor fraction and the constrained tracer-kinetic parameters blood flow and mean capillary transit time between the different measurement days were statistically analyzed using a repeated

measures ANOVA. Differences in the tracer-kinetic parameters extraction fraction and washout rate constant between measurement days and between the different contrast agents were analyzed using a mixed-model repeated-measures ANOVA with post-hoc Games-Howell test, with the time point as the within-subjects factor and the contrast agent as the between subject-factor. The level of statistical significance was set at $\alpha=0.05$.

4.3. Results

4.3.1. Simulations

Simulated data for low (LMW), medium (MMW) and high (HMW) molecular weight contrast agents are shown in Figure 2. Regressions with the unconstrained model are shown in the upper three panels, while the constrained multi-agent regressions are shown in the bottom panel.

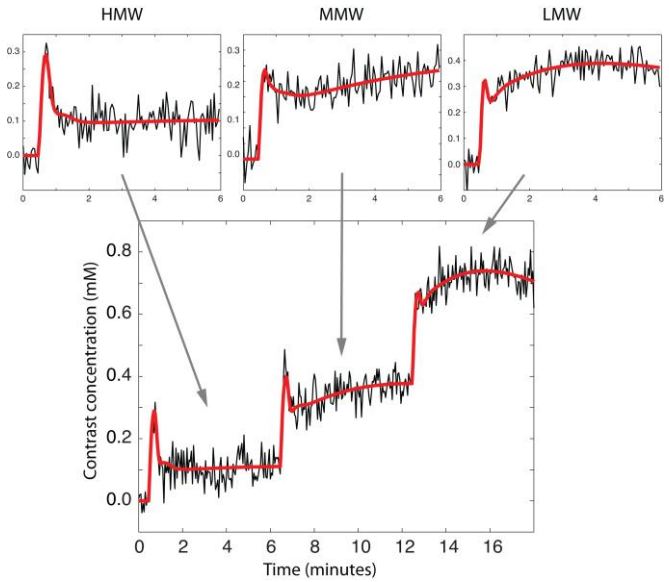

Figure 2: Unconstrained and constrained regressions to simulated data.
Simulated data for low (LMW), medium (MMW) and high (HMW) molecular weight contrast media (black curves). Regressions to simulated data are shown by the red curves. Data in the top three panels are fit separately with the unconstrained model, while in the lower panel all data are simultaneously fit.

The simulated data demonstrated differences in the enhancement pattern, dependent on the molecular weight of the contrast agents, and the multi-agent regressions were observed to fit the simulated data well. Box plots of the results from the Monte Carlo simulations of the multi-agent and single-bolus modeling are shown in Figure 3, in which the estimated model parameters are compared to the known true parameter values. The median parameter estimates from the multi-agent modeling were consistently closer to the true parameter values compared to the single-bolus modeling approach. In addition, the bias and uncertainty in estimated tracer-kinetic parameters were consistently lower for the multi-agent than for the single-bolus data. With the exception of v_e, the low molecular weight contrast agent data are associated with the largest bias and uncertainty in the estimated tracer-kinetic parameters.

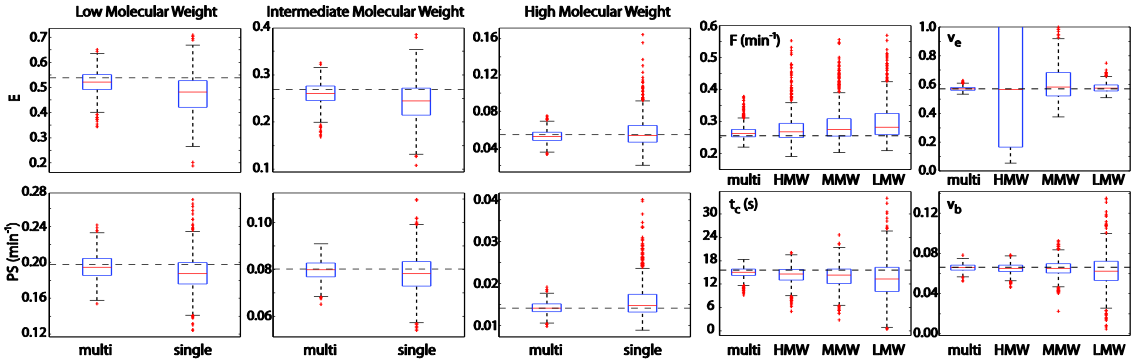

Figure 3. Monte Carlo multi-agent simulation results.
Box plots showing results for Monte Carlo simulation of 1000 noise realizations. True parameter values are shown by the horizontal dashed lines (black) and median estimates by the red lines, with the 25th and 75th percentiles indicated by the blue boxes. Outliers are plotted with red crosses. The three leftmost columns show E and PS for the three different molecular weights, with the multi-agent model estimates on the left of each panel and the single bolus estimates on the right. The two rightmost columns show the constrained parameter estimates, with the multi-agent estimates on the left, followed by the HMW, MMW, and LMW estimates.

4.3.2. In vivo multi-agent measurements and modeling

Contrast enhancement in the tumor after injection of the different contrast agents is shown in Figure 4. One minute after injection of the G5 dendrimer (1 min post G5) an increase in signal intensity could be observed, especially in the well vascularized tumor rim. In addition, some enhancement was visible in the tumor center. After injection of the G2 dendrimer (1 min post G2), a further increase in signal intensity was visible in most of the tumor area. Injection of gadoterate (1 min post Gadoterate) resulted in further contrast enhancement, with a diffuse enhancement pattern throughout the tumor tissue. A small tumor region was characterized by an apparent lack of contrast enhancement.

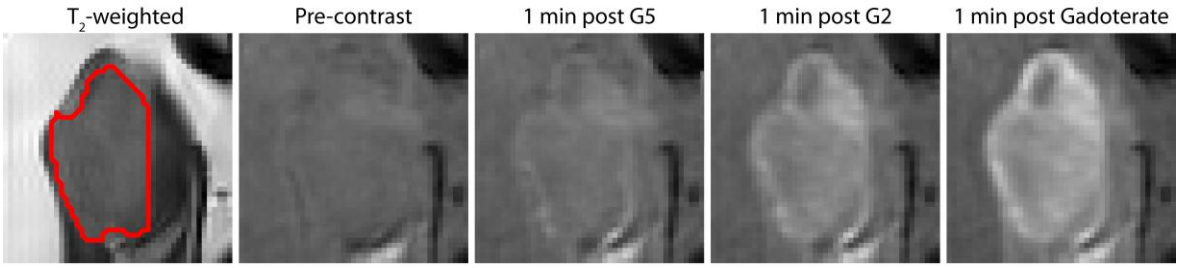

Figure 4. Contrast enhancement in the tumor at different time points after contrast agent injection.
On the left side of the figure, a T_2-weighted image of the tumor-bearing paw of a mouse at measurement day one is shown. The tumor is delineated with a red line. Peritumoral edema was not included in the ROIs. The paw is surrounded by a thin layer of ultrasound gel (visible as light gray). At the right side of this image, dynamic contrast-enhanced images of the corresponding tumor slice are shown at different time points during the dynamic acquisition. From left to right: a pre-contrast image, an image acquired one minute after injection of the G5 dendrimer (1 min post G5), an image acquired one minute after injection of the G2 dendrimer (1 min post G2) and an image acquired one minute after injection of gadoterate (1 min post Gadoterate).

Representative multi-agent dynamic contrast-enhanced curves, measured in single pixels in different locations within the tumor, are depicted in Figure 5. Figure 5A shows the multi-agent data from a single pixel in the tumor rim. A pronounced increase in ΔR_1 could be observed upon injection of the different contrast agents. Enhancement curves were well-defined and a distinct enhancement pattern was visible after injection of the different agents. Contrast enhancement after injection of the G5 dendrimer was characterized by a step-wise increase in ΔR_1, after which the ΔR_1 remained relatively constant. A less steep upslope and a more pronounced washout phase were observed after injection of the G2 dendrimer. After injection of gadoterate, a rapid increase in ΔR_1 was followed by a rapid decrease afterwards due to contrast agent washout. These differences in enhancement pattern were reflected by the different pharmacokinetic parameter estimates for the different agents (legend of Figure 5). Figure 5B shows representative data from a pixel in the tumor center. Whereas contrast enhancement was generally lower in this pixel, similar differences in enhancement pattern between the different agents could be observed. Contrast enhancement in a pixel in a relatively poorly perfused tumor region is depicted in Figure 5C. While only minor signal enhancement was visible, the different contrast agent boluses could still be discriminated.

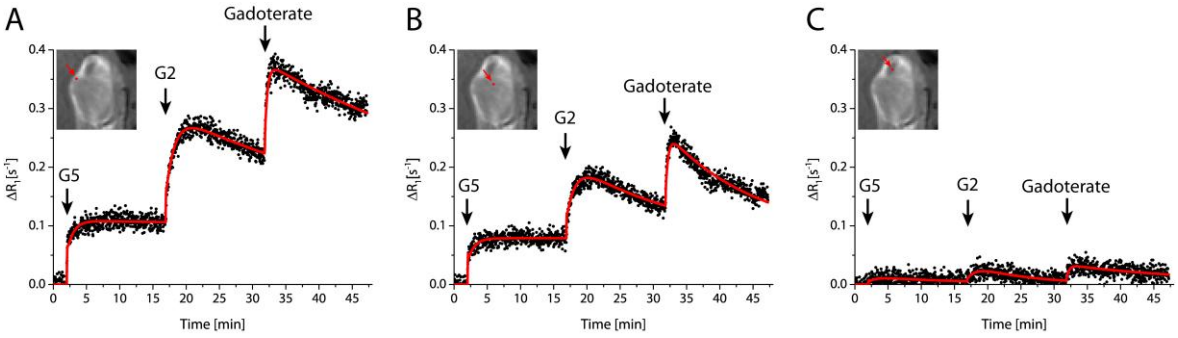

Figure 5. Representative ΔR_1 curves measured in a single tumor-pixel in the same slice as shown in Figure 4 and the multi-agent fits through the data. The location of the different pixels is indicated by the red dots, overlaid on the contrast-enhanced image at 45 minutes after the first contrast agent injection. The measured data are shown by the black dots and the multi-agent regressions are shown by the red lines. The moment of injection of the G5 and G2 dendrimer and gadoterate is indicated with the black arrows. One pixel in the tumor rim (Figure 5A), one pixel in the tumor center (Figure 5B) and one pixel in a relatively poorly perfused region of the tumor (Figure 5C) were selected. Estimated parameters for the pixel in the tumor rim (Figure 5A) were: F=0.87 min^{-1}, t_c=0.08 min, E(G5)=0.20, k_{ep}(G5)=0.00 min^{-1}, E(G2)=0.34, k_{ep}(G2)=0.03 min^{-1}, E(Gadoterate)=0.85, k_{ep}(Gadoterate)=0.02 min^{-1}. Estimated parameters for the pixel in the tumor center (Figure 5B) were: F=0.77 min^{-1}, t_c=0.06 min, E(G5)=0.17, k_{ep}(G5)=0.00 min^{-1}, E(G2)=0.26, k_{ep}(G2)=0.06 min^{-1}, E(Gadoterate)=0.75, k_{ep}(Gadoterate)=0.07 min^{-1}. Estimated parameters for the pixel in the relatively poorly perfused region were: F=0.13 min^{-1}, t_c=0.03 min, E(G5)=0.15, k_{ep}(G5)=0.06 min^{-1}, E(G2)=0.32, k_{ep}(G2)=0.13 min^{-1}, E(Gadoterate)=1.00, k_{ep}(Gadoterate)=0.04 min^{-1}. Whereas F is scaled by the amplitude of the initial population-averaged AIF provided to the MCBE algorithm and absolute values of F are dependent on the global scaling factor of the AIF, relative differences in F between the curves can be directly compared. Note that if k_{ep} is estimated to be equal to zero, it is not possible to provide an estimate for v_e. Similarly, if E is estimated to be equal to 1, PS cannot be determined.

Figure 6 shows representative pharmacokinetic parameter maps in the same slice as shown in Figure 4. Pharmacokinetic parameters that were constrained to be identical between the different boluses are shown on the left side of the figure. In agreement with the level of contrast enhancement as shown in Figure 4, both the blood flow and blood volume were higher in the tumor rim than in the tumor center. In addition, a small region with a lack of contrast enhancement could be observed where the blood flow and volume were low. On the right side of the figure, the contrast agent specific pharmacokinetic parameters are displayed. In the upper panels it can be seen that for the high molecular weight G5 dendrimer, the extraction fraction was low throughout the tumor. The medium molecular weight G2 dendrimer possessed intermediate extraction fractions, while the highest extractions were observed for the low molecular weight gadoterate. Washout rate constants were also lowest and close to zero for the G5 dendrimer. Washout rate constants of the G2 dendrimer and gadoterate were higher and washout rate constant maps of these contrast agents were very similar.

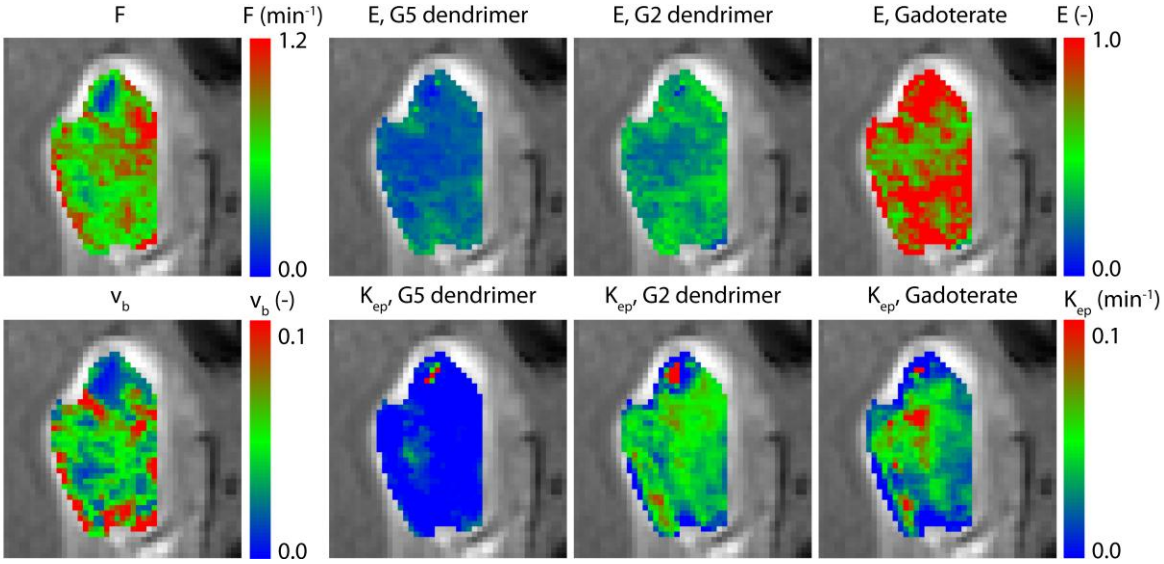

Figure 6. Pharmacokinetic parameter maps in the same slice as shown in Figure 4. The estimated pharmacokinetic parameter values are overlaid on the contrast-enhanced image at 45 minutes after the first contrast agent injection. Peritumoral edema (the enhancing rim) was not included in the ROIs. The plotted parameter range is indicated by the scale bars. The leftmost images show pharmacokinetic parameters of the constrained parameters blood flow F (min^{-1}) and derived parameter fractional blood volume v_b (-) in the upper and lower row, respectively. Note that F and v_b are scaled by the amplitude of the initial population-averaged AIF provided to the MCBE algorithm and absolute values of these parameters are dependent on the global scaling factor of the AIF. The images on the right show pharmacokinetic parameter maps of the contrast agent specific parameters extraction fraction E (-) and washout rate constant k_{ep} (min^{-1}) in the upper and lower row, respectively.

The median perfused tumor fraction at the different measurement days is shown in Figure 7A. At measurement day one, approximately the entire tumor tissue was well perfused. However, a significant decrease in perfused tumor fraction was observed at measurement day 3 (P=0.01). No significant differences in median tumor blood flow (Figure 7B) or capillary transit time (Figure 7C) in the perfused pixels were observed between the different measurement days.

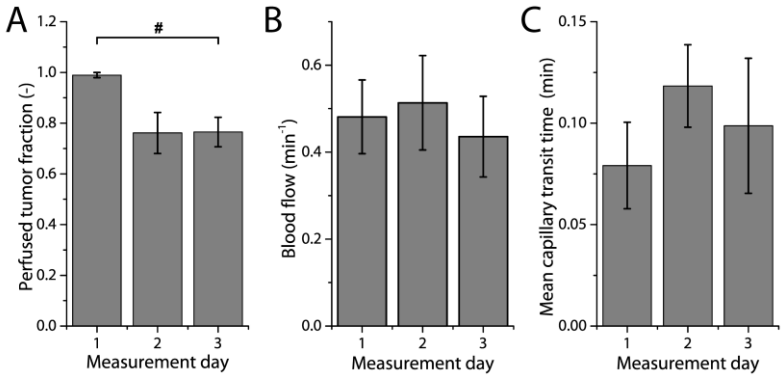

Figure 7. Median perfused tumor fraction and constrained parameter estimates.
Median±MAD perfused tumor fraction (Figure 7A), blood flow (Figure 7B) and mean capillary transit time (Figure 7C) of the five mice at the different measurement days. Whereas the blood flow is scaled by the amplitude of the initial population-averaged AIF provided to the MCBE algorithm and its absolute value is dependent on the global scaling factor of the AIF, differences in blood flow between the measurement days can be directly compared. # indicates a significant difference with $P<0.05$ between measurement day one and three.

The median parameter values of the contrast agent specific pharmacokinetic parameters extraction fraction and washout rate constant are shown in Figure 8.

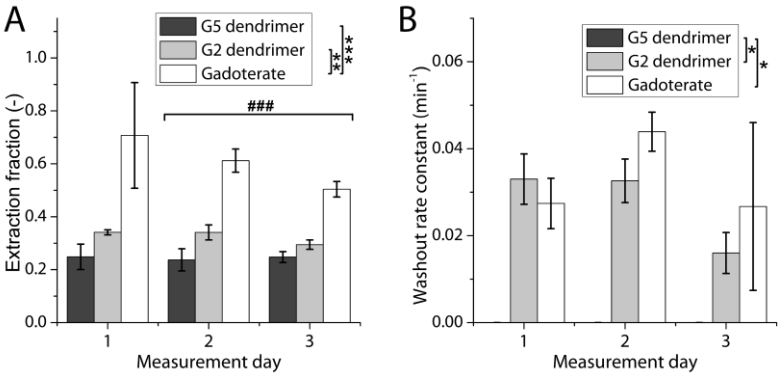

Figure 8. Median extraction fraction and washout rate constant of the different contrast agents.
Median±MAD extraction fraction (Figure 8A) and washout rate constant (Figure 8B) of the five mice at the different measurement days. The estimated parameter values for the G5 dendrimer, G2 dendrimer and gadoterate are shown with the dark gray, light gray and white bars respectively. ### indicates a significant difference with $P<0.001$ between measurement day two and three. *,**,*** indicate a significant difference with $P<0.05,0.01,0.001$ respectively between the different contrast agents.

The extraction fraction of gadoterate was consistently and significantly higher than that of both the G2 ($P=0.002$) and G5 dendrimer ($P=0.001$) (Figure 8A), which was a main effect of the contrast agent on the extraction fraction. No significant difference was observed between the extraction fractions of the G2 and G5 dendrimers ($P=0.172$), although the extraction fraction of the G2 dendrimer was consistently higher on all measurement days. A significant general decrease in extraction fractions was observed between measurement day 2 and 3 ($P=0.0005$). The washout rate constants of both the G2 dendrimer ($P=0.017$) and gadoterate ($P=0.025$) were consistently and significantly higher than those of the G5 dendrimer, of which the rate constants were essentially zero, as would be expected for a largely intravascular agent

with slow elimination kinetics. This was a main effect of the contrast agent on the washout rate constant. No significant differences were observed between the washout rate constants of the G2 dendrimer and gadoterate.

4.4. Discussion and Conclusions

In the present study, a novel multi-agent tracer-kinetic modeling strategy has been demonstrated, allowing blood flow and microvascular permeability to be simultaneously and self-consistently determined within one individual. The use of macromolecular contrast agents for better assessment of specific vascular biomarkers has been previously proposed and sequential injection of multiple contrast agents has been reported earlier. However, in these studies injection of the different contrast agents was generally performed in separate animals or tracer-kinetic modeling was performed on the individual boluses. Importantly, in the present study constrained tracer-kinetic modeling was performed simultaneously on the multi-agent DCE-MRI data. This approach exploits the combined information of the different agents and uses the fact that a number of parameters can be constrained to be identical between the agents (based on physiological grounds) to obtain robust tracer-kinetic parameter estimates.

Monte Carlo simulations demonstrated superior accuracy and precision in determination of model parameters when using the multi-agent modeling approach relative to separate modeling of individual boluses. The better performance can be partly explained by the fact that a number of tracer-kinetic parameters were constrained to be identical between the boluses for the multi-agent approach. This will improve the modeling outcome because of the decrease in degrees of freedom in the model regressions (48). In addition, the multi-agent approach exploits the added information from measurement of uptake kinetics of contrast agents of different size. Compared to the HMW and MMW agents, the LMW agent consistently had the highest bias and uncertainty in estimated parameters, except for the estimates of v_e. Accurate determination of v_e requires sufficient sampling of contrast agent extravasation to the interstitial space and subsequent washout. For short measurement times both the extraction of the HMW agent into the interstitial space and subsequent washout are limited (21), which results in a high uncertainty in estimated v_e values. This problem can potentially be overcome by increasing the measurement times, although undesirably long measurement times are needed to fully sample washout of the HMW agents. Nevertheless, the lowest bias and uncertainty in estimations of v_e were obtained with the multi-agent approach, which further demonstrates its potential in comparison with single-bolus tracer-kinetic modeling.

The feasibility of the constrained multi-agent modeling approach was shown in vivo in a mouse tumor model. Multi-agent DCE-MRI was performed with dendrimer-based contrast agents and gadoterate, which provided a large range of molecular weights. The advantage of the dendrimers over commercially available macromolecular agents is that the size of the agents can be tuned, while the chemical composition of the agents is similar (49). Similar physiochemical properties between different agents are

advantageous for multi-agent DCE-MRI, since this will minimize differences in in vivo characteristics.

Non-perfused tumor regions were excluded from tracer-kinetic analysis, since measurable blood flow is required to reliably estimate the different pharmacokinetic parameters. These non-perfused regions were assessed based on the level of signal enhancement after injection of the G5 dendrimer. Since the extraction fraction of the G5 dendrimer is low, significant signal enhancement after injection of this dendrimer is indicative of relevant blood flow in this area. Whereas contrast-enhancement after injection of the G5 dendrimer was most pronounced in the highly vascular tumor rim, significant contrast-enhancement could also be observed throughout the tumor (Figure 4). Only small non-perfused fractions were observed on measurement day 1, which slightly increased on measurement day 2 and 3, likely due to natural tumor necrosis as a result of tumor growth. Therefore, multi-agent modeling could be reliably performed in the major part of the tumor.

Clear differences in contrast-enhancement in the tumor (Figure 4) and the enhancement pattern (Figure 5) could be observed after injection of the differently sized contrast agents. These differences in enhancement pattern translated to different tracer-kinetic parameter estimates (Figure 8). The difference in extraction fractions between the contrast agents (Figure 8A) shows that these agents extravasate to a different extent from the tumor vasculature into the interstitial space. Gadoterate possessed a significantly higher extraction fraction compared to the G2 and G5 dendrimers, which likely have a more intravascular distribution. This is in agreement with findings by de Lussanet et al., who reported a molecular weight cut-off between 3000 and 12000 Da above which dendrimers possessed a mostly intravascular distribution (21). No significant differences were observed between the extraction fractions of the G2 and G5 dendrimers. Nevertheless, the extraction fractions of the dendrimers used in the present study were in close agreement with findings reported by Michoux et al. in a rat tumor model. They assessed differences in extraction fractions of contrast agents with very similar molecular weights as used in the present study with the St Lawrence and Lee model and measured an extraction fraction of 0.51±0.17 for gadoterate meglumine (754 Da), 0.36±0.07 for gadomelitol (P792, Vistarem, 6470 Da) and 0.23±0.10 for carboxymethyldextran-Gd-DOTA (P717, 52000 Da) (50).

A significant general decrease in extraction fraction was observed from measurement day 2 to 3 (Figure 8A). This may be due to elevated interstitial pressure, which may have resulted in decreased extravasation of contrast agents from the tumor microvasculature (24). Elevated interstitial pressure may also lead to reduced blood flow, which is consistent with the observed decrease in perfused tumor volume on measurement day 3 compared to day 1 (Figure 7) (51).
Also the washout rate constant of the G2 dendrimer and gadoterate was found to be significantly higher than that of the G5 dendrimer. The washout rate constant was essentially zero for the G5 dendrimer (Figure 8B). As can be observed from the uptake curves in Figure 5, no clear washout could be observed for this high molecular weight

agent. Therefore, washout rate constant estimates of the G5 dendrimer had a high uncertainty. This high uncertainty was also observed in the simulation results (Figure 3). However, undesirably long acquisition times would be required to fully sample G5 dendrimer washout.

The present study has a number of limitations. The AIF was determined with the previously described MCBE algorithm, which is able to determine the AIF shape from measured tissue concentrations curves (41). Schabel et al. have shown a good agreement between MCBE based and measured AIFs (42). However, the scaling of the AIF has to be performed by a secondary measurement of the blood contrast agent concentration (41). Absolute AIF scaling is known to be inherently difficult in mice. Since no animal-specific scaling of the AIF was performed in the present study, absolute pharmacokinetic parameter values could not be quantitatively compared to other studies. However, the in vivo differences in extraction fraction and rate constant between the different agents are consistent regardless of the bolus profile and AIF scaling, which would only affect absolute estimates of F and v_b (16). Increasing the temporal resolution of the dynamic acquisition and optimizing the flip angle to be optimally sensitive to the expected range of contrast agent concentrations in the plasma compartment and interstitial space might further improve measurement accuracy and AIF extraction by the MCBE algorithm (40).

The multi-agent modeling approach uses the fact that a number of parameters can be constrained to be identical between the agents to obtain robust tracer-kinetic parameter estimates. Whereas this may be generally valid, it has been reported that tumors could display intermittent blood flow that can occur rapidly in independent single blood vessels, or regionally at cyclic time intervals (in the order of 15 min to over 1 hour) (52-57). It is expected that blood flow fluctuations in single vessels have a minor effect in their contribution to the whole voxel signal intensity. High frequency fluctuations (on time scales of seconds) will be mostly averaged out considering the 1.89 s acquisition time. However, regional blood flow fluctuations occurring at longer time scales could possibly be of influence on tracer-kinetic parameter estimations. However, in the vast majority of cases, the multi-agent modeling was able to fit all three boluses with a single flow value. If the voxel level flow values would vary strongly between the different boluses, good multi-agent model fits could not be obtained and the accuracy in the estimated blood flow would be low. Since voxels with low blood flow fitting accuracy were excluded from further analysis, this limits the effect of strong blood flow fluctuations on the results. Nevertheless, in future studies the total multi-agent acquisition time could be reduced to approximately 10 min in order to ensure that the constrained parameters are more constant during the DCE-MRI acquisition.

Extensive validation of the estimated tracer-kinetic parameters was beyond the scope of this study. Multi-agent blood flow estimations could be validated with ultrahigh sensitive optical microangiography (UHS-OMAG), which is a label-free optical imaging method that is able to measure microcirculatory blood flow via endogenous backscattered light from flowing red blood cells (58). The mean capillary transit times

could be validated with in vivo 2-photon laser microscopy measurements of fluorescently labeled dextrans of comparable molecular weight (59), or alternatively the contrast agents that were used in the multi-agent approach could be fluorescently labeled and tracked in vivo to assess the dynamics of the passing bolus in the tumor. In addition, this technique could be employed to assess differences in the extent of extravasation of the different contrast agents (59,60).

In conclusion, a novel approach to tracer-kinetic modeling of macromolecular DCE-MRI data was demonstrated. Simulations showed that constrained multi-agent model regressions led to less uncertainty and bias in estimated tracer-kinetic parameters in comparison with single-bolus modeling. The approach was successfully applied in vivo in a mouse tumor model and significant differences in extraction fraction and washout rate constant between the different agents, dependent on their molecular weight, were consistently observed on the different measurement days. The in vivo results indicated that tumor blood flow could be separately determined from contrast agent specific permeability and washout related tracer-kinetic parameters. It is expected that the multi-agent modeling approach can be applied to accurately evaluate treatment effects on different vascular biomarkers. In addition, by assessment of the differential leakage of the contrast agents of various molecular weight, the method may be able to predict the efficacy of nanomedicine delivery to the tumor (61).

4.5. Acknowledgements

This research was performed within the framework of CTMM, the Center for Translational Molecular Medicine (www.ctmm.nl), project VOLTA (grant 05T-201).

4.6. References

1. Eichhorn ME, Strieth S, Dellian M. Anti-vascular tumor therapy: recent advances, pitfalls and clinical perspectives. Drug Resist Updat 2004;7(2):125-138.
2. Jackson A. Imaging microvascular structure with contrast enhanced MRI. Br J Radiol 2003;76 Spec No 2:S159-173.
3. Padhani AR, Leach MO. Antivascular cancer treatments: functional assessments by dynamic contrast-enhanced magnetic resonance imaging. Abdom Imaging 2005;30(3):324-341.
4. Zweifel M, Padhani AR. Perfusion MRI in the early clinical development of antivascular drugs: decorations or decision making tools? Eur J Nucl Med Mol Imaging 2010;37 Suppl 1:S164-182.
5. O'Connor JP, Jackson A, Parker GJ, Roberts C, Jayson GC. Dynamic contrast-enhanced MRI in clinical trials of antivascular therapies. Nat Rev Clin Oncol 2012;9(3):167-177.
6. O'Connor JP, Jackson A, Parker GJ, Jayson GC. DCE-MRI biomarkers in the clinical evaluation of antiangiogenic and vascular disrupting agents. Br J Cancer 2007;96(2):189-195.

7. O'Connor JP, Jackson A, Asselin MC, Buckley DL, Parker GJ, Jayson GC. Quantitative imaging biomarkers in the clinical development of targeted therapeutics: current and future perspectives. Lancet Oncol 2008;9(8):766-776.
8. Koh TS, Thng CH, Hartono S, Tai BC, Rumpel H, Ong AB, Sukri N, Soo RA, Wong CI, Low AS, Humerickhouse RA, Goh BC. A comparative study of dynamic contrast-enhanced MRI parameters as biomarkers for anti-angiogenic drug therapy. NMR Biomed 2011;24(9):1169-1180.
9. Tofts PS, Kermode AG. Measurement of the blood-brain barrier permeability and leakage space using dynamic MR imaging. 1. Fundamental concepts. Magn Reson Med 1991;17(2):357-367.
10. Tofts PS, Brix G, Buckley DL, Evelhoch JL, Henderson E, Knopp MV, Larsson HB, Lee TY, Mayr NA, Parker GJ, Port RE, Taylor J, Weisskoff RM. Estimating kinetic parameters from dynamic contrast-enhanced T1-weighted MRI of a diffusable tracer: standardized quantities and symbols. J Magn Reson Imaging 1999;10(3):223-232.
11. Sourbron SP, Buckley DL. On the scope and interpretation of the Tofts models for DCE-MRI. Magn Reson Med 2011;66(3):735-745.
12. Tozer GM, Prise VE, Wilson J, Cemazar M, Shan S, Dewhirst MW, Barber PR, Vojnovic B, Chaplin DJ. Mechanisms associated with tumor vascular shut-down induced by combretastatin A-4 phosphate: intravital microscopy and measurement of vascular permeability. Cancer Res 2001;61(17):6413-6422.
13. Tozer GM, Kanthou C, Parkins CS, Hill SA. The biology of the combretastatins as tumour vascular targeting agents. Int J Exp Pathol 2002;83(1):21-38.
14. Carmeliet P, Jain RK. Principles and mechanisms of vessel normalization for cancer and other angiogenic diseases. Nat Rev Drug Discov 2011;10(6):417-427.
15. Jain RK. Normalization of tumor vasculature: an emerging concept in antiangiogenic therapy. Science 2005;307(5706):58-62.
16. Sourbron SP, Buckley DL. Classic models for dynamic contrast-enhanced MRI. NMR Biomed 2013;26(8):1004-1027.
17. Sourbron SP, Buckley DL. Tracer kinetic modelling in MRI: estimating perfusion and capillary permeability. Phys Med Biol 2012;57(2):R1-33.
18. Larsson HB, Courivaud F, Rostrup E, Hansen AE. Measurement of brain perfusion, blood volume, and blood-brain barrier permeability, using dynamic contrast-enhanced T1-weighted MRI at 3 tesla. Magn Reson Med 2009;62(5):1270-1281.
19. Lopata RG, Backes WH, van den Bosch PP, van Riel NA. On the identifiability of pharmacokinetic parameters in dynamic contrast-enhanced imaging. Magn Reson Med 2007;58(2):425-429.
20. Sourbron S. Technical aspects of MR perfusion. Eur J Radiol 2010;76(3):304-313.
21. de Lussanet QG, Langereis S, Beets-Tan RG, van Genderen MH, Griffioen AW, van Engelshoven JM, Backes WH. Dynamic contrast-enhanced MR imaging kinetic parameters and molecular weight of dendritic contrast agents in tumor angiogenesis in mice. Radiology 2005;235(1):65-72.
22. Jaspers K, Aerts HJ, Leiner T, Oostendorp M, van Riel NA, Post MJ, Backes WH. Reliability of pharmacokinetic parameters: small vs. medium-sized contrast agents. Magn Reson Med 2009;62(3):779-787.

23. Fruytier AC, Magat J, Neveu MA, Karroum O, Bouzin C, Feron O, Jordan B, Cron GO, Gallez B. Dynamic contrast-enhanced MRI in mouse tumors at 11.7 T: comparison of three contrast agents with different molecular weights to assess the early effects of combretastatin A4. NMR Biomed 2014;27(11):1403-1412.
24. Hompland T, Gulliksrud K, Ellingsen C, Rofstad EK. Assessment of the interstitial fluid pressure of tumors by dynamic contrast-enhanced magnetic resonance imaging with contrast agents of different molecular weights. Acta Oncol 2013;52(3):627-635.
25. Weidensteiner C, Rausch M, McSheehy PM, Allegrini PR. Quantitative dynamic contrast-enhanced MRI in tumor-bearing rats and mice with inversion recovery TrueFISP and two contrast agents at 4.7 T. J Magn Reson Imaging 2006;24(3):646-656.
26. Delrue LJ, Casneuf V, Van Damme N, Blanckaert P, Peeters M, Ceelen WP, Duyck PC. Assessment of neovascular permeability in a pancreatic tumor model using dynamic contrast-enhanced (DCE) MRI with contrast agents of different molecular weights. MAGMA 2011;24(4):225-232.
27. Ivanusa T, Beravs K, Medic J, Sersa I, Sersa G, Jevtic V, Demsar F, Mikac U. Dynamic contrast enhanced MRI of mouse fibrosarcoma using small-molecular and novel macromolecular contrast agents. Phys Med 2007;23(3-4):85-90.
28. Preda A, Novikov V, Moglich M, Turetschek K, Shames DM, Brasch RC, Cavagna FM, Roberts TP. MRI monitoring of Avastin antiangiogenesis therapy using B22956/1, a new blood pool contrast agent, in an experimental model of human cancer. J Magn Reson Imaging 2004;20(5):865-873.
29. Beaumont M, Lemasson B, Farion R, Segebarth C, Remy C, Barbier EL. Characterization of tumor angiogenesis in rat brain using iron-based vessel size index MRI in combination with gadolinium-based dynamic contrast-enhanced MRI. J Cereb Blood Flow Metab 2009;29(10):1714-1726.
30. Pike MM, Stoops CN, Langford CP, Akella NS, Nabors LB, Gillespie GY. High-resolution longitudinal assessment of flow and permeability in mouse glioma vasculature: Sequential small molecule and SPIO dynamic contrast agent MRI. Magn Reson Med 2009;61(3):615-625.
31. Orth RC, Bankson J, Price R, Jackson EF. Comparison of single- and dual-tracer pharmacokinetic modeling of dynamic contrast-enhanced MRI data using low, medium, and high molecular weight contrast agents. Magn Reson Med 2007;58(4):705-716.
32. Henderson E, Sykes J, Drost D, Weinmann HJ, Rutt BK, Lee TY. Simultaneous MRI measurement of blood flow, blood volume, and capillary permeability in mammary tumors using two different contrast agents. J Magn Reson Imaging 2000;12(6):991-1003.
33. Su MY, Muhler A, Lao XY, Nalcioglu O. Tumor characterization with dynamic contrast-enhanced MRI using MR contrast agents of various molecular weights. Magn Reson Med 1998;39(2):259-269.
34. Jacobs I, Strijkers GJ, Keizer HM, Janssen HM, Nicolay K, Schabel MC. A novel approach to tracer-kinetic modeling of (macromolecular) multi-bolus DCE-MRI data, applied in a murine tumor model. Proceedings of the 22nd Annual Meeting of ISMRM, Milan, Italy, 2014:Nr 0042.

35. Schabel MC. A unified impulse response model for DCE-MRI. Magn Reson Med 2012;68(5):1632-1646.
36. Renkin EM. Transport of potassium-42 from blood to tissue in isolated mammalian skeletal muscles. Am J Physiol 1959;197:1205-1210.
37. Crone C. The Permeability of Capillaries in Various Organs as Determined by Use of the 'Indicator Diffusion' Method. Acta Physiol Scand 1963;58:292-305.
38. Jensen RL, Mumert ML, Gillespie DL, Kinney AY, Schabel MC, Salzman KL. Preoperative dynamic contrast-enhanced MRI correlates with molecular markers of hypoxia and vascularity in specific areas of intratumoral microenvironment and is predictive of patient outcome. Neuro Oncol 2014;16(2):280-291.
39. Deoni SC, Rutt BK, Peters TM. Rapid combined T1 and T2 mapping using gradient recalled acquisition in the steady state. Magn Reson Med 2003;49(3):515-526.
40. Schabel MC, Parker DL. Uncertainty and bias in contrast concentration measurements using spoiled gradient echo pulse sequences. Phys Med Biol 2008;53(9):2345-2373.
41. Schabel MC, Fluckiger JU, DiBella EV. A model-constrained Monte Carlo method for blind arterial input function estimation in dynamic contrast-enhanced MRI: I. Simulations. Phys Med Biol 2010;55(16):4783-4806.
42. Schabel MC, DiBella EV, Jensen RL, Salzman KL. A model-constrained Monte Carlo method for blind arterial input function estimation in dynamic contrast-enhanced MRI: II. In vivo results. Phys Med Biol 2010;55(16):4807-4823.
43. Corot C, Port M, Raynal I, Dencausse A, Schaefer M, Rousseaux O, Simonot C, Devoldere L, Lin J, Foulon M, Bourrinet P, Bonnemain B, Meyer D. Physical, chemical, and biological evaluations of P760: a new gadolinium complex characterized by a low rate of interstitial diffusion. J Magn Reson Imaging 2000;11(2):182-191.
44. Dowell NG, Tofts PS. Fast, accurate, and precise mapping of the RF field in vivo using the 180 degrees signal null. Magn Reson Med 2007;58(3):622-630.
45. Liberman G, Louzoun Y, Ben Bashat D. T1 mapping using variable flip angle SPGR data with flip angle correction. J Magn Reson Imaging 2014;40(1):171-180.
46. Yarnykh VL. Optimal radiofrequency and gradient spoiling for improved accuracy of T1 and B1 measurements using fast steady-state techniques. Magn Reson Med 2010;63(6):1610-1626.
47. van Nierop BJ, Coolen BF, Dijk WJ, Hendriks AD, de Graaf L, Nicolay K, Strijkers GJ. Quantitative first-pass perfusion MRI of the mouse myocardium. Magn Reson Med 2013;69(6):1735-1744.
48. Kershaw LE, Cheng HL. Temporal resolution and SNR requirements for accurate DCE-MRI data analysis using the AATH model. Magn Reson Med 2010;64(6):1772-1780.
49. Langereis S, de Lussanet QG, van Genderen MH, Meijer EW, Beets-Tan RG, Griffioen AW, van Engelshoven JM, Backes WH. Evaluation of Gd(III)DTPA-terminated poly(propylene imine) dendrimers as contrast agents for MR imaging. NMR Biomed 2006;19(1):133-141.
50. Michoux N, Huwart L, Abarca-Quinones J, Dorvillius M, Annet L, Peeters F, Van Beers BE. Transvascular and interstitial transport in rat hepatocellular carcinomas:

dynamic contrast-enhanced MRI assessment with low- and high-molecular weight agents. J Magn Reson Imaging 2008;28(4):906-914.
51. Milosevic MF, Fyles AW, Hill RP. The relationship between elevated interstitial fluid pressure and blood flow in tumors: A bioengineering analysis. Int J Radiat Oncol 1999;43(5):1111-1123.
52. Chaplin DJ, Hill SA. Temporal heterogeneity in microregional erythrocyte flux in experimental solid tumours. Br J Cancer 1995;71(6):1210-1213.
53. Dewhirst MW, Kimura H, Rehmus SW, Braun RD, Papahadjopoulos D, Hong K, Secomb TW. Microvascular studies on the origins of perfusion-limited hypoxia. Br J Cancer Suppl 1996;27:S247-251.
54. Kimura H, Braun RD, Ong ET, Hsu R, Secomb TW, Papahadjopoulos D, Hong K, Dewhirst MW. Fluctuations in red cell flux in tumor microvessels can lead to transient hypoxia and reoxygenation in tumor parenchyma. Cancer Res 1996;56(23):5522-5528.
55. Baudelet C, Ansiaux R, Jordan BF, Havaux X, Macq B, Gallez B. Physiological noise in murine solid tumours using T2*-weighted gradient-echo imaging: a marker of tumour acute hypoxia? Phys Med Biol 2004;49(15):3389-3411.
56. Brurberg KG, Benjaminsen IC, Dorum LM, Rofstad EK. Fluctuations in tumor blood perfusion assessed by dynamic contrast-enhanced MRI. Magn Reson Med 2007;58(3):473-481.
57. Brurberg KG, Gaustad JV, Mollatt CS, Rofstad EK. Temporal heterogeneity in blood supply in human tumor xenografts. Neoplasia 2008;10(7):727-735.
58. Jia Y, Qin J, Zhi Z, Wang RK. Ultrahigh sensitive optical microangiography reveals depth-resolved microcirculation and its longitudinal response to prolonged ischemic event within skeletal muscles in mice. J Biomed Opt 2011;16(8):086004.
59. Bragin DE, Bush RC, Nemoto EM. Effect of cerebral perfusion pressure on cerebral cortical microvascular shunting at high intracranial pressure in rats. Stroke 2013;44(1):177-181.
60. Dreher MR, Liu W, Michelich CR, Dewhirst MW, Yuan F, Chilkoti A. Tumor vascular permeability, accumulation, and penetration of macromolecular drug carriers. J Natl Cancer Inst 2006;98(5):335-344.
61. Chauhan VP, Stylianopoulos T, Martin JD, Popovic Z, Chen O, Kamoun WS, Bawendi MG, Fukumura D, Jain RK. Normalization of tumour blood vessels improves the delivery of nanomedicines in a size-dependent manner. Nat Nanotechnol 2012;7(6):383-388.

Supporting information 1: Dendrimer synthesis and characterization

Materials.

All reagents, chemicals, materials and solvents were obtained from commercial sources, and were used as received: Biosolve, Merck and Cambridge Isotope Laboratories for (deuterated) solvents; Aldrich, Acros, ABCR, Merck and Fluka for chemicals, materials and reagents. The amine terminated poly(propylene imine) (PPI) dendrimers were acquired from SyMO-Chem BV (Eindhoven, the Netherlands). All solvents were of AR quality. Moisture or oxygen-sensitive reactions were performed under an Ar atmosphere. Bio-Beads S-X1 was obtained from Bio-Rad Laboratories. Sephadex G-10, G-25 was obtained from GE Healthcare.

Methods.

^{1}H-NMR, ^{13}C-NMR spectra were recorded on a Varian Mercury (400 MHz for ^{1}H-NMR and 100 MHz for ^{13}C-NMR) spectrometer at 298 K. Chemical shifts are reported in ppm downfield from TMS at r.t. using deuterated chloroform ($CDCl_3$) as a solvent and internal standard unless otherwise indicated. Abbreviations used for splitting patterns are s = singlet, t = triplet, q = quartet, m = multiplet and br = broad. Infrared (IR) spectra were recorded on a Perkin Elmer 1600 FT-IR (UATR). Preparative size exclusion chromatography was performed using Bio-Rad Bio-Beads S-X1 (200-400 mesh) for organic eluents or Sephadex G-25 for water as eluent. Liquid Chromatography Electrospray Ionization Mass Spectrometry (LC-ESI-MS) was performed using a Shimadzu LC-10 AD VP series HPLC coupled to a diode array detector (Finnigan Surveyor PDA Plus detector, Thermo Electron Corporation) and an Ion-Trap (LCQ Fleet, Thermo Scientific) where ions were created via electrospray ionization. LC-analyses (on **1** and precursors to **1**) were performed using an Alltech Alltima HP C_{18} 3µ column using an injection volume of 1-4 µL, a flow rate of 0.2 mL min^{-1} and typically a gradient (5% to 100% in 10 min, held at 100% for a further 3 min) of CH_3CN in H_2O (both containing 0.1% formic acid) at 298 K. Gel permeation chromatography (GPC) analyses were measured on a TSKgel G3000PWxl column, where the eluent was 0.1 M citric acid with 0.025w% sodium azide in water, using a flow rate of 0.55 mL/min, and applying an RI (Shimadzu RID-10A) detector. The gadolinium content of the dendrimers was measured with Inductively Coupled Plasma-Atomic Emission Spectrometry (ICP-AES) (Philips Innovation Services, Eindhoven, The Netherlands).

Synthesis

The synthesis scheme of G2-PPI-(PEG$_6$-GdDOTA)$_8$ and G5-PPI-(PEG$_6$-GdDOTA)$_{64}$ is shown in Supporting Figure 1.1.

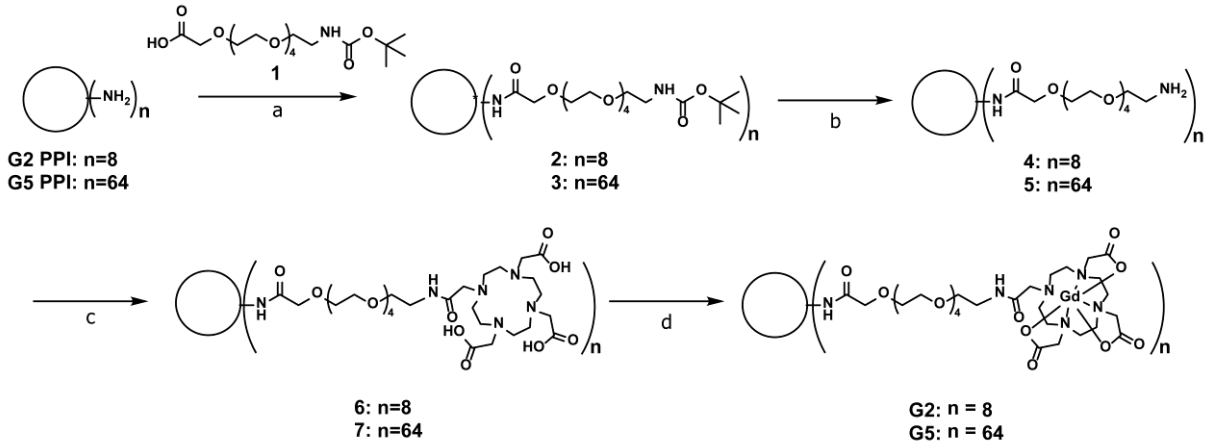

Supporting Figure 1.1. Synthesis of G2-PPI-(PEG$_6$-GdDOTA)$_8$ and G5-PPI-(PEG$_6$-GdDOTA)$_{64}$. The building block with a discrete number of ethylene glycol units (**1**) was synthesized according to literature procedure (1-3). a) PyBOP, DiPEA, DCM; b) TFA, DCM; c) DOTA-NHS, TEA, MeOH; d) Gd(OAc)$_3$, H_2O, pH~7.

G2-PPI-(PEG$_6$-NHBoc)$_8$ ***(2)***

G2-PPI-(NH$_2$)$_8$ (136 mg, 176 µmol), **1** (670 mg, 1.7 mmol, 1.2 eq per NH$_2$) and *N*,*N*-diisopropylethylamine (0.89 mL, 5.1 mmol, 3 eq to **1**) were dissolved in dichloromethane (6 mL). After the addition of PyBOP (896 mg, 1.7 mmol, 1.2 eq per NH$_2$) and dichloromethane (1 mL) the solution was stirred at room temperature for 1 h. Chloroform (150 mL) was added and the solution was washed with 0.1 M NaOH (40 mL). The organic layer was dried using Na_2SO_4, filtrated and the solvent was removed *in vacuo*. Preparative size-exclusion chromatography (BioBeads SX-1, 10% MeOH in $CHCl_3$) yielded **2** (666 mg, 176 µmol, 100%) as a yellowish oil. ^{1}H-NMR: δ = 7.17 (t, 8H, N*H*COCH$_2$), 5.10 (br, 8H, N*H*COO), 3.97 (s, 16H, COC*H*$_2$), 3.70-3.58 (m, 144H, C*H*$_2$O), 3.53 (t, 16H, C*H*$_2$O), 3.30 (q, 16H, C*H*$_2$NH), 2.48-2.34 (m, 36H, C*H*$_2$NC*H*$_2$), 1.69-1.51 (m, 28H, NCH$_2$C*H*$_2$CH$_2$N, NCH$_2$C*H*$_2$C*H*$_2$CH$_2$N), 1.44 (s, 72H, C(C*H*$_3$)$_3$). ^{13}C-NMR(CD_3OD): δ = 172.53, 158.37, 80.19, 71.86, 71.46, 71.45, 71.41, 71.39, 71.31, 71.26, 71.18, 71.02, 52.96, 52.46, 47.31, 41.21, 38.46, 28.83, 27.48. ESI-MS m/z calcd ($C_{176}H_{344}N_{22}O_{64}$) 3792.8 g/mol; found 948.9 $[M+4H]^{4+}$, 1265.1 $[M+3H]^{3+}$ and 1896.8 $[M+2H]^{2+}$. FT-IR (ATR): υ (cm^{-1}) = 3346, 2869, 1707, 1664, 1530, 1455, 1391, 1365, 1275, 1250, 1104, 1043, 947, 863, 845, 781, 758, 578.

G2-PPI-(PEG$_6$-NH$_2$)$_8$ ***(4)***

Under an Ar atmosphere, **2** (666 mg, 176 µmol) was dissolved in dichloromethane (6 mL). The flask was put on an ice bath, TFA (9 mL) was added and the solution was stirred at room temperature for 2 h. The solvent was removed *in vacuo* (oil pump, 40 °C), the resulting oil was dissolved in methanol (3 mL) and ether (30 mL) was added, and the solvents were removed *in vacuo*. This co-evaporation procedure was repeated. The oil was then washed with ether to further remove TFA. Preparative size-

exclusion chromatography (BioBeads SX-1, 10% MeOH in $CHCl_3$) gave **4** (800 mg) as a yellowish oil that still contained residual TFA. ^{1}H-NMR (CD_3OD): δ = 4.06 (s, 16H, COCH_2), 3.78-3.65 (m, 144H, CH_2O), 3.40-3.08 (m, 52H, CH_2NH, CH_2NCH_2), 3.16 (t, 16H, C$H_2$$NH_3^+$), 2.18 (br, 8H, $NCH_2CH_2CH_2N$), 1.99 (m, 16H, $NCH_2CH_2CH_2N$), 1.77 (br, 4H, $NCH_2CH_2CH_2CH_2N$). ^{13}C-NMR: δ = 171.6, 161.0 (q, TFA), 116.6 (q, TFA), 70.4, 70.0, 69.9, 69.7, 66.5, 50.5, 49.5, 39.2, 35.6, 23.6, 18.2. ESI-MS m/z calcd ($C_{136}H_{280}N_{22}O_{48}$) 2991.8 g/mol; found 499.8 $[M+6H]^{6+}$, 599.6 $[M+5H]^{5+}$, 749.0 $[M+4H]^{4+}$, 998.3 $[M+3H]^{3+}$ and 1496.6 $[M+2H]^{2+}$. FT-IR (ATR): υ (cm^{-1}) = 3421, 2881, 1673, 1537, 1472, 1424, 1350, 1290, 1250, 1200, 1178, 1123, 948, 832, 800, 721, 597, 519.

G2-PPI-(PEG$_6$-DOTA)$_8$ ***(6)***

Amine **4** (300 mg, 100 µmol) was dissolved in methanol (8 mL) and triethylamine (1.7 mL, 12 mmol, 121 eq). Thereafter, *N*-hydroxysuccinimide activated DOTA (973 mg, 1.2 mmol, 1.5 eq per NH_2) was added. Note that triethylamine is used in excess to neutralize the residual TFA in amine **4**, and further note that NHS-activated DOTA also contains residual TFA and has an estimated purity of 62%. The solution was stirred at r.t. for 65 h, was filtrated and the filtrate was concentrated *in vacuo*. Preparative size-exclusion chromatography (Sephadex G-25, H_2O) yielded **6** (478 mg, 79 µmol, 79%) as a tough oil. ^{1}H-NMR: δ = 4.10 (s, 16H, COCH_2), 3.86-3.02 (m, 404H, CH_2O, COCH_2N, NCH_2CH_2N, CH_2NH, CH_2NCH_2), 2.18 (br, 8H, $NCH_2CH_2CH_2N$), 1.98 (m, 16H, $NCH_2CH_2CH_2N$), 1.77 (br, 4H, $NCH_2CH_2CH_2CH_2N$). ESI-MS m/z calcd ($C_{136}H_{280}N_{22}O_{48}$) 6083.1 g/mol; found 761.6 $[M+8H]^{8+}$, 870.1 $[M+7H]^{7+}$, 1014.9 $[M+6H]^{6+}$, 1217.7 $[M+5H]^{5+}$ and 1521.5 $[M+4H]^{4+}$. FT-IR (ATR): υ (cm^{-1}) = 3418, 2870, 1704, 1622, 1464, 1435, 1387, 1322, 1245, 1104, 1088, 1006, 936, 840, 716, 570, 499.

G2-PPI-(PEG$_6$-GdDOTA)$_8$ ***(G2)***

Dendrimer ligand **6** (478 mg, 79 µmol) was dissolved in H_2O (7 mL) and the pH was adjusted to 7.1 using 1 M NaOH. $Gd(OAc)_3 \cdot xH_2O$ (508 mg, 1.26 mmol, 2 eq per DOTA) in H_2O (4 mL, dissolved by shortly heating) was added, and the pH was again adjusted to 7.0 using 1 M NaOH. The solution was stirred at r.t. for 93 h. The solvent was removed *in vacuo* and repeated preparative size-exclusion chromatography (Sephadex G-25, H_2O) yielded **G2** (430 mg, 59 µmol, 74%) as an off-white solid after lyophilization. A xylenol orange test was negative, so the material did not contain free gadolinium ions. The material gave a clear colorless solution in phosphate buffered saline (PBS). ESI-MS m/z calcd ($C_{264}H_{464}Gd_8N_{54}O_{104}$) 7316.9 g/mol; found 919.8 $[M+8H]^{8+}$, 1046 $[M+7H]^{7+}$, 1220.7 $[M+6H]^{6+}$, and 1464.3 $[M+5H]^{5+}$. FT-IR (ATR): υ (cm^{-1}) = 3372, 3264, 2869, 1595, 1463, 1434,1387, 1317, 1283, 1243, 1084, 1103, 937, 905, 839, 801, 716, 644, 566, 496. Aqueous GPC showed a dominant peak with a shoulder at lower retention time (so at higher molecular weight), as also observed for related pegylated PPI-based materials (4). ICP-MS Gd: calcd wt%= 17.2%, found wt% = 14.9%.

A similar procedure as used for **G2** was followed for the synthesis of the **G5** product.

G5-PPI-(PEG$_6$-NHBoc)$_{64}$ ***(3)***
Yield: 800 mg (100%) as a yellowish oil. ^{1}H-NMR: δ = 7.32 (t, 64H, N*H*COCH$_2$), 5.22 (br, 64H, N*H*COO), 3.96 (s, 128H, COC*H*$_2$), 3.72-3.56 (m, 1152H, C*H*$_2$O), 3.52 (t, 128H, C*H*$_2$O), 3.28 (q, 128H, C*H*$_2$NH), 2.42 (m, 372H, C*H*$_2$NC*H*$_2$), 1.70-1.50 (m, 252H, NCH$_2$C*H*$_2$CH$_2$N, NCH$_2$C*H*$_2$C*H*$_2$CH$_2$N), 1.43 (s, 576H, C(C*H*$_3$)$_3$). ^{13}C-NMR: δ = 169.8, 156.0, 78.9, 70.7, 70.5, 70.4, 70.2, 70.14, 70.08, 52.3, 51.8, 51.4, 40.2, 37.3, 28.4, 26.9, 23.9. FT-IR (ATR): υ (cm^{-1}) = 3346, 2931, 2869, 2817, 1707, 1660, 1530, 1455, 1391, 1365, 1349, 1273, 1249, 1170, 1099, 1042, 947, 862, 845, 780, 757, 732, 698.

G5-PPI-(PEG$_6$-NH$_2$)$_{64}$ ***(5)***
During work-up, part of the TFA was removed by co-evaporating the oil with a mixture of methanol and toluene. Yield: 400 mg (contains residual TFA). ^{1}H-NMR (CD$_3$OD): δ = 4.00 (s, 128H, COC*H*$_2$), 3.72-3.56 (m, 1152H, C*H*$_2$O), 3.36-3.16 (m, 500H, C*H*$_2$NH, C*H*$_2$NC*H*$_2$), 3.11 (t, 128H, C*H*$_2$NH$_3^+$), 2.28 (br, 120H, NCH$_2$C*H*$_2$CH$_2$N), 1.95 (m, 128H, NCH$_2$C*H*$_2$CH$_2$N), the signal of the NCH$_2$C*H*$_2$C*H*$_2$CH$_2$N group is not differentiated. ^{13}C-NMR (CD$_3$OD): δ = 171.6, 161.0 (q, TFA), 116.6 (q, TFA), 70.4, 70.0, 69.9, 69.7, 66.5, 50.5, 49.5, 39.2, 35.6, 23.6, 18.2. FT-IR (ATR): υ (cm^{-1}) = 3334, 3092, 2880, 1668, 1541, 1471, 1455, 1422, 1350, 1293, 1251, 1198, 1177, 1118, 947, 832, 799, 720, 707, 595, 558, 518.

G5-PPI-(PEG$_6$-DOTA)$_{64}$ ***(7)***
Repeated preparative size-exclusion chromatography (Sephadex G-25, H$_2$O) yielded **7** (516 mg, 93%) as a tough oil. ^{1}H-NMR: δ = 4.10 (s, 128H, COC*H*$_2$), 3.88-3.00 (m, 3320H, C*H*$_2$O, COC*H*$_2$N, NC*H*$_2$C*H*$_2$N, C*H*$_2$NH, C*H*$_2$NC*H*$_2$), 1.97 (br, 252H, NCH$_2$C*H*$_2$CH$_2$N, NCH$_2$C*H*$_2$C*H*$_2$CH$_2$N). FT-IR (ATR): υ (cm^{-1}) = 3346, 2917, 2876, 1708, 1664, 1530, 1455, 1391, 1365, 1275, 1254, 1104, 1043, 947, 863, 845, 781, 578.

G5-PPI-(PEG$_6$-GdDOTA)$_{64}$ ***(G5)***
Preparative size-exclusion chromatography (Sephadex G-25, H$_2$O) yielded a product that did not completely dissolve in PBS, so removal of residual salts was brought about by dissolving the compound in PBS buffer (0.1 M, pH = 7.4) and storing the solution at 5 °C overnight. Centrifugation (4000 rpm, 10 min) to remove these solids was followed by decantation and dialysis of the solution against demineralized H$_2$O (membrane MWCO = 1000 Da, duration 6d with refreshing the aqueous phase once after 3d). This yielded **G5** (371 mg, 60%) as an off-white solid after lyophilization. A xylenol orange test was negative, so the material did not contain free gadolinium ions.

FT-IR (ATR): υ (cm^{-1}) = 3376, 2917, 2869, 1591, 1457, 1435, 1393, 1369, 1319, 1245, 1084, 1003, 393, 840, 801, 716, 558, 495. Aqueous GPC showed a dominant peak with a minor shoulder at lower retention time (so at higher molecular weight), as also observed for related pegylated PPI-based materials (4). ICP-MS Gd: calcd wt%= 16.9%, found wt% = 13.5%.

Dynamic Light Scattering (DLS)

The hydrodynamic size of the G2-PPI-$(PEG_6$-GdDOTA$)_8$ (G2) and G5-PPI-$(PEG_6$-GdDOTA$)_{64}$ (G5) dendrimers was determined with DLS on a Zetasizer Nano-S (Malvern Instruments, Malvern, Worcestershire, United Kingdom) at 20 °C using the volume-weighted particle size distribution. Dendrimers were dissolved in filtered PBS of pH 7.4 and filtered through a 0.45 µm pore Millex membrane filter (Merck Millipore Ltd., Tullagreen, Carrigtwohill, County Cork, Ireland) to remove dust or other potential contaminants that may affect the DLS measurements. The results of the DLS measurements are shown in Supporting Figure 1.2. The volume-weighted size distribution showed a single peak for the G2 and G5 dendrimers and a narrow size distribution. The average hydrodynamic diameter and distribution widths of the G2 and G5 dendrimers were 4.3±1.1 and 10.0±3.6 nm, respectively.

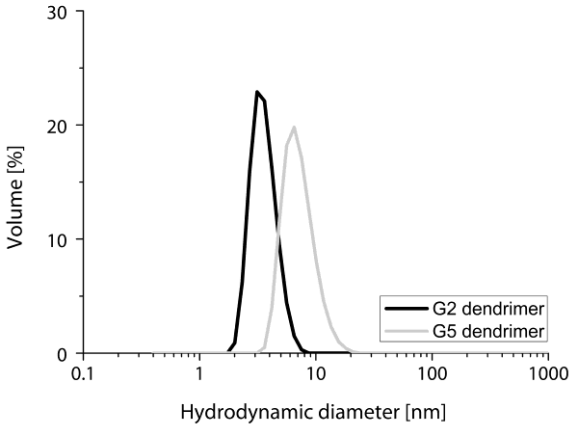

Supporting Figure 1.2. The volume-weighted size (hydrodynamic diameter) distribution of the G2 and G5 dendrimer, measured in PBS of pH 7.4 at 20 °C.

References

1. Bonnet M, Flanagan JU, Chan DA, Giaccia AJ, Hay MP. Identifying novel targets in renal cell carcinoma: design and synthesis of affinity chromatography reagents. Bioorg Med Chem 2014;22(2):711-720.

2. Muller MK, Brunsveld L. A Supramolecular Polymer as a Self-Assembling Polyvalent Scaffold. Angew Chem Int Edit 2009;48(16):2921-2924.

3. Araki J, Zhao CM, Kohzo I. Efficient production of polyrotaxanes from alpha-cyclodextrin and poly(ethylene glycol). Macromolecules 2005;38(17):7524-7527.

4. Tack F, Bakker A, Maes S, Dekeyser N, Bruining M, Elissen-Roman C, Janicot M, Brewster M, Janssen HM, De Waal BFM, Fransen PM, Lou X, Meijer EW. Modified poly(propylene imine) dendrimers as effective transfection agents for catalytic DNA enzymes (DNAzymes). J Drug Target 2006;14(2):69-86.

Supporting information 2: phantom validation of the variable flip angle pre-contrast T_1 mapping and dynamic T_1 mapping method

Phantom measurements were performed for validation of the variable flip angle pre-contrast T_1 mapping and dynamic T_1 mapping method. For the phantom measurements, the same sequences (B_1 mapping, T_1 mapping, and dynamic T_1 mapping) and sequence parameters were used as those employed for the in vivo measurements in tumor-bearing mice.

The variable flip angle T_1 mapping protocol was compared with the inversion recovery T_1 mapping method, using samples containing various concentrations (0.05-1.5 mM) of gadoterate meglumine in 5 mg/L Manganese(II) chloride. Data were acquired at 7 T at room temperature.

Supporting Figure 2.1 shows a correlation plot between the variable FA R_1 data and the inversion recovery R_1 data.

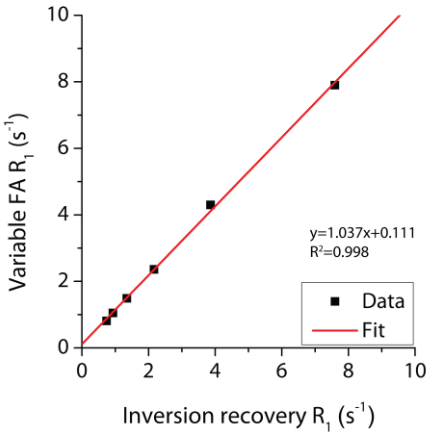

Supporting Figure 2.1. Correlation plot between the variable flip angle R_1 (s^{-1}) and the inversion recovery R_1 (s^{-1}) of samples containing various concentrations (0.05-1.5 mM) of gadoterate in 5 mg/L Manganese(II) chloride. The red line is the linear fit to the data, with the equation and R^2 of the linear fit displayed in the graph.

The variable flip angle R_1 data were in excellent agreement with the inversion recovery R_1 data, as shown by the slope of the linear fit to the data, which was close to unity.

In addition to this, we 'simulated' an in vivo DCE-MRI experiment as follows:

We determined the R_1 value of the tube with the lowest gadolinium concentration with the variable flip angle analysis (which would be a so-called pre-contrast R_1 value). With this R_1 value and the dynamic signal intensity (that would correspond to the DCE-MRI acquisition), we calculated the proportionality constant ρ for this tube using the standard equation for a steady state spoiled gradient echo sequence. With this ρ and the dynamic signal intensities in the other tubes, we determined the 'dynamic' R_1 of the other tubes (with higher concentrations of gadolinium).

Supporting Figure 2.2 shows a correlation plot between the dynamic R_1 data and the inversion recovery R_1 data.

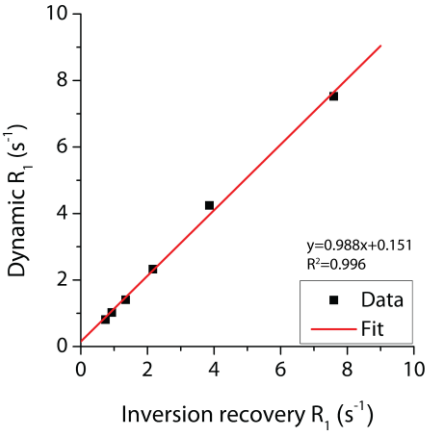

Supporting Figure 2.2. Correlation plot between the dynamic R_1 (s^{-1}) and the inversion recovery R_1 (s^{-1}) of samples containing various concentrations (0.05-1.5 mM) of gadoterate in 5 mg/L Manganese(II) chloride. The red line is the linear fit to the data, with the equation and R^2 of the linear fit displayed in the graph.

Calculated dynamic R_1 values were in excellent agreement with the inversion recovery R_1 values, as shown by the slope of the linear fit to the data.

These phantom validation results demonstrated that the variable flip angle T_1 mapping and dynamic T_1 mapping measurements produced accurate T_1 values.

Supporting information 3: typical AIFs of the dendrimers and gadoterate, as determined with the MCBE algorithm

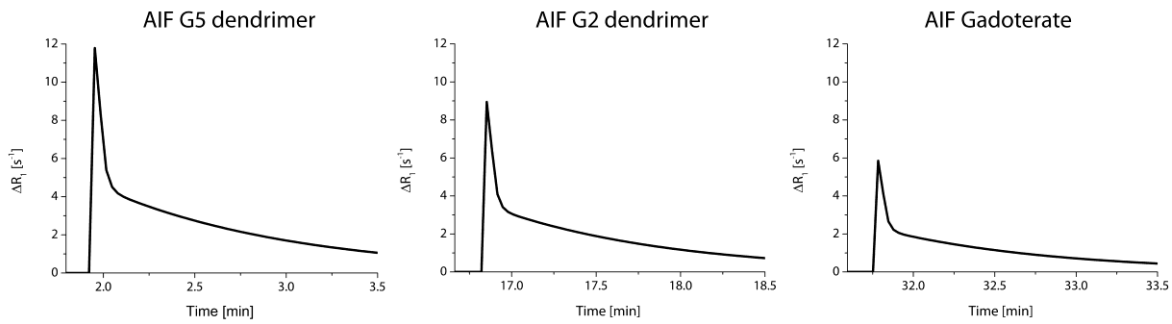

Supporting Figure 3.1. Typical AIFs of the different agents, as determined with the MCBE algorithm. The time scale on the x-axis refers to the time after start of the acquisition.

Chapter 5

Multiparametric MRI Analysis for the Identification of High Intensity Focused Ultrasound-treated Tumor Tissue

Igor Jacobs[1,2,*], Stefanie JCG Hectors[1,2,*], Gustav J Strijkers[1,2,3], Klaas Nicolay[1,2]

[1] Biomedical NMR, Department of Biomedical Engineering, Eindhoven University of Technology, Eindhoven, The Netherlands
[2] Center for Imaging Research and Education (CIRE), Eindhoven, The Netherlands
[3] Biomedical Engineering and Physics, Academic Medical Center, University of Amsterdam, Amsterdam, The Netherlands

* These authors contributed equally to this work.

Published in PLoS One 2014;9(6):e99936.

Abstract

Purpose
In this study endogenous magnetic resonance imaging (MRI) biomarkers for accurate segmentation of High Intensity Focused Ultrasound (HIFU)-treated tumor tissue and residual or recurring non-treated tumor tissue were identified.

Methods
Multiparametric MRI, consisting of quantitative T_1, T_2, Apparent Diffusion Coefficient (ADC) and Magnetization Transfer Ratio (MTR) mapping, was performed in tumor-bearing mice before (n=14), 1 h after (n=14) and 72 h (n=7) after HIFU treatment. A non-treated control group was included (n=7). Cluster analysis using the Iterative Self Organizing Data Analysis (ISODATA) technique was performed on subsets of MRI parameters (feature vectors). The clusters resulting from the ISODATA segmentation were divided into a viable and non-viable class based on the fraction of pixels assigned to the clusters at the different experimental time points. ISODATA-derived non-viable tumor fractions were quantitatively compared to histology-derived non-viable tumor volume fractions.

Results
The highest agreement between the ISODATA-derived and histology-derived non-viable tumor fractions was observed for feature vector {T_1, T_2, ADC}. R_1 ($1/T_1$), R_2 ($1/T_2$), ADC and MTR each were significantly increased in the ISODATA-defined non-viable tumor tissue at 1 h after HIFU treatment compared to viable, non-treated tumor tissue. R_1, ADC and MTR were also significantly increased at 72 h after HIFU.

Conclusions
This study demonstrates that non-viable, HIFU-treated tumor tissue can be distinguished from viable, non-treated tumor tissue using multiparametric MRI analysis. Clinical application of the presented methodology may allow for automated, accurate and objective evaluation of HIFU treatment.

5.1. Introduction

Thermal ablation of tumors with High Intensity Focused Ultrasound (HIFU) (1,2) is currently being introduced in the clinic for the treatment of both benign tumors, mainly uterine fibroids (3,4), and malignant tumors, such as prostate (5-7) and breast tumors (8) and liver metastases (9,10). HIFU treatment of malignant tumors should cover the entire tumor, which requires adequate treatment planning, monitoring and evaluation. HIFU therapy is therefore commonly performed under image guidance, often using magnetic resonance imaging (MRI) (11,12). MRI facilitates treatment planning because of its excellent soft tissue contrast. Furthermore, MR thermometry allows for real-time temperature feedback during the procedure (12). MRI is also well-suited for the evaluation of treatment outcome. With MR thermometry, lethal thermal dose areas (i.e. tissue regions that received a thermal dose of at least 240 equivalent minutes (EM) at 43 °C) can be identified (13). However, a recent study on MR-guided HIFU treatment of a rabbit tumor model showed that the 240-EM thermal dose limit underestimates the necrotic tissue area immediately after HIFU treatment (14), possibly caused by the dependence of thermal dose necrosis thresholds on tissue type (13,15).

For treatment evaluation commonly conventional MRI techniques are used, including T_2-weighted and contrast-enhanced T_1-weighted imaging. Kirkham et al. (7) reported a heterogeneous appearance of the tumor tissue on T_2-weighted images up to 1 month after HIFU ablation of human prostate tumors, showing that T_2-weighted imaging alone is inadequate for the assessment of necrosis. Furthermore, on contrast-enhanced T_1-weighted imaging, an enhancing rim, surrounding the non-enhancing central core of necrosis, was observed, that can either originate from residual tumor tissue or from inflammation-induced hyperemia. A similar enhancement pattern was observed in other clinical studies on HIFU treatment of prostate tumors (6) and on radiofrequency (RF) ablation of kidney (16) and liver tumors (17). Furthermore, the aforementioned study of HIFU treatment of a rabbit tumor model reported that contrast-enhanced T_1-weighted imaging underestimates the area of necrosis in histology directly after HIFU treatment (14). An additional drawback of contrast-enhanced T_1-weighted imaging for the evaluation of HIFU treatment is the need for the injection of a Gadolinium (Gd) contrast agent. If immediate retreatment needs to be performed directly after treatment evaluation, the Gd contrast agent could interfere with the HIFU procedure. Presence of Gd in the tissue could induce susceptibility artifacts in the thermometry acquisitions, resulting in inaccurate temperature maps (18).

Several studies have reported on the evaluation of HIFU treatment with more advanced MRI protocols. In clinical studies, preliminary experiments were conducted in which diffusion-weighted imaging was used to evaluate HIFU treatment. A recent study on HIFU ablation of malignant liver lesions showed a significant increase in the Apparent Diffusion Coefficient (ADC) in the necrotic, HIFU-treated tumor tissue (19). In contrast, a decrease in ADC was observed after HIFU treatment of uterine fibroids (20,21). The Magnetization Transfer Ratio (MTR) is another MRI parameter that has

potential sensitivity for the distinction between HIFU-treated and non-treated tumor tissue. The MTR is a measure for the level of magnetization exchange between water protons and semi-solid macromolecular protons in tissue (22). An increase in tissue MTR has been observed after thermal treatment of ex vivo porcine muscle tissue (23). Overall, multiple studies have been published in which different MRI parameters for HIFU treatment evaluation were proposed. However, no quantitative studies on the correlation between changes in the different MRI parameters and histological analysis of the HIFU-treated lesion have been reported. Recently, multiparametric MRI has been proposed as a possibly suitable approach for the evaluation of HIFU treatment of prostate tumors (24). To the best of our knowledge, multiparametric MR analysis consisting of quantitative assessment of HIFU-induced changes in the tumor tissue based on different combinations of MRI parameters has not yet been performed.

Therefore, the goal of the present study was to identify endogenous MRI biomarkers that can be used to distinguish between HIFU-treated and non-treated tumor tissue, using multiparametric MRI analysis combined with quantitative histological evaluation. Specifically, the multiparametric MRI protocol consisted of quantitative assessment of T_1, T_2, ADC and MTR and was used to assess changes in tumor tissue status as induced by HIFU treatment in a murine tumor model. The HIFU treatment consisted of partial ablation of the tumors to allow for internal reference between HIFU-treated and residual non-treated tumor tissue. MR evaluation of the tumor tissue was performed before and at 1 h and at 72 h after HIFU. The Iterative Self Organizing Data Analysis (ISODATA) clustering algorithm (25) was implemented and employed to segment the multispectral data into tissue populations with similar MRI parameter values. Cluster analysis was performed on different subsets of MRI parameters. The optimal set of MR parameters for the segmentation of HIFU-treated and non-treated tissue was determined by quantitative comparison between ISODATA-derived and histology-derived non-viable tumor volume fractions.

5.2. Methods

5.2.1. Ethics Statement

All animal experiments were performed according to the Directive 2010/63/EU of the European Parliament and approved by the Animal Care and Use Committee of Maastricht University (protocol: 2010-097).

5.2.2. Murine tumor model

CT26.WT murine colon carcinoma cells (American Type Culture Collection (ATCC; CRL-2638)) were cultured as a monolayer at 37 °C and 5% CO_2 in RPMI-1640 medium (Invitrogen, Breda, The Netherlands), supplemented with 10% fetal bovine serum (Greiner Bio-One, Alphen a/d Rijn, The Netherlands) and 50 U/ml penicillin/streptomycin (Lonza Bioscience, Basel, Switzerland). Early passages (5-10) of the original ATCC batch were used for inoculation.

10-12 week-old Balb/c mice (Charles River, Maastricht, The Netherlands) were inoculated with $2x10^6$ CT26.WT cells subcutaneously in the right hind limb. Approximately 10 days after inoculation, tumors became palpable in all animals.

5.2.3. Study design

Animals were subjected to MRI examination 24 h before (n=14), 1 h after (n=14) and 72 h after HIFU treatment (n=7). A control group of non-treated animals (n=7) was included. The time points of MRI examinations of the control animals were the same as for the HIFU-treated animals and are referred to as Day 0, Day 1 and Day 4. Directly after the last MRI experiment, the mice were sacrificed, and the tumors were dissected and processed for histological analysis. This study design led to three different groups for quantitative histology: animals sacrificed after the MRI examination at 1 h after HIFU treatment (n=7, referred to as '1 h after HIFU'), animals sacrificed after the MRI examination at 72 h after HIFU treatment (n=7, referred to as '72 h after HIFU') and non-treated control animals (n=7, referred to as 'Control').

5.2.4. HIFU treatment

HIFU treatment was performed with the preclinical Therapy and Imaging Probe System (TIPS, Philips Research, Briarcliff Manor, NY, USA) (26), outside the MR system. Animals were initially anesthetized with 3% isoflurane in medical air and maintained with 1-2% isoflurane during HIFU treatment. Precautionary analgesia (buprenorphine, 0.1 mg/kg s.c.) was administered 30 min before treatment. The non-treated control animals received an equal dose of analgesia at the corresponding time point. Animal temperature was maintained with an infrared lamp controlled by feedback from a rectal temperature sensor, supplemented with a warm water pad. The tumor-bearing paw was positioned underneath the therapeutic transducer. The paw was fully covered with degassed ultrasound transmission gel (Aquasonic 100, Parker Laboratories, Fairfield, NJ, USA). An acoustic absorber (Aptflex F28P, Precision Acoustics, Dorchester, UK) was positioned underneath the paw to prevent far-field heating. A photograph and a schematic drawing of the HIFU set-up are shown in Supporting Figure S1.

Partial tumor ablation was performed such that both HIFU-treated and non-treated tumor tissue were present after treatment. Positioning of the tumor in the focal point of the therapeutic transducer was confirmed by use of an ultrasound imaging system (HDI5000 imaging system combined with a P7-4 phased array transducer, Philips Ultrasound, Bothell, WA, USA). Ultrasound imaging was solely used for treatment planning; ultrasound-based treatment monitoring was beyond the scope of the present study. A square 4x4 mm^2 treatment grid consisting of 25 equally-spaced treatment points was defined within the tumor. A wait time of 120 s was applied between the point-wise HIFU treatments to allow sufficient cooling of the tissue. Treatment settings were: frequency=1.4 MHz, pulse repetition frequency=20 Hz, acoustic power=12 W, duty cycle=50%, treatment time=30 s. In three pilot experiments, a thermocouple (T-type thermocouple; T-150A, Physitemp Instruments, Clifton, NJ, USA) was positioned in the focal point of the therapeutic transducer to monitor temperature during the treatment. The temperature increased to approximately 66 °C during the sonication and decreased again to the pre-sonication temperature (approximately 35 °C) during the wait time. A representative temperature profile is shown in Supporting Figure S2. The thermocouple was not

inserted during the treatment of the experimental groups to prevent non-HIFU-related damage to the tumor tissue.

5.2.5. MRI measurements

MRI measurements were performed with a 6.3 T scanner (Bruker BioSpin, Ettlingen, Germany) using a 3.2-cm-diameter quadrature birdcage RF coil (Rapid Biomedical, Rimpar, Germany). Anesthesia was maintained with 1-2% isoflurane during the MRI experiments. The mice were positioned in a custom-made cradle, equipped with a mask for anesthetic gas. The tumor-bearing paw was fixed in the set-up by adhesive tape in order to prevent motion artifacts. No motion was observed between the images of the different sequences and therefore no further post-processing image registration proved necessary. Respiration was monitored with a balloon sensor. Body temperature was monitored and maintained with a warm water pad. For reduction of susceptibility artifacts in the Echo Planar Imaging (EPI) sequence, the tumor-bearing paw was covered with degassed ultrasound gel (Aquasonic 100, Parker Laboratories). Artifacts were further reduced by local shimming of the tumor-bearing paw. To illustrate the obtained image quality of the EPI sequence, representative images of a conventional T_2-weighted spin-echo acquisition and a T_2-prepared gradient-echo EPI (GE-EPI) sequence are shown in Supporting Figure S3. No apparent geometric distortion artifacts were present in the EPI images.

The multi-slice MRI protocol, covering the whole tumor, started with a fat-suppressed T_2-weighted spin-echo sequence (echo time TE=30 ms, repetition time TR=1000 ms, number of averages NA=1) for anatomical reference. Subsequently, T_1, T_2, ADC and MTR mapping were performed. T_1 mapping was performed with an inversion recovery Look-Locker EPI method (TE=8 ms, TR=10000 ms, inversion time=30 ms, flip angle=20°, pulse separation=400 ms, number of points=15, NA=2). For T_2 mapping, a T_2-weighted MLEV-prepared (27) GE-EPI sequence (TR=2000 ms, NA=2) was acquired with 7 TE's ranging from 1 to 82 ms. For ADC mapping, a diffusion-weighted double spin-echo prepared EPI sequence (TE=41 ms, TR=4000 ms, NA=4) was used to acquire images with 4 different b-values (0, 100, 200 and 400 s/mm^2). The diffusion-sensitizing gradient was applied separately in three orthogonal directions. The MTR mapping protocol consisted of two GE-EPI acquisitions (TE=8 ms, TR=8000 ms, NA=2) with and without an off-resonance preparation pulse (4000 ms block pulse, B_1=1.3 μT, -10 ppm from water resonance frequency). All acquired images had a matrix size of 128x128, FOV of 4x4 cm^2 and 1 mm slice thickness. Twelve to 16 slices were acquired covering the whole tumor volume.

5.2.6. Image processing and generation of parameter maps

Image analysis was performed in Mathematica 7.0 (Wolfram Research, Champaign, IL, USA). Regions of interest (ROIs) were defined on the T_2-weighted images by manually drawing contours around the tumor tissue on each slice. Diffusion-weighted images were used as an additional reference for tumor demarcation. Parameter maps were calculated on a pixel-by-pixel basis in each slice. T_1 maps were generated as described previously (28). T_2 maps were calculated from mono-exponential fitting of the multi-echo data. For the generation of ADC maps, mono-exponential fitting was performed

through the signal intensities at the different b-values for each diffusion-encoding direction separately. Next, ADC values of the different directions were averaged to obtain the final (orientation-invariant) ADC value for each pixel. MTR maps were generated according to MTR=(1-S/S_0)*100%, in which S and S_0 are the pixel signal intensities with and without off-resonance irradiation, respectively.

5.2.7. ISODATA analysis

ISODATA cluster analysis was employed to segment the multiparametric data into groups of pixels, *i.e.* clusters, with similar MR parameter values. The ISODATA technique was implemented in Mathematica 7.0 according to the description given by Jacobs et al. (25). A schematic overview of the ISODATA algorithm can be found in Supporting Information S1. The ISODATA clustering technique is similar to the widely applied clustering algorithm *k*-means (29). However, as opposed to *k*-means, the number of clusters does not have to be determined *a priori* for the ISODATA algorithm. The number of clusters is rather adjusted iteratively according to the Euclidean distance between and within the clusters. ISODATA clustering was performed on the multi-slice parametric images of all animals (HIFU-treated and control) at all time points simultaneously. Prior to ISODATA clustering, features were normalized (mean μ=0, standard deviation (SD)=1) to remove scaling differences between the different parameters. Pixels of which the signal intensity in the T_2-weighted images was at noise level, *e.g.* because of HIFU-induced hemorrhage, were excluded from ISODATA analysis. ISODATA clustering was performed on the following subsets of MRI parameters, termed feature vectors: {T_2}, {ADC}, {T_1,T_2}, {T_2,ADC}, {T_1,ADC}, {ADC,MTR}, {T_1,T_2,ADC}, {T_2,ADC,MTR}, {T_1,ADC,MTR}, {T_1,T_2,MTR} and {T_1,T_2,ADC,MTR}. The resulting clusters were divided into two different classes:

- Non-viable: clusters of which the fraction of assigned pixels increased significantly after HIFU (either at 1 h or 72 h) compared to before HIFU (paired Student's t-test, $p<0.05$);
- Viable: all remaining clusters.

Subsequently, all tumor pixels of both the HIFU-treated and non-treated animals at all experimental time points were assigned as either viable or non-viable based on the class of the cluster to which the pixel belongs. A schematic view of the classification of the clusters into either non-viable or viable tumor tissue is given in Figure 1.

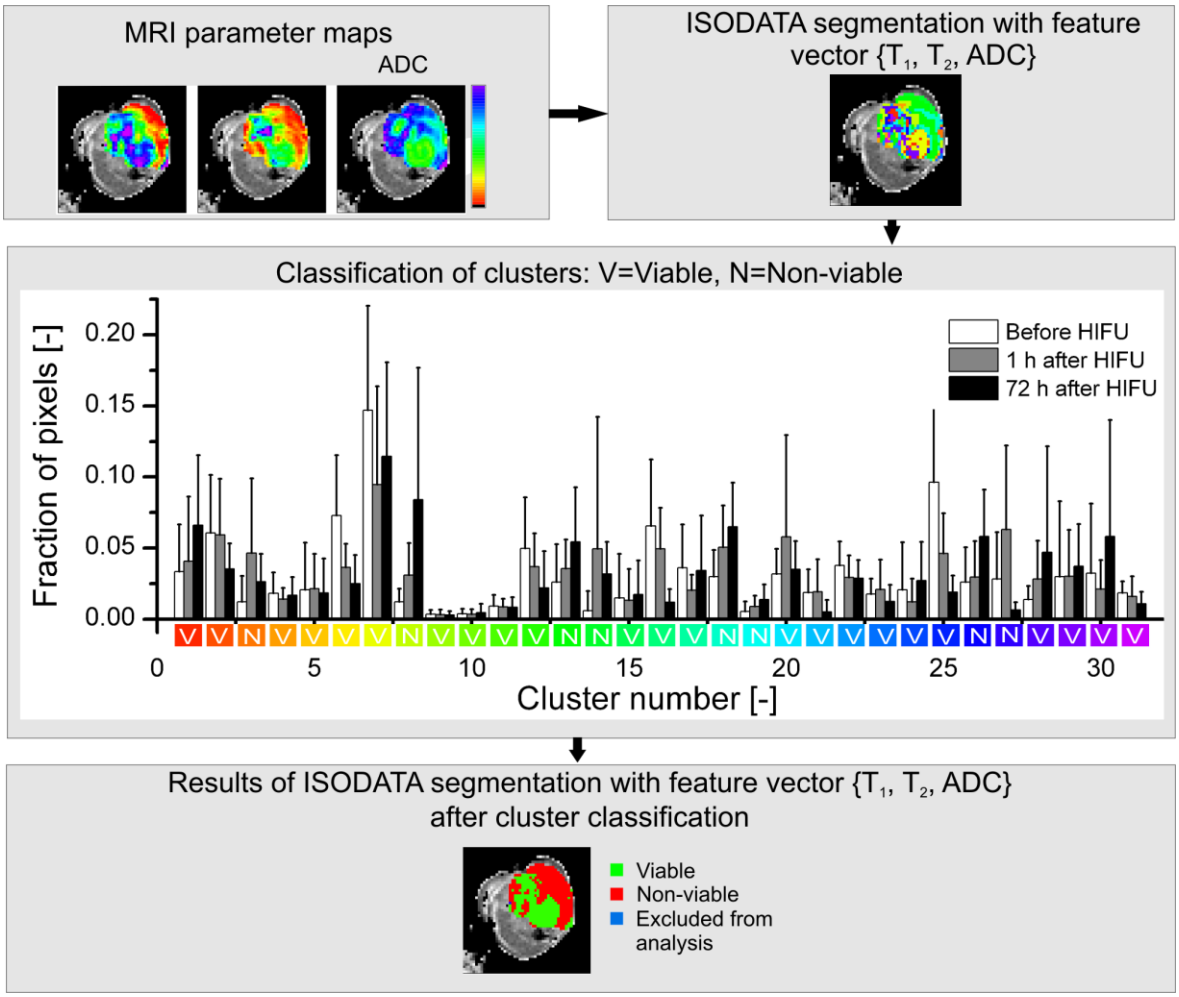

Figure 1. Flow chart of ISODATA segmentation. Flow chart of the classification of clusters resulting from ISODATA segmentation with feature vector {T_1, T_2, ADC}. MRI parameter maps were generated from the multiparametric MRI data (top left). The displayed MRI results originate from a tumor scanned at 72 h after HIFU treatment. Pixels were clustered into tissue populations with similar MRI parameters (top right; different colors represent different clusters). The resulting clusters were classified as either viable (labeled 'V' in the histogram) or non-viable (labeled 'N' in the histogram) based on the fraction of pixels assigned to the clusters at the different time points. Clusters of which the fraction of pixels had increased significantly (paired Student's t-test, $p<0.05$) after HIFU compared to before HIFU were assigned to non-viable tumor tissue. The remaining clusters were assigned to viable tumor tissue. The histogram of the fractions of tumor pixels in each cluster at the different time points is displayed in the center of the figure. The white, grey and black bars represent mean ± SD of the fractions of tumor pixels before, at 1 h after and at 72 h after HIFU, respectively. The color coding on the x-axis of the histogram corresponds to the cluster colors in the ISODATA segmentation results (top right). The result of the ISODATA segmentation after classification of the clusters as either viable or non-viable tumor tissue is shown in the bottom part of the figure. A small number of tumor pixels was excluded from ISODATA analysis, because of a low signal-to-noise ratio (see Methods).

Based on this classification, ISODATA-derived non-viable tumor volume fractions were calculated for each tumor for the different feature vectors. These tumor fractions were compared to histology-derived non-viable tumor volume fractions in order to select the optimal feature vector, *i.e*. the combination of MRI indices, which led to the best agreement with the histological differentiation between non-viable and viable tumor tissue.
Mean MRI parameter values in the pixels classified as viable and non-viable tumor tissue were calculated to quantify the effects of HIFU treatment on the measured MRI parameters.

5.2.8. Histological analysis

Dissected tumors were snap-frozen in isopentane and stored at -80 °C. Tumors were cut into 5 µm thick sections with a distance of approximately 300 µm between the sections. The cryo-sections were briefly air-dried and subsequently stained for nicotinamide adenine dinucleotide (NADH) diaphorase activity to assess cell viability. NADH-diaphorase staining is a powerful histological tool for demarcation between viable and non-viable tumor tissue after HIFU treatment (30). Sections were incubated at 37 °C for 1 h in Gomori-Tris-HCl buffer (pH 7.4) containing β-NAD reduced disodium salt hydrate (Sigma-Aldrich, St. Louis, MO, USA, 0.71 mg/ml buffer solution) and nitro blue tetrazolium (Sigma-Aldrich, 0.29 mg/ml buffer solution). Brightfield microscopy was performed on all sections and consisted of mosaic acquisition of the entire section at 5x magnification.

Analysis of the microscopy images was performed in Mathematica 7.0. ROIs were manually drawn around the pale non-viable tumor tissue and the entire tumor tissue on all sections of each tumor. From the ratio between the ROI areas of non-viable tumor tissue and entire tumor tissue on all tumor sections, a histology-derived non-viable tumor volume fraction was determined for each tumor.

5.2.9. Statistical analysis

Data are reported as mean±SD. For the determination of the optimal feature vector, non-viable tumor fractions derived from ISODATA segmentation with the different feature vectors were quantitatively compared to the histology-derived non-viable tumor volume fractions. Initial feature vector selection was based on the one-to-one correspondence between histology-derived and ISODATA-derived non-viable tumor fractions. The one-to-one correspondence was determined by calculation of the coefficient of determination (R^2) of the data points, consisting of the ISODATA-derived and the histology-derived non-viable tumor fraction of each tumor, to the line of identity (y=x). This initial selection led to the elimination of feature vectors for which the ISODATA-derived non-viable tumor fractions were either strongly over- or underestimated compared to the histology-derived non-viable tumor fractions. Subsequently, Pearson's correlation coefficients were determined between the histology-derived and ISODATA-derived tumor fractions, as a measure for the strength of the linear relationship between the histology-derived and ISODATA-derived non-viable tumor fractions. These correlation values were determined for two different groups of animals: one group consisting of the animals sacrificed after the MRI

examination at 1 h after HIFU and the non-treated control animals (referred to as '1 h after HIFU + Control') and one group consisting of the animals sacrificed after the MRI examination at 72 h after HIFU and the control animals (referred to as '72 h after HIFU + Control'). This division in groups was made to take into account the temporal changes in tumor tissue after HIFU treatment, which might lead to a different optimal feature vector for the different time points after HIFU. The control animals were included in both groups to increase the statistical power and to obtain a larger range of non-viable tumor fractions. Differences in correlation values between the different feature vectors were tested for significance with a Wolfe's test for Comparing Dependent Correlation Coefficients (31).
For the HIFU-treated animals, the MRI parameter values in ISODATA-defined non-treated tumor tissue at all time points were compared to the parameter values in ISODATA-defined non-viable tumor tissue at 1 h and 72 h after HIFU with a paired Student's t-test. For all tests the level of significance was set at α=0.05.

5.3. Results

5.3.1. MRI parameter maps

Representative MRI parameter maps as measured before, 1 h and 72 h after HIFU treatment are shown in Figure 2.

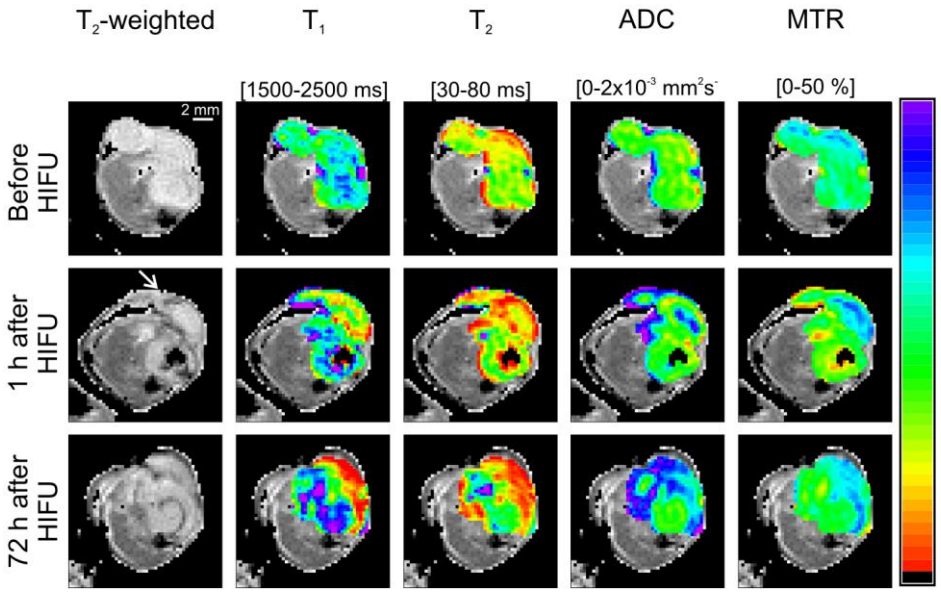

Figure 2. MRI parameter maps before and longitudinally after HIFU treatment. Representative example of multiparametric MRI of the hind limb region of a HIFU-treated tumor-bearing mouse before and 1 h and 72 h after HIFU treatment. T_2-weighted images of an axial slice of the tumor-bearing paw are shown in the left panel. The hyper-intense tumor tissue is surrounded by hypo-intense muscle tissue. In the other panels the same T_2-weighted images are displayed except that the tumor pixels are overlaid with MRI parameter maps. The parameter maps were scaled according to the color scale bar shown at the right-hand side of the figure. The corresponding parameter range for this scale bar is indicated above each panel. The approximate direction of the HIFU treatment is shown by the white arrow on the T_2-weighted image, which was collected 1 h after HIFU treatment.

A heterogeneous appearance of the HIFU-treated lesion was visible on the T_2-weighted images at both time points after HIFU treatment. Distinct regions with decreased T_1 and T_2 were observed at 1 h after HIFU. A further increase in the area of T_1 and T_2 decline was observed in these regions at 72 h after HIFU. Increased ADC and MTR values were observed in roughly the same regions of T_1 and T_2 change, both at 1 h and 72 h after HIFU. However, no sharp demarcation between HIFU-treated and non-treated tumor tissue was visible on the individual MRI parameter maps obtained after HIFU. Tumor regions with altered MRI parameters co-localized only partially for the different parameters. This implied that more advanced analysis of the multiparametric data is necessary to enable MRI-based identification of the HIFU-treated tumor tissue. Therefore, quantitative multiparametric analysis of the MRI parameter changes after HIFU treatment was performed using the ISODATA technique. Clusters resulting from the ISODATA segmentation were classified as either viable or non-viable based on the fraction of pixels assigned to the clusters at the different experimental time points (Figure 1). ISODATA clustering was applied on different combinations of the MRI parameters (*i.e.* feature vectors), to determine the feature vector that led to the most accurate segmentation between viable and non-viable tumor tissue.

5.3.2. Feature vector selection

Selection of the optimal feature vector for the discrimination between HIFU-treated, non-viable and non-treated, viable tumor tissue was performed based on quantitative comparison between non-viable tumor fractions resulting from ISODATA segmentation with different feature vectors and non-viable tumor fractions derived from whole-tumor-based histology.

Plots of the histology-derived non-viable tumor fractions versus the ISODATA-derived non-viable tumor fractions were processed for all assessed feature vectors. The R^2 of the data points to the line of identity, indicative of the level of one-to-one correspondence between the results from ISODATA analysis and histology, was used as an initial criterion for feature vector selection. R^2 values for all assessed feature vectors are listed in Table 1.

Table 1. R^2 values of ISODATA-derived versus histology-derived non-viable tumor fractions to the line of identity for all assessed feature vectors.

Feature vector	R^2 to line of identity [-]
$\{T_2\}$	0.60
{ADC}	0.74
$\{T_1, T_2\}$	0.70
$\{T_2, ADC\}$	0.77
$\{T_1, ADC\}$	0.68
{ADC, MTR}	-1.67
$\{T_1, T_2, ADC\}$	0.77
$\{T_2, ADC, MTR\}$	-0.09
$\{T_1, ADC, MTR\}$	0.42
$\{T_1, T_2, MTR\}$	-0.79
$\{T_1, T_2, ADC, MTR\}$	-0.16

Relatively high R^2 values (>0.7) were observed for three feature vectors: {ADC}, $\{T_2, ADC\}$ and $\{T_1, T_2, ADC\}$, which were therefore considered candidates for the segmentation of HIFU-treated tumor tissue. Scatter plots of the ISODATA-derived and histology-derived non-viable tumor fractions are displayed in Figure 3 for these candidate feature vectors.

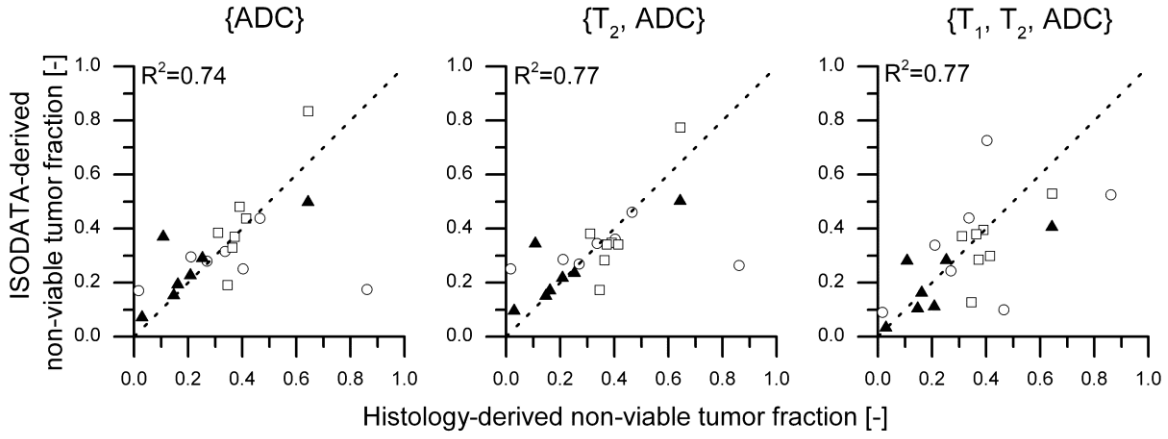

Figure 3. One-to-one correspondence between histology-derived and ISODATA-derived non-viable tumor fractions. Scatter plots of the ISODATA-derived non-viable tumor fractions following segmentation with feature vectors {ADC}, $\{T_2, ADC\}$ and $\{T_1, T_2, ADC\}$ as a function of the histology-derived non-viable tumor fractions. The symbols ○, □ and ▲ indicate groups '1 h after HIFU', '72 h after HIFU' and 'Control', respectively. The line of identity is shown as visual reference. The R^2 values of the data to the line of identity are shown in the top left corner of each plot.

The correlation between the histology-derived and ISODATA-derived non-viable tumor fractions was used as a second criterion for feature vector selection. The experimental groups were divided into two groups for this correlation analysis: '1 h after HIFU + Control' and '72 h after HIFU + Control' (see Methods). Correlation plots for the three candidate feature vectors are depicted in Figure 4 for both groups.

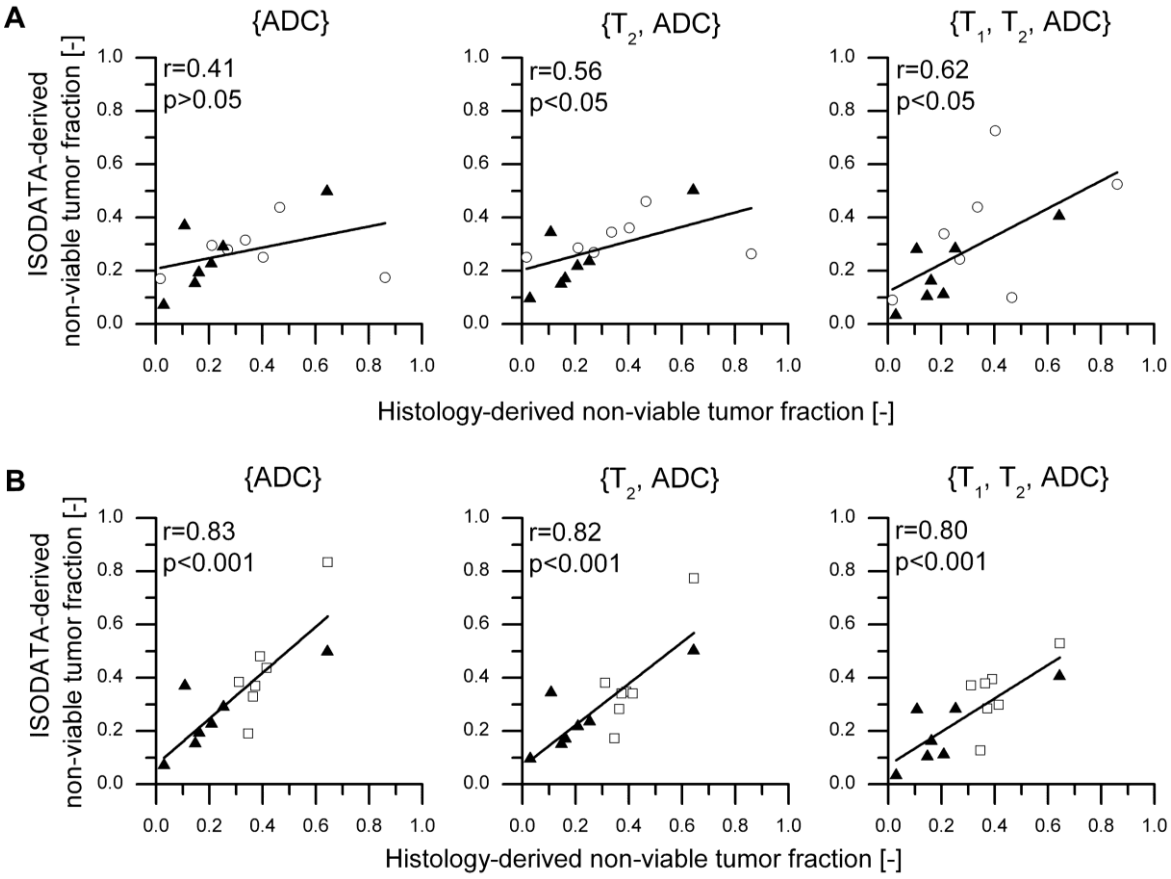

Figure 4. Correlation between histology-derived and ISODATA-derived non-viable tumor fractions. Correlation plots of ISODATA-derived non-viable tumor fractions following segmentation with feature vectors {ADC}, {T_2, ADC} and {T_1, T_2, ADC} as a function of the histology-derived non-viable tumor fractions for two different groups of animals: '1 h after HIFU + Control' (A) and '72 h after HIFU + Control' (B). The symbols ○, □ and ▲indicate groups '1 h after HIFU', '72 h after HIFU' and 'Control', respectively. Correlation values between the ISODATA-derived and the histology-derived tumor fractions are listed in the top left corner of each plot.

For group '1 h after HIFU + Control' the strongest correlation was found for feature vector {T_1, T_2, ADC} (r=0.62, moderate correlation; Figure 4A). However, for this group, no statistically significant differences between the correlation values of the different candidate feature vectors were observed. A strong correlation was observed for all three feature vectors for group '72 h after HIFU + Control' (Figure 4B). The strongest correlation in this case was found for feature vector {ADC} (r=0.83), which was significantly higher than the correlation value found for feature vector {T_1, T_2, ADC} (r=0.80).

The third criterion for feature selection consisted of minimization of the number of pixels incorrectly assigned to non-viable tissue before ablation.

Most notably for the feature vectors {ADC} and {T_2, ADC}, a portion of pixels in the tumor rim was incorrectly assigned to non-viable tissue before HIFU, whereas this was observed to a lesser extent for feature vector {T_1, T_2, ADC}. The incorrect classification of the tumor pixels was caused by presence of peritumoral edema at the tumor rim. Visual inspection during excision of the tumors confirmed presence of edema around the HIFU-treated tumors. The fraction of rim pixels (rim thickness of 3 pixels) that was incorrectly assigned as non-viable before HIFU application was therefore used as a further selection measure. The fractions of incorrectly assigned rim pixels were significantly lower for feature vector {T_1, T_2, ADC} (0.15±0.09) as compared to feature vectors {ADC} and {T_2, ADC} (0.28±0.10 and 0.25±0.08, respectively).

Based on the above three criteria, feature vector {T_1, T_2, ADC} provided the optimal combination of MRI parameters for differentiation between HIFU-treated and non-treated tumor tissue.

5.3.3. Evaluation of MRI parameter changes

In Figure 5A representative results of the ISODATA segmentation with feature vector {T_1, T_2, ADC} are displayed for two HIFU-treated animals.

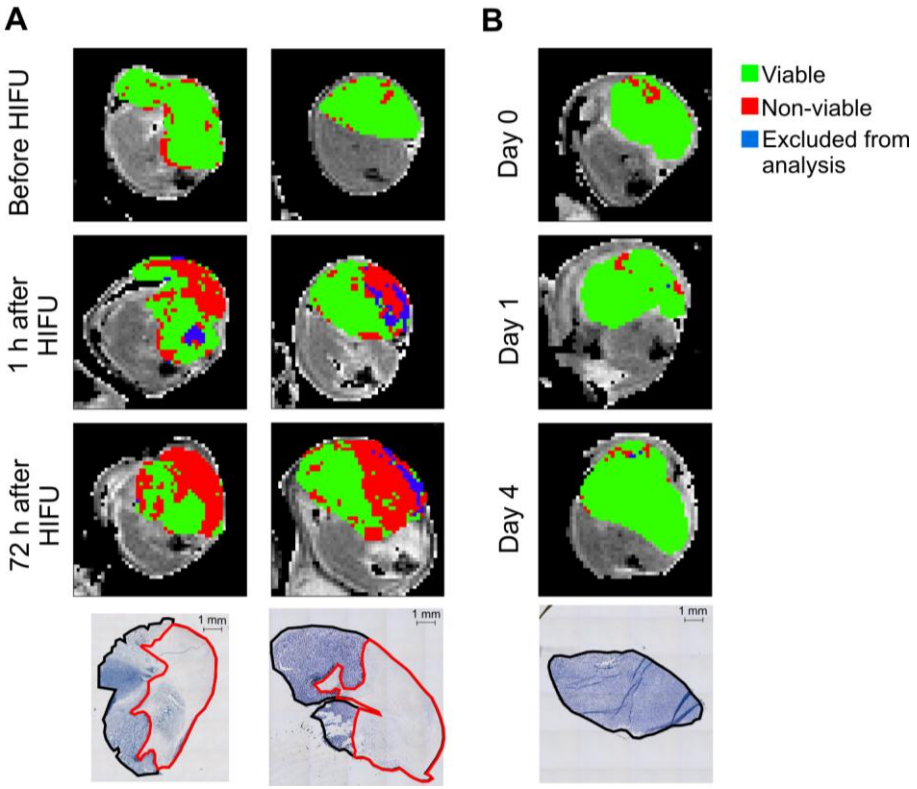

Figure 5. Visual correspondence between ISODATA-derived and histology-derived non-viable tumor areas. A) Representative T_2-weighted images of the hind limb region of two HIFU-treated mice before, 1 h after and 72 h after HIFU. The results of ISODATA segmentation with feature vector {T_1, T_2, ADC} are overlaid on the tumor pixels. NADH-diaphorase stained sections of tumors dissected at 72 h after HIFU were made at approximately the same location within the tumor and are shown at the bottom of each column. ROIs around the entire (black line) and non-viable (red line) tumor tissue were drawn manually. Data in the left column are from the animal presented in Figure 2. B) Similar data of a non-treated control mouse that was subjected to serial MRI measurements at the same time points (Day 0, Day 1 and Day 4) as the HIFU-treated animals. Scale bar = 1 mm.

As anticipated, at baseline the largest fraction of pixels (0.85±0.10 for all HIFU-treated animals) was assigned to viable tumor tissue. At 1 h after HIFU a region emerged in which pixels were assigned to HIFU-treated, *i.e.* non-viable tumor tissue. At 72 h after HIFU this region had grown and showed good spatial agreement with a region of non-viable tumor tissue on an NADH-diaphorase stained section at approximately the same location within the tumor. A 3D reconstruction of the ISODATA segmentation of the tumor displayed in the right panel of Figure 5A at 72 h after HIFU can be seen in the supporting content (Supporting Movie S1). This 3D reconstruction was processed by interpolation of the tumor pixel data resulting from the ISODATA segmentation. The reconstruction shows a distinct, contiguous non-viable, HIFU-treated tumor volume surrounded by viable tumor tissue. In comparison, Figure 5B shows representative results of ISODATA segmentation of a non-treated control animal that was subjected to MRI examination at the same time points. Here only a small number of pixels was assigned to non-viable tumor tissue at all time points, in agreement with a fully viable tumor observed by NADH-diaphorase staining.

Average MRI parameter values of ISODATA-defined viable tumor tissue at all experimental time points and non-viable tumor tissue at both time points after HIFU are listed in Table 2 for feature vector $\{T_1, T_2, ADC\}$.

Table 2. Mean MRI parameter values in ISODATA-defined viable and non-viable tumor tissue. MRI parameter values (mean±SD) in viable tumor tissue (tumor tissue assigned as viable tumor tissue at all time points (n=14)), non-viable tumor tissue at 1 h after HIFU (n=14) and non-viable tumor tissue at 72 h after HIFU (n=7) of the HIFU-treated animals following ISODATA segmentation with feature vector $\{T_1, T_2, ADC\}$. * and ** denote a significant difference between viable and non-viable tumor tissue with $p<0.05$ and $p<0.001$, respectively (paired Student's t-test).

MRI parameter	Viable tumor tissue	Non-viable tumor tissue 1 h after HIFU	Non-viable tumor tissue 72 h after HIFU
R_1 [s^{-1}]	0.45±0.01	0.61±0.13 **	0.60±0.06 **
R_2 [s^{-1}]	21.7±1.4	35.8±19.5 **	34.0±21.0
ADC [10^{-3} mm^2s^{-1}]	0.84±0.12	1.09±0.20 **	1.25±0.16 **
MTR [%]	23.3±1.2	26.4±2.7 **	26.4±3.5 *

R_1 ($1/T_1$), R_2 ($1/T_2$), ADC and MTR were significantly increased in the non-viable, HIFU-treated tumor tissue 1 h after HIFU compared to viable tumor tissue. R_1, ADC and MTR remained significantly increased in non-viable tumor tissue 72 h after HIFU. No significant differences in parameter values were observed between 1 h and 72 h after HIFU treatment.

5.4. Discussion and Conclusions

In the present study multiparametric MR analysis was performed to distinguish non-viable, HIFU-treated tumor tissue from viable, non-treated tumor tissue in a murine tumor model. The longitudinal multiparametric MRI measurements consisted of quantitative assessments of T_1, T_2, ADC and MTR. ISODATA segmentation was applied on various feature vectors. ISODATA-derived non-viable tumor volume fractions were compared to non-viable tumor fractions derived from quantitative histology to identify the optimal feature vector for differentiation between non-viable, HIFU-treated and viable, non-treated tumor tissue.

The most accurate distinction between HIFU-treated and non-treated tumor tissue was obtained with feature vector {T_1, T_2, ADC}. For this feature vector, the correlation between the histology-derived and ISODATA-derived fractions of non-viable tumor tissue was lower for group '1 h after HIFU + Control' than for group '72 h after HIFU + Control'. These results suggest that time is needed before HIFU-induced changes in the tumor tissue produce sufficient detectable contrast in the MRI images.

A multiparametric protocol consisting of T_1, T_2 and ADC mapping was sufficient to segment HIFU-treated and non-treated tumor tissue. Inclusion of MTR to the protocol led to less agreement of the ISODATA segmentation with the histological analysis. Nevertheless, a significant increase in MTR was observed in the non-viable tumor tissue identified from ISODATA analysis with feature vector {T_1, T_2, ADC} (Table 2). However, since this increase was only subtle, clustering with inclusion of MTR led to merging of clusters of non-viable and viable tumor tissue, resulting in a lower specificity and sensitivity of the cluster method.

ISODATA clustering with feature vector {T_1, T_2, ADC} yielded 31 different clusters (Figure 1), which indicated a large heterogeneity of the HIFU-treated tumor tissue. Extensive analysis of each cluster separately would yield additional information about the status of the different segmented tissue populations. However, the focus of this study was the binary distinction between non-viable, HIFU-treated and viable, non-treated tumor tissue. Therefore, it was decided to allocate the clusters resulting from ISODATA segmentation to two distinct classes, designated as non-viable and viable. A cluster was assigned to the non-viable class if the fraction of pixels within the cluster significantly increased by HIFU treatment. This criterion could however also be met if the cluster is associated with reversible HIFU-induced tissue changes instead of with non-viable tumor tissue. Nevertheless, since a high one-to-one correspondence between histology-derived and ISODATA-derived non-viable tumor fractions was observed for the optimal feature vector {T_1, T_2, ADC}, it seems reasonable to assume that the majority of the non-viable clusters for that feature vector indeed represents non-viable tumor tissue.
A minor part of the tumor pixels after HIFU treatment (fractions of 0.05±0.03 and 0.02±0.02 of the entire tumor tissue at 1 h and 72 h after HIFU, respectively) needed to be excluded from the multiparametric MR analysis, because the signal intensity of these tumor pixels was at noise level in the T_2-weighted images (see Methods). This

low signal intensity was most likely caused by HIFU-induced hemorrhage. Exclusion of these hemorrhage-associated pixels from the analysis did not influence the correlation results presented here, because it only involved a very low fraction of tumor pixels.

A reconstruction of the ISODATA segmentation results was made to visualize the HIFU-treated volume in 3D space (Supporting Movie S1). A similar reconstruction of the histological data and registration of these data with the MRI findings would allow for analysis of the spatial correlation between the ISODATA-segmented and histology-based non-viable volumes. However, 3D reconstruction of histological tumor sections was not performed in the present study. Accurate 3D histological reconstruction and its registration with MRI would have required an intermediate MRI scan after tumor excision, a robust anatomical reference and denser histological sampling (32). Additionally, spatial correlation of histology with MRI would require a higher spatial resolution of the MR images. This would lead to a substantially longer acquisition time of the multiparametric MR protocol and result in unacceptably long anesthesia times for the animals.

Instead of assessment of spatial correlation, the ISODATA analysis method was optimized based on the correlation between histology-derived and ISODATA-derived non-viable tumor fractions for different feature vectors. A similar correlation analysis has been performed for the detection of necrotic tumor tissue after radiotherapy, which yielded comparably strong correlations between clustering and histology (33), showing that this global correlation analysis is suitable for the optimization of clustering methods. For the optimized feature vector $\{T_1, T_2, ADC\}$, a strong spatial agreement between the region of ISODATA-derived non-viable tumor tissue and the region of non-viable tumor tissue on NADH-diaphorase-stained histological sections (Figure 5) was observed visually, which indicates that the proposed methodology allows for accurate segmentation of HIFU-treated, non-viable tumor tissue.

Mean MRI parameter values were determined in non-viable and viable tumor tissue following ISODATA segmentation with feature vector $\{T_1, T_2, ADC\}$ (Table 2). R_1 was significantly increased in the non-viable, HIFU-treated tumor tissue both at 1 h and 72 h after HIFU as compared to viable, non-treated tumor tissue. Such increased R_1 (or decreased T_1) was previously also observed ex vivo in (non-cancerous) tissues after heat treatment (34), which was explained by a combination of coagulation of the blood volume fraction and disruption of biological barriers, which facilitates access of water molecules to paramagnetic sites in the coagulated blood. Decreased T_1 was also observed as a result of tissue necrosis after chemotherapy (35).
Graham et al. observed an increase in T_2 after heating of ex vivo tissue, which was explained as vacuolization of water molecules caused by increased hydrophobic interactions induced by protein denaturation (34). We observed significantly increased R_2 (and thus decreased T_2) in non-viable tumor tissue 1 h after HIFU treatment, whereas at 72 h after HIFU treatment no significant R_2 differences between non-viable and viable tumor tissue were observed. This initially decreased T_2 could be explained by the aforementioned increased access of water molecules to paramagnetic centers in the coagulated blood. Furthermore, the large standard deviation of R_2 in the non-

viable, HIFU-treated tumor tissue (Table 2) indicated large T_2 heterogeneity due to the presence of areas with increased and decreased T_2.
The observed increased ADC values in the non-viable tumor tissue have been described earlier ex vivo in thermally treated tissue samples (34) and in vivo in preclinical experiments on the effects of HIFU treatment in a murine tumor model (36) and in clinical studies of RF ablation of liver lesions (19). Diffusion of water molecules could have been facilitated by HIFU-induced disruption of obstructing barriers, leading to an increased ADC.
Reports on the effects of thermal treatment on the MTR are conflicting. Both a decreased (34) and increased (23) MTR have been observed in ex vivo thermally treated samples. An MTR decrease could be explained by denaturation of structural proteins (34), whereas an increase might be caused by increased access of water molecules to macromolecules due to disruption of barriers. Furthermore, T_1 effects may play a role, since the MTR is known to be affected by tissue T_1 (37). In the current study, a combination of these factors has probably influenced the observed MTR, which is also illustrated by the subtle yet significant increase in MTR in the non-viable, HIFU-treated tumor tissue compared to viable tumor tissue.

The HIFU treatment was performed outside the MR system, since the preclinical therapeutic ultrasound transducer is not (yet) MRI-compatible. In an MRI-guided HIFU set-up, results from the multiparametric MR analysis could be quantitatively compared to thermal dose maps derived from MR thermometry during HIFU treatment. Furthermore, the MRI examinations before and directly after HIFU could then be combined within the same anesthesia period. This was not feasible in this study, since the ablation procedure was rather lengthy for the current set-up (~1 hour) and the subject would have to be positioned in the MR system twice. Nevertheless, no significant differences in MRI parameters were observed between the measurements of the control animals at Day 0 and Day 1, corresponding in time with the measurements of the HIFU-treated animals before and at 1 h after HIFU. This indicated that the time between the examinations before and after HIFU did not influence the results presented here.

A murine tumor model was used to assess the effects of HIFU treatment on tumor tissue status. The CT26 colon carcinoma was chosen because previous studies have shown that subcutaneous inoculations of CT26 cell suspensions lead to well-vascularized tumors (38) with limited necrosis (39). This is beneficial for the current study, because extensive natural necrosis could mask the effects of HIFU-induced necrosis. However, the method is not restricted to this tumor model, since similar approaches, consisting of multispectral MR imaging combined with cluster analysis, have been employed for the identification of viable and non-viable tissue after chemotherapy (40) and radiotherapy (33) in other preclinical tumor models.
Clinical translation of the multiparametric protocol is feasible, since MR sequences for acquisition of the proposed MRI parameters, T_1, T_2 and ADC, are already clinically available. The total acquisition time of the multi-slice T_1, T_2 and ADC protocol was approximately 25 minutes. Further reduction of the measurement time would facilitate inclusion of the multiparametric MR measurements in clinical HIFU treatment

protocols. The MR parameter mapping acquisitions could be accelerated by for example rapid imaging techniques, such as parallel imaging and compressed sensing. Prior to clinical introduction of the proposed multiparametric MR analysis, it would be necessary to further confirm that the ISODATA-derived non-viable tumor tissue spatially corresponds to non-viable tumor tissue in histology. This could for example be achieved by image-guided biopsies from the ISODATA-derived viable and non-viable tumor tissue. Since clinical trials on HIFU treatment of malignant tumors generally use treat-and-resect protocols (41), it would be feasible to include image-guided biopsies in the workflow of these studies. Such extensive validation should be performed in different tumor subtypes to assess the full clinical potential of the proposed methodology.

In summary, we have shown that non-viable, HIFU-treated tumor tissue could be distinguished from non-treated tumor tissue using quantitative multiparametric MRI combined with the ISODATA clustering technique. Clustering with feature vector {T_1, T_2, ADC} yielded a strong correlation between ISODATA-derived and histology-derived non-viable tumor fractions. The presented methodology not only offers clear insights in the HIFU-induced changes in MRI parameters, but could also ultimately be made suitable for clinical application and might offer the unique possibility to automatically detect residual or recurring tumor tissue after HIFU treatment in an objective manner. Furthermore, since the proposed MRI analysis is solely based on endogenous contrast, immediate retreatment is possible when residual or recurring tumor tissue is detected, without the risk of inaccurate temperature mapping due to presence of a Gd-based contrast agent.

5.5. Acknowledgements

The authors thank Ralf Seip from Philips Research for his advice on the HIFU treatment settings. Furthermore, the authors want to acknowledge Holger Grüll from Eindhoven University of Technology and Philips Research for useful discussions.

5.6. References

1. Kennedy JE. High-intensity focused ultrasound in the treatment of solid tumours. Nat Rev Cancer 2005;5(4):321-327.
2. ter Haar G. Therapeutic applications of ultrasound. Prog Biophys Mol Biol 2007;93(1-3):111-129.
3. Hesley GK, Gorny KR, Woodrum DA. MR-guided focused ultrasound for the treatment of uterine fibroids. Cardiovasc Intervent Radiol 2013;36(1):5-13.
4. Voogt MJ, Trillaud H, Kim YS, Mali WP, Barkhausen J, Bartels LW, Deckers R, Frulio N, Rhim H, Lim HK, Eckey T, Nieminen HJ, Mougenot C, Keserci B, Soini J, Vaara T, Kohler MO, Sokka S, van den Bosch MA. Volumetric feedback ablation of uterine fibroids using magnetic resonance-guided high intensity focused ultrasound therapy. Eur Radiol 2012;22(2):411-417.
5. Murat FJ, Poissonnier L, Pasticier G, Gelet A. High-intensity focused ultrasound (HIFU) for prostate cancer. Cancer Control 2007;14(3):244-249.

6. Rouviere O, Girouin N, Glas L, Ben Cheikh A, Gelet A, Mege-Lechevallier F, Rabilloud M, Chapelon JY, Lyonnet D. Prostate cancer transrectal HIFU ablation: detection of local recurrences using T2-weighted and dynamic contrast-enhanced MRI. Eur Radiol 2010;20(1):48-55.
7. Kirkham AP, Emberton M, Hoh IM, Illing RO, Freeman AA, Allen C. MR imaging of prostate after treatment with high-intensity focused ultrasound. Radiology 2008;246(3):833-844.
8. Schmitz AC, Gianfelice D, Daniel BL, Mali WP, van den Bosch MA. Image-guided focused ultrasound ablation of breast cancer: current status, challenges, and future directions. Eur Radiol 2008;18(7):1431-1441.
9. Leslie TA, Kennedy JE, Illing RO, Ter Haar GR, Wu F, Phillips RR, Friend PJ, Roberts IS, Cranston DW, Middleton MR. High-intensity focused ultrasound ablation of liver tumours: can radiological assessment predict the histological response? Br J Radiol 2008;81(967):564-571.
10. Leslie T, Ritchie R, Illing R, Ter Haar G, Phillips R, Middleton M, Bch B, Wu F, Cranston D. High-intensity focused ultrasound treatment of liver tumours: post-treatment MRI correlates well with intra-operative estimates of treatment volume. Br J Radiol 2012;85(1018):1363-1370.
11. Hynynen K. MRI-guided focused ultrasound treatments. Ultrasonics 2010;50(2):221-229.
12. Rieke V, Butts Pauly K. MR thermometry. J Magn Reson Imaging 2008;27(2):376-390.
13. Yarmolenko PS, Moon EJ, Landon C, Manzoor A, Hochman DW, Viglianti BL, Dewhirst MW. Thresholds for thermal damage to normal tissues: an update. Int J Hyperthermia 2011;27(4):320-343.
14. Wijlemans JW, Deckers R, van den Bosch MA, Seinstra BA, van Stralen M, van Diest PJ, Moonen CT, Bartels LW. Evolution of the ablation region after magnetic resonance-guided high-intensity focused ultrasound ablation in a Vx2 tumor model. Invest Radiol 2013;48(6):381-386.
15. Dewhirst MW, Viglianti BL, Lora-Michiels M, Hanson M, Hoopes PJ. Basic principles of thermal dosimetry and thermal thresholds for tissue damage from hyperthermia. Int J Hyperthermia 2003;19(3):267-294.
16. Merkle EM, Nour SG, Lewin JS. MR imaging follow-up after percutaneous radiofrequency ablation of renal cell carcinoma: findings in 18 patients during first 6 months. Radiology 2005;235(3):1065-1071.
17. Dromain C, de Baere T, Elias D, Kuoch V, Ducreux M, Boige V, Petrow P, Roche A, Sigal R. Hepatic tumors treated with percutaneous radio-frequency ablation: CT and MR imaging follow-up. Radiology 2002;223(1):255-262.
18. Hijnen NM, Elevelt A, Pikkemaat J, Bos C, Bartels LW, Grull H. The magnetic susceptibility effect of gadolinium-based contrast agents on PRFS-based MR thermometry during thermal interventions. J Ther Ultrasound 2013;1:8.
19. Zhang Y, Zhao J, Guo D, Zhong W, Ran L. Evaluation of short-term response of high intensity focused ultrasound ablation for primary hepatic carcinoma: utility of contrast-enhanced MRI and diffusion-weighted imaging. Eur J Radiol 2011;79(3):347-352.

20. Jacobs MA, Ouwerkerk R, Kamel I, Bottomley PA, Bluemke DA, Kim HS. Proton, diffusion-weighted imaging, and sodium (23Na) MRI of uterine leiomyomata after MR-guided high-intensity focused ultrasound: a preliminary study. J Magn Reson Imaging 2009;29(3):649-656.
21. Pilatou MC, Stewart EA, Maier SE, Fennessy FM, Hynynen K, Tempany CM, McDannold N. MRI-based thermal dosimetry and diffusion-weighted imaging of MRI-guided focused ultrasound thermal ablation of uterine fibroids. J Magn Reson Imaging 2009;29(2):404-411.
22. Wolff SD, Balaban RS. Magnetization transfer imaging: practical aspects and clinical applications. Radiology 1994;192(3):593-599.
23. Peng HH, Huang TY, Tseng WY, Lin EL, Chung HW, Wu CC, Wang YS, Chen WS. Simultaneous temperature and magnetization transfer (MT) monitoring during high-intensity focused ultrasound (HIFU) treatment: preliminary investigation on ex vivo porcine muscle. J Magn Reson Imaging 2009;30(3):596-605.
24. Rouviere O, Gelet A, Crouzet S, Chapelon JY. Prostate focused ultrasound focal therapy--imaging for the future. Nat Rev Clin Oncol 2012;9(12):721-727.
25. Jacobs MA, Knight RA, Soltanian-Zadeh H, Zheng ZG, Goussev AV, Peck DJ, Windham JP, Chopp M. Unsupervised segmentation of multiparameter MRI in experimental cerebral ischemia with comparison to T2, diffusion, and ADC MRI parameters and histopathological validation. J Magn Reson Imaging 2000;11(4):425-437.
26. Seip R, Chin CT, Hall CS, Raju BI, Ghanem A, Tiemann K. Targeted ultrasound-mediated delivery of nanoparticles: on the development of a new HIFU-based therapy and imaging device. IEEE Trans Biomed Eng 2010;57(1):61-70.
27. Levitt MH, Freeman R. Compensation for Pulse Imperfections in Nmr Spin-Echo Experiments. J Magn Reson 1981;43(1):65-80.
28. Karlsson M, Nordell B. Phantom and in vivo study of the Look-Locher T1 mapping method. Magn Reson Imaging 1999;17(10):1481-1488.
29. Omran MGH, Engelbrecht AP, Salman A. An overview of clustering methods. Intelligent Data Analysis 2007;11(6):583-605.
30. Hijnen NM, Heijman E, Kohler MO, Ylihautala M, Ehnholm GJ, Simonetti AW, Grull H. Tumour hyperthermia and ablation in rats using a clinical MR-HIFU system equipped with a dedicated small animal set-up. Int J Hyperthermia 2012;28(2):141-155.
31. Wolfe DA. On testing equality of related correlation coefficients. Biometrica 1976;63:214-215.
32. Alic L, Haeck JC, Bol K, Klein S, van Tiel ST, Wielepolski PA, de Jong M, Niessen WJ, Bernsen M, Veenland JF. Facilitating tumor functional assessment by spatially relating 3D tumor histology and in vivo MRI: image registration approach. PLoS One 2011;6(8):e22835.
33. Henning EC, Azuma C, Sotak CH, Helmer KG. Multispectral quantification of tissue types in a RIF-1 tumor model with histological validation. Part I. Magn Reson Med 2007;57(3):501-512.
34. Graham SJ, Stanisz GJ, Kecojevic A, Bronskill MJ, Henkelman RM. Analysis of changes in MR properties of tissues after heat treatment. Magn Reson Med 1999;42(6):1061-1071.

35. McSheehy PM, Weidensteiner C, Cannet C, Ferretti S, Laurent D, Ruetz S, Stumm M, Allegrini PR. Quantified tumor t1 is a generic early-response imaging biomarker for chemotherapy reflecting cell viability. Clin Cancer Res 2010;16(1):212-225.
36. Hundt W, Yuh EL, Steinbach S, Bednarski MD. Effect of continuous high intensity focused ultrasound in a squamous cell carcinoma tumor model compared to muscle tissue evaluated by MRI, histology, and gene expression. Technol Cancer Res Treat 2009;8(2):85-98.
37. Henkelman RM, Stanisz GJ, Graham SJ. Magnetization transfer in MRI: a review. NMR Biomed 2001;14(2):57-64.
38. Ogawara K, Un K, Minato K, Tanaka K, Higaki K, Kimura T. Determinants for in vivo anti-tumor effects of PEG liposomal doxorubicin: importance of vascular permeability within tumors. Int J Pharm 2008;359(1-2):234-240.
39. Aulino P, Berardi E, Cardillo VM, Rizzuto E, Perniconi B, Ramina C, Padula F, Spugnini EP, Baldi A, Faiola F, Adamo S, Coletti D. Molecular, cellular and physiological characterization of the cancer cachexia-inducing C26 colon carcinoma in mouse. BMC Cancer 2010;10:363.
40. Carano RA, Ross AL, Ross J, Williams SP, Koeppen H, Schwall RH, Van Bruggen N. Quantification of tumor tissue populations by multispectral analysis. Magn Reson Med 2004;51(3):542-551.
41. Merckel LG, Bartels LW, Kohler MO, van den Bongard HJ, Deckers R, Mali WP, Binkert CA, Moonen CT, Gilhuijs KG, van den Bosch MA. MR-guided high-intensity focused ultrasound ablation of breast cancer with a dedicated breast platform. Cardiovasc Intervent Radiol 2013;36(2):292-301.

Supporting Information

Supporting Information S1.
Theory: the ISODATA clustering algorithm.

The ISODATA clustering described in the manuscript was performed with different feature vectors, consisting of either 1, 2, 3 or all 4 (T_1, T_2, ADC and MTR) MR contrast parameters. Extensive details of the ISODATA clustering algorithm can be found in the original paper by Jacobs et al. (1). A brief theoretical description of the concepts of the clustering algorithm is given below.
If the clustering would be performed with a feature vector consisting of for example three parameters, the values in the tumor pixels can be represented in a 3D space, as schematically shown below, in which each black spot represents a single tumor pixel. To explain the ISODATA concept and for reasons of clarity, the clustering steps described in the figures below were performed on simulated data describing a limited number of well-separated clusters. The actual tumor data yielded typically 20-40 clusters, which would make the figures unclear.

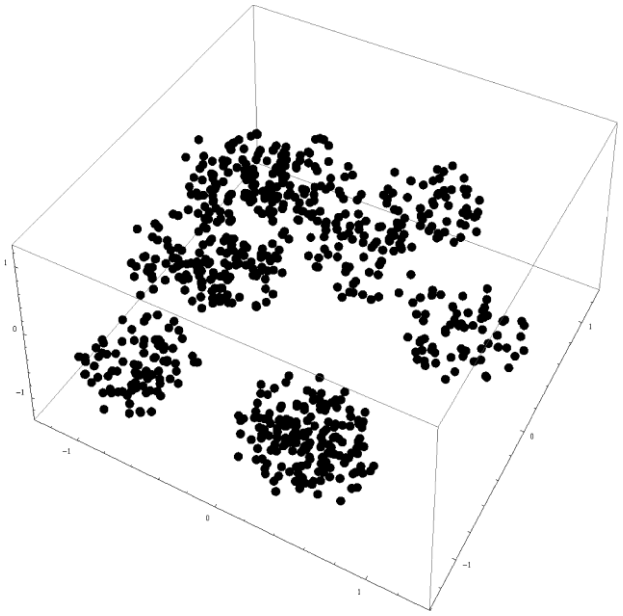

As the first step in the algorithm, an initial number of clusters is defined. In this example the initial number of clusters was set to 8. Cluster centroids (red spots below) are randomly defined for each cluster.

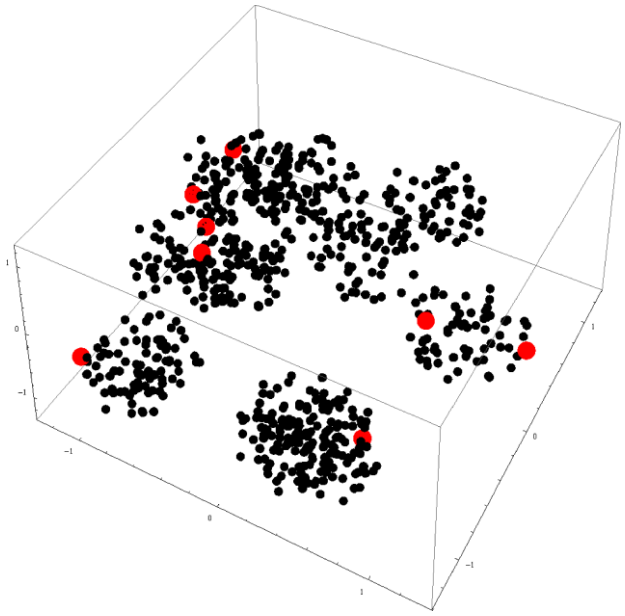

Next, pixels are assigned to the cluster of which the centroid is closest to the parameter values of the pixel. The different clusters that are the results of this step in the process are given by the different colors.

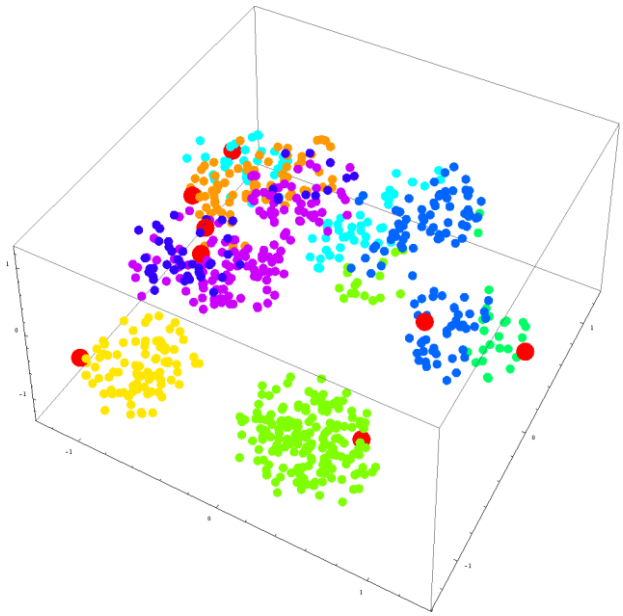

Subsequently, the centroids of each cluster are re-calculated. Clusters are split into two separate clusters, if the intra-Euclidean distances between the pixel vectors and the centroid of each cluster are larger than a pre-defined threshold. These intra-Euclidean distances are a measure of the spread within a certain cluster. Furthermore, pairs of clusters are merged into one cluster if the inter-Euclidean distance between the two cluster centroids is smaller than a pre-defined threshold, which means that the clusters are close to each other. In the example, the dark-blue and purple clusters were merged in this step, as can be seen below.

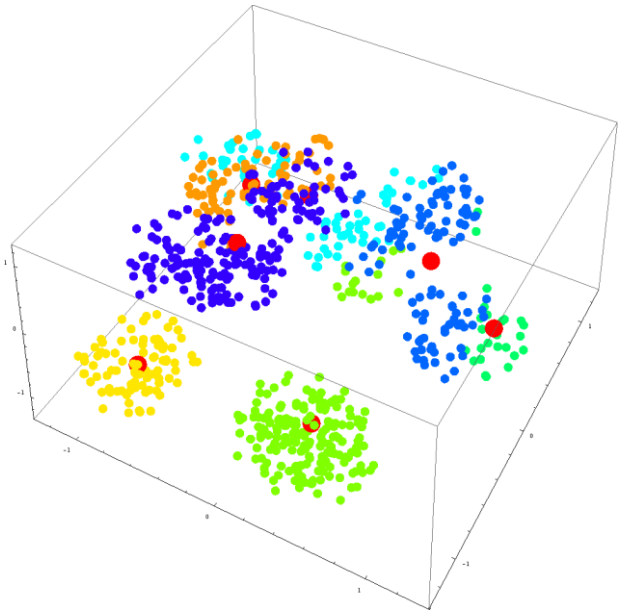

The previous step is repeated until convergence of the algorithm is reached. The algorithm is converged if the objective function (1) has not changed between subsequent iterations, which means that no alterations in the composition of the clusters occurred in the last iteration.

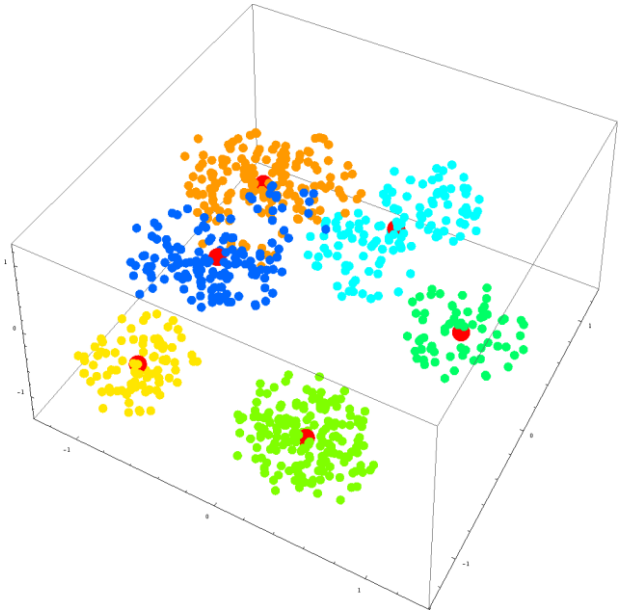

1. Jacobs MA, Knight RA, Soltanian-Zadeh H, Zheng ZG, Goussev AV, et al. (2000). Unsupervised segmentation of multiparameter MRI in experimental cerebral ischemia with comparison to T2, diffusion, and ADC MRI parameters and histopathological validation. J Magn Reson Imaging 11: 425-437.

Supporting Figures

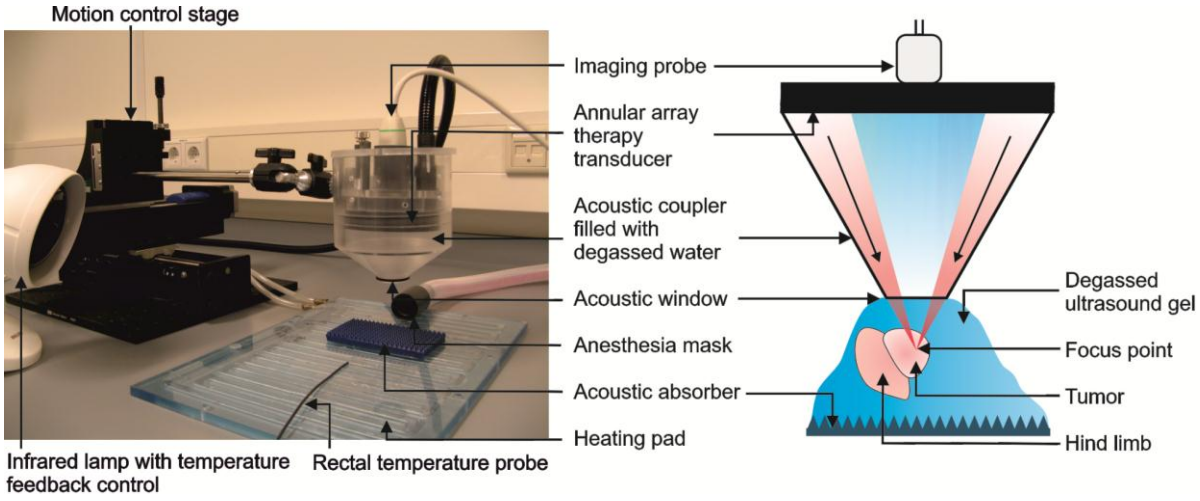

Supporting Figure S1. HIFU set-up. Left: Photograph of the HIFU set-up. The animal was positioned underneath the acoustic coupler. Animal temperature was maintained with an infrared lamp with temperature feedback control from a rectal temperature probe. The motion control stage allowed for accurate movement of the therapy transducer between the pre-defined treatment points. Right: Schematic drawing of the HIFU set-up, showing positioning of the tumor tissue in the focus point of the therapy transducer. The surrounding hind limb tissue was positioned outside the focal zone.

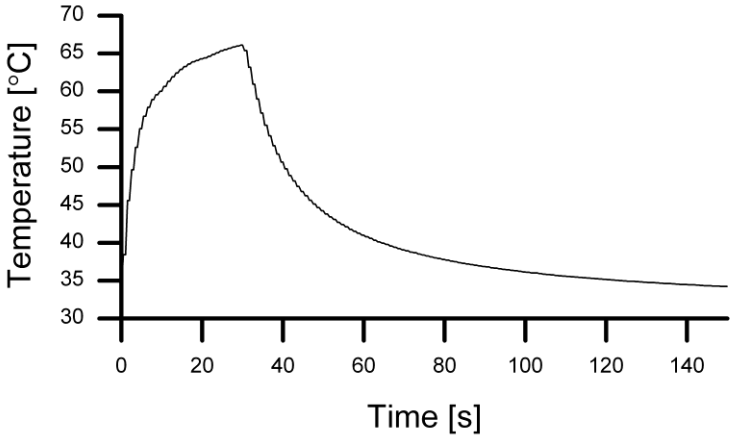

Supporting Figure S2. Temperature profile. Typical example of a temperature profile during HIFU treatment. The tumor tissue temperature increased to 66 °C during the sonication of 30 seconds, followed by cooling of the tissue to pre-sonication temperature during the wait time of 120 seconds. The temperature information was acquired by a thermocouple, which was inserted into the tumor tissue during the pilot experiments. The focal point of the therapeutic transducer co-localized with the tip of the thermocouple. This co-localization was verified by multiple low-power sonications around the expected thermocouple position. The exact thermocouple position was determined as the position at which the highest temperature increase was observed during the sonication.

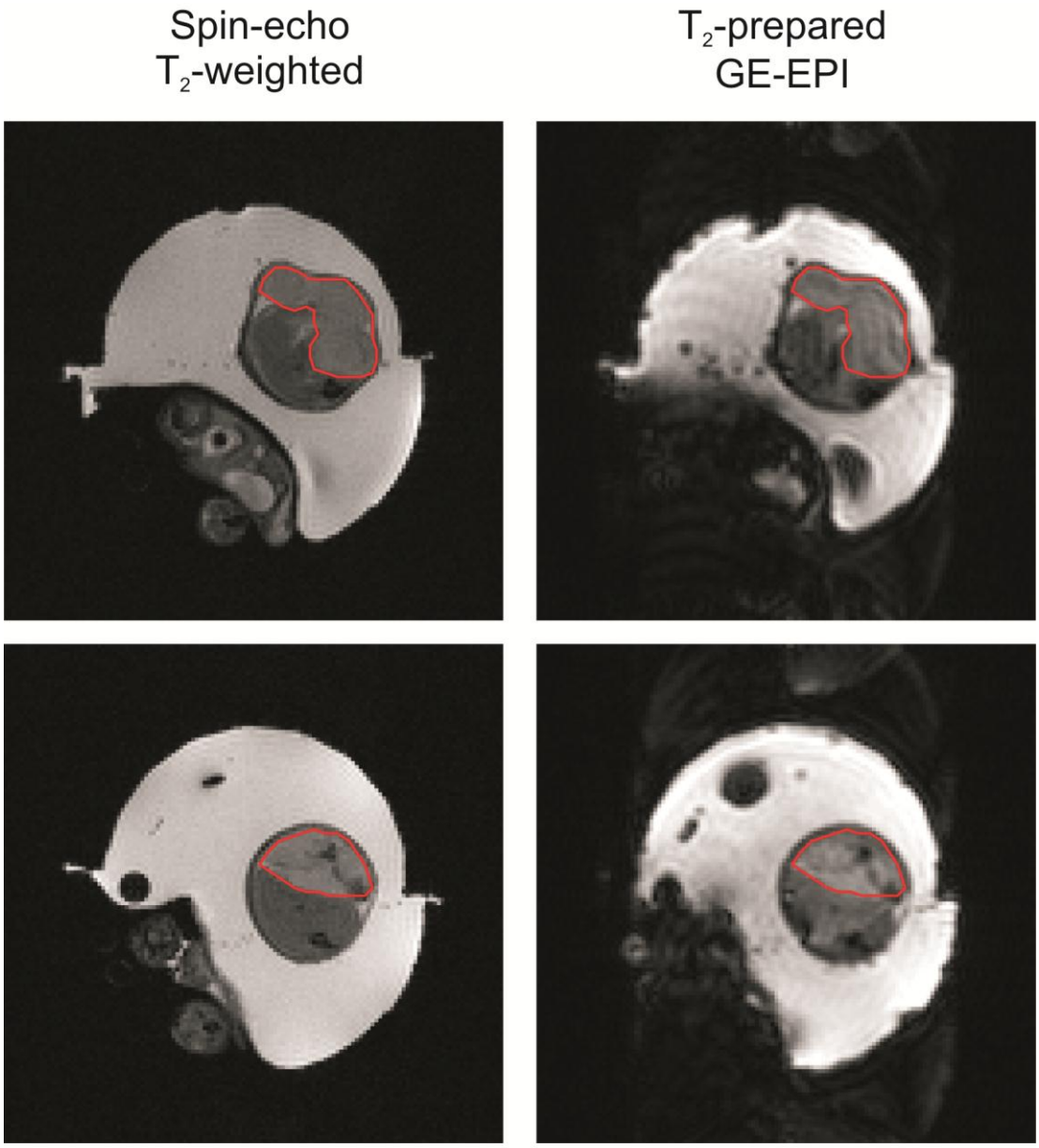

Supporting Figure S3. EPI image quality. Two representative examples of conventional T_2-weighted spin-echo images (left column of panels) and T_2-prepared GE-EPI images (right column of panels). The effective echo times are similar for both images (30 ms for the conventional T_2-weighted images; 28 ms for the T_2-prepared GE-EPI images). Regions of interest (ROIs) of the tumor tissue are indicated with the red lines, showing absence of apparent geometric distortion within the tumor tissue in the EPI images.

Chapter 6

Cluster analysis of DCE-MRI data identifies regional tracer-kinetic changes after tumor treatment with High Intensity Focused Ultrasound

Igor Jacobs[1,*], Stefanie JCG Hectors[1,*], Matthias C Schabel[2,3], Holger Grüll[1,4], Gustav J Strijkers[1,5], Klaas Nicolay[1]

[1] Biomedical NMR, Department of Biomedical Engineering, Eindhoven University of Technology, Eindhoven, The Netherlands
[2] Advanced Imaging Research Center, Oregon Health & Science University, Portland, Oregon, USA
[3] Utah Center for Advanced Imaging Research, University of Utah, Salt Lake City, Utah, USA
[4] Oncology solutions, Philips Research, Eindhoven, The Netherlands
[5] Biomedical Engineering and Physics, Academic Medical Center, University of Amsterdam, Amsterdam, The Netherlands

* These authors contributed equally to this work.

Submitted

Abstract

Evaluation of High Intensity Focused Ultrasound (HIFU) treatment with MRI is generally based on assessment of the non-perfused volume from contrast-enhanced T_1-weighted images. However, the vascular status of tissue surrounding the non-perfused volume has not been extensively investigated with MRI. In this study, cluster analysis of the transfer constant K^{trans} and extravascular extracellular volume fraction v_e, derived from dynamic contrast-enhanced MRI (DCE-MRI) data, was performed in tumor tissue surrounding the non-perfused volume to identify tumor subregions with distinct contrast agent uptake-kinetics.

DCE-MRI was performed in CT26.WT colon carcinoma-bearing Balb/c mice before (n=12), directly after (n=12) and 3 days after (n=6) partial tumor treatment with HIFU. In addition, a non-treated control group (n=6) was included. The non-perfused volume was identified based on the level of contrast enhancement. Quantitative comparison between non-perfused tumor fractions and non-viable tumor fractions derived from NADH-diaphorase histology showed a stronger agreement between these fractions at 3 days after treatment (R^2 to line of identity=0.91), compared to directly after treatment (R^2=0.74). Next, k-means clustering with 4 clusters was applied on K^{trans} and v_e parameter values of all significantly enhanced pixels. The fraction of pixels within two clusters, characterized by a low K^{trans} and either a low or high v_e, significantly increased after HIFU. Changes in composition of these clusters were considered to be HIFU-induced. Qualitative haematoxylin and eosin (H&E) histology showed that HIFU-induced alterations in these clusters may be associated with hemorrhage and structural tissue disruption. Combined microvasculature and hypoxia staining suggested that these tissue changes may affect blood vessel functionality and thereby tumor oxygenation.

In conclusion, it was demonstrated that, in addition to assessment of the non-perfused tumor volume, the presented methodology gives further insight in HIFU-induced effects on tumor vascular status. This method may aid in assessment of the consequences of vascular alterations for the fate of the tissue.

6.1. Introduction

High Intensity Focused Ultrasound (HIFU) is an emerging technique for the non-invasive thermal treatment of tumors. While routine clinical use of HIFU treatment is mainly restricted to noncancerous growths, such as uterine fibroids (1-3), its application range is now being extended to malignant tumors, such as breast (4,5), prostate (6-9) and liver cancer (10-12). Ultrasound-guided and magnetic resonance imaging-guided HIFU (MR-HIFU) systems have been developed that provide spatial guidance of the treatment (13-16). In addition, an MR-HIFU system facilitates treatment monitoring using MR thermometry and can be exploited for assessment of treatment outcome (17-19).
Contrast-enhanced T_1-weighted imaging is one of the most commonly used MRI methods for the evaluation of HIFU treatment (7,8,20). A lack of contrast enhancement is generally observed in the central ablation volume, that was exposed to temperatures of approximately 60 °C during treatment. The region with low contrast enhancement is referred to as the non-perfused volume, which serves as an important readout parameter for HIFU treatment evaluation (8,20-22). In the transition zone between the central ablation volume and unaffected surrounding tissue, milder temperature elevations may result in indirect heat-induced injury and more subtle vascular alterations. The vascular changes in this peripheral zone are strongly dependent on the exact temperature and/or thermal dose that is reached during the HIFU intervention and can be transient in nature. Directly after HIFU, hyperthermic conditions in the peripheral zone could (transiently) increase tumor blood flow and microvascular permeability and increase tumor oxygenation (23,24). Within a few days after treatment, the immune response may be enhanced in the transition zone and inflammation-associated hyperemia may be observed (7,20,25). At a later stage (approximately 7 days) after treatment, also fibrosis and revascularization may alter the tumor vascular status (26-28). On contrast-enhanced T_1-weighted images, often an enhancing rim is reported in the region surrounding the central ablation zone, which may be due to these vascular alterations or result from residual unaffected tumor tissue in case of incomplete ablation (7,20). Since the observed contrast enhancement is almost equal in regions of different vascular changes and in unaffected residual tumor tissue, conventional contrast-enhanced MRI does not have a high specificity for the identification of subtle vascular effects after HIFU treatment.

It is however important to gain further insights in the vascular status of the peripheral tumor zone, since HIFU-induced changes in the microvascular function of the tumor tissue in this region may have substantial consequences for the microenvironment and fate of the tumor. In addition, if residual tumor is present after HIFU treatment, this may be treated with adjuvant tumor therapies. The sensitivity of the tumor to these therapies may also be affected by the vascular status (25).

Compared to conventional contrast-enhanced MRI, assessment of changes in contrast-agent uptake-kinetics by dynamic contrast-enhanced MRI (DCE-MRI) may be a more suitable method to gain insight in the altered vascular status in the tissue around the

coagulated lesion. Pharmacokinetic modeling of DCE-MRI data can be applied to determine biomarkers that are sensitive to vascular changes; *e.g.* with the widely employed Tofts model the transfer constant K^{trans} and the extravascular extracellular volume fraction v_e can be determined (29). Hijnen et al. have used these kinetic parameters for HIFU therapy assessment in a rat tumor model (30). Cheng et al. have shown that these parameters could give insight in regional changes in the microvasculature after HIFU treatment of rabbit muscle tissue (26,31). However, there are no studies in which the anticipated subtle changes in tumor vascular status around the HIFU ablation volume have been investigated with pharmacokinetic modeling of DCE-MRI data, while knowledge of changes in DCE-MRI-derived kinetic parameters may provide a more refined picture of the tumor vascular status after HIFU treatment compared to conventional contrast-enhanced MRI.

To address this, in the present study, DCE-MRI was performed before, directly after and at 3 days after HIFU treatment of a murine subcutaneous tumor model. Partial tumor treatment was performed to allow for the presence of both HIFU-treated and residual tumor tissue after the HIFU procedure. Tracer-kinetic modeling was performed on the tumor pixels outside the non-perfused volume to assess HIFU-induced changes in contrast agent uptake-kinetics. Cluster analysis based on K^{trans} and v_e was employed to identify subregions with different uptake-kinetics and the regional distribution of these clusters within the tumor was determined.

6.2. Materials and methods

6.2.1. Ethics Statement

All animal experiments were performed according to the Directive 2010/63/EU of the European Parliament and approved by the Animal Care and Use Committee of Maastricht University (protocol: 2010-097 and 2010-132).

6.2.2. Murine tumor model

10-12 week-old Balb/c mice (Charles River, Maastricht, The Netherlands) were inoculated with $2x10^6$ CT26.WT murine colon carcinoma cells (American Type Culture Collection (ATCC; CRL-2638), early passages (5-10)), subcutaneously in the right hind limb. The tumors were grown in the hind limb to prevent potential HIFU-induced damage to vital organs and respiration artifacts in the MR measurements. Approximately 10 days after inoculation, tumors became palpable in all animals.

6.2.3. Study design

MRI was performed 1 day before (n=12), directly (2-3 h) after (n=12) and 3 days after HIFU treatment (n=6). A control group of non-treated animals (n=6) was included that underwent MRI at the same time points as the HIFU-treated animals. The time points of the control animals are referred to as day -1, day 0 and day 3. Directly after the last MRI experiment, the mice were sacrificed, and the tumors were excised for histological analysis. This study design led to three different groups for quantitative histology: animals sacrificed after the MRI examination directly after HIFU treatment (n=6, referred to as 'Directly after HIFU'), animals sacrificed after the MRI

examination at 3 days after HIFU treatment (n=6, referred to as '3 days after HIFU') and non-treated control animals (n=6, referred to as 'Control').

6.2.4. HIFU treatment

HIFU treatment was performed outside the MR scanner with the preclinical Therapy Imaging Probe System (TIPS, Philips Research, Briarcliff Manor, NY, USA) (32). Treatment was performed under general anesthesia (1-2% isoflurane) and precautionary analgesia (buprenorphine, 0.1 mg/kg s.c., administered at least 30 min before treatment). Control animals received an equal dose of analgesia at the corresponding time point. Partial tumor treatment was performed by definition of a square 4x4 mm^2 treatment grid within the tumor area, consisting of 25 equally-spaced ablation volumes (1x1x9 mm^3) that were placed within the tumor under guidance of an ultrasound imaging system (HDI5000 imaging system combined with a P7-4 phased array transducer, Philips Ultrasound, Bothell, WA, USA). This resulted in the presence of both HIFU-treated and non-treated tumor tissue after the HIFU procedure. Treatment settings were: frequency 1.4 MHz, pulse repetition frequency 20 Hz, acoustic power 12 W, duty cycle 50%, treatment time 30 s. A wait time of 120 s was applied between sonication of consecutive treatment points to allow for sufficient cooling of the treated tissue. A temperature increase to approximately 66 °C during HIFU treatment was confirmed by insertion of a thermocouple into the tumor in 3 pilot experiments, as previously described (33).

6.2.5. MRI measurements

MRI measurements were performed with a 6.3 T horizontal-bore scanner (Bruker BioSpin, Ettlingen, Germany) using a 3.2-cm-diameter quadrature birdcage RF coil (Rapid Biomedical, Rimpar, Germany) under general anesthesia (1-2% isoflurane). The mice were positioned in a custom-made cradle, equipped with a mask for anesthetic gas. Respiration was monitored with a balloon sensor. Body temperature was monitored and maintained with a warm water pad. For reduction of susceptibility artifacts in Echo Planar Imaging (EPI), the tumor-bearing paw was covered with degassed ultrasound gel (Aquasonic® 100, Parker Laboratories). Artifacts were further reduced by local shimming.

A fat-suppressed T_2-weighted spin-echo sequence (TE=30 ms, TR=1000 ms, number of averages NA=1) was used for anatomical reference.

Pre-contrast T_1 mapping was performed using an inversion recovery Look-Locker EPI sequence (TE=8 ms, TR=10000 ms, inversion time=30 ms, flip angle=20°, pulse separation=400 ms, number of points=15, NA=2).

DCE-MRI measurements were performed using a gradient-spoiled dual gradient echo EPI sequence (TR=1250 ms, TE1/TE2=7.5/26.1 ms, NA=2, number of segments=2, flip angle=80°, temporal resolution=5 s, number of repetitions=100). At 1.5 min after start of the acquisition, a bolus of 0.3 mmol/kg Gd-DOTA (Dotarem®; Guerbet, Villepinte, France) with a saline flush was injected in 5 s via the tail vein using an infusion pump (Chemyx Fusion 100, Stafford, TX, USA).

All images were acquired with a matrix size of 128x128, FOV of 4x4 cm^2 and 1 mm slice thickness. 12-16 slices were acquired covering the whole tumor volume.

6.2.6. DCE-MRI data processing

Image analysis was performed in Mathematica 8.0 (Wolfram Research, Champaign, IL, USA) and MATLAB R2013a (The MathWorks, Natick, MA, USA). Regions of interest (ROIs) were defined on the T_2-weighted images by manually drawing contours around the tumor tissue on each slice. From these ROIs the tumor volumes at the different experimental time points were determined. Pre-contrast T_1 maps were generated as described previously (34).

A T_2^* correction was performed on the dynamic signal intensities to account for the T_2^* changes caused by contrast agent influx (35,36). The dynamic T_2^* values in the tumor pixels were determined based on the ratio of the signal intensities at the two echo times. Dynamic T_1 values were calculated from the signal equation for a spoiled gradient-echo sequence using the T_2^*-corrected dynamic signal intensities and the pre-contrast T_1 values. A B_1 correction was applied to the flip angle used in the dynamic acquisition, using a B_1 map acquired with the same RF coil in a 2% agarose/0.05 mM $CuSO_4$ phantom. Dynamic T_1 values were converted to dynamic contrast agent concentrations ([CA]) using the Dotarem plasma relaxivity at 7 T at 37 °C (3.53 $mM^{-1}s^{-1}$ (37)).

6.2.7. Pharmacokinetic analysis of DCE-MRI data

Pharmacokinetic analysis of the DCE-MRI data was performed with a custom-written MATLAB tool. For determination of K^{trans} and v_e in each tumor pixel, the standard Tofts model (29,38) was used, in which the dynamic contrast agent concentration in the tumor tissue is defined as:

$$C_t(t) = K^{trans} \int_0^t C_p(\tau) e^{-k_{ep}(t-\tau)} d\tau$$

in which C_t and C_p are the contrast agent concentrations in the tumor tissue and the blood plasma, respectively and k_{ep} is the rate constant ($k_{ep}=K^{trans}/v_e$). A delay term (t_d) was included in the model to allow for a delay between bolus arrival in the blood and the tissue response. A literature-based bi-exponential arterial input function (AIF), measured in the mouse iliac artery upon injection of a similar dose of Dotarem (39), was used and modified to match with our data. The bi-exponential AIF is described by:

$$C_p(t) = \begin{cases} 0 & t < t_i \\ a_1 e^{-m_1 t} + a_2 e^{-m_2 t} & t \geq t_i \end{cases}$$

in which t_i is the injection time.

The peak amplitude of the AIF was adapted based on the injected dose and the mouse plasma volume. In addition, the second exponent of the AIF, describing the AIF tail, was adapted based on blood kinetics data of Dotarem from five separate CT26.WT tumor-bearing Balb/c mice. For this purpose, the gadolinium concentration of blood plasma samples acquired at different time points after CA injection was determined by means of Inductively Coupled Plasma-Atomic Emission Spectrometry or Inductively Coupled Plasma-Mass Spectrometry. These adaptations resulted in the following bi-

exponential AIF parameters: a_1=5.36 (mM), m_1=11.20 (min^{-1}), a_2=1.27 (mM), m_2=0.0655 (min^{-1}).

The standard Tofts model was fitted to the dynamic [CA] curves using the MATLAB function lsqcurvefit, with constraints $K^{trans} \geq 0$ min^{-1}, $k_{ep} \geq 0$ min^{-1} and $0 \leq t_d \leq 7$ repetitions.

6.2.8. Identification of non-perfused tumor volume

Non-perfused pixels were selected based on the level of contrast enhancement. Pixels were considered non-perfused if the median [CA] after injection was lower than 5 times the standard deviation (SD) of the data points in the dynamic [CA] curve before injection. Non-perfused volumes were calculated from the total number of non-perfused pixels in each tumor multiplied by the pixel volume. Non-perfused fractions were derived from the ratio between the non-perfused volume and the total tumor volume. The non-perfused pixels were not included in the subsequent histogram and cluster analyses. The other tumor pixels are for reasons of simplicity referred to as perfused pixels. It should however be noted that the significant contrast enhancement in these pixels does not necessarily reflect substantial perfusion, since it may also be caused by an enhanced vascular permeability.

6.2.9. Selection of pixels for cluster analysis

A number of criteria were defined to select the perfused tumor pixels that were included in the cluster analysis. Pixels in which the dynamic T_1 became lower than 250 ms or the dynamic T_2^* became lower than the first echo time (7.5 ms) were excluded for further analysis, since such low T_1 and T_2^* values could not be accurately determined with the present DCE-MRI acquisition settings. Furthermore pixels of which the fitted curves had a goodness-of-fit (R^2) value lower than 0.8 were excluded from analysis. In addition, pixels with non-physiological v_e values higher than 1 were omitted.

To get insight in the K^{trans} and v_e distribution in the perfused tumor tissue of the HIFU-treated and control animals at the different experimental time points, histograms of K^{trans} (20 bins, bin width 0.025 min^{-1}, range 0-0.5 min^{-1}) and v_e (20 bins, bin width 0.025, range 0-0.5) in the selected perfused tumor pixels were made.

6.2.10. Cluster analysis

k-means clustering with 3, 4, 5 and 6 clusters was performed on the combined K^{trans} and v_e data of the selected perfused pixels of all (HIFU-treated and non-treated) animals at all time points simultaneously with a custom-written Mathematica function. Prior to clustering, data were normalized (mean=0, SD=1) to remove scaling differences between K^{trans} and v_e. Changes in the fraction of pixels in the different clusters were defined as treatment-associated if the fraction of pixels assigned to the particular cluster increased significantly (one-sided paired t-test, $p<0.05$) after HIFU treatment (either directly or at 3 days after HIFU) compared to before HIFU treatment.

6.2.11. Regional distribution of clusters

To assess the spatial distribution of the different clusters with respect to the non-perfused volume, the distance of each pixel in each cluster to the non-perfused volume was determined. For each pixel in a particular cluster, the distances between that pixel and all non-perfused pixels in the same MRI slice were determined. The minimum of these distances was taken as a measure for the distance between the particular pixel and the non-perfused volume. Histograms (6 bins, binwidth 1 pixel, range 1-7 pixels) of these minimal distances to the non-perfused volume were made for each cluster at each time point after HIFU treatment to visualize the regional distribution of the different clusters with respect to the non-perfused volume. In addition, the median minimal distance of each cluster to the non-perfused volume was calculated for each HIFU-treated mouse at both time points after HIFU treatment.

6.2.12. Histological analysis

Dissected tumors were snap-frozen in isopentane and stored at -80 °C. Tumors were cut into 5 µm thick sections with a distance of approximately 300 µm between the sections. The cryo-sections were briefly air-dried and subsequently stained for nicotinamide adenine dinucleotide (NADH) diaphorase activity to assess cell viability. Sections were incubated at 37 °C for 1 h in Gomori-Tris-HCl buffer (pH 7.4) containing β-NAD reduced disodium salt hydrate (Sigma-Aldrich, St. Louis, MO, USA, 0.71 mg/ml buffer solution) and nitro blue tetrazolium (Sigma-Aldrich, 0.29 mg/ml buffer solution). Brightfield microscopy was performed on all sections and consisted of mosaic acquisition of the entire section at 5x magnification. Analysis of the microscopy images was performed in Mathematica 7.0. ROIs were manually drawn around the pale non-viable tumor tissue and the entire tumor tissue on all sections of each tumor. From the ratio between the ROI areas of non-viable tumor tissue and entire tumor tissue on all tumor sections, a histology-derived non-viable tumor volume fraction was determined for each tumor. Subsequently the MRI-derived non-perfused tumor fractions were compared to the histology-derived non-viable tumor fractions.

Apart from the NADH-diaphorase staining, haematoxylin and eosin (H&E) staining was performed on paraffin sections of a separate CT26.WT tumor that was treated with the same HIFU settings. This tumor was excised at ~2.5 h after HIFU treatment. Brightfield microscopy was performed to inspect morphological changes in the tumor tissue after treatment.

In order to further interrogate the causes and consequences of HIFU-induced changes in contrast agent uptake-kinetics, a dual vascular endothelium and hypoxia staining was performed on tumor cryo-sections of the mice sacrificed at 3 days after HIFU. For each mouse, two sections were selected that were located either close to (section with the largest non-viable tumor fraction) or far from (section with the lowest non-viable tumor fraction) the HIFU-treated non-viable tumor region.
After aceton-fixation, a fluorescent dual staining was performed using an anti-mouse glucose transporter 1 (glut-1) antibody conjugated with a DyLight 650 fluorescent label (4 h, room temperature, 1:150 dilution, Novus Biologicals, Littleton, CO, USA) as an intrinsic marker for hypoxia (40) and rat anti-mouse CD31 antibody (overnight, 4

°C, 1:250 dilution, clone mec 13.3, BioLegend, San Diego, CA, USA) and secondary goat anti-rat Alexa-488 antibody (1 h, room temperature, 1:500 dilution, BioLegend) for vascular endothelium. Fluorescence microscopy images of the entire tumor sections were acquired with a pannoramic MIDI digital slide scanner (3DHistech Ltd, Budapest, Hungary) at 31x magnification with optimal settings for each staining and equal settings for all sections. An additional fluorescence microscopy image, at the same channel as for CD31 detection, was acquired with a longer exposure time to assess autofluorescence in the sections. ROIs were manually drawn to segment the non-viable and viable tumor, based on the level of autofluorescence, which has been reported as a reliable method to accurately identify heat-fixed non-viable cells (41). Adjacent NADH-diaphorase stained sections were used as a visual reference, to confirm the correct delineation of the non-viable tumor area. Only the viable tumor tissue was used for further analysis, since the cluster analysis was also only performed on perfused, likely viable, tumor pixels. The viable tumor tissue in the section with the largest non-viable fraction was referred to as 'Near non-viable' and the viable tumor tissue in the mostly viable remote section was referred to as 'Remote'.
The vascular surface fraction in the viable tumor region was calculated by division of the total number of CD31-positive pixels by the total number of viable tumor pixels. The level of glut-1 expression was assessed by determination of the mean glut-1 intensity in the viable tumor tissue.

6.2.13. Statistical analysis

Data are presented as mean±SD. At all experimental time points, the relative tumor sizes of the HIFU-treated and non-treated tumors were statistically compared with a two-sided t-test assuming equal variances. The non-perfused tumor volumes at the different experimental time points were compared for statistical significance with a two-sided paired t-test. Correlation analysis between the MRI-derived non-perfused tumor fractions and histology-derived non-viable tumor fractions was performed for all groups by calculation of the Pearson correlation coefficient. In addition, the one-to-one correspondence between the non-viable and non-perfused tumor fractions was determined by calculation of the R^2 of the data points to the line of identity. The difference between non-viable tumor fractions of the HIFU-treated and non-treated control tumors at the last experimental time point was tested for significance with a two-sided t-test assuming equal variances. Changes in the K^{trans} and v_e histograms between the two time points after HIFU and before HIFU were tested for significance with a two-sided paired t-test. A one-sided paired t-test was performed for each cluster to assess if the fraction of pixels in that cluster was increased after HIFU. The median minimal distances to the non-perfused volume of the different clusters were statistically compared with a two-sided paired t-test. Histological differences in vascular surface fraction and mean glut-1 intensity were tested for significance with a two-sided paired t-test. For all tests, the level of significance was set to $\alpha=0.05$.

6.3. Results

Partial tumor ablation with HIFU resulted in a significantly lower relative tumor size at day 3 compared to the control mice (Figure 1).

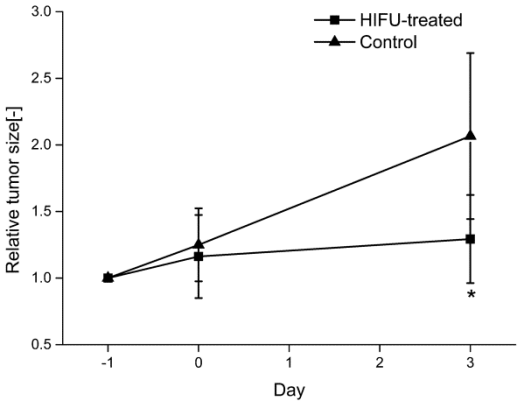

Figure 1. Tumor growth. Mean±SD relative tumor size, based on ROIs drawn on the anatomical MRI images, at the different experimental time points for the HIFU-treated and the control animals. For the HIFU-treated animals day 0 corresponds to the day of treatment. * indicates a significant difference in relative tumor size between the HIFU-treated and control animals at measurement day 3 (two-sided t-test, $p<0.05$).

Representative pharmacokinetic parameter maps in the tumor tissue before and at both time points after HIFU treatment are shown in Figure 2A (for the same animal). Before HIFU treatment, the tumor vasculature was characterized by higher K^{trans} values in the tumor rim than in the tumor center. Furthermore, a small region of low K^{trans} was observed in the tumor core. The v_e values were also generally higher in the tumor rim than in the center. Directly after partial HIFU treatment of the tumors, a large area of decreased K^{trans} emerged. Such area of decreased K^{trans} was also present at 3 days after HIFU treatment. At both time points after HIFU treatment, the area of decreased K^{trans} corresponded to regions with low v_e with small subregions of high v_e. No substantial differences in K^{trans} and v_e were detected for the non-treated control animals between measurement day -1 and day 0, although a reduction in K^{trans} was observed at day 3 (Figure 2B).

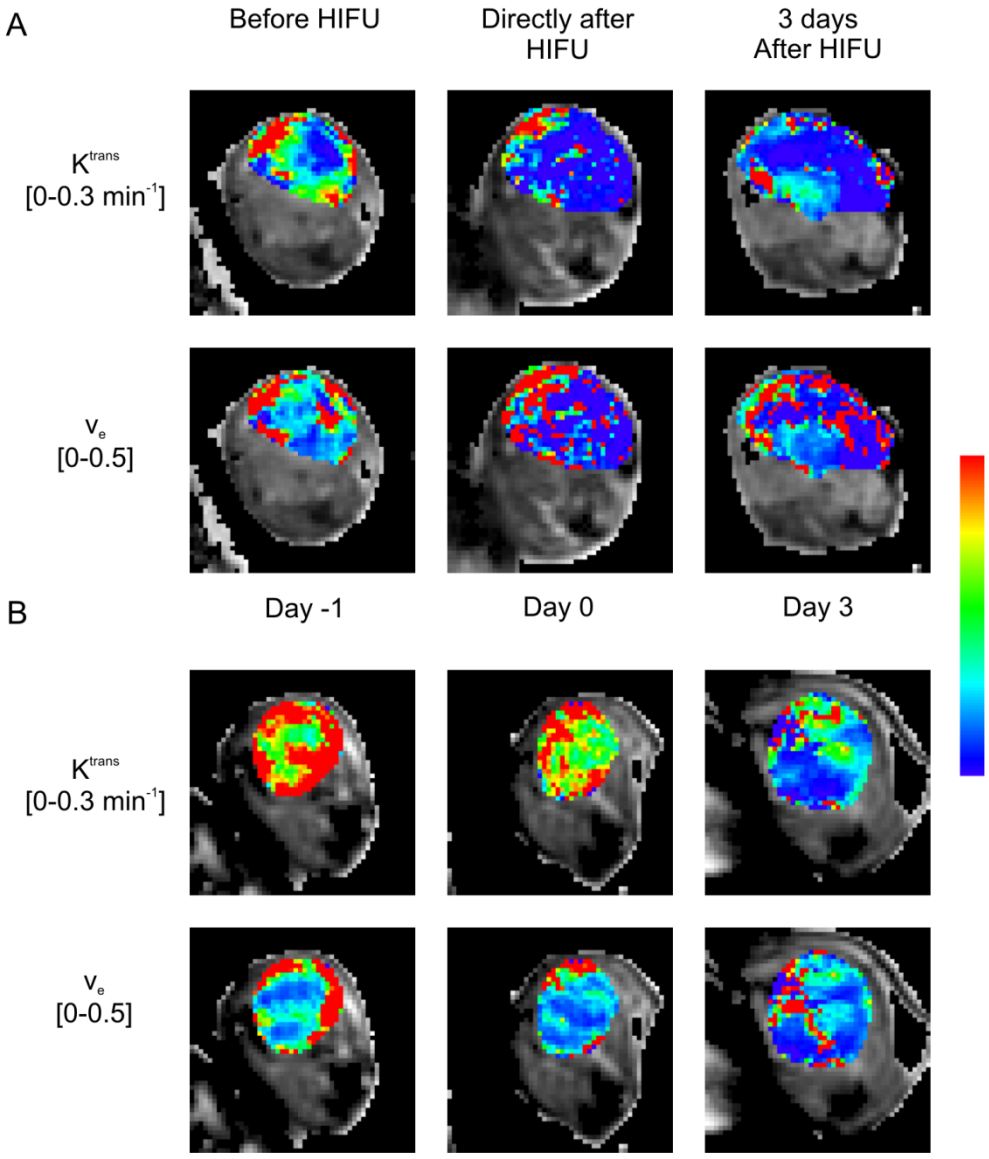

Figure 2. Pharmacokinetic parameter maps. A) Representative pharmacokinetic parameter maps overlaid on the tumor pixels of an axial T_2-weighted image of a tumor-bearing paw before, directly after and at 3 days after HIFU treatment. B) Representative pharmacokinetic parameters maps for a control animal at the corresponding experimental time points. The parameters were scaled according to the color bar shown at the right side of the figure. The corresponding parameter range for this scale bar is indicated at the left side of the parameter maps.

To assess the effect of partial ablation on tumor perfusion, non-perfused tumor volumes were determined first, based on the level of contrast enhancement in the tumor pixels. The average non-perfused tumor volumes of the HIFU-treated and control animals at the different experimental time points are displayed in Figure 3A and B, respectively.

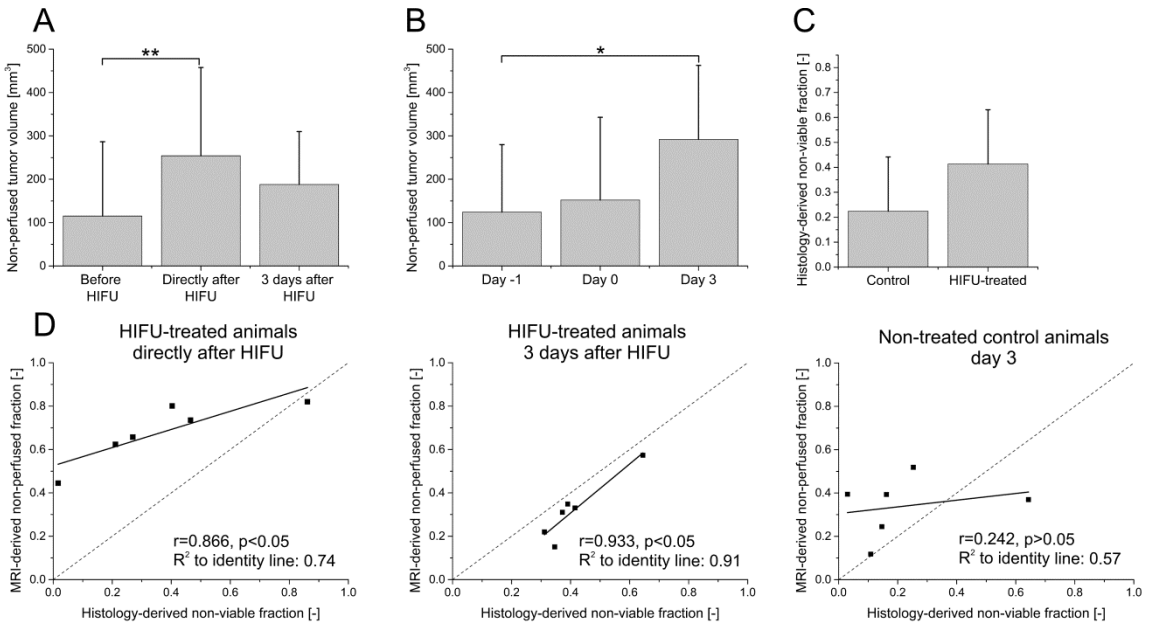

Figure 3. Non-perfused tumor volumes. A) Mean±SD non-perfused tumor volumes before, directly after and at 3 days after HIFU treatment. ** indicates a significant increase in the non-perfused tumor volume directly after HIFU compared to before HIFU (two-sided paired t-test, $p<0.001$). B) Mean±SD non-perfused tumor volumes at measurement day -1, 0 and 3 for the control animals. * indicates a significant increase in the non-perfused tumor volumes between measurement day 0 and 3 (two-sided paired t-test, $p<0.05$). C) Mean±SD histology-derived non-viable tumor fractions of the control and HIFU-treated animals at measurement day 3. D) Correlation plots of MRI-derived non-perfused tumor fractions vs. histology-derived non-viable tumor fractions for the three different experimental groups. The line of identity is shown as a visual reference. The correlation coefficient and the R^2 to the line of identity are displayed in the right bottom corner of each figure.

Directly after HIFU treatment, the non-perfused tumor volume significantly increased compared to before HIFU treatment. No significant difference between the non-perfused tumor volume at 3 days after HIFU compared with either before or directly after HIFU was observed. For the control animals, the non-perfused tumor volume remained constant between measurement day -1 and 0, whereas the non-perfused tumor volume was significantly increased at day 3.

The average histology-derived non-viable tumor fraction at the last experimental time point was higher for the HIFU-treated animals than for the control animals, although this difference was not significant (Figure 3C). Correlation plots between MRI-derived non-perfused tumor volume fractions and histology-derived non-viable tumor volume fractions are displayed in Figure 3D for the different experimental groups. For the HIFU-treated animals sacrificed directly after HIFU, a high, significant correlation ($r=0.866$) was observed between the MRI-derived non-perfused and histology-derived non-viable tumor fractions. However, the non-perfused tumor fractions were generally higher than the non-viable tumor fractions at that time point after HIFU treatment, resulting in a relatively low one-to-one correspondence (R^2 to line of identity = 0.74). At 3 days after HIFU treatment, also a high correlation ($r=0.933$) was observed between the non-perfused and non-viable tumor fractions. At this time point after HIFU treatment, a good one-to-one correspondence between the non-perfused and non-viable tumor fractions was observed ($R^2=0.91$). For the control animals, both the

correlation (r=0.242) and one-to-one correspondence (R^2=0.57) between the non-perfused and non-viable tumor volume fractions were low.

In addition to the above measurements of non-perfused tumor fractions and volumes, a detailed analysis of the pharmacokinetic parameters in the perfused tumor surrounding the non-perfused ablation volume was performed. Average distributions of K^{trans} and v_e in the perfused pixels in the HIFU-treated tumors at all time points are shown in Figure 4A and B, respectively.

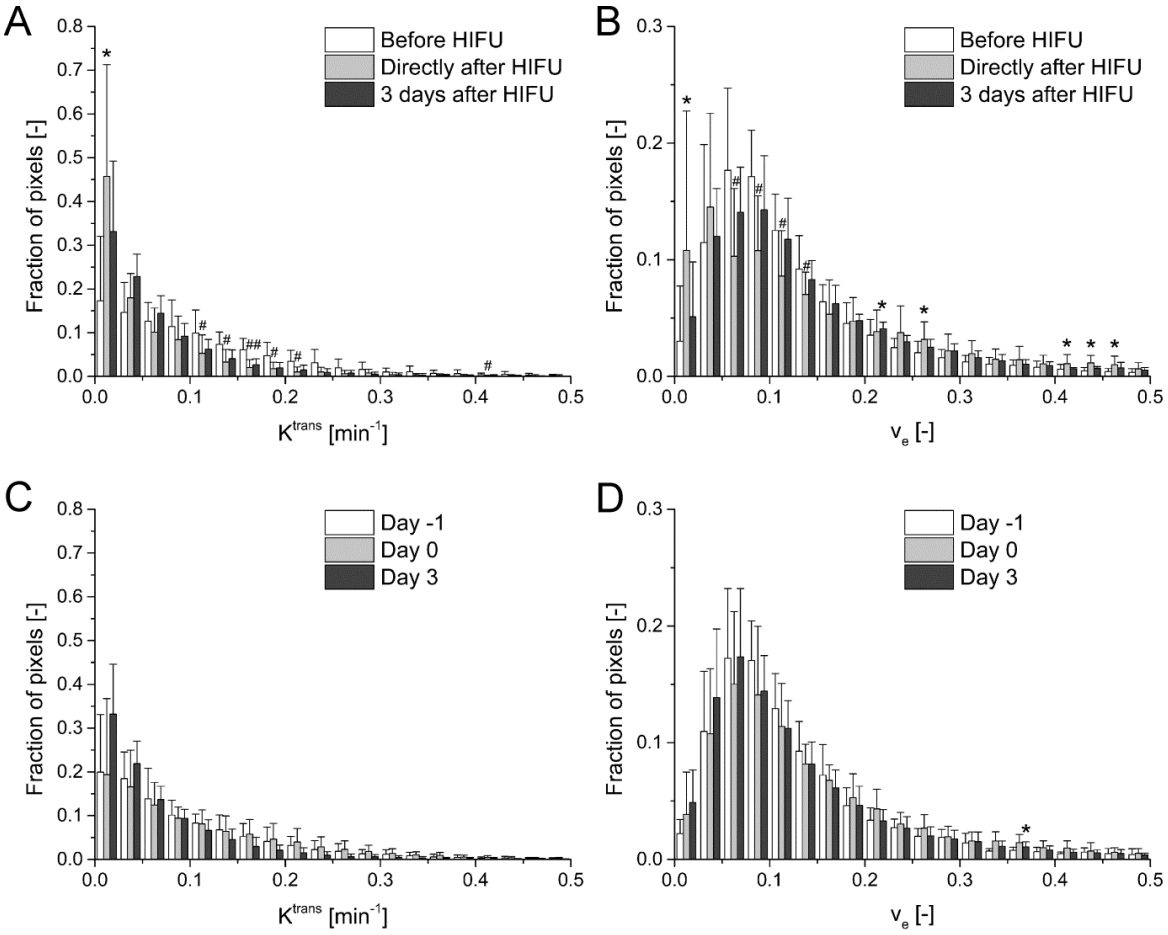

Figure 4. Pharmacokinetic parameter histograms. A and B) Average K^{trans} and v_e histograms in the HIFU-treated tumors at the different experimental time points, respectively. The error bars represent the SD. * and # indicate a significant increase and decrease in the fraction of pixels after HIFU compared to before HIFU, respectively (two sided paired t-test, $p<0.05$). C and D) Average K^{trans} and v_e histograms in the non-treated control animals at the different experimental time points, respectively. The error bars represent the SD. * indicates a significant increase in the fraction of pixels at day 3 compared to day -1 (two sided paired t-test, $p<0.05$).

Directly after HIFU treatment, the fraction of pixels with a K^{trans} value between 0 and 0.025 min^{-1} was significantly increased compared to before HIFU. In addition, the fraction of pixels in a number of bins with a higher K^{trans} (>0.1 min^{-1}) was significantly decreased directly after HIFU. At this time point, the fraction of pixels with a v_e value between 0.05 and 0.15 was significantly lower than before HIFU, whereas a significant

increase in the fraction of pixels with both a lower v_e value (0-0.025) and a higher v_e value (>0.25) was observed. At 3 days after HIFU treatment, the fraction of pixels in most bins was not significantly different from that before treatment. The average K^{trans} and v_e distributions in the perfused pixels of the non-treated control animals at the different time points are displayed in Figure 4C and D, respectively. No significant changes in the K^{trans} and v_e of the perfused pixels were observed between the different time points, except for one bin in the v_e histogram in which the fraction of pixels was significantly increased at day 3 compared to day -1. In addition, a non-significant shift toward lower K^{trans} values was observed at day 3 compared to day -1 and 0.

Cluster analysis was performed on the perfused pixels of all tumors and all time points to identify subregions with different contrast agent uptake-kinetics. Four clusters appeared to be the minimal number of clusters with which the most prominent vascular changes could be identified. In Figure 5 the results of the cluster analysis with four clusters are overlaid on the tumor pixels of the same slice from the same animal as shown in Figure 2. The white region represents the non-perfused tumor pixels. The different colors represent the four clusters that were identified. The median dynamic [CA] curves of all pixels assigned to the different clusters are shown in the bottom of Figure 5.

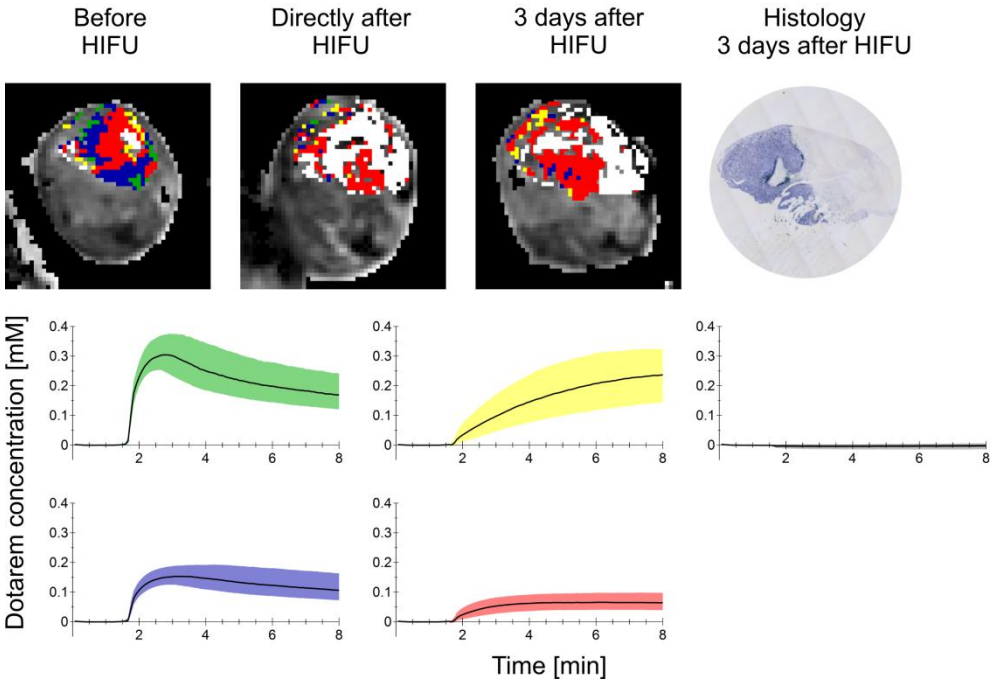

Figure 5. Clustering of pharmacokinetic parameter values. Representative clustering results overlaid on the tumor pixels of the T_2-weighted image of the tumor-bearing paw of the same animal as shown in Figure 2 before, directly after and at 3 days after HIFU treatment. The four clusters are represented by the different colors (yellow, green, red and blue). The non-perfused pixels, that were excluded from cluster analysis, are represented by the white color. An NADH-diaphorase stained tumor section obtained at approximately the same location as the MRI slice at 3 days after HIFU treatment is shown at the top right corner of the figure. A clear pale, non-viable tumor region was observed next to NADH-diaphorase positive, viable tumor tissue. The median dynamic [CA] curves of all pixels in each of the 4 clusters (shown by the different colors) and the non-perfused pixels are shown in the figure bottom (from top to bottom, left to right: green cluster, yellow cluster, non-perfused pixels, blue cluster and red cluster). The bands around the curves represent the range between the 25th and 75th percentiles.

After HIFU treatment, the number of pixels assigned to the blue and green clusters strongly decreased. The DCE-MRI curves in these clusters were characterized by a rapid upslope, a clear wash-out and substantial contrast agent influx. At both time points after HIFU, a large region of non-perfused tissue emerged. Curves in the non-perfused tumor area, shown at the right of the figure, were characterized by a lack of contrast agent inflow. The area around the non-perfused volume consisted mostly of pixels assigned to the red and yellow clusters. Contrast agent uptake in pixels assigned to the red cluster was low and relatively slow. The curves in the yellow cluster typically indicated slow uptake-kinetics, but pronounced contrast agent influx. The area of non-perfused pixels visually corresponded well to the area of non-viable tissue on the NADH-diaphorase stained section obtained at 3 days after HIFU treatment at approximately the same location in the tumor, in agreement with the data presented in Figure 3D.

In Figure 6 the average fraction of pixels assigned to the four clusters is shown for the HIFU-treated animals at the different time points.

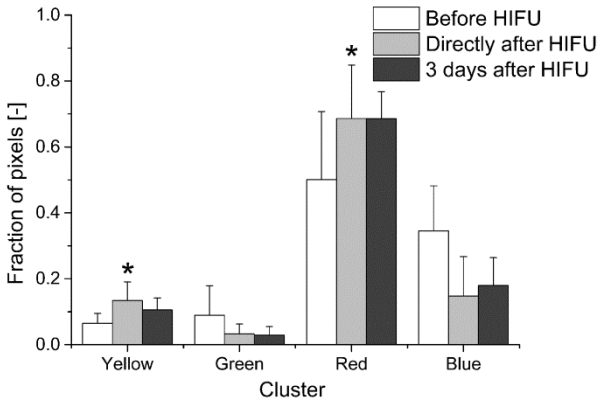

Figure 6. Cluster composition at the different experimental time points. Mean±SD fraction of pixels assigned to the four different clusters before, directly after and at 3 days after HIFU treatment. * indicates a significant increase in the fraction of pixels directly after HIFU compared to before HIFU ($p<0.05$, one-sided paired t-test).

Directly after HIFU treatment, the fraction of pixels in the yellow and red cluster was significantly increased compared to before HIFU. At 3 days after HIFU treatment, the fraction of pixels in these clusters was not significantly higher than before HIFU. Because of the HIFU-induced increase in the fraction of pixels in the yellow and red clusters, changes in these clusters were considered as treatment-associated.

In Table 1 the K^{trans} and v_e parameter values in the different clusters are displayed. In the clusters with a treatment-associated increase in fraction of pixels (yellow and red clusters), K^{trans} was lower than in the other (green and blue) clusters. The v_e in these clusters was either higher (yellow cluster) or lower (red cluster) than in the other clusters.

Table 1. K^{trans} and v_e values (mean±SD) in the four clusters.

Cluster	K^{trans} [min^{-1}]	v_e [-]
Yellow	0.066±0.054	0.495±0.170
Green	0.356±0.107	0.223±0.098
Red	0.039±0.026	0.095±0.061
Blue	0.150±0.044	0.138±0.067

To gain insight in the regional distribution of the different clusters with respect to the non-perfused volume, the minimal distance of each perfused pixel in each cluster to the closest non-perfused pixel was determined. The histograms in Figure 7 show the distribution of these minimal distances for all clusters at the two time points after HIFU treatment and provide information on the proximity of the different clusters to the non-perfused volume.

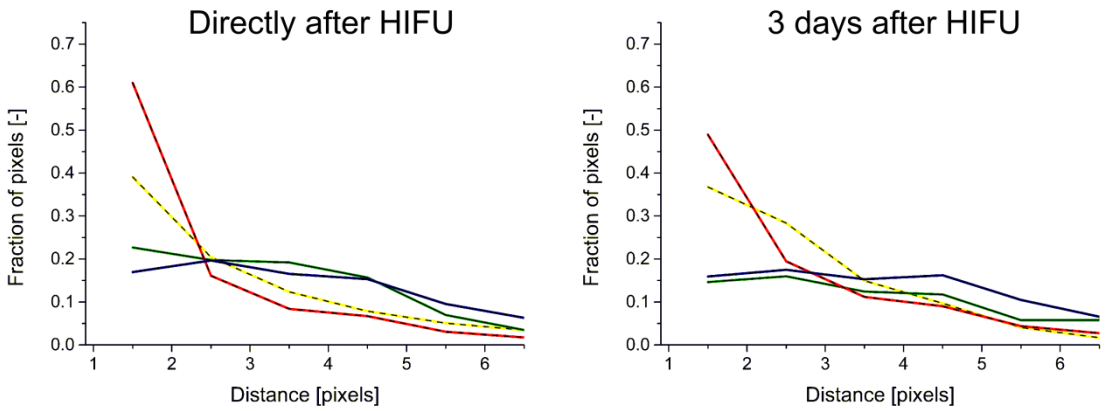

Figure 7. Spatial distribution of clusters with respect to non-perfused volume. Distribution of the minimal distance of the pixels in each of the four different clusters to the closest non-perfused pixel directly after and at 3 days after HIFU treatment. The yellow, green, red and blue lines represent the different clusters. The dashed lines represent the clusters with a treatment-associated increase in the fraction of pixels (yellow and red clusters) and the solid lines represent the other (blue and green) clusters.

Both directly and at 3 days after HIFU treatment, the red cluster was most closely located to the non-perfused volume. The yellow cluster was more closely located to the non-perfused volume than the green and blue clusters, but further away from the non-perfused volume than the red cluster. The median minimal distances between the four clusters and the non-perfused volume, averaged for all HIFU-treated animals, are given in Table 2 for both time points after treatment. Directly after HIFU, the average distance to the non-perfused volume was significantly smaller for the red cluster compared to all other clusters. Furthermore, a significantly smaller distance to the non-perfused volume was observed for the yellow cluster compared to the blue cluster. At 3 days after HIFU treatment, the red cluster was still significantly closer to the non-perfused volume than the blue cluster.

Table 2. Distance of clusters to the non-perfused volume. Median minimal distance from the different clusters to the non-perfused volume averaged for all HIFU-treated animals, at both time points after HIFU treatment. Data are presented as mean±SD. # and ## indicate a significantly smaller distance of a cluster to the non-perfused volume compared to the cluster(s) indicated between the parentheses, with $p<0.05$ and $p<0.001$, respectively.

Cluster	Distance directly after HIFU [pixels]	Distance 3 days after HIFU [pixels]
Yellow	2.31±0.67 # (blue)	2.51±0.34
Green	2.79±1.67	3.67±1.78
Red	1.52±0.51 #(green, blue) ##(yellow)	2.15±0.68 # (blue)
Blue	3.13±1.50	3.41±1.25

Representative microscopy images of H&E-stained sections of a tumor excised at ~2.5 h after HIFU treatment are shown in Figure 8. A region of viable tumor tissue was observed, which was structurally intact (Figure 8A). The cells in the viable tumor tissue were densely packed and cell nuclei had a normal appearance. In addition, a zone of coagulated tissue was observed, surrounded by a region characterized by structural disruption (Figure 8B). The nuclei of the cells in the coagulated zone were typically dark and shrunken. Gaps between the tumor cells were visible in the structurally disrupted tumor tissue (Figure 8B and C). Disrupted tumor blood vessels and presence of red blood cells in the extravascular space were observed, indicative of hemorrhages (Figure 8B and D). These hemorrhages were mainly located close to the coagulated areas.

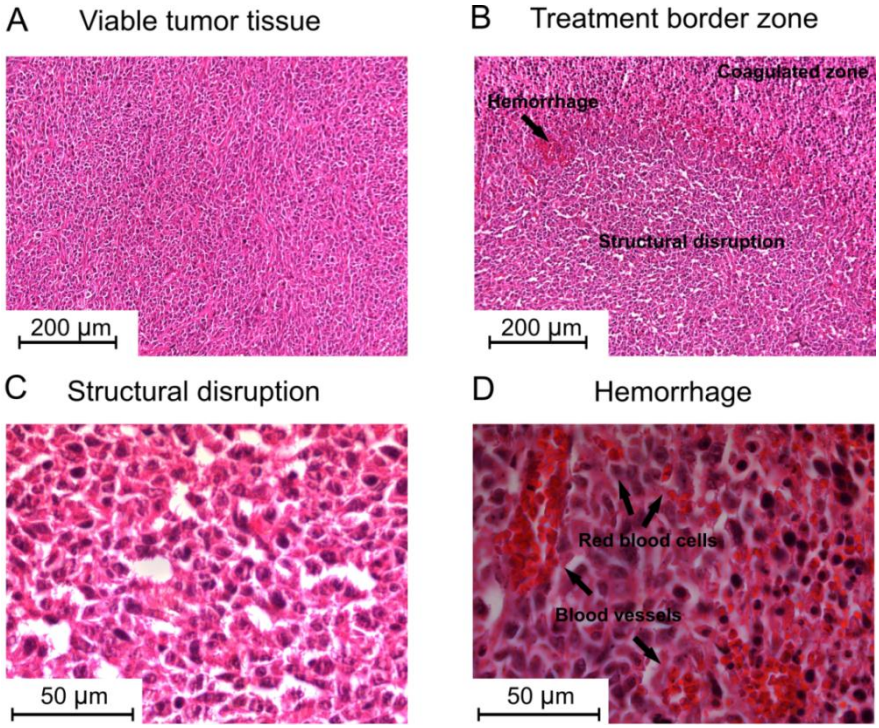

Figure 8. H&E microscopy. Representative brightfield microscopy images of H&E-stained sections of a HIFU-treated CT26.WT tumor excised at ~2.5 h after treatment. A) Viable tumor tissue at 20x magnification. B) Border zone of coagulated tumor tissue surrounded by structurally disrupted tumor tissue at 20x magnification. C) Structurally disrupted tumor tissue at 100x magnification. D) Region with hemorrhage at 100x magnification.

Analysis of microvascular functionality, by a combined CD31 and glut-1 staining, was focused on the viable tumor tissue of tumors excised at 3 days after HIFU. The good agreement between non-perfused and non-viable tumor fractions at that time point (Figure 3D) allowed for comparison of the cluster results of the perfused pixels with changes in CD31 and glut-1 staining in the viable tumor tissue. Representative CD31 and glut-1 microscopy images of a tumor excised at 3 days after HIFU are shown in Figure 9B, with the corresponding NADH-diaphorase staining shown in Figure 9A. Generally, a larger number of CD31 positive tumor pixels and a higher glut-1 intensity were observed in the 'Near non-viable' tumor tissue than in the 'Remote' tumor tissue. Quantitative analysis (Figure 9C) showed that the vascular surface fraction of the different mice was slightly higher in the 'Near non-viable' tumor tissue than in the 'Remote' tumor, although these differences were not significant (p=0.32). The mean glut-1 intensity of the different mice was higher (not significantly, p=0.16) in the 'Near non-viable' tumor tissue compared to the 'Remote' tumor tissue.

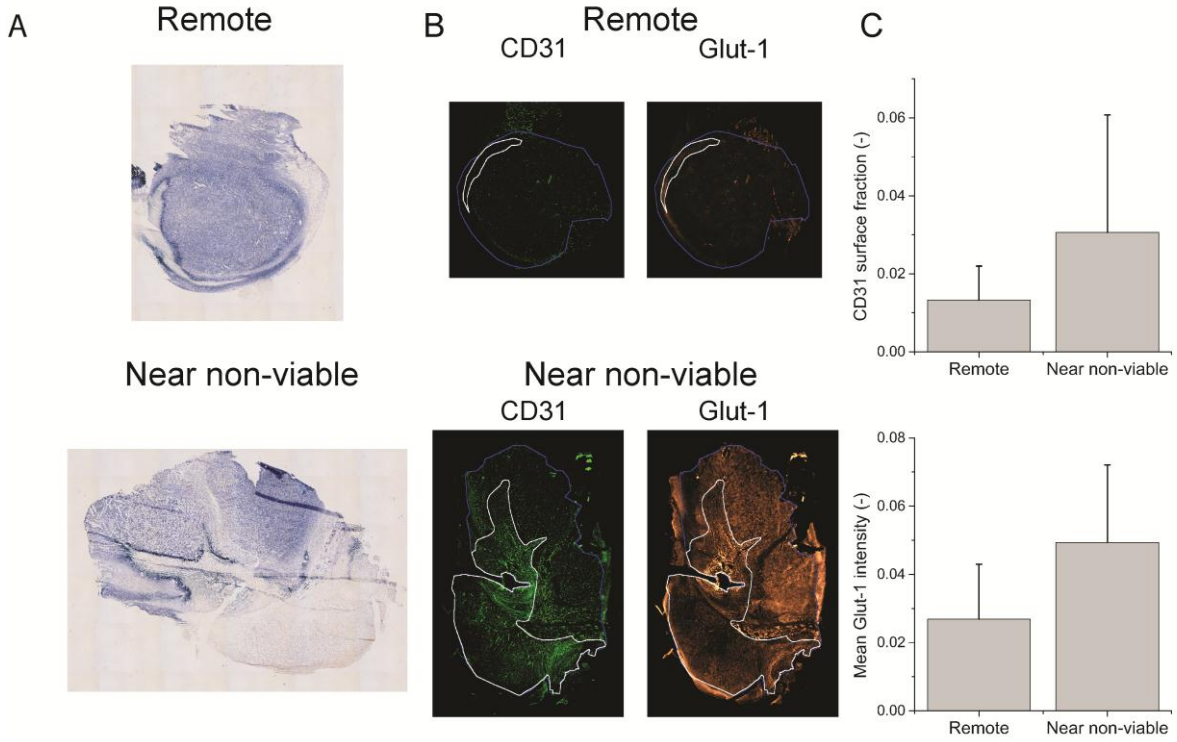

Figure 9. Microvascular endothelium (CD31) and hypoxia (glut-1) immunohistochemistry. A) NADH-diaphorase staining for cell viability of a section with a large non-viable tumor fraction (with 'Near non-viable' tumor tissue) and a distant section with a low non-viable tumor fraction (with 'Remote' tumor tissue). Both sections originate from the same tumor, excised at 3 days after HIFU. B) Representative CD31 and glut-1 fluorescence microscopy images of adjacent tumor sections. The non-viable and entire tumor tissue are delineated in white and blue, respectively. The analysis was performed on the viable (either 'Remote' or 'Near non-viable') tumor tissue. C) Quantification of the mean±SD microvascular density and mean±SD glut-1 intensity in the 'Remote' and 'Near non-viable' tumor tissue of the '3 days after HIFU' animals.

6.4. Discussion

In this study, pharmacokinetic analysis of DCE-MRI data was performed to identify tumor regions with different contrast agent uptake-kinetics longitudinally after HIFU treatment. In addition to the commonly performed assessment of non-perfused volumes, cluster analysis of pharmacokinetic parameters was performed to gain insight in more subtle underlying changes in vascular status in the area surrounding the non-perfused central ablation volume.

A significant increase in the non-perfused tumor volume was observed directly after HIFU treatment (Figure 3A). At this time point, the non-perfused tumor fractions were generally higher than the histology derived non-viable tumor fractions (Figure 3D). This finding is possibly caused by HIFU-induced destruction of tumor vasculature in the zone surrounding the ablated region, which could lead to delayed cell death (23,25,27,42). This delayed cell death may explain the better agreement between the non-viable and non-perfused tumor fractions at 3 days after treatment. Temporary HIFU-induced vascular constriction (43) could also have contributed to the higher non-perfused fraction directly after treatment, although this contribution is probably minor since the non-perfused tumor volume at 3 days after HIFU was not significantly lower than directly after HIFU (Figure 3A). The correlation between non-viable and non-perfused tumor fractions for the non-treated control animals was low, in contrast to the treated animals (Figure 3D). For the control animals, the non-perfused tumor fraction was generally higher than the non-viable tumor fraction. Likely, part of the non-perfused pixels represented hypoxic, yet viable, tumor tissue, which is also known to be poorly perfused (44,45). This hypoxic tissue may become necrotic at a later stage of tumor progression. Therefore, non-perfused pixels do not necessarily represent necrosis leading to a disagreement between the non-viable and non-perfused tumor fractions. This complicates the classification of tumor as non-viable solely based on the lack of contrast enhancement after HIFU in a setting in which tumors were already relatively non-perfused before treatment.

Nevertheless, pharmacokinetic analysis can still give additional insights in uptake-kinetics and thereby provide information on changes in the underlying vascular status in the zone peripheral to the central ablation volume. Histogram and cluster analysis (Figure 4, 5 and 6) of the pharmacokinetic parameters in the perfused pixels showed that there were subtle yet significant HIFU-induced changes in the pharmacokinetic parameter values in the areas surrounding the non-perfused volume. Since in two clusters the fraction of pixels significantly increased directly after HIFU treatment (Figure 6), these alterations were assumed to be treatment-associated. The composition of the clusters was very similar directly and at 3 days after HIFU treatment, which indicated that there were no apparent changes in contrast agent uptake-kinetics in the perfused tumor tissue between these time points. One of the treatment-associated clusters was characterized by a low K^{trans} and high v_e (yellow cluster) and the other by a low K^{trans} and low v_e (red cluster) combination (Table 1). The uptake-kinetics (Figure 5) characterizing the region with low K^{trans} and high v_e could be explained by a more difficult contrast agent access due to HIFU-induced

vascular congestion and hemorrhage, but a higher capacity for accumulation due to the presence of vacuolation and structural disruption in the extravascular tissue space. The low K^{trans} and low v_e in the other cluster with a treatment-associated increase in fraction of pixels (red cluster) was likely caused by more severe vascular damage, which may include vascular disruption, congestion and hemorrhage. Regions with these types of vascular characteristics around the central region of coagulative necrosis were previously also identified with DCE-MRI analysis and confirmed by extensive histological evaluation in a study on HIFU treatment of rabbit thigh muscle (31).

Pixels in the clusters with treatment-associated changes (yellow and red clusters) were located more closely to the non-perfused pixels than pixels in the other clusters (Figure 7). In addition, H&E staining confirmed the presence of tumor regions with structural disruption and hemorrhage after HIFU (Figure 8). Vascular endothelium (CD31) and hypoxia (glut-1) dual staining was performed to gain more insight in the cause and consequences of the treatment-associated changes in the perfused tumor pixels. Since the pixels in the clusters with treatment-associated changes (yellow and red clusters) were located more closely to the non-perfused pixels than pixels in the other clusters (Figure 7), a section close to the non-perfused tumor and a remote section were selected for these histological analyses. No decreased vascular density could be observed in the 'Near non-viable' tumor tissue compared to the 'Remote' tumor tissue (Figure 9). This suggested that the increased fraction of pixels in the red and yellow cluster, both characterized by a low K^{trans}, was mainly a result of a decreased vascular function rather than a reduction of microvascular density. The decreased vascular function was also suggested by the higher glut-1 intensity in these regions. These findings were in agreement with the observed structural disruption and hemorrhage on H&E staining (Figure 8). Furthermore, the higher glut-1 intensity indicated that the observed treatment-associated changes in vascular status may have consequences for tumor oxygenation. Association of low K^{trans} and v_e values in non-necrotic tumor regions with hypoxic tumor tissue has been previously shown by Egeland et al. (46).
However, although the observed changes in the fractions of pixels in the different clusters were induced by HIFU treatment and histology provided information on the causes and consequences of these changes, the kinetic uptake characteristics of the red and yellow clusters cannot be regarded as specific for HIFU-treated tumor based on the presented results. The relatively high fraction of pixels in the red cluster before treatment (Figure 6), indicates that pixels with these characteristics can be naturally present in this tumor model. This could be explained by the fact that for this tumor model perfusion was relatively low in the tumor center. Therefore, most likely hypoxic regions with an impaired perfusion are naturally present. The large extent of poorly perfused tumor tissue in the non-treated tumors was rather unexpected, because it has been previously described that subcutaneous CT26 tumors are generally well-vascularized (47) with limited necrosis (48). The overall lower perfusion observed in the present study could be caused by the difference in inoculation site (hind limb in our study vs. back in the referred studies). Application of the cluster analysis in better perfused tumor models could potentially allow for the detection of more pronounced

HIFU-induced changes in contrast agent uptake-kinetics and clusters that are more specific for HIFU-induced vascular alterations. The MRI measurements could not be performed earlier after tumor cell inoculation, because a minimal tumor volume of approximately 400 mm^3 was required during HIFU treatment to prevent substantial damage to the surrounding muscle tissue.

The HIFU treatment generally led to a decreased blood flow in the region around the coagulated zone. No evidence for an increased blood flow or enhanced microvascular permeability due to mild hyperthermia was observed. Hyperthermia of 43.5 °C has been shown to induce a gradual perfusion increase during the first 30 min after treatment, followed by a substantial decrease in perfusion up to 24 h after treatment (49). In our case, the heating times were most likely too short to induce any considerable perfusion increase. It is of key importance to verify that the hyperthermic conditions have indeed led to tumor regions with such vascular status in case one would want to exploit the increased perfusion or vascular permeability for adjuvant therapies (25). The delivery of chemotherapeutics in the tumor tissue is more effective in better-perfused tumors with permeabilized blood vessels. In addition, radiotherapy may become more effective, since an increase in perfusion leads to higher levels of oxygen, which acts as a radiosensitizer. In contrast, decreased microvascular functionality of the residual tumor tissue, as observed by DCE-MRI and histology in the present study, could severely affect adjuvant therapies. In addition, presence of hypoxic tumor cells after HIFU treatment may increase the risk of tumor progression, since hypoxic conditions can stimulate the pathway of angiogenesis (50,51). The cluster analysis of DCE-MRI data performed in the present study provides a way to non-invasively identify regions with such distinct vascular characteristics that are potentially clinically relevant with respect to adjuvant therapies.
Additional histological analysis, in which the clusters with specific vascular characteristics are spatially compared to histological features, could give further insights in the underlying effects causing the observed vascular changes. The use of MRI-visible and histology-visible fiducial markers or tissue-marking dyes could aid in retrieving the MRI slice orientation on histology and thereby enable more direct histological validation of the cluster results (52). In order to establish exact spatial registration between the clustering results and histological data, a multi-step registration process, involving an intermediate ex-vivo MRI scan to account for tissue changes caused by tumor excision and histological processing, may be required (53).

Furthermore, the histological analysis could be extended in order to allow for a more complete assessment of vascular status after HIFU treatment. The combined glut-1 and CD31 staining represents a relatively indirect evaluation of vascular function and is therefore probably not sensitive enough to spatially differentiate between the different clusters. Infusion of the fluorescent vascular perfusion marker Hoechst (54-56), or vascular permeability marker Evans Blue (57,58), would allow for a more direct and complete assessment of the tumor vascular characteristics and altered tumor vascular status after HIFU treatment.

HIFU treatment was performed outside the MR system, since the preclinical therapeutic ultrasound transducer is not MR-compatible. In a HIFU set-up with MRI guidance, temperature maps could be acquired during the treatment allowing changes in the pharmacokinetic parameters to be compared with the applied thermal dose (31). This information would also allow for a better definition of the danger zones around the central ablation volumes and a more detailed comparison between applied thermal dose, temperature-dependent changes in uptake-kinetics and histological appearance of these regions. In addition, it would be interesting to compare the DCE-MRI results after HIFU treatment with the HIFU-induced changes in endogenous MRI parameters. Recently, we have shown that multiparametric MRI analysis based on T_1, T_2 and apparent diffusion coefficient data (33), amide proton transfer imaging (59) and $T_{1\rho}$ mapping (60) are all promising methods for the identification of HIFU-treated tumor tissue. Inclusion of these methods may improve discrimination between non-perfused viable and non-perfused non-viable regions (61). In addition, T_2^* measurements could supplement the DCE-MRI acquisition for the identification of vascular changes after HIFU treatment, since T_2^* has been shown to strongly correlate with the extent of intratumoral hemorrhage (62).

Measurements performed longitudinally during a longer time period after HIFU treatment would give further insight in the temporal response of tumor tissue to HIFU treatment. The DCE-MRI data in the current study were acquired up to 3 days after treatment. At a later time point after HIFU, repair processes such as regeneration, fibrosis and revascularization are expected that could alter the pharmacokinetic parameter values (26). In addition, it would be of interest whether early changes in contrast agent uptake-kinetics can be of prognostic value for the ultimate fate of the tissue.

In conclusion, it was demonstrated that analysis of DCE-MRI data by means of cluster analysis on pharmacokinetic parameters can be used to identify regions with different contrast agent uptake-kinetics after HIFU treatment, that may be reflective of their vascular status. In addition to the commonly performed analysis of non-perfused tumor volume after HIFU treatment, the presented methodology gives additional insight in uptake-kinetics in the transition zone adjacent to central ablation volume. This method could aid in assessment of the consequences of the different vascular alterations after HIFU for the microenvironment and fate of the tissue and the sensitivity of the tumor to additional therapies.

6.5. Acknowledgements

The authors acknowledge Ralf Seip from Philips Research for his advice on the HIFU treatment settings. This research was supported by the Center for Translational Molecular Medicine (VOLTA).

6.6. References

1. Hesley GK, Gorny KR, Woodrum DA. MR-guided focused ultrasound for the treatment of uterine fibroids. Cardiovasc Intervent Radiol 2013;36(1):5-13.
2. Voogt MJ, Trillaud H, Kim YS, Mali WP, Barkhausen J, Bartels LW, Deckers R, Frulio N, Rhim H, Lim HK, Eckey T, Nieminen HJ, Mougenot C, Keserci B, Soini J, Vaara T, Kohler MO, Sokka S, van den Bosch MA. Volumetric feedback ablation of uterine fibroids using magnetic resonance-guided high intensity focused ultrasound therapy. Eur Radiol 2012;22(2):411-417.
3. Napoli A, Anzidei M, Ciolina F, Marotta E, Cavallo Marincola B, Brachetti G, Di Mare L, Cartocci G, Boni F, Noce V, Bertaccini L, Catalano C. MR-guided high-intensity focused ultrasound: current status of an emerging technology. Cardiovasc Intervent Radiol 2013;36(5):1190-1203.
4. Schmitz AC, Gianfelice D, Daniel BL, Mali WP, van den Bosch MA. Image-guided focused ultrasound ablation of breast cancer: current status, challenges, and future directions. Eur Radiol 2008;18(7):1431-1441.
5. Merckel LG, Bartels LW, Kohler MO, van den Bongard HJ, Deckers R, Mali WP, Binkert CA, Moonen CT, Gilhuijs KG, van den Bosch MA. MR-guided high-intensity focused ultrasound ablation of breast cancer with a dedicated breast platform. Cardiovasc Intervent Radiol 2013;36(2):292-301.
6. Murat FJ, Poissonnier L, Pasticier G, Gelet A. High-intensity focused ultrasound (HIFU) for prostate cancer. Cancer Control 2007;14(3):244-249.
7. Rouviere O, Girouin N, Glas L, Ben Cheikh A, Gelet A, Mege-Lechevallier F, Rabilloud M, Chapelon JY, Lyonnet D. Prostate cancer transrectal HIFU ablation: detection of local recurrences using T2-weighted and dynamic contrast-enhanced MRI. Eur Radiol 2010;20(1):48-55.
8. Kirkham AP, Emberton M, Hoh IM, Illing RO, Freeman AA, Allen C. MR imaging of prostate after treatment with high-intensity focused ultrasound. Radiology 2008;246(3):833-844.
9. Rouviere O, Gelet A, Crouzet S, Chapelon JY. Prostate focused ultrasound focal therapy--imaging for the future. Nat Rev Clin Oncol 2012;9(12):721-727.
10. Leslie T, Ritchie R, Illing R, Ter Haar G, Phillips R, Middleton M, Bch B, Wu F, Cranston D. High-intensity focused ultrasound treatment of liver tumours: post-treatment MRI correlates well with intra-operative estimates of treatment volume. Br J Radiol 2012;85(1018):1363-1370.
11. Wijlemans JW, Bartels LW, Deckers R, Ries M, Mali WP, Moonen CT, van den Bosch MA. Magnetic resonance-guided high-intensity focused ultrasound (MR-HIFU) ablation of liver tumours. Cancer Imaging 2012;12:387-394.
12. Leslie TA, Kennedy JE, Illing RO, Ter Haar GR, Wu F, Phillips RR, Friend PJ, Roberts IS, Cranston DW, Middleton MR. High-intensity focused ultrasound ablation of liver tumours: can radiological assessment predict the histological response? Br J Radiol 2008;81(967):564-571.
13. Tempany CM, McDannold NJ, Hynynen K, Jolesz FA. Focused ultrasound surgery in oncology: overview and principles. Radiology 2011;259(1):39-56.
14. Kennedy JE. High-intensity focused ultrasound in the treatment of solid tumours. Nat Rev Cancer 2005;5(4):321-327.

15. Hynynen K. MRI-guided focused ultrasound treatments. Ultrasonics 2010;50(2):221-229.
16. ter Haar G. Therapeutic applications of ultrasound. Prog Biophys Mol Biol 2007;93(1-3):111-129.
17. Kohler MO, Mougenot C, Quesson B, Enholm J, Le Bail B, Laurent C, Moonen CT, Ehnholm GJ. Volumetric HIFU ablation under 3D guidance of rapid MRI thermometry. Med Phys 2009;36(8):3521-3535.
18. Ishihara Y, Calderon A, Watanabe H, Okamoto K, Suzuki Y, Kuroda K, Suzuki Y. A precise and fast temperature mapping using water proton chemical shift. Magn Reson Med 1995;34(6):814-823.
19. de Senneville BD, Mougenot C, Quesson B, Dragonu I, Grenier N, Moonen CT. MR thermometry for monitoring tumor ablation. Eur Radiol 2007;17(9):2401-2410.
20. Zhou YF. High intensity focused ultrasound in clinical tumor ablation. World J Clin Oncol 2011;2(1):8-27.
21. Venkatesan AM, Partanen A, Pulanic TK, Dreher MR, Fischer J, Zurawin RK, Muthupillai R, Sokka S, Nieminen HJ, Sinaii N, Merino M, Wood BJ, Stratton P. Magnetic resonance imaging-guided volumetric ablation of symptomatic leiomyomata: correlation of imaging with histology. J Vasc Interv Radiol 2012;23(6):786-794 e784.
22. Kim YS, Lim HK, Kim JH, Rhim H, Park BK, Keserci B, Kohler MO, Bae DS, Kim BG, Lee JW, Kim TJ, Sokka S, Lee JH. Dynamic contrast-enhanced magnetic resonance imaging predicts immediate therapeutic response of magnetic resonance-guided high-intensity focused ultrasound ablation of symptomatic uterine fibroids. Invest Radiol 2011;46(10):639-647.
23. Vaupel PW, Kelleher DK. Pathophysiological and vascular characteristics of tumours and their importance for hyperthermia: heterogeneity is the key issue. Int J Hyperthermia 2010;26:211-223.
24. Kong G, Braun RD, Dewhirst MW. Characterization of the effect of hyperthermia on nanoparticle extravasation from tumor vasculature. Cancer Res 2001;61(7):3027-3032.
25. Chu KF, Dupuy DE. Thermal ablation of tumours: biological mechanisms and advances in therapy. Nat Rev Cancer 2014;14(3):199-208.
26. Cheng HL, Purcell CM, Bilbao JM, Plewes DB. Usefulness of contrast kinetics for predicting and monitoring tissue changes in muscle following thermal therapy in long survival studies. J Magn Reson Imaging 2004;19(3):329-341.
27. Luo W, Zhou X, Gong X, Zheng M, Zhang J, Guo X. Study of sequential histopathologic changes, apoptosis, and cell proliferation in rabbit livers after high-intensity focused ultrasound ablation. J Ultrasound Med 2007;26(4):477-485.
28. Khiat A, Gianfelice D, Amara M, Boulanger Y. Influence of post-treatment delay on the evaluation of the response to focused ultrasound surgery of breast cancer by dynamic contrast enhanced MRI. Br J Radiol 2006;79(940):308-314.
29. Tofts PS, Brix G, Buckley DL, Evelhoch JL, Henderson E, Knopp MV, Larsson HB, Lee TY, Mayr NA, Parker GJ, Port RE, Taylor J, Weisskoff RM. Estimating kinetic parameters from dynamic contrast-enhanced T(1)-weighted MRI of a diffusable tracer: standardized quantities and symbols. J Magn Reson Imaging 1999;10:223-232.
30. Hijnen NM, Heijman E, Kohler MO, Ylihautala M, Ehnholm GJ, Simonetti AW, Grull H. Tumour hyperthermia and ablation in rats using a clinical MR-HIFU system

equipped with a dedicated small animal set-up. Int J Hyperthermia 2012;28(2):141-155.
31. Cheng HL, Purcell CM, Bilbao JM, Plewes DB. Prediction of subtle thermal histopathological change using a novel analysis of Gd-DTPA kinetics. J Magn Reson Imaging 2003;18(5):585-598.
32. Seip R, Chin CT, Hall CS, Raju BI, Ghanem A, Tiemann K. Targeted ultrasound-mediated delivery of nanoparticles: on the development of a new HIFU-based therapy and imaging device. IEEE Trans Biomed Eng 2010;57(1):61-70.
33. Hectors SJ, Jacobs I, Strijkers GJ, Nicolay K. Multiparametric MRI analysis for the identification of high intensity focused ultrasound-treated tumor tissue. PLoS One 2014;9(6):e99936.
34. Karlsson M, Nordell B. Phantom and in vivo study of the Look-Locher T1 mapping method. Magn Reson Imaging 1999;17(10):1481-1488.
35. Kleppesto M, Larsson C, Groote I, Salo R, Vardal J, Courivaud F, Bjornerud A. T2*-correction in dynamic contrast-enhanced MRI from double-echo acquisitions. J Magn Reson Imaging 2014;39(5):1314-1319.
36. Yu Y, Jiang Q, Wang H, Bao S, Haacke EM, Hu J. Quantitative Perfusion and Permeability Analysis of Animal Brain Using Dual echo DCE-MRI. Proceedings of the 19th ISMRM Annual Meeting, Montréal, Canada 2011.
37. Vander Elst L, Raynaud J-S, Vives V, Santus R, Louin G, Robert P, Port M, Corot C, Muller R. Comparative Relaxivities and Efficacies of Gadolinium-based Commercial Contrast Agents. Proceedings of the 21st ISMRM Annual Meeting, Salt Lake City, USA 2013.
38. Tofts PS, Kermode AG. Measurement of the blood-brain barrier permeability and leakage space using dynamic MR imaging. 1. Fundamental concepts. Magn Reson Med 1991;17(2):357-367.
39. Fruytier AC, Magat J, Colliez F, Jordan B, Cron G, Gallez B. Dynamic contrast-enhanced MRI in mice at high field: Estimation of the arterial input function can be achieved by phase imaging. Magn Reson Med 2013.
40. Coer A, Legan M, Stiblar-Martincic D, Cemazar M, Sersa G. Comparison of two hypoxic markers: pimonidazole and glucose transporter 1 (Glut-1). 11th Mediterranean Conference on Medical and Biological Engineering and Computing 2007, Vols 1 and 2 2007;16(1-2):465-468.
41. Hennings L, Kaufmann Y, Griffin R, Siegel E, Novak P, Corry P, Moros EG, Shafirstein G. Dead or alive? Autofluorescence distinguishes heat-fixed from viable cells. Int J Hyperthermia 2009;25(5):355-363.
42. Wu F, Chen WZ, Bai J, Zou JZ, Wang ZL, Zhu H, Wang ZB. Tumor vessel destruction resulting from high-intensity focused ultrasound in patients with solid malignancies. Ultrasound Med Biol 2002;28(4):535-542.
43. Hynynen K, Chung AH, Colucci V, Jolesz FA. Potential adverse effects of high-intensity focused ultrasound exposure on blood vessels in vivo. Ultrasound Med Biol 1996;22(2):193-201.
44. Gillies RJ, Schornack PA, Secomb TW, Raghunand N. Causes and effects of heterogeneous perfusion in tumors. Neoplasia 1999;1(3):197-207.

45. Tozer GM, Lewis S, Michalowski A, Aber V. The Relationship between Regional Variations in Blood-Flow and Histology in a Transplanted Rat Fibrosarcoma. Brit J Cancer 1990;61(2):250-257.
46. Egeland TA, Gulliksrud K, Gaustad JV, Mathiesen B, Rofstad EK. Dynamic contrast-enhanced-MRI of tumor hypoxia. Magn Reson Med 2012;67(2):519-530.
47. Ogawara K, Un K, Minato K, Tanaka K, Higaki K, Kimura T. Determinants for in vivo anti-tumor effects of PEG liposomal doxorubicin: importance of vascular permeability within tumors. Int J Pharm 2008;359(1-2):234-240.
48. Aulino P, Berardi E, Cardillo VM, Rizzuto E, Perniconi B, Ramina C, Padula F, Spugnini EP, Baldi A, Faiola F, Adamo S, Coletti D. Molecular, cellular and physiological characterization of the cancer cachexia-inducing C26 colon carcinoma in mouse. BMC Cancer 2010;10:363.
49. Song CW, Lin JC, Chelstrom LM, Levitt SH. The kinetics of vascular thermotolerance in SCK tumors of A/J mice. Int J Radiat Oncol Biol Phys 1989;17(4):799-802.
50. Moon EJ, Sonveaux P, Porporato PE, Danhier P, Gallez B, Batinic-Haberle I, Nien YC, Schroeder T, Dewhirst MW. NADPH oxidase-mediated reactive oxygen species production activates hypoxia-inducible factor-1 (HIF-1) via the ERK pathway after hyperthermia treatment. Proc Natl Acad Sci U S A 2010;107(47):20477-20482.
51. Wu L, Fu Z, Zhou S, Gong J, Liu CA, Qiao Z, Li S. HIF-1alpha and HIF-2alpha: siblings in promoting angiogenesis of residual hepatocellular carcinoma after high-intensity focused ultrasound ablation. PLoS One 2014;9(2):e88913.
52. McGrath DM, Vlad RM, Foltz WD, Brock KK. Technical note: fiducial markers for correlation of whole-specimen histopathology with MR imaging at 7 tesla. Med Phys 2010;37(5):2321-2328.
53. Alic L, Haeck JC, Bol K, Klein S, van Tiel ST, Wielepolski PA, de Jong M, Niessen WJ, Bernsen M, Veenland JF. Facilitating tumor functional assessment by spatially relating 3D tumor histology and in vivo MRI: image registration approach. PLoS One 2011;6(8):e22835.
54. Reinhold HS, Visser JW. In vivo fluorescence of endothelial cell nuclei stained with the dye Bis-benzamide H 33342. Int J Microcirc Clin Exp 1983;2(2):143-146.
55. Smith KA, Hill SA, Begg AC, Denekamp J. Validation of the fluorescent dye Hoechst 33342 as a vascular space marker in tumours. Br J Cancer 1988;57(3):247-253.
56. Fallowfield ME. Vascular volume in B16 allografts and human melanoma xenografts estimated by means of Hoechst 33342. J Pathol 1989;157(3):249-252.
57. Matsumura Y, Maeda H. A new concept for macromolecular therapeutics in cancer chemotherapy: mechanism of tumoritropic accumulation of proteins and the antitumor agent smancs. Cancer Res 1986;46(12 Pt 1):6387-6392.
58. Graff BA, Bjornaes I, Rofstad EK. Microvascular permeability of human melanoma xenografts to macromolecules: relationships to tumor volumetric growth rate, tumor angiogenesis, and VEGF expression. Microvasc Res 2001;61(2):187-198.
59. Hectors SJ, Jacobs I, Strijkers GJ, Nicolay K. Amide proton transfer imaging of high intensity focused ultrasound-treated tumor tissue. Magn Reson Med 2014;72(4):1113-1122.

60. Hectors SJ, Moonen RP, Strijkers GJ, Nicolay K. T1ρ mapping for the evaluation of High Intensity Focused Ultrasound tumor treatment. Magn Reson Med 2014.
61. Thoeny HC, De Keyzer F, Chen F, Ni Y, Landuyt W, Verbeken EK, Bosmans H, Marchal G, Hermans R. Diffusion-weighted MR imaging in monitoring the effect of a vascular targeting agent on rhabdomyosarcoma in rats. Radiology 2005;234(3):756-764.
62. Tosaka M, Sato N, Hirato J, Fujimaki H, Yamaguchi R, Kohga H, Hashimoto K, Yamada M, Mori M, Saito N, Yoshimoto Y. Assessment of hemorrhage in pituitary macroadenoma by T2*-weighted gradient-echo MR imaging. AJNR Am J Neuroradiol 2007;28(10):2023-2029.

Chapter 7

Multiparametric Magnetic Resonance Imaging analysis for the Evaluation of Magnetic Resonance-guided High Intensity Focused Ultrasound tumor treatment

Igor Jacobs[1,*], Stefanie JCG Hectors[1,*], Edwin Heijman[2], Jochen Keupp[3], Monique Berben[2], Gustav J Strijkers[1,4], Holger Grüll[1,2], Klaas Nicolay[1]

[1] Biomedical NMR, Department of Biomedical Engineering, Eindhoven University of Technology, Eindhoven, The Netherlands
[2] Oncology Solutions, Philips Research Europe, Eindhoven, The Netherlands
[3] Tomographic Imaging Systems, Philips Research Europe, Hamburg, Germany
[4] Biomedical Engineering and Physics, Academic Medical Center, University of Amsterdam, Amsterdam, The Netherlands

* These authors contributed equally to this work.

Submitted

Abstract

For the clinical application of High Intensity Focused Ultrasound (HIFU) for thermal ablation of malignant tumors, accurate treatment evaluation is of key importance. In this study, we have employed a multiparametric MRI protocol, consisting of quantitative $T_{1,}$ T_2, ADC, amide proton transfer (APT), $T_{1\rho}$ and DCE-MRI measurements, to evaluate MR-guided HIFU treatment of subcutaneous tumors in rats. K-means clustering using all different combinations of the endogenous contrast MRI parameters (feature vectors) was performed to segment the multiparametric data into tissue populations with similar MR parameter values. The optimal feature vector for identification of the extent of non-viable tumor tissue after HIFU treatment was determined by quantitative comparison between clustering-derived and histology-derived non-viable tumor fractions. The highest one-to-one correspondence between these clustering-based and histology-based non-viable tumor fractions was observed for feature vector {ADC, APT-weighted signal} (R^2 to line of identity ($R^2_{y=x}$)=0.92) and the strongest agreement was seen at 3 days after HIFU ($R^2_{y=x}$=0.97). To compare the multiparametric MRI analysis results with conventional HIFU monitoring and evaluation methods, the histology-derived non-viable tumor fractions were also quantitatively compared with non-perfused tumor fractions (derived from the level of contrast enhancement in the DCE-MRI measurements) and 240CEM tumor fractions (i.e. thermal dose>240 cumulative equivalent minutes at 43 °C). The correlation between histology-derived non-viable tumor fractions directly after HIFU and the 240CEM fractions was high, but not significant. The non-perfused fractions overestimated the extent of non-viable tumor tissue directly after HIFU, whereas an underestimation was observed at 3 days after HIFU.
In conclusion, we have shown that a multiparametric MR analysis, based on the ADC and the APT-weighted signal, can determine the extent of non-viable tumor tissue at 3 days after HIFU treatment. We expect that this method can be incorporated in the current clinical workflow of MR-HIFU ablation therapies.

7.1. Introduction

High Intensity Focused Ultrasound (HIFU) is a promising technique for the non-invasive thermal treatment of tumors (1,2). For the clinical introduction of HIFU for thermal ablation of malignant tumors, accurate treatment planning, monitoring and therapy assessment are of critical importance to ensure a successful and safe treatment. To fulfill these needs, HIFU treatment is generally performed under image guidance, either by magnetic resonance imaging (MRI) or ultrasound. In an MR-guided HIFU (MR-HIFU) system, the HIFU transducer is e.g. integrated in the patient bed of a clinical MR scanner. MR thermometry can be utilized to monitor the temperature evolution in real-time (3) allowing for the definition of thermal dose areas which are lethal to the tumor tissue (i.e. tumor regions in which the delivered thermal dose was at least 240 cumulative equivalent minutes (CEM) at 43 °C) (4,5). In addition, the excellent soft tissue contrast of MRI offers unique possibilities for treatment planning and evaluation.

Clinical evaluation of HIFU treatment with MRI has been mainly restricted to T_2-weighted and contrast-enhanced T_1-weighted imaging. Although these methods provide useful information about treatment response (6-10), they often lack the sensitivity and/or specificity to accurately identify the non-viable tumor tissue after HIFU (10-12).

We have previously shown that HIFU-treated non-viable tumor tissue can be accurately identified at 3 days after HIFU treatment using a multiparametric MRI analysis of combined T_1, T_2 and apparent diffusion coefficient (ADC) data (13). However, directly after treatment, the multiparametric analysis performed less well with respect to the identification of non-viable tumor tissue. Other MRI methods, especially those that are sensitive to protein denaturation and aggregation, which occur instantly during HIFU treatment, may be more suitable for direct treatment evaluation. Amide proton transfer (APT) imaging is a very promising method for tumor tissue characterization (14-19) and treatment evaluation (20). APT imaging selectively measures the saturation transfer from amide protons of mobile proteins and peptides to bulk water protons. Another MR parameter that is sensitive to macromolecular changes in the tumor tissue is the longitudinal relaxation time in the rotating frame ($T_{1\rho}$). $T_{1\rho}$ is primarily sensitive to protein-water interactions. In recent studies we have shown that APT imaging and $T_{1\rho}$ mapping are both promising MRI methods for the detection of HIFU-induced macromolecular tissue changes (21,22).

We hypothesized that inclusion of these advanced MR contrast parameters in the previously described multiparametric analysis leads to a more accurate identification of successfully HIFU-treated tumor tissue. Therefore, the goal of the current study was to identify a subset of MRI parameters that are suitable for accurate early HIFU therapy assessment. In addition, we aimed to compare the performance of this optimal multiparametric analysis with conventional HIFU monitoring and evaluation methods, namely MR thermometry and contrast-enhanced MRI. Such quantitative comparison with conventional techniques could not be performed in our previous studies (13,21,22), mainly because the HIFU treatment was performed outside the MR system. In the present study, the HIFU treatment was performed in a rat tumor model on a clinical 3 Tesla MR-HIFU system, allowing for real-time acquisition of MR

temperature maps during treatment. The multiparametric MRI protocol, consisting of quantitative T_1, T_2, ADC, APT and $T_{1\rho}$ mapping was performed in the same MR-HIFU system before, directly after and at 3 days after HIFU treatment. In addition, dynamic contrast-enhanced MRI (DCE-MRI) was performed after HIFU to assess changes in the tumor vascular status and to determine the non-perfused tumor volume after treatment. Cluster analysis, that segments the multiparametric data into tissue populations with similar MR parameter values, was performed on all possible combinations of the endogenous MR contrast parameters. The optimal subset of MRI parameters for HIFU treatment evaluation was determined by quantitative comparison between clustering-derived and histology-derived non-viable tumor fractions. The performance of the proposed multiparametric analysis with respect to the identification of non-viable tumor tissue was compared to contrast-enhanced MRI and MR thermometry by quantitative correlation analyses between clustering-derived non-viable tumor fractions, non-perfused tumor fractions, 240CEM tumor fractions (i.e. the fraction of the tumor in which the thermal dose exceeded 240CEM) and histology-derived non-viable tumor fractions.

7.2. Experimental

7.2.1. Ethics statement

All animal experiments were performed according to the Directive 2010/63/EU of the European Commission and approved by the Animal Care and Use Committee of Maastricht University (protocol: 2012-171).

7.2.2. Rat tumor model

5 to 7-week old female Fischer 344 rats (Charles River, Maastricht, The Netherlands) were inoculated with $1*10^6$ GS 9L cells (early passages of the original batch obtained from Public Health England, London, UK) in 100 µL phosphate buffered saline (PBS, Sigma-Aldrich, St. Louis, MO, USA), subcutaneously in the left hind limb. The average tumor size at the time of the first MRI examination was 878±533 mm^3 as determined from region-of-interest (ROI) analysis on the anatomical MR images.

7.2.3. Study design

The tumor-bearing rats underwent MRI directly before (n=12), directly after (n=12) and 3 days after (n=6) HIFU treatment. A non-treated control group (n=6) was included that underwent MRI at the same time points, but did not undergo MR-HIFU treatment. Immediately after the final MRI measurement, rats were sacrificed by cervical dislocation and tumors were excised for histological analysis. This study design resulted in three different groups for histology; rats that were sacrificed immediately after the MRI scan directly after MR-HIFU ablation (referred to as 'Directly after HIFU', n=6), rats that were sacrificed directly after the MRI scan at 3 days after MR-HIFU ablation (referred to as '3 days after HIFU', n=6) and a non-treated control group (referred to as 'Control', n=6).

7.2.4. MR-guided HIFU treatment

7.2.4.1. MR-HIFU system and small animal setup

HIFU treatment was performed using a clinical 3T MR-HIFU system (Philips Sonalleve, Philips Healthcare, Vantaa, Finland). A dedicated small animal HIFU-compatible MR receiver coil (Philips Healthcare, Vantaa, Finland) with a multi-channel volumetric design was used to obtain optimal signal to noise ratio. The utilized MR-HIFU system and small animal set-up have been described in detail previously (23).

7.2.4.2. Animal handling

Animals were anesthetized with 3% isoflurane in medical air (0.6 L/min) and maintained with 1.0-2.5% isoflurane during the HIFU treatment and MRI measurements. At least 30 minutes prior to HIFU treatment, precautionary analgesia was given (carprofen; rhymadyl, 4 mg/kg s.c.). An equal dose of analgesia was administered to the control animals before the first MRI measurement. For optimal coupling of the ultrasound to the skin, fur was removed from the tumor and hind limb by shaving and application of a depilatory cream (Veet, Hoofddorp, The Netherlands). During MRI measurements and MR-HIFU treatment, the animal's respiration rate was monitored with a pressure balloon sensor (Graseby, Smiths Medical, St Paul, MN, USA) and core body temperature was monitored using a rectal optical temperature probe (Neoptix, Québec City, Canada) and maintained at 37 °C using a custom-made warm-water circuit with temperature feedback. The tumor-bearing paw was submerged in a mixture of degassed ultrasound gel and water. Similar to regulation of the animal's temperature, the temperature of the gel/water mixture was monitored and maintained at 37 °C using an optical temperature probe and a warm-water circuit. More specific details on the used MR-HIFU system can be found elsewhere (23).

7.2.4.3. HIFU treatment

A 4-mm diameter treatment cell was positioned within the tumor using anatomical MR images. Volumetric thermal ablation of the tumor tissue was performed with a 256-element spherical phased array transducer (aperture=13 cm, focal length=12 cm, ellipsoid focal spot size (-6 dB)=1x1x7 mm^3). A single focus point was electronically steered along a circular trajectory, consisting of 8 points (50 ms sonication time/point), perpendicular to the direction of ultrasound propagation, as described previously (23,24). The order of sonication was chosen in such a way that the distance between successive points was maximized, ensuring an even temperature rise over the entire circle. Ultrasound was applied as a continuous wave with a frequency of 1.44 MHz. Thermal ablation was performed by 90 seconds of sonication at 35 W acoustic power (resulting in an average maximum ablation temperature of 58.5±5.6 °C (n=12)). The sonication time was intentionally kept constant rather than using the MR thermometry-based feedback control to stop the sonication when a certain target temperature or thermal dose was reached. It has been previously described that HIFU treatment using a constant power and sonication time without feedback results in a wider spread of temperatures in the treatment volume and subsequently to a larger variation in the thermal lesion size, as compared to sonications with MR thermometry feedback (25). Since a large spread in thermal lesion size and subsequently a large

range of non-viable tumor fractions was beneficial for the correlation analyses between MRI-derived and histology-derived non-viable tumor fractions in the current study, the sonications were performed without thermometry feedback. Tumors were only partially treated with a single treatment cell, which was smaller than the typical tumor diameter, to allow for the presence of both treated and untreated tumor tissue in the multiparametric MR images.

7.2.4.4. MRI protocol

The MRI protocol started with a T_2*-weighted 3D gradient-echo acquisition (TR=15 ms, TE=12 ms, field of view (FOV)=280x280x20 mm^3, acquisition matrix=256x256x10, reconstruction matrix=1008x1008x10, reconstructed voxel size=0.28x0.28x2 mm^3, flip angle (FA)=10°, number of averages (NA)=2, scan duration=1 min 58 s) to check for the presence of air bubbles in the HIFU beam path or in close proximity to the tumor tissue. A relatively large FOV was chosen for this sequence in order to visualize the entire water/gel mixture surrounding the tumor-bearing paw.

The HIFU treatment cell was planned on anatomical images covering the entire tumor, acquired with a multi-slice steady-state gradient-echo sequence (TR=793 ms, TE=13 ms, FOV=40x48x20 mm^3, acquisition and reconstruction matrix=160x192x20, reconstructed voxel size=0.25x0.25x1 mm^3, FA=20°, NA=2, scan duration=5 min 6 s).

The temperature rise in the treatment area during MR-HIFU ablation was monitored with a dynamic gradient-echo segmented EPI acquisition (TR=38 ms, TE=20 ms, FOV=250x250 mm^2, acquisition matrix=176x169, reconstruction matrix=176x176, reconstructed voxel size=1.42x1.42x4.08 mm^3, FA=19.5°, EPI factor=7, NA=2, temporal resolution=4.8 s) in 3 adjacent slices perpendicular and 1 slice parallel to the acoustic beam path.

The multiparametric MRI protocol consisted of quantitative assessment of the T_1, T_2, ADC, APT-weighted signal and $T_{1\rho}$, as well as a DCE-MRI acquisition. For the HIFU-treated animals, DCE-MRI was only performed after the HIFU treatment, since the presence of the paramagnetic Gd could affect the assessment of the endogenous contrast parameters directly after treatment and induce inaccuracies in the temperature mapping due to magnetic susceptibility changes (26). The multiparametric acquisitions performed directly after treatment were started after the temperature of the tumor-bearing paw was decreased to baseline temperature again (5-10 min waiting time) to prevent influences of temperature changes on the MRI parameter estimations. The acquisitions of the multiparametric protocol were performed with a FOV of 150x150x10 mm^3 and reconstructed at a voxel size of 0.94x0.94x2 mm^3, resulting in a 3D matrix size of 160x160x5. For the DCE-MRI sequence the FOV was extended to 150x150x30 mm^3 (matrix size 160x160x15) to avoid aliasing artifacts, with the same center slice positions and reconstructed voxel size as for the other sequences. The orientation of the central slice of all imaging methods of the multiparametric MRI protocol was aligned with the central slice of the temperature mapping sequence, perpendicular to the acoustic beam axis.

T_1 mapping was performed using a 3D Look-Locker segmented gradient-echo (turbo field echo) sequence. T_1-weighted images were acquired with inversion times ranging from 18-6418 ms in steps of 100 ms. Further acquisition parameters were: TR=5.6 ms, TE=2.8 ms, FA=5°, turbo-factor 10, NA=1, scan duration: 8 min.
T_2 mapping was performed by acquisition of T_2-weighted images with TE ranging from 4.1-251.7 ms in steps of 16.5 ms using a multi-slice fast spin-echo sequence (TR=14526 ms, NA=1, scan duration=12 min 35 s).
For ADC mapping a diffusion-weighted echo planar imaging (EPI) sequence was used, with b-values of 0, 100, 200, 400, 600, 800, 1200 s/mm^2. Other imaging parameters were: TR=1000 ms, TE=71 ms, FA=90°, EPI factor=11, NA=2, scan duration=9 min 22 s.
For APT imaging, a z-spectrum was recorded using a 3D turbo gradient-echo sequence with irradiation offsets ranging from -6 to 6 ppm with 0.5 ppm steps. The saturation pulses were continuous wave RF pulses with a duration of 2 s at a saturation power level corresponding to a field amplitude of $B_{1,rms}$=1.8 μT. In addition, a control acquisition (S_0) was performed with irradiation at ~-1560 ppm. Further acquisition parameters were: TR=7.5 ms, TE=3.8 ms, FA=20°, turbo-factor=75, NA=2, scan duration=17 min 50 s. B_0 homogeneity was improved by local second-order pencil-beam shimming.
$T_{1\rho}$ was acquired with a 3D gradient-echo sequence (TR=3.6 ms, TE=2.1 ms, FA=20°, NA=8, scan duration 3 min 54 s), with a spin-lock preparation compensated for B_1 and B_0 field imperfections (27). Images were acquired with 2 different spin-lock durations (5 and 40 ms) using a spin-lock amplitude of 350 Hz.
DCE-MRI was performed with an RF-spoiled 3D T_1-weighted turbo gradient-echo sequence with the following acquisition parameters: TR=5.2 ms, TE=2.6 ms, FA=15°, NA=1, dynamic scan time=4.3 s, total scan duration=10 min 46 s. After 1 minute of pre-contrast images acquisition, a bolus of 0.2 mmol/kg Gd-DOTA (Dotarem; Guerbet, Villepente, France) with a saline flush was injected in 5 s at a rate of 3 mL/min by use of an infusion pump (Chemyx Fusion 100, Stafford, TX, USA).

The total acquisition time of the multi-slice multiparametric protocol was approximately 75 minutes.

7.2.5. Image processing and generation of parameter maps

Data analysis was performed with Mathematica 8.0 (Wolfram Research, Champaign, IL, USA) and MATLAB R2013a (MathWorks, Natick, MA, USA). Tumor ROIs were manually drawn using the image with TE=37.1 ms of the T_2 mapping dataset. Diffusion-weighted images were used as a visual reference for the correct identification of tumor tissue. Parameter maps were calculated on a pixel-by-pixel basis in each slice. Only the central slice of the multiparametric images was selected for all further analyses, since the orientation of this slice corresponded to the central slice of the temperature maps perpendicular to the HIFU beam axis. T_1 maps were generated as described previously (28). To calculate the T_2 maps, mono-exponential fitting was performed through the multi-echo data, omitting the first two echoes due to signal fluctuations. The ADC was determined by mono-exponential fitting through the signal intensities at the 4 highest b-values (400, 600, 800, 1200 s/mm^2).

For analysis of the APT data, first the minimum of the z-spectrum was determined by fitting a 23rd-order polynomial function through the z-spectrum after which the minimum of this function was calculated. An example of a fitted z-spectrum curve can be found in Supplemental Information 1 (Figure S1). Subsequently, the minimum of the z-spectrum was centered at 0 ppm and the APT-weighted signal maps were generated via a magnetization transfer asymmetry (MTR_{asym}) analysis using MTR_{asym} = (S_{sat}(-3.5 ppm)-S_{sat}(3.5 ppm))/S_0, in which S_{sat}(-3.5 ppm) and S_{sat}(3.5 ppm) are the signal intensities in the z-spectrum at -3.5 ppm and 3.5 ppm from the water frequency, respectively, and S_0 is the signal intensity in the acquisition with the saturation offset far from the water peak (~-1560 ppm). The $T_{1\rho}$ values were determined by calculation of ($t_{sl,2}$-$t_{sl,1}$)/ln($SI_{sl,1}$/$SI_{sl,2}$), where $t_{sl,1}$ and $t_{sl,2}$ are the different spin-lock durations and $SI_{sl,1}$ and $SI_{sl,2}$ are the corresponding signal intensities.
From the DCE-MRI data, dynamic T_1 values were calculated in the tumor ROIs from the dynamic signal intensities and the pre-contrast T_1 values using the signal equation for an RF-spoiled gradient-echo sequence (29). Dynamic T_1 values were converted to dynamic contrast agent concentrations ([CA]) using the relaxivity of Dotarem (3.78 $mM^{-1}s^{-1}$), which was measured *ex vivo* in rat plasma at 3 T at 37 °C. Tracer-kinetic analysis of the DCE-MRI data was performed with a custom-written MATLAB tool. The standard Tofts model (30) was fitted to the DCE-MRI data to determine the transfer constant K^{trans} and extravascular extracellular volume fraction v_e in each tumor pixel. A delay term (t_d) was included in the model to allow for a delay between bolus arrival in the blood and the tissue response. A population-averaged bi-exponential arterial input function (AIF) was used as proposed by McGrath et al. (31). The bi-exponential AIF is described by:

$$C_p(t) = \begin{cases} 0 & t < t_i \\ a_1 e^{-m_1 t} + a_2 e^{-m_2 t} & t \geq t_i \end{cases}$$

in which t_i is the injection time. The exponents of the bi-exponential function were determined based on blood kinetics data of Dotarem acquired in 3 separate female Fischer 344 rats. Blood sampling in these separate animals was performed from the saphenous vein at different time points (0.5, 2, 5, 10, 15, 20, 30 min) after contrast agent injection. The Gd^{3+} concentration in the blood samples was determined by means of Inductively Coupled Plasma Atomic Emission Spectrometry or Inductively Coupled Plasma Mass Spectrometry. The blood concentrations of Gd^{3+} were converted to plasma concentrations using a hematocrit value of 53.8%, as reported for the used rat strain (32). Subsequently, the bi-exponential model was fitted to the plasma concentration-time data points. The a_1 and a_2 parameters following from this fit were adapted such that the sum of a_1 and a_2 was equal to the theoretical peak concentration, which was calculated based on the injected dose and the rat plasma volume. These adaptations led to the following bi-exponential AIF parameters: a_1=5.38 mM, a_2=1.38 mM, m_1=2.82 min^{-1}, m_2=0.04 min^{-1}.

The Standard Tofts model was fitted to the dynamic [CA] curves using the MATLAB function lsqcurvefit, with constraints $K^{trans} \geq 0$ min^{-1}, k_{ep} (=K^{trans}/v_e) ≥0 min^{-1} and $0 \leq t_d \leq 7$ repetitions. Tumor pixels were considered non-perfused if the median dynamic

[CA] after injection was lower than 5 times the standard deviation (SD) of the data points in the dynamic [CA] curve before injection.

Maximum temperature maps were generated from the acquired MR thermometry data. Thermal dose maps were calculated using the Sapareto-Dewey equation (33) with 43 °C as reference temperature. Although the slice orientation was the same for the temperature maps and the multiparametric MR images, the image resolution and position within the slice plane of the temperature maps and multiparametric MR images were different. Therefore, registration of the temperature maps to the multiparametric images was performed by translation and interpolation in the slice plane. 240CEM thermal dose areas were defined and MR parameter changes directly after MR-HIFU treatment were related to the maximum temperature and thermal dose.
Histograms of the parameter values in the tumor pixels at the different time points were calculated for all MRI parameters to assess HIFU-induced changes in the parameter distributions.

7.2.6. Cluster analysis

k-means cluster analysis was performed to segment the multiparametric MRI data into groups of pixels, i.e. clusters, with similar MR parameter values (34). Clustering was performed on all data (i.e. of all animals (both treated and non-treated) and all time points) simultaneously. Prior to clustering, the parameter values were normalized (mean=0, standard deviation=1) to prevent scaling bias between the different MR parameters. Clustering was performed with a custom-written Mathematica tool with 2 to 6 clusters and all possible feature vectors (i.e. all different combinations of MR parameters). The pharmacokinetic parameters resulting from the DCE-MRI analysis were not included in the cluster analysis, since DCE-MRI was only performed after treatment.
After clustering with the different feature vectors, clusters were defined as non-viable if the fraction of pixels that was assigned to that cluster significantly increased after MR-HIFU ablation (either directly or at 3 days after ablation) compared to before treatment (one-sided paired Student's t-test, $P<0.05$). The remaining clusters were defined as viable. Subsequently, all tumor pixels were classified as either viable or non-viable based on the cluster to which they were assigned. Based on this classification, the k-means clustering-derived non-viable tumor fractions were calculated for each tumor and for each feature vector.

7.2.7. Histology

After sacrifice, the skin was removed from the tumor and four lines of different colors were drawn on the tumor tissue using a tissue marking dye kit (Sigma-Aldrich). The planes in which the lines were applied were perpendicular to the direction of the MRI slices, which was retrieved by using the acquired anatomical MRI images as a visual reference. The exact positioning of the four lines can be observed in Supplemental information 2 (Figure S2). Subsequently, the entire tumor was removed and put in a dedicated tissue holder. Using the applied color lines and the MRI images as reference, the tumor was cut in two pieces, such that the cutting face matched with the central

slice of the multiparametric and MR thermometry acquisitions. Subsequently, one of the pieces was processed to prepare paraffin sections and the other to prepare cryosections. For cryosections, tumors were embedded in Cryomatrix (Shandon, Thermo Scientific, Waltham, MA, USA), snap-frozen in isopentane of -40 °C and stored at -80 °C. For paraffin sections, the tumors were fixed in 4% formaldehyde solution for approximately 40 hours and then stored in 70% ethanol until they were embedded in paraffin. Both the paraffin-embedded and the snap-frozen tumor pieces were subsequently cut in 5-6 µm thick sections.
For quantitative assessment of the non-viable tumor fraction, cryosections were briefly air-dried and subsequently stained for nicotinamide adenine dinucleotide (NADH) diaphorase activity as a marker for cell viability. Tumor sections were incubated in filtered Gomori-Tris-HCl buffer of pH 7.4, with 0.71 mg/mL β-NAD reduced disodium salt hydrate (Sigma-Aldrich) and 0.29 mg/mL nitro blue tetrazolium (Sigma-Aldrich) for 1 hour at 37 °C.
The paraffin sections were used for hematoxylin and eosin (H&E; Sigma-Aldrich) staining to assess morphological tumor changes after MR-HIFU ablation.
After staining, one paraffin section and one cryosection were selected (blinded from the MRI results) for each tumor and brightfield microscopy was performed on a Pannoramic MIDI digital slide scanner (3DHistech Ltd, Budapest, Hungary) at 41x magnification to obtain images of the entire tumor section.
Analysis of the microscopy images of the NADH diaphorase-stained tumor sections was performed in Mathematica 8.0. For quantification of the non-viable tumor fraction, ROIs were manually drawn around the entire tumor tissue and around the pale non-viable tumor tissue. For each tumor the non-viable tumor fraction was determined from the ratio between the two ROI areas.

7.2.8. Comparison between MRI and histology

The cluster results of the different feature vectors were analyzed by quantitative comparison between clustering-derived and histology-derived non-viable tumor fractions. This comparison was done by assessment of the Pearson's correlation coefficient and the one-to-one correspondence between the fractions. The latter was determined by calculation of the coefficient of determination ($R^2_{y=x}$) between the data points and the line of identity. The $R^2_{y=x}$ was calculated using the following formula (35):

$$R^2{}_{y=x} = 1 - \frac{\sum(y_i - x_i)^2}{\sum {y_i}^2},$$

in which x_i and y_i are the non-viable fractions derived from histology and clustering, respectively. All groups ('Directly after HIFU', '3 days after HIFU' and 'Control') were combined in this analysis. The feature vector with the highest one-to-one correspondence between clustering-derived and histology-derived non-viable tumor fractions was selected as the optimal feature vector for the identification of non-viable tumor tissue. After selection of the optimal feature vector, the one-to-one correspondence and Pearson's correlation coefficient between clustering-derived non-viable tumor fractions and histology-derived non-viable tumor fractions were also

determined separately for the different experimental groups. The histology-derived non-viable fractions were also quantitatively compared to the DCE-MRI-derived non-perfused fractions and the 240CEM fractions, again by calculation of the $R^2_{y=x}$ and the correlation coefficient.

7.2.9. Statistical analysis

All data are shown as mean±SD. Two-sided paired t-tests were used to compare: the average parameter values in the tumor ROI at both time points after HIFU treatment with before treatment; the histograms of the endogenous contrast MRI parameters at both time points after HIFU treatment with before treatment; and the average parameter values in the 240CEM area before and directly after HIFU ablation. Two-sided t-tests assuming equal variances were used to compare: the average pharmacokinetic parameter values in the HIFU-treated and non-treated control tumors at the corresponding timepoints; and the K^{trans} and v_e histograms of the HIFU-treated and non-treated control animals at corresponding time points. The calculated Pearson's correlation coefficients were tested for significance with a one-sample t-test. For all tests, the level of significance was set to $\alpha=0.05$.

7.3. Results

7.3.1. MR parameter maps and average parameter values

Representative MR parameter maps at the different experimental time points ('Before HIFU', Directly after HIFU' and '3 days after HIFU') are shown in Figure 1A. The observed changes in the individual endogenous MR parameter values after HIFU treatment were rather subtle and heterogeneous between the different endogenous contrast parameters. The K^{trans} maps derived from the DCE-MRI measurements showed that the tumor was largely non-perfused directly after treatment, while the perfusion was partly restored at 3 days after treatment. On the maximum temperature maps (Figure 1B) a circular region was observed in which a significant temperature increase was measured. This circular region was more distinctly visible on the thermal dose maps (Figure 1B), because of the exponential increase of thermal dose at higher temperatures. The NADH-diaphorase-stained tumor section shown in Figure 1C, obtained at approximately the same position and orientation in the tumor as the MRI slice at 3 days after HIFU treatment, shows mostly non-viable tumor (pale) with a small amount of viable tumor (blue) on either side of the non-viable region.

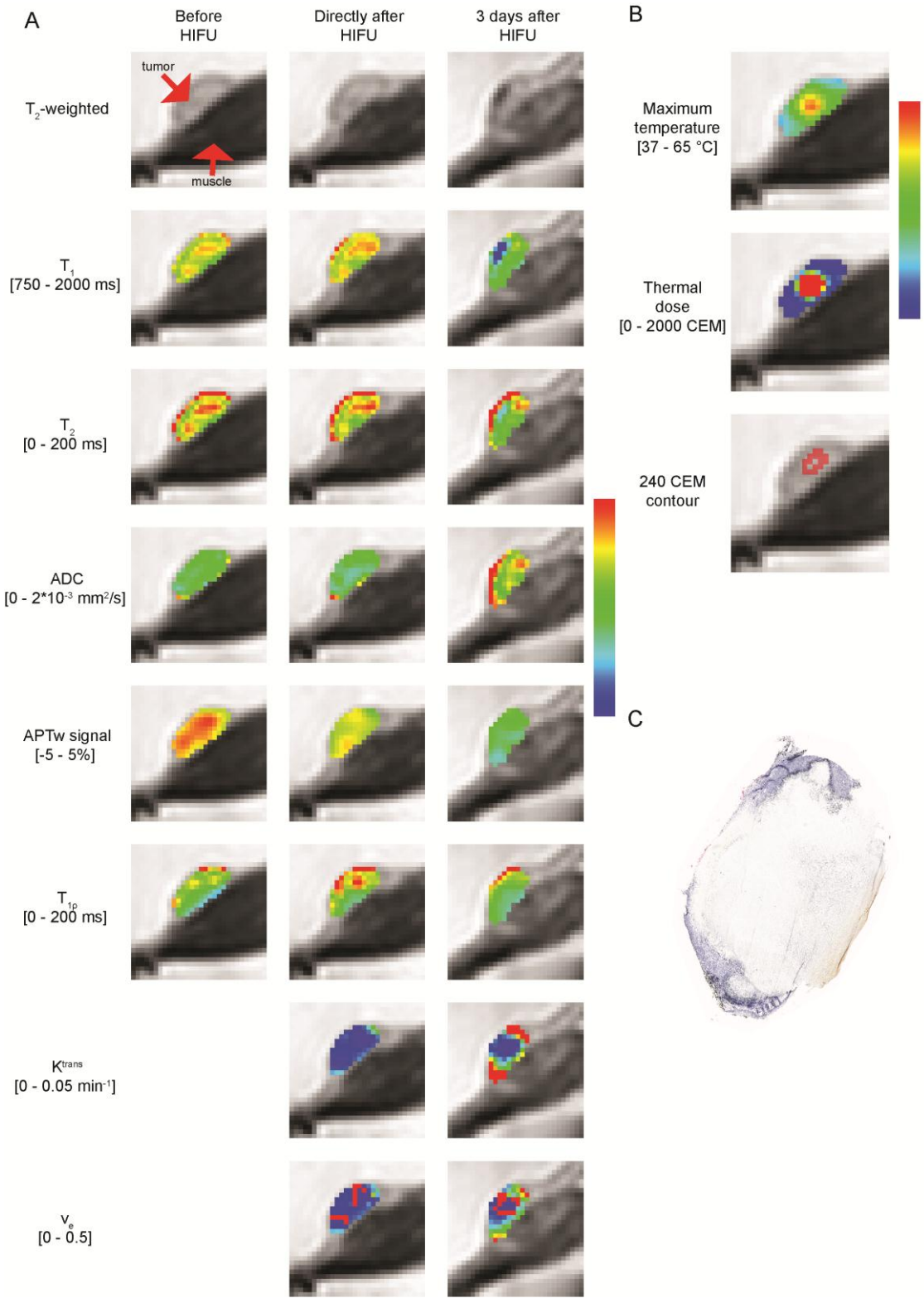

Figure 1. A) Representative T_2-weighted images and MR parameter maps (T_1, T_2, ADC, APTw signal, $T_{1\rho}$, K^{trans} and v_e) superimposed on the T_2-weighted images in the center slice of the tumor-bearing hind limb, before, directly after and at 3 days after HIFU treatment. The parameter maps of K^{trans} and v_e before HIFU are absent, since DCE-MRI was not performed at this time point. The color coding represents the MR parameter values in the tumor, of which the scaling is given by the scale bar on the right and the range is indicated on the left side of each row. B) Maps of the maximum temperature that was reached (top) and the applied thermal dose in each tumor pixel (bottom). The scale bar on the right and the numbers on the left represent the range in parameter values. C) The NADH diaphorase-stained tumor section at the same location as the shown MRI slice, excised at 3 days after HIFU treatment. The blue region is viable tumor and the pale region is non-viable tumor.

Table 1 shows average MRI parameter values in the entire center slice, consisting of both HIFU-treated and non-treated tumor tissue because of the partial tumor ablation.

Table 1. MR parameter values (mean±SD) in the entire center tumor slice of the HIFU-treated rats before HIFU, directly after HIFU, 3 days after HIFU, as well as in the control animals at day 0 and day 3. For the HIFU-treated animals, the p-values below the average endogenous parameter values (T_1, T_2, ADC, APTw signal and $T_{1\rho}$) result from a paired two-sided Student's t-test between the 'Directly after HIFU' (n=12; * indicates a significant difference) or '3 days after HIFU' (n=6, # indicates a significant difference) data and the data of the corresponding rats in the 'Before HIFU' group. The p-values below the average pharmacokinetic parameter values (K^{trans} and v_e) result from a two-sided Student's t-test between the HIFU-treated and non-treated control tumors at the corresponding time points, either day 0 (& indicates a significant difference) or 3 ($ indicates a significant difference). The p-values given for the control animals at day 3 result from a two-sided paired Student's t-test (P<0.05) between the data at day 0 and day 3. The p-values are highlighted bold if the mean MR parameter values showed statistically significant differences (P<0.05). 'n.a.' Indicates that these parameters were not measured before HIFU treatment.

	HIFU-treated animals			**Control animals**	
Parameter	**Before HIFU**	**Directly after HIFU**	**3 days after HIFU**	**Day 0**	**Day 3**
T_1 [ms]	1674±41	1694±57; P=0.085	1520±134; **P=0.041 #**	1624±63	1581±96; P=0.347
T_2 [ms]	183±16	173±29; P=0.152	160±17; P=0.111	198±45	177±39; P=0.423
ADC [10^{-3} mm^2/s]	1.14±0.14	1.04±0.14; **P=0.030 ***	1.65±0.17; **P=0.001 #**	1.21±0.19	1.27±0.13; P=0.614
APTw signal [%]	2.23±0.71	2.39±0.66; P=0.538	1.55±1.36; P=0.150	2.67±0.86	2.63±1.25; P=0.925
$T_{1\rho}$ B_1=350 Hz [ms]	127±9	136±18; P=0.178	119±15; P=0.604	116±20	115±22; P=0.918
K^{trans} [min^{-1}]	n.a.	0.013±0.010; **P=0.013 &**	0.044±0.013; **P=0.048 $**	0.076±0.034	0.085±0.041; P=0.560
v_e [-]	n.a.	0.093±0.046; **P=0.000 &**	0.205±0.068; P=0.095	0.258±0.040	0.332±0.151; P=0.301

HIFU treatment resulted in a subtle, yet significant, decrease in ADC directly after HIFU, whereas ADC values were pronouncedly, and significantly, increased at 3 days after HIFU. In addition, T_1 values were significantly decreased at 3 days after HIFU compared to before HIFU. The K^{trans} and v_e values were significantly lower in the HIFU-treated tumors directly after HIFU compared to the control tumors at day 0. At 3 days after HIFU treatment, K^{trans} remained significantly lower in the HIFU-treated tumors compared to the control tumors.

Further insight in the MR parameter distributions in the tumor tissue at the different experimental time points is provided by the histograms of MR parameter values in all tumor pixels in the center slice, which can be found in the supplemental information (Supplemental Information 3). The most notable changes in these histograms were observed at 3 days after HIFU treatment. At that time point, a pronounced significant shift toward high ADC values and a slight, non-significant, shift toward low APT-weighted signal values were observed. Results of the analysis of the relation between temperature/thermal dose and changes in MR parameter values directly after treatment can also be found in the supplemental information (Supplemental Information 4).

7.3.2. Cluster analysis and feature vector selection

After evaluation of the changes in the individual MR parameters, cluster analysis was performed to combine information of the different endogenous contrast MR parameters to identify HIFU-treated non-viable tumor tissue. Clusters were classified as non-viable when the fraction of pixels within the clusters significantly increased after HIFU treatment. Subsequently, the one-to-one correspondence ($R^2_{y=x}$) between the non-viable tumor fractions derived from clustering with all different feature vectors and the histology-derived non-viable tumor fractions was determined. All experimental groups were included in this analysis. Clustering with 4 clusters led to a stronger one-to-one correspondence between histology and clustering compared to other numbers of clusters. $R^2_{y=x}$ values between histology-derived non-viable tumor fractions and non-viable tumor fractions derived from clustering with 4 clusters are displayed in Table 2 for all feature vectors. Feature vector {ADC, APTw signal} was identified as the optimal feature vector, since clustering with these two MR parameters resulted in the best one-to-one correspondence ($R^2_{y=x}$ =0.92) between the histology-derived and clustering-derived non-viable tumor fractions.

Table 2. One-to-one correspondence ($R^2_{y=x}$) between histology-derived non-viable tumor fractions and non-viable tumor fractions resulting from k-means clustering with 4 clusters and all possible feature vectors (i.e. combinations of MR parameters). All groups ('Directly after HIFU', '3 days after HIFU' and 'Control') were combined in this analysis. The $R^2_{y=x}$ values are given for all feature vectors, grouped per number of MR parameters of which the feature vector consisted, and ordered from low to high values. The highest $R^2_{y=x}$ value is highlighted in bold (for feature vector {ADC, APTw signal}).

	Feature vector	$R^2_{y=x}$
1 parameter	{$T_{1\rho}$}	-21.7
	{T_2}	0.00
	{APTw signal}	0.00
	{T_1}	0.16
	{ADC}	0.63
2 parameters	{T_2, APTw signal}	0.00
	{T_2, $T_{1\rho}$}	0.00
	{APTw signal, $T_{1\rho}$}	0.23
	{T_1, ADC}	0.29
	{T_1, APT}	0.37
	{T_1, $T_{1\rho}$}	0.48
	{T_1, T_2}	0.58
	{ADC, $T_{1\rho}$}	0.60
	{T_2, ADC}	0.81
	{ADC, APTw signal}	**0.92**
3 parameters	{T_1, T_2, $T_{1\rho}$}	0.50
	{T_1, APTw signal, $T_{1\rho}$}	0.51
	{T_2, APTw signal, $T_{1\rho}$}	0.59
	{T_1, T_2, APTw signal}	0.61
	{T_2, ADC, $T_{1\rho}$}	0.61
	{T_1, T_2, ADC}	0.68
	{T_1, ADC, $T_{1\rho}$}	0.71
	{T_2, ADC, APTw signal}	0.72
	{T_1, ADC, APTw signal}	0.74
4 parameters	{T_1, T_2, ADC, $T_{1\rho}$}	0.55
	{T_1, T_2, APTw signal, $T_{1\rho}$}	0.55
	{ADC, APTw signal, $T_{1\rho}$}	0.73
	{T_2, ADC, APTw signal, $T_{1\rho}$}	0.74
	{T_1, T_2, ADC, APTw signal}	0.86
	{T_1, ADC, APTw signal, $T_{1\rho}$}	0.91
5 parameters	{T_1, T_2, ADC, APTw signal, $T_{1\rho}$}	0.77

Representative cluster maps, resulting from clustering with the optimal feature vector {ADC, APTw signal} and 4 clusters, for all rats that underwent MRI follow-up until 3 days after MR-HIFU are shown in Figure 2 at the three experimental time points.

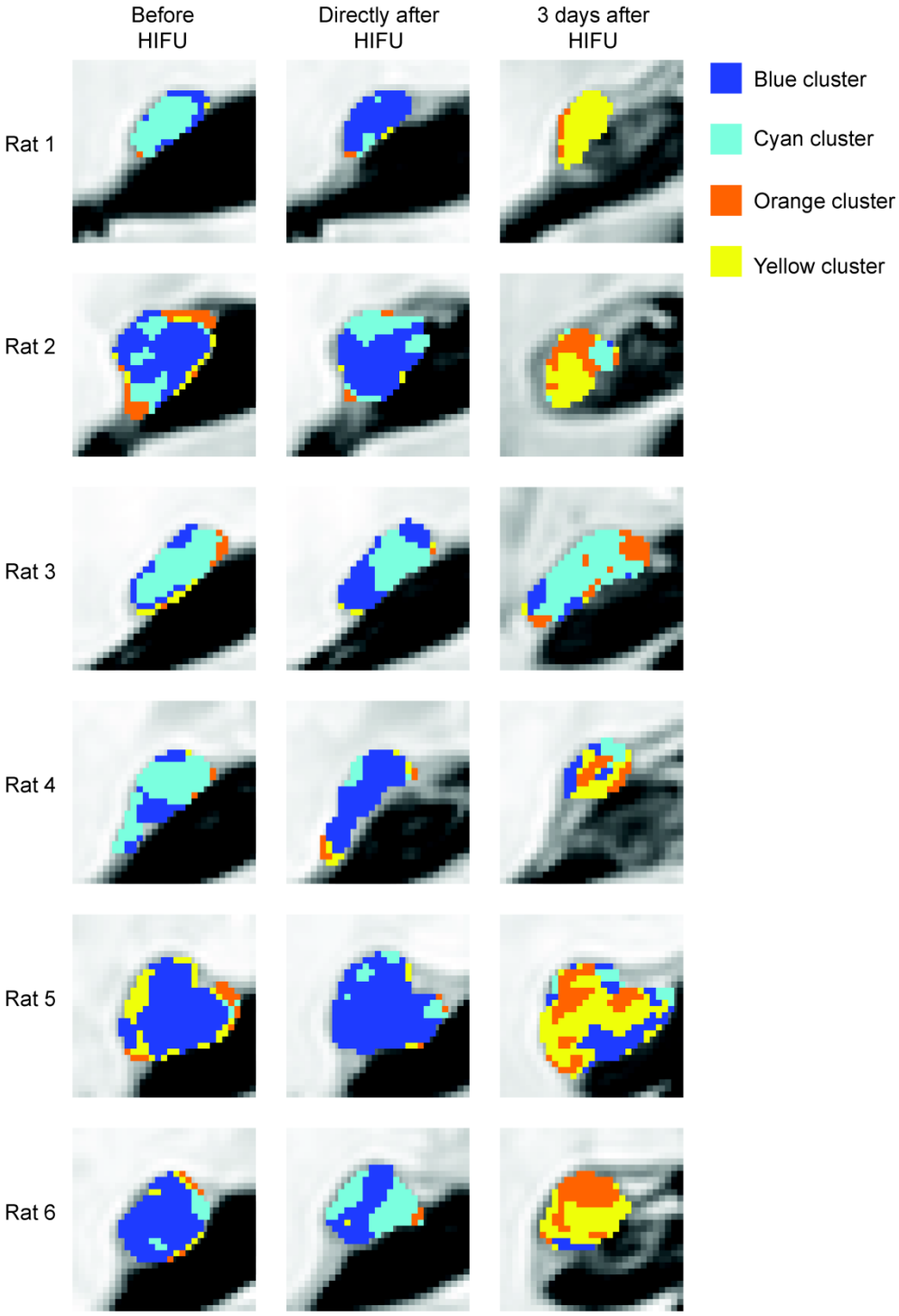

Figure 2. Representative results of k-means clustering with feature vector {ADC, APTw signal} and 4 clusters at the different experimental time points of all animals in the experimental group '3 days after HIFU', superimposed on the tumor pixels in the T_2-weighted images. The MR slice of rat 1 is the same as the slice shown in Figure 1. The four colors (cyan, blue, orange and yellow) indicate to which of the four clusters the tumor pixels were assigned.

Before HIFU, almost all tumor pixels were assigned to the cyan and blue clusters. Also directly after HIFU treatment, only a minor number of pixels was assigned to the yellow and orange clusters. However, at 3 days after HIFU treatment large regions emerged in which pixels were assigned to the yellow and orange clusters. Remarkably, in rat 3 most tumor pixels remained in the blue and cyan clusters at 3 days after treatment, indicative of presence of a substantial amount of residual viable tumor tissue, which was confirmed by histology (see later in this section). However, the MR thermometry measurements suggested a successful ablation of this particular tumor (maximum temperature = 65.3 °C, 240CEM fraction = 0.32).

The fractions of pixels assigned to the different clusters following from segmentation with feature vector {ADC, APTw signal} at the three time points of the HIFU-treated animals are shown in Figure 3.

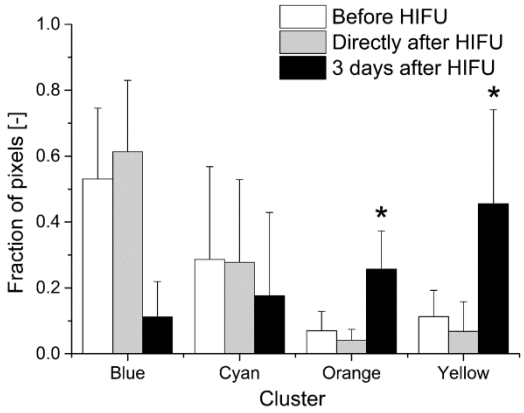

Figure 3. Bar chart of the fraction of pixels within the different clusters at the different experimental time points. * denotes a significant increase in the fraction of pixels within the cluster compared to before HIFU (one-sided paired Student's t-test, $P<0.05$).

Indeed, a significantly increased fraction of pixels in the yellow and orange clusters was observed at 3 days after HIFU compared to before treatment. These clusters were therefore classified as non-viable.
The average MR parameter values in the clusters resulting from segmentation with the optimal feature vector {ADC, APTw signal} are listed in Table 3. The clusters that were classified as non-viable were characterized by a high ADC value and either a low APT-weighted signal (yellow cluster) or an APT-weighted signal that is comparable to values measured before HIFU (orange cluster).

Table 3. MR parameter values (mean±SD) in the different clusters resulting from k-means clustering with feature vector {ADC, APTw signal} and 4 clusters.

Cluster	ADC [10^{-3} mm^2/s]	APTw signal [%]
Blue	0.97±0.18	1.83±0.62
Cyan	1.11±0.26	3.69±0.76
Orange	2.20±0.36	2.24±1.13
Yellow	1.52±0.26	0.97±0.95

The qualitative visual agreement between the clustering-derived and histology-derived non-viable tumor tissue at 3 days after HIFU treatment is depicted in Figure 4.

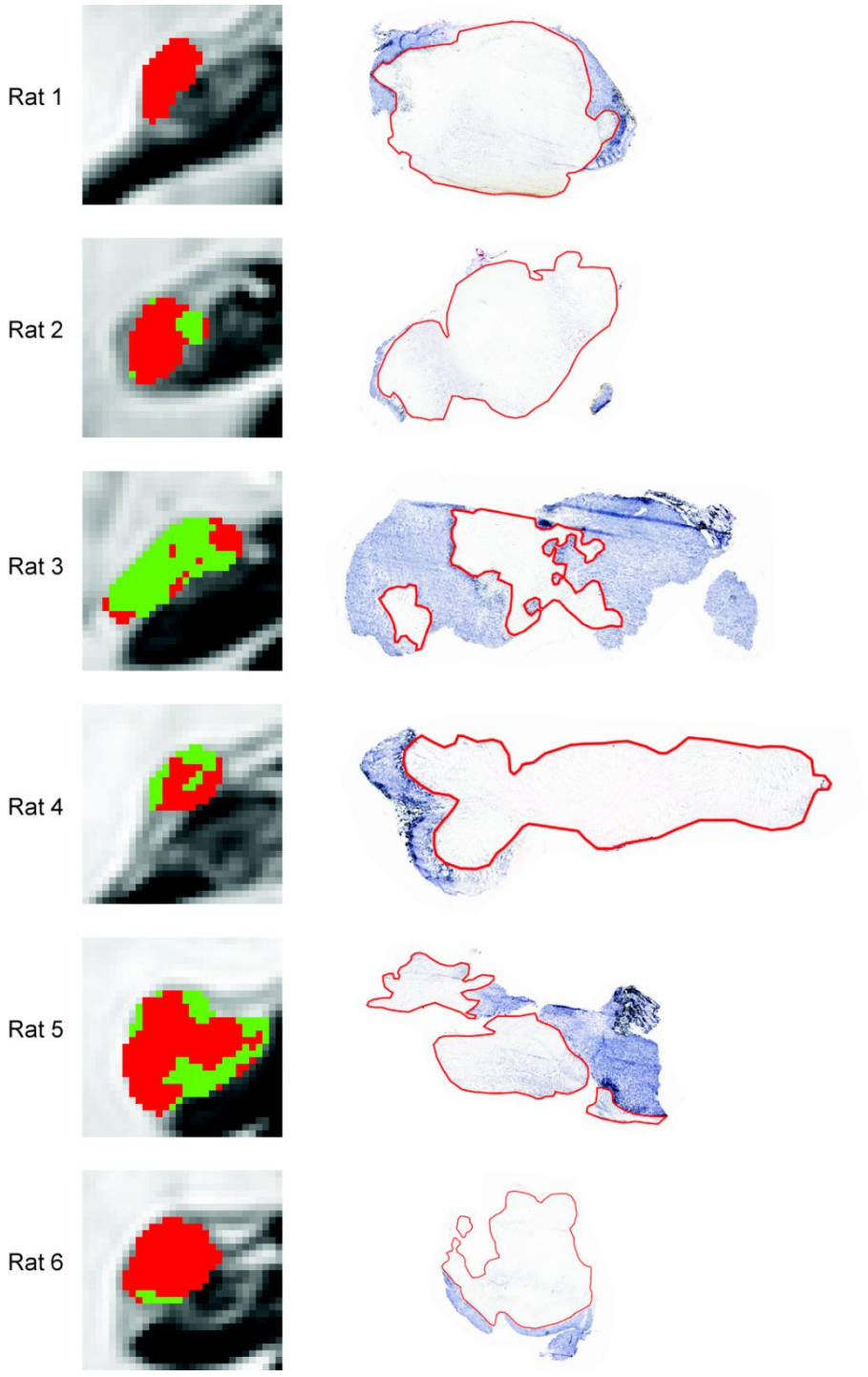

Figure 4. Classification of the tumor pixels as viable (green) or non-viable (red) from clustering with 4 clusters and feature vector {ADC, APTw signal} for all animals in the experimental group '3 days after HIFU', superimposed on the tumor pixels in the T_2-weighted images. The MR slice of rat 1 is the same as the slice shown in Figure 1. On the right side of the figure, the corresponding NADH-diaphorase-stained tumor sections are shown. The tumor regions that were identified as non-viable on histology is delineated by red contours.

Large tumor regions were classified as non-viable by the cluster analysis. These regions were generally in good visual agreement with areas of non-viable tumor tissue in histology. The remarkable cluster results of rat 3, that showed that the major part of the tumor was classified as viable at 3 days after treatment in contrast to what would be expected from the lethal thermal dose maps, were supported by histology. The NADH-diaphorase stained tumor section of this rat also indicated that a large part of the tumor was still viable at 3 days after HIFU. A similar figure of the visual qualitative comparison between clustering and histology for the animal sacrificed directly after treatment is given in Supplemental Information 5 (Figure S5). The visual agreement between clustering and histology was substantially lower at this time point after treatment.

The correlation plot in Figure 5A demonstrates that clustering with 4 clusters and the optimal feature vector {ADC, APTw signal} resulted in a strong correlation (r=0.92) and good one-to-one correspondence ($R^2_{y=x}$=0.92, corresponding to the value in Table 2) between clustering-derived and histology-derived non-viable tumor fractions, when all data points of all experimental groups were combined.

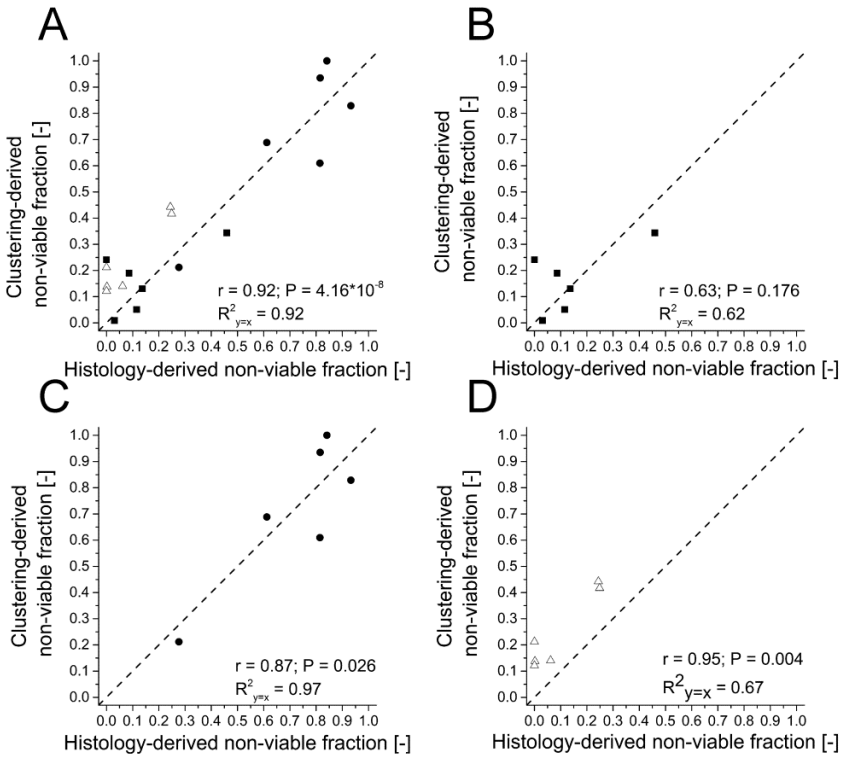

Figure 5. Correlation plots between clustering-derived and histology-derived non-viable tumor fractions resulting from k-means clustering with 4 clusters and feature vector {ADC, APTw signal}, for all data ('Directly after HIFU', '3 days after HIFU' and 'Control') (A) and for the individual experiment time points (B, C and D). The symbols ■, ● and Δ indicate the experimental groups 'Directly after HIFU', '3 days after HIFU' and 'Control', respectively. The dashed lines represent the line of identity y=x. The Pearson's correlation coefficient with corresponding p-value and $R^2_{y=x}$ are listed in each correlation plot.

Directly after HIFU treatment, the agreement with histology was less (r=0.63, $R^2_{y=x}$=0.62; Figure 5B). Nevertheless, Figure 5C demonstrates that there was a strong correlation (r=0.87) and excellent one-to-one correspondence ($R^2_{y=x}$=0.97) between clustering-derived and histology-derived non-viable tumor fractions at 3 days after HIFU treatment. For the control animals (Figure 5D) the correlation with histology was strong (r=0.95), although the clustering-derived non-viable tumor fractions were consistently higher than the histology-derived non-viable tumor fractions ($R^2_{y=x}$=0.67).

7.3.3. Correlation between 240CEM fractions, non-perfused tumor fractions and histology

In order to compare the performance of the proposed multiparametric analysis with conventionally used HIFU treatment monitoring and evaluation methods, a similar correlation analysis between 240CEM fractions, non-perfused fractions, deduced from DCE-MRI, and histology-derived non-viable fractions was performed (Figure 6).

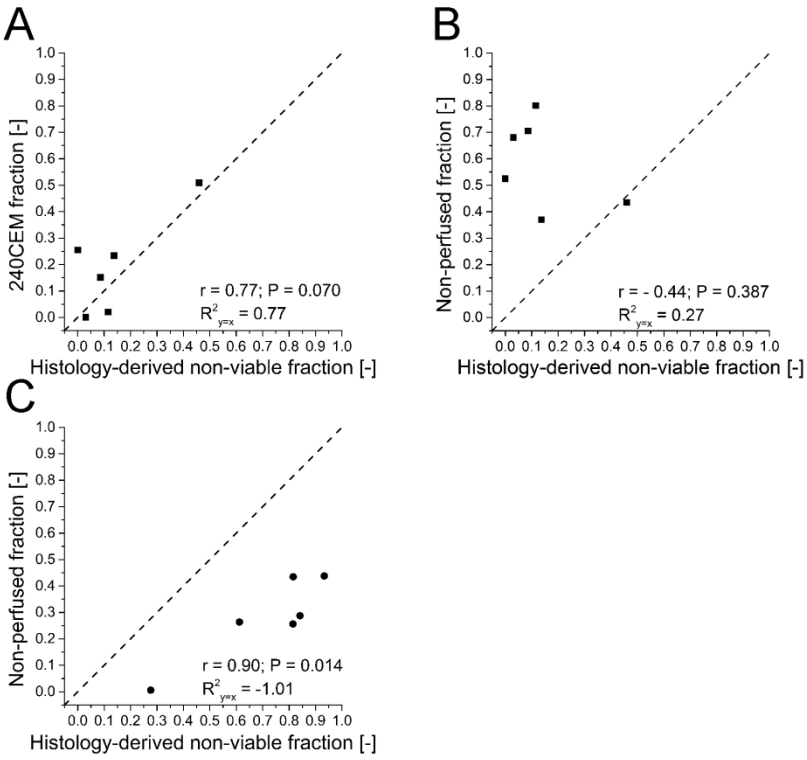

Figure 6. Correlation plots between the 240CEM fractions and histology-derived non-viable fractions (A), non-perfused fractions and histology-derived non-viable fractions directly after HIFU (B) and non-perfused fractions and histology-derived non-viable fractions at 3 days after HIFU (C). The symbols ■ and ● represent the experimental groups 'Directly after HIFU' (A-B) and '3 days after HIFU' (C), respectively. The dashed line represents the line of identity y=x. The Pearson's correlation coefficient with corresponding p-value and $R^2_{y=x}$ are listed in each correlation plot.

A trend (P=0.070) toward a strong correlation between the 240CEM fraction and the histology-derived non-viable tumor fraction directly after HIFU was observed (Figure 6A). Directly after treatment, no relation was found between the non-perfused and

histology-derived non-viable tumor fractions (Figure 6B). The non-perfused tumor fractions were consistently larger than the histology-derived non-viable tumor fractions. At 3 days after HIFU, a strong positive correlation (r=0.90) between the non-perfused fraction and histology-derived non-viable fraction was observed, although the non-perfused tumor fraction was consistently lower than the histology-derived non-viable tumor fraction (Figure 6C).
A summary of the results of the correlation analyses between the histology-derived non-viable fractions and the 240CEM, non-perfused and clustering-derived non-viable tumor fractions is displayed in Table 4. This table further illustrates that only the clustering-derived non-viable fractions at 3 days after HIFU had a significant correlation and good agreement with the histology-derived non-viable tumor fractions.

Table 4. Overview of the results of the correlation analysis between the histology-derived non-viable fractions and the 240CEM, non-perfused and clustering-derived (feature vector {ADC, APTw signal} and 4 clusters) non-viable fractions. S and NS indicate whether there was a significant or non-significant correlation ($P<0.05$), respectively. The symbols >, <, ≈ and = indicate whether the fractions indicated in the corresponding row heading were generally larger, smaller, almost equal or equal compared to the histology-derived non-viable fractions. - indicates that the correlation analysis was not performed, because the fractions could not be compared between the day of HIFU treatment and 3 days after HIFU treatment due to tumor progression (see Discussion).

		Histology-derived non-viable fraction	
		Directly after	3 days after
240 EM fraction		NS, ≈	-
Non-perfused fraction	Directly after	NS, >	-
	3 days after	-	S, <
Clustering-derived non-viable fraction	Directly after	NS, ≈	-
	3 days after	-	S, =

7.3.4. H&E histology

Representative microscopy images of H&E-stained sections of tumors excised directly and at 3 days after HIFU are shown in Figure 7. At both time points, extensive necrosis was observed throughout the tumor tissue. Other major morphological changes observed directly after HIFU treatment were dilated and coagulated blood vessels and the infiltration of immune cells. HIFU-induced tissue damage was more pronouncedly visible at 3 days after treatment. At that time point, extensive inflammation was seen in areas around the central zone of coagulative necrosis. In addition, cell debris and hemorrhages were observed.

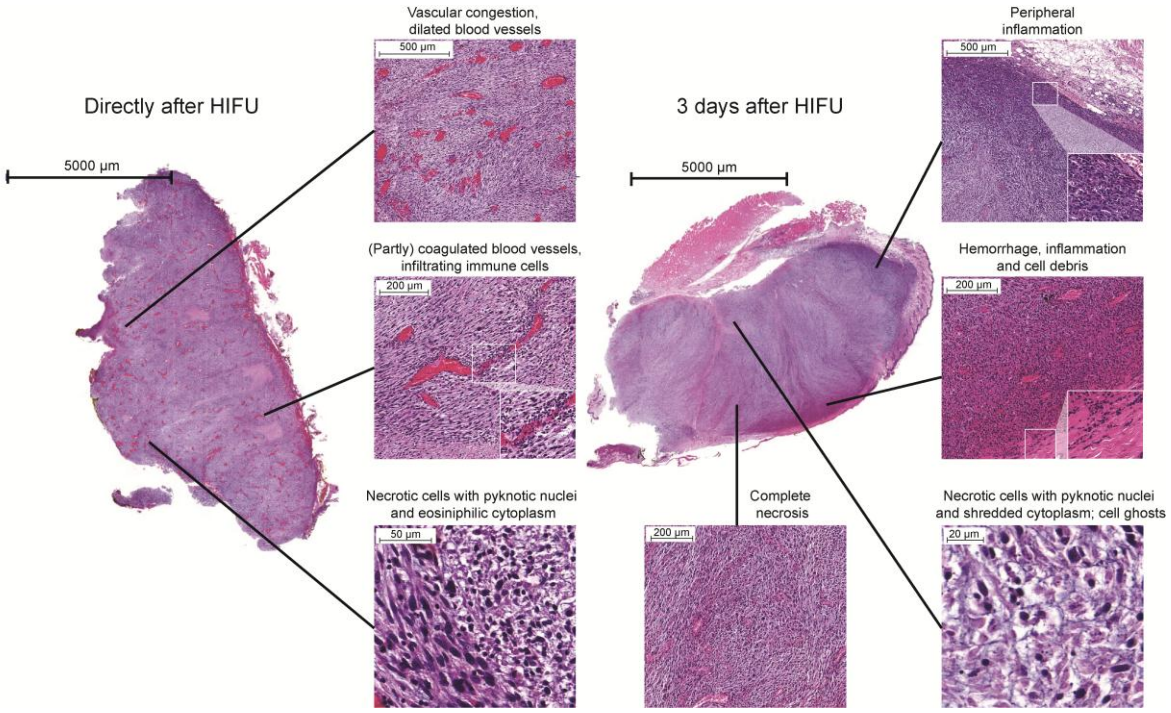

Figure 7. Representative brightfield microscopy images of H&E-stained sections of tumors excised directly (~2 h) and at 3 days after treatment. Regions of specific interest are magnified and shown as separate images. The position of these regions within the tumor section is indicated with the black lines. The inset in the center image of the tumor section obtained directly after HIFU shows a magnification of infiltrating immune cells. The insets in the top-right and center-right image of the tumor section obtained 3 days after HIFU show magnifications of inflammatory cells and cell debris, respectively.

7.4. Discussion

In the present study, a multiparametric analysis was employed to identify treated (non-viable) and residual non-treated tumor tissue after MR-HIFU treatment. Global analysis of the MRI parameter values in the tumor tissue in the central MRI slice showed that HIFU-induced changes in the MRI parameters were more pronounced at 3 days after HIFU compared to directly after treatment (Table 1). For the individual MR parameters only a subtle, yet significant, change in the average ADC in the tumor was observed directly after HIFU treatment. The detected decrease in ADC may be caused by cytotoxic cell swelling (36,37). In contrast, a strong increase in ADC was observed at 3 days after HIFU treatment. This more pronounced change is likely attributable to necrosis-induced cell shrinkage, increased cell membrane permeability and disruption of diffusion barriers in the necrotic tumor region (9,38). Related to that, the significant decrease in T_1 at 3 days after treatment was probably caused by an increased access of water molecules to paramagnetic sites and an increased macromolecular content in the interstitial space (38). Furthermore, a population of pixels with decreased APT-weighted signal intensity was identified in the APT parameter distribution at 3 days after HIFU (Supplemental Information 3, Figure S3). This can be explained by protein aggregation due to thermal stress, which results in a decreased availability of mobile

amide protons for exchange with the bulk water (21). In addition, changes in pH, for example due to ischemia, may have contributed to the decrease in APT-weighted signal (21). These above alterations in tumor morphology, to which the different MRI parameters are sensitive, apparently require time to develop and seem too subtle to allow for detection of endogenous MR contrast changes shortly after the thermal ablation. This was supported by the qualitative assessment of morphological changes after HIFU treatment with H&E staining (Figure 7), which indicated that HIFU-induced tissue damage was more pronounced at 3 days after treatment compared to directly after treatment.

The cluster analysis, in which multiple MRI parameters were combined in a single analysis, also showed the overall highest sensitivity for HIFU-induced cell death at 3 days after treatment. At that time point, a strong correlation and high one-to-one correspondence was observed between histology-derived non-viable tumor fractions and non-viable tumor fractions derived from clustering with 4 clusters and feature vector {ADC, APTw signal}. The clustering-derived non-viable tumor fractions were determined by classification of clusters as non-viable if the fraction of pixels within the cluster significantly increased by HIFU treatment. For some of the evaluated feature vectors, this criterion could however also be met if the cluster is associated with non-lethal HIFU-induced tissue changes. Nevertheless, because of the strong correlation between clustering-derived and histology-derived non-viable tumor fractions observed for feature vector {ADC, APTw signal}, it seems fair to assume that the non-viable clusters indeed represent non-viable tumor tissue for this particular feature vector.

In our previous study on multiparametric MRI analysis of HIFU-treated tumor tissue, we also found the largest correlation between MRI and histology at 3 days after treatment. In that particular study, {T_1, T_2, ADC} was identified as the optimal feature vector for the identification of HIFU-treated, non-viable tumor tissue (13). In the current study it was hypothesized that addition of the advanced MRI parameters APT-weighted signal and $T_{1\rho}$ to the multiparametric MR analysis would improve its efficacy for early HIFU treatment evaluation, because these advanced MRI methods are expected to be sensitive to early HIFU treatment effects including protein denaturation. However, even with inclusion of these advanced parameters, the overall correlation between clustering and histology was lower directly after MR-HIFU ablation compared to 3 days after treatment. Directly after HIFU treatment, the highest one-to-one correspondence between clustering-derived and histology-derived non-viable fractions was observed for feature vector {T_1, $T_{1\rho}$}. At that time point, the $R^2_{y=x}$ value was 0.63 for that particular feature vector, which was substantially lower than the $R^2_{y=x}$ value of the feature vector that was identified as optimal ({ADC, APTw signal}) at 3 days after treatment ($R^2_{y=x}$=0.97; Figure 5C). Nevertheless, the APT-weighted signal appeared to be a valuable addition to the multiparametric analysis. In contrast to our previous study, in which three MRI parameters were needed for the accurate identification of non-viable tumor tissue at 3 days after treatment (13), in the current study the combined ADC and the APT data were sufficient to obtain an excellent agreement between the extent of non-viable tumor tissue identified by clustering and histology.

Importantly, measurement of a single endogenous contrast MRI parameter appeared to be unsuitable for accurate identification of HIFU-treated tumor tissue. No clear demarcation of the HIFU-treated tumor region could be observed in the different MR parameter maps (Figure 1). In addition, the one-to-one correspondence between clustering-derived and histology-derived non-viable tumor fractions was low for all feature vectors consisting of one single MRI parameter (Table 2), which strongly indicates the additional value of multiparametric analysis for the evaluation of HIFU treatment as compared to therapy assessment based on analysis of separate MR images.

Inclusion of the DCE-MRI data to the cluster analysis may increase its sensitivity to early HIFU treatment effects by measuring changes in tumor vascular status. A significant reduction in K^{trans} and v_e was observed in the HIFU-treated tumors compared to control tumors. This decline in the DCE-MRI-derived pharmacokinetic parameters was probably caused by vascular destruction (39,40), which results in a lack of contrast agent inflow in the treated tumor. However, although (D)CE-MRI may be more sensitive to HIFU-induced tissue changes directly after HIFU, the changes in contrast enhancement after HIFU treatment do not necessarily represent cell death. In fact, a poor agreement between non-perfused and histology-derived non-viable tumor fractions was observed both directly and at 3 days after HIFU treatment. Directly after HIFU treatment, the non-perfused fraction was consistently larger than the non-viable fraction. This may be explained by the fact that HIFU-induced vascular destruction could extend beyond the central ablation zone, due to heat stress in regions surrounding this zone. It has been found in multiple studies that the non-perfused volume is generally larger than the estimated treatment volume (41-43) directly after HIFU thermal ablation. While coagulative necrosis is immediately induced in the central zone of ablation due to protein denaturation, cellular and nuclear membrane damage and halted metabolism (44), the vascular destruction in the peripheral zone may not directly result in tumor necrosis. Furthermore, temporary vascular occlusion (45) could have contributed to the relatively high non-perfused tumor fractions directly after HIFU. In contrast to directly after HIFU, at 3 days after treatment the non-perfused tumor fraction was consistently lower than the non-viable tumor fraction, which might be due to contrast agent diffusion into the borders of the non-viable tumor area. A similar underestimation of the extent of non-viable tumor tissue by contrast-enhanced MRI has been reported in a study on HIFU treatment of rabbit tumors (46).

The 240CEM thermal dose threshold can also not be regarded suitable for predicting the extent of non-viable tissue after HIFU treatment. The thermal sensitivity varies largely between tissue types and therefore 240CEM cannot be regarded as a universal threshold for lethal thermal dose (4,5). In the present study we observed a strong, but non-significant, correlation between histology-derived non-viable fractions and 240CEM fractions (Figure 6A). This correlation was higher than correlations between clustering-derived non-viable fractions based on any other single parameter and histology-derived non-viable fractions (Table 2), which would suggest that the 240CEM threshold is promising for the detection of non-viable tumor tissue directly after HIFU. One should however take into account that HIFU-induced necrosis can extend beyond the thermal coagulation zone, because of delayed cell death due to vascular damage.

Identification of non-viable tumor tissue after HIFU treatment solely based on the 240CEM fraction would therefore likely underestimate the total extent of HIFU-induced cell death. An underestimation of the extent of tumor necrosis by the 240CEM fraction was also reported in a pre-clinical study of HIFU-treated rabbit tumors (46).

A limitation of the current study is the lack of spatial registration between the subsequent MRI examinations of the same animal. Repositioning the tumor-bearing paw in exactly the same position as during the first MRI examination was practically impossible, mainly due to tumor progression between the examinations. Hence, quantitative comparison between MRI findings directly and at 3 days after HIFU treatment was mainly restricted to global analysis of MRI parameter changes across the entire tumor. The effect of HIFU treatment on the MRI parameters is likely underestimated in this global analysis of average tumor parameter values, since both successfully treated and non-treated tumor tissue were included because of the partial tumor treatment. For the same reason, the 240CEM, non-perfused and clustering-derived and histology-derived non-viable tumor fractions could not be quantitatively compared between the day of HIFU treatment and 3 days after HIFU treatment, because changes in fractions between these time points are not only influenced by the treatment, but also by tumor growth and slight differences in animal positioning. Potential follow-up studies on multiparametric MR evaluation of HIFU treatment could focus on the spatial registration between subsequent MRI examinations. This would require a set-up in which animals could be positioned repetitively in exactly the same orientation. In addition, a more slowly growing tumor model should be used to minimize tumor progression between subsequent time points. In such ideal setting, the potential predictive value of the MRI measurements obtained directly after HIFU treatment on the extent of non-viable tumor tissue at later time points after treatment could be assessed.

Although best effort was taken to match the cutting plane of histology with the center MRI slice, tissue deformation during histological processing is inevitable and therefore exact spatial registration between MRI and histology remained difficult. Consequently, the correlation analyses were based on tumor fractions rather than on absolute tumor areas. Furthermore, one should take into account that the thickness of the histological sections (5-6 μm) was substantially smaller than the MR slice thickness (2 mm), which can further explain deviations in the appearance of the tumor on MRI and in histology.

For clinical application of the proposed multiparametric analysis a reduction of scan time of the multiparametric protocol may be necessary. The total acquisition time of the ADC and APT measurements was approximately 27 minutes. The scan time could possibly be shortened, without affecting accuracy, by decreasing the number of b-values and irradiation offsets in the ADC and APT measurements, respectively. In addition, acceleration techniques such as parallel imaging (47,48) and compressed sensing (49) could be employed.

In the current study, we particularly chose for the time points of 3 days after HIFU treatment, because it has been shown in rabbit tumors that the ablation region increases in size in the first 3 days after HIFU treatment, after which it decreases again (46). Nevertheless, in follow-up studies on multiparametric MRI for evaluation of HIFU treatment it would be interesting to assess whether the proposed

multiparametric analysis is also suitable for the assessment of the extent of non-viable tumor tissue at later stages of HIFU treatment. At these later stages, for example repair processes could influence the MRI parameter values (50).
In the current study an unsupervised clustering method was used for the segmentation of non-viable tumor tissue after HIFU treatment. While this clustering algorithm is particularly useful for data of groups of subjects, a supervised segmentation method may be more suitable for the segmentation of data of a single subject, such as in clinical studies. Supervised segmentation algorithms, such as support vector machines, are regularly employed in MRI tumor segmentation studies (51) and may also be used in clinical studies on multiparametric MRI assessment of HIFU treatment.

In summary, we demonstrated that a multiparametric MR analysis, based on ADC and the APT-weighted signal, can determine the extent of non-viable tumor tissue at 3 days after HIFU treatment. The presented analysis outperformed the conventional methods that are used for monitoring and evaluation of HIFU therapy, *i.e.* thermal dose mapping and CE-MRI, respectively, with respect to the identification of non-viable tissue after treatment. We expect that, after extensive validation in different human tumor types, the proposed method can be incorporated in the current clinical workflow of MR-HIFU therapies.

7.5. Acknowledgement

The authors thank professor Paul van Diest (University Medical Center Utrecht) and Nathalia Vykhodtseva (Harvard Medical School) for their assistance with the evaluation of the H&E-stained tumor sections. In addition, Marije Janssen and Caren van Kammen (both from Maastricht University) are acknowledged for their support with the animal experiments. This research was performed within the framework of CTMM, the Center for Translational Molecular Medicine (www.ctmm.nl), project VOLTA (grant 05T-201).

7.6. References

1. Kennedy JE. High-intensity focused ultrasound in the treatment of solid tumours. Nat Rev Cancer 2005;5(4):321-327.
2. ter Haar G. Therapeutic applications of ultrasound. Prog Biophys Mol Biol 2007;93(1-3):111-129.
3. de Senneville BD, Mougenot C, Quesson B, Dragonu I, Grenier N, Moonen CT. MR thermometry for monitoring tumor ablation. Eur Radiol 2007;17(9):2401-2410.
4. Yarmolenko PS, Moon EJ, Landon C, Manzoor A, Hochman DW, Viglianti BL, Dewhirst MW. Thresholds for thermal damage to normal tissues: an update. Int J Hyperthermia 2011;27(4):320-343.
5. Dewhirst MW, Viglianti BL, Lora-Michiels M, Hanson M, Hoopes PJ. Basic principles of thermal dosimetry and thermal thresholds for tissue damage from hyperthermia. Int J Hyperthermia 2003;19(3):267-294.
6. Zhou YF. High intensity focused ultrasound in clinical tumor ablation. World J Clin Oncol 2011;2:8-27.

7. Venkatesan AM, Partanen A, Pulanic TK, Dreher MR, Fischer J, Zurawin RK, Muthupillai R, Sokka S, Nieminen HJ, Sinaii N, Merino M, Wood BJ, Stratton P. Magnetic resonance imaging-guided volumetric ablation of symptomatic leiomyomata: correlation of imaging with histology. J Vasc Interv Radiol 2012;23:786-794 e784.
8. Kim YS, Lim HK, Kim JH, Rhim H, Park BK, Keserci B, Kohler MO, Bae DS, Kim BG, Lee JW, Kim TJ, Sokka S, Lee JH. Dynamic contrast-enhanced magnetic resonance imaging predicts immediate therapeutic response of magnetic resonance-guided high-intensity focused ultrasound ablation of symptomatic uterine fibroids. Invest Radiol 2011;46(10):639-647.
9. Zhang Y, Zhao J, Guo D, Zhong W, Ran L. Evaluation of short-term response of high intensity focused ultrasound ablation for primary hepatic carcinoma: utility of contrast-enhanced MRI and diffusion-weighted imaging. Eur J Radiol 2011;79(3):347-352.
10. Rouviere O, Girouin N, Glas L, Ben Cheikh A, Gelet A, Mege-Lechevallier F, Rabilloud M, Chapelon JY, Lyonnet D. Prostate cancer transrectal HIFU ablation: detection of local recurrences using T2-weighted and dynamic contrast-enhanced MRI. Eur Radiol 2010;20(1):48-55.
11. Kirkham AP, Emberton M, Hoh IM, Illing RO, Freeman AA, Allen C. MR imaging of prostate after treatment with high-intensity focused ultrasound. Radiology 2008;246(3):833-844.
12. Sung HY, Jung SE, Cho SH, Zhou K, Han JY, Han ST, Kim JI, Kim JK, Choi JY, Yoon SK, Yang JM, Han CW, Lee YS. Long-term outcome of high-intensity focused ultrasound in advanced pancreatic cancer. Pancreas 2011;40(7):1080-1086.
13. Hectors SJ, Jacobs I, Strijkers GJ, Nicolay K. Multiparametric MRI analysis for the identification of high intensity focused ultrasound-treated tumor tissue. PLoS One 2014;9(6):e99936.
14. Zhou J, Lal B, Wilson DA, Laterra J, van Zijl PC. Amide proton transfer (APT) contrast for imaging of brain tumors. Magn Reson Med 2003;50(6):1120-1126.
15. Salhotra A, Lal B, Laterra J, Sun PZ, van Zijl PC, Zhou J. Amide proton transfer imaging of 9L gliosarcoma and human glioblastoma xenografts. NMR Biomed 2008;21(5):489-497.
16. Jones CK, Schlosser MJ, van Zijl PC, Pomper MG, Golay X, Zhou J. Amide proton transfer imaging of human brain tumors at 3T. Magn Reson Med 2006;56(3):585-592.
17. Zhou J, Blakeley JO, Hua J, Kim M, Laterra J, Pomper MG, van Zijl PC. Practical data acquisition method for human brain tumor amide proton transfer (APT) imaging. Magn Reson Med 2008;60(4):842-849.
18. Dula AN, Arlinghaus LR, Dortch RD, Dewey BE, Whisenant JG, Ayers GD, Yankeelov TE, Smith SA. Amide proton transfer imaging of the breast at 3 T: establishing reproducibility and possible feasibility assessing chemotherapy response. Magn Reson Med 2013;70(1):216-224.
19. Jia G, Abaza R, Williams JD, Zynger DL, Zhou J, Shah ZK, Patel M, Sammet S, Wei L, Bahnson RR, Knopp MV. Amide proton transfer MR imaging of prostate cancer: a preliminary study. J Magn Reson Imaging 2011;33(3):647-654.
20. Zhou JY, Tryggestad E, Wen ZB, Lal B, Zhou TT, Grossman R, Wang SL, Yan K, Fu DX, Ford E, Tyler B, Blakeley J, Laterra J, van Zijl PCM. Differentiation between

glioma and radiation necrosis using molecular magnetic resonance imaging of endogenous proteins and peptides. Nature Medicine 2011;17(1):130-U308.
21. Hectors SJ, Jacobs I, Strijkers GJ, Nicolay K. Amide proton transfer imaging of high intensity focused ultrasound-treated tumor tissue. Magn Reson Med 2014;72:1113-1122.
22. Hectors SJ, Moonen RP, Strijkers GJ, Nicolay K. T1ρ mapping for the evaluation of High Intensity Focused Ultrasound tumor treatment. Magn Reson Med 2014;doi:10.1002/mrm.25269.
23. Hijnen NM, Heijman E, Kohler MO, Ylihautala M, Ehnholm GJ, Simonetti AW, Grull H. Tumour hyperthermia and ablation in rats using a clinical MR-HIFU system equipped with a dedicated small animal set-up. Int J Hyperthermia 2012;28(2):141-155.
24. Kohler MO, Mougenot C, Quesson B, Enholm J, Le Bail B, Laurent C, Moonen CT, Ehnholm GJ. Volumetric HIFU ablation under 3D guidance of rapid MRI thermometry. Med Phys 2009;36(8):3521-3535.
25. Köhler MO, Enholm J, Mougenot C, Andreae T. Sonalleve MR-HIFU - Philips MR-guided High Intensity Focused Ultrasound. 2011;Available at: http://www.healthcare.philips.com/pwc_hc/ru_ru/about/Events/RSNA/pdfs/MR_Sonalleve_HIFU_whitepaper.pdf. Accessed August 29, 2014.
26. Hijnen NM, Elevelt A, Grull H. Stability and trapping of magnetic resonance imaging contrast agents during high-intensity focused ultrasound ablation therapy. Invest Radiol 2013;48(7):517-524.
27. Witschey II WR, Borthakur A, Elliott MA, Mellon E, Niyogi S, Wallman DJ, Wang C, Reddy R. Artifacts in T1 rho-weighted imaging: compensation for B(1) and B(0) field imperfections. J Magn Reson 2007;186:75-85.
28. Deichmann R, Haase A. Quantification of T1 Values by Snapshot-Flash Nmr Imaging. J Magn Reson 1992;96(3):608-612.
29. Deoni SC, Rutt BK, Peters TM. Rapid combined T1 and T2 mapping using gradient recalled acquisition in the steady state. Magn Reson Med 2003;49(3):515-526.
30. Tofts PS, Brix G, Buckley DL, Evelhoch JL, Henderson E, Knopp MV, Larsson HB, Lee TY, Mayr NA, Parker GJ, Port RE, Taylor J, Weisskoff RM. Estimating kinetic parameters from dynamic contrast-enhanced T(1)-weighted MRI of a diffusable tracer: standardized quantities and symbols. J Magn Reson Imaging 1999;10:223-232.
31. McGrath DM, Bradley DP, Tessier JL, Lacey T, Taylor CJ, Parker GJ. Comparison of model-based arterial input functions for dynamic contrast-enhanced MRI in tumor bearing rats. Magn Reson Med 2009;61(5):1173-1184.
32. Charles River Laboratories International, Inc. Rat hematology data sheet; Available at http://www.criver.com/files/pdfs/rms/fischer-cdf/rm_rm_r_cdf_fisher_rat_clinical_pathology_data.aspx. Accessed: January 2014.
33. Sapareto SA, Dewey WC. Thermal dose determination in cancer therapy. Int J Radiat Oncol Biol Phys 1984;10(6):787-800.
34. Omran MGH, Engelbrecht AP, Salman A. An overview of clustering methods. Intelligent Data Analysis 2007;11(6):583-605.
35. Chatterjee S, Hadi AS. Regression Analysis by Example: Wiley; 2006.

36. Jacobs MA, Ouwerkerk R, Kamel I, Bottomley PA, Bluemke DA, Kim HS. Proton, diffusion-weighted imaging, and sodium (23Na) MRI of uterine leiomyomata after MR-guided high-intensity focused ultrasound: a preliminary study. J Magn Reson Imaging 2009;29(3):649-656.
37. Jacobs MA, Gultekin DH, Kim HS. Comparison between diffusion-weighted imaging, T2-weighted, and postcontrast T1-weighted imaging after MR-guided, high intensity, focused ultrasound treatment of uterine leiomyomata: preliminary results. Med Phys 2010;37(9):4768-4776.
38. Graham SJ, Stanisz GJ, Kecojevic A, Bronskill MJ, Henkelman RM. Analysis of changes in MR properties of tissues after heat treatment. Magn Reson Med 1999;42(6):1061-1071.
39. Wu F, Chen WZ, Bai J, Zou JZ, Wang ZL, Zhu H, Wang ZB. Tumor vessel destruction resulting from high-intensity focused ultrasound in patients with solid malignancies. Ultrasound Med Biol 2002;28(4):535-542.
40. Cheng HL, Purcell CM, Bilbao JM, Plewes DB. Prediction of subtle thermal histopathological change using a novel analysis of Gd-DTPA kinetics. J Magn Reson Imaging 2003;18(5):585-598.
41. Pilatou MC, Stewart EA, Maier SE, Fennessy FM, Hynynen K, Tempany CM, McDannold N. MRI-based thermal dosimetry and diffusion-weighted imaging of MRI-guided focused ultrasound thermal ablation of uterine fibroids. J Magn Reson Imaging 2009;29(2):404-411.
42. Tempany CM, Stewart EA, McDannold N, Quade BJ, Jolesz FA, Hynynen K. MR imaging-guided focused ultrasound surgery of uterine leiomyomas: a feasibility study. Radiology 2003;226(3):897-905.
43. McDannold N, Tempany CM, Fennessy FM, So MJ, Rybicki FJ, Stewart EA, Jolesz FA, Hynynen K. Uterine leiomyomas: MR imaging-based thermometry and thermal dosimetry during focused ultrasound thermal ablation. Radiology 2006;240(1):263-272.
44. Chu KF, Dupuy DE. Thermal ablation of tumours: biological mechanisms and advances in therapy. Nat Rev Cancer 2014;14(3):199-208.
45. Hynynen K, Chung AH, Colucci V, Jolesz FA. Potential adverse effects of high-intensity focused ultrasound exposure on blood vessels in vivo. Ultrasound Med Biol 1996;22(2):193-201.
46. Wijlemans JW, Deckers R, van den Bosch MA, Seinstra BA, van Stralen M, van Diest PJ, Moonen CT, Bartels LW. Evolution of the ablation region after magnetic resonance-guided high-intensity focused ultrasound ablation in a Vx2 tumor model. Invest Radiol 2013;48(6):381-386.
47. Pruessmann KP, Weiger M, Scheidegger MB, Boesiger P. SENSE: sensitivity encoding for fast MRI. Magn Reson Med 1999;42(5):952-962.
48. Griswold MA, Jakob PM, Heidemann RM, Nittka M, Jellus V, Wang J, Kiefer B, Haase A. Generalized autocalibrating partially parallel acquisitions (GRAPPA). Magn Reson Med 2002;47(6):1202-1210.
49. Geethanath S, Reddy R, Konar AS, Imam S, Sundaresan R, D RR, Venkatesan R. Compressed sensing MRI: a review. Crit Rev Biomed Eng 2013;41(3):183-204.

50. Cheng HL, Purcell CM, Bilbao JM, Plewes DB. Usefulness of contrast kinetics for predicting and monitoring tissue changes in muscle following thermal therapy in long survival studies. J Magn Reson Imaging 2004;19(3):329-341.
51. Gordillo N, Montseny E, Sobrevilla P. State of the art survey on MRI brain tumor segmentation. Magn Reson Imaging 2013;31(8):1426-1438.

Supplemental information 1

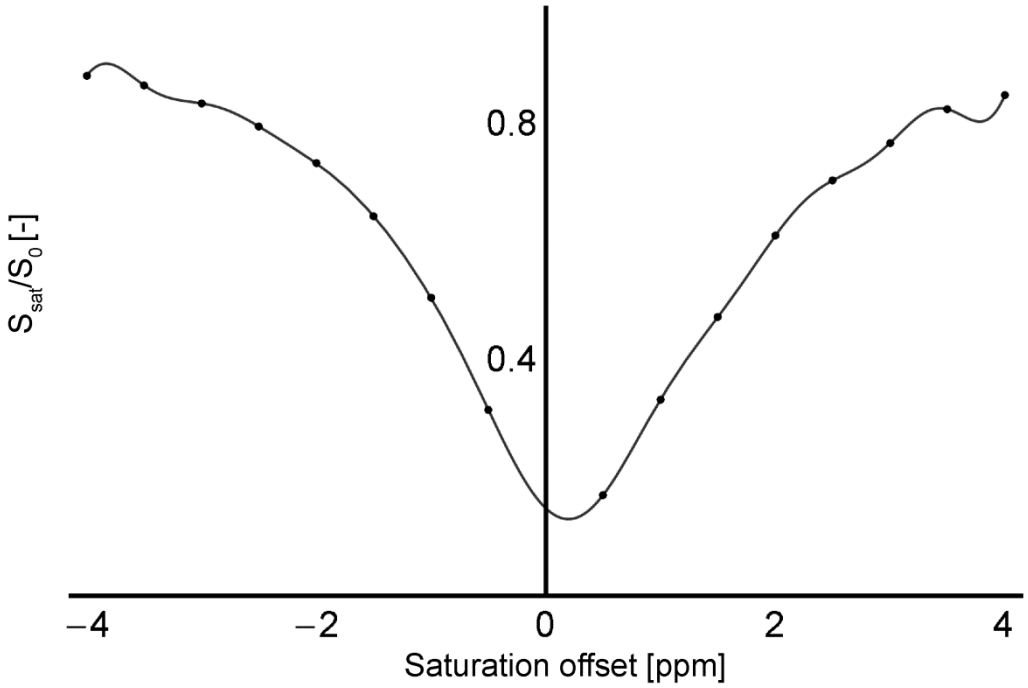

Figure S1. Example curve of the acquired z-spectrum (black dots) and the 23rd order polynomial fit through the data points (solid line) that was performed to find the minimum in the z-spectrum.

Supplemental information 2

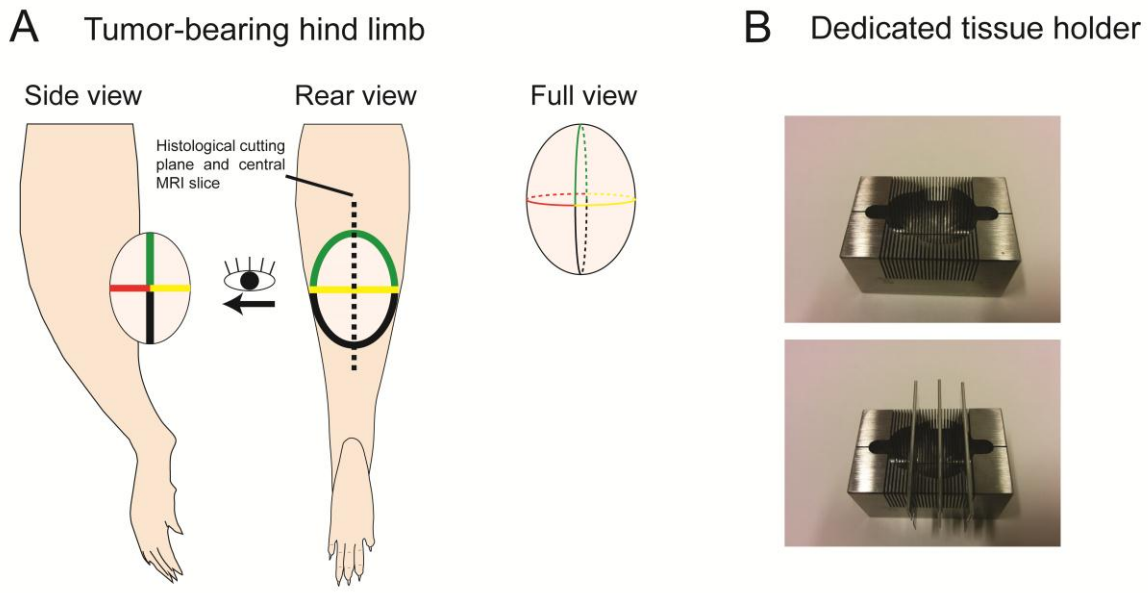

Figure S2. Application of tissue marking dyes on the tumor during histological processing, to retrieve the central MRI slice. Before excision, the skin was removed from the tumor and four lines of different colors were drawn on the tumor tissue using a tissue marking dye kit. The planes in which the lines were applied were perpendicular to the direction of the MRI slices, which was retrieved by using the acquired anatomical MRI images as a visual reference. A) The side and rear view of the tumor-bearing hind limb, showing the positioning of the 4 differently colored (red, green, yellow and black) lines on the tumor tissue. The black dotted line indicates the direction of the histological cutting plane and central MRI slice. The full view shows how the lines were applied on all sides of the tumor. B) After application of the 4 lines, the entire tumor was removed and put in a dedicated tissue holder. Using the applied color lines and the MRI images as reference, the tumor was sliced in two pieces, such that the cutting face matched with the central slice of the multiparametric and MR thermometry acquisitions.

Supplemental information 3

Tumor MR parameter distributions

Histograms of MR parameter values in all tumor pixels in the center slice at the different experimental time points are displayed in Figure S3. A significant increase in the fraction of pixels with T_1 values between 1250 and 1450 ms was observed at 3 days after HIFU (Figure S3A). In the distribution of T_2, a slight but significant shift towards lower T_2 values was visible both directly and at 3 days after HIFU (Figure S3B). The distributions of the ADC values (Figure S3C) show that the fraction of pixels with a low ADC (between $0.65*10^{-3}$ and $0.75*10^{-3}$ mm^2/s) was significantly higher directly after HIFU compared to before HIFU. In contrast, at 3 days after HIFU, a pronounced shift towards high ADC (larger than $1.4*10^{-3}$ mm^2/s) values was observed. In the APT-weighted signal histograms (Figure S3D) a population of pixels with APT-weighted signal between -2.25 and 0.25 % emerged at 3 days after HIFU, although these changes were not significant. The $T_{1\rho}$ distribution (Figure S3E) was not evidently altered at either of the time points after HIFU treatment compared to before HIFU, except for a minor decrease in fraction of pixels with a relatively low $T_{1\rho}$ value (45-75 ms).
In the distributions of the pharmacokinetic parameters K^{trans} (Figure S3F) and v_e (Figure S3G), the data from the control rats at the same experimental time points are shown as a reference since no DCE-MRI was performed before HIFU in the treatment groups. The fraction of pixels with a K^{trans} close to zero (0.0-0.0075 min^{-1}) was significantly higher directly after HIFU than for the control rats. At 3 days after HIFU, the fraction of pixels with low K^{trans} values (0.0-0.0225 min^{-1}) was still significantly higher than for the control rats. For the control rats, a significantly higher fraction of pixels with intermediate K^{trans} values between 0.01125-0.1425 min^{-1} was observed at day 0 compared to day 3. In the distribution of v_e, the fraction of pixels with a low v_e, mainly between 0.0-0.045, was significantly higher for the HIFU-treated rats than for the control rats, at both experimental time points.

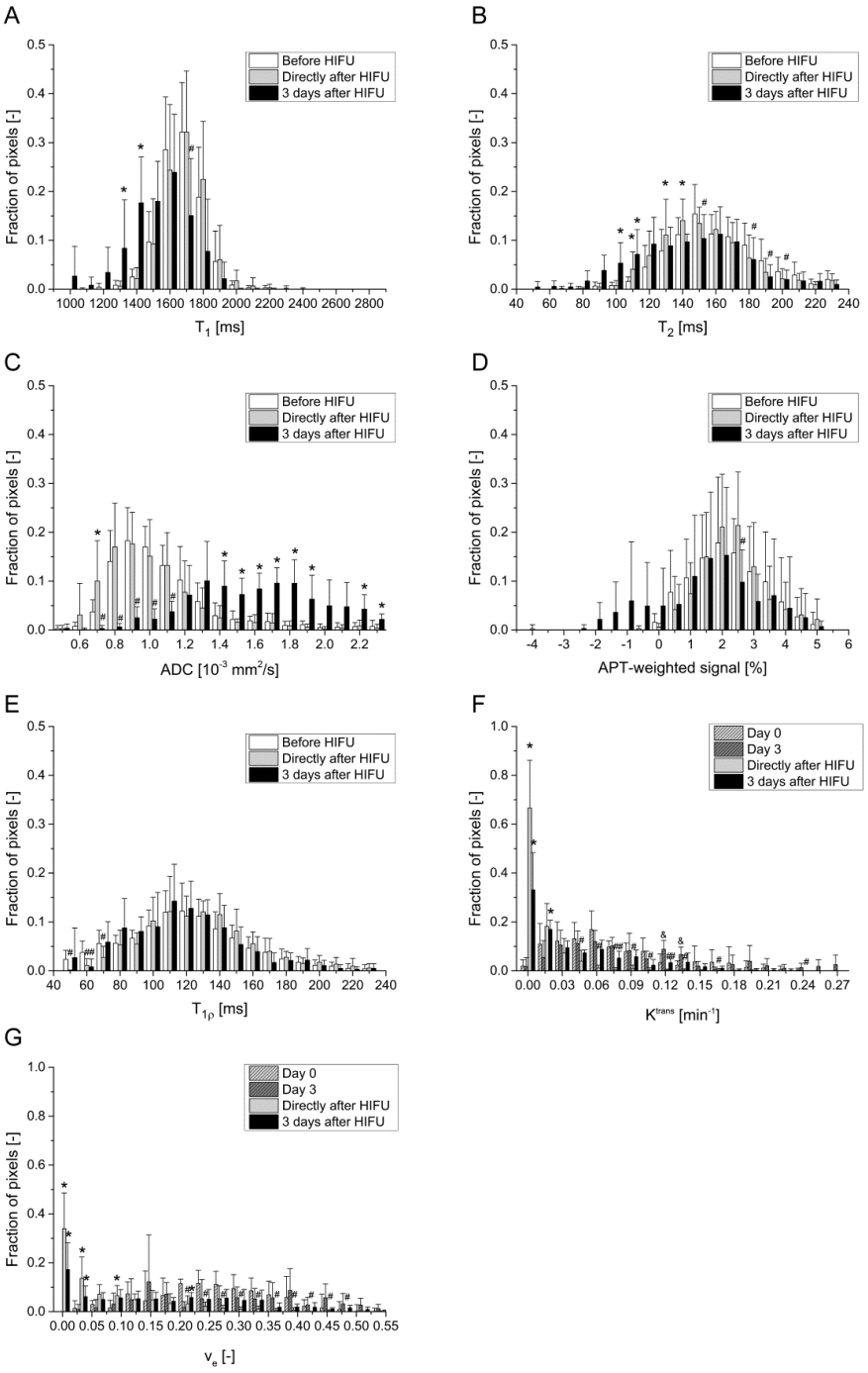

Figure S3. Average MR parameter distributions in the central tumor slice for the HIFU-treated animals at the different time experimental points ('Before HIFU', Directly after HIFU', '3 days after HIFU'). Since DCE-MRI was not performed before HIFU, in the histograms of K^{trans} and v_e the mean parameter values of the control animals at the corresponding measurement days (day 0 and day 3) are shown. The error bars represent the standard deviation. For all endogenous MR parameters (T_1, T_2, ADC, APT-weighted signal, $T_{1\rho}$) * and # denote a significant increase and decrease in the fraction of pixels after HIFU compared to before HIFU, respectively (two-sided paired Student's t-test, $P<0.05$). For the DCE-MRI parameters (K^{trans} and v_e), * and # denote a significantly higher or lower fraction of pixels after HIFU compared to the control animals, respectively (two-sided paired Student's t-test, $P<0.05$). & denotes a significant difference in fraction of pixels at day 3 compared to day 0 for the control animals.

Supplemental information 4

Relation between temperature, thermal dose and changes in MR parameter values

In addition to evaluation of MR parameter changes in the entire center tumor slice, the relation between HIFU-induced temperature elevation and changes in MR parameter values directly after treatment was more closely investigated. For all endogenous MR parameters, the average MR parameter values inside and outside the 240CEM area (*i.e.,* the area in which the thermal dose is generally considered as lethal to cells), directly after HIFU and in the same tumor area before HIFU are shown in Table S1. Both inside and outside the 240CEM area, the only significant change was observed for T_2. In both areas, the T_2 was significantly lower after HIFU compared to before HIFU. A similar decrease in T_2 was observed in our previous study on multiparametric MRI analysis of HIFU-treated tumor tissue and may be explained by an increased access of water molecules to paramagnetic centers in the coagulated/deoxygenated blood (13,38).
For the pharmacokinetic parameters, the average K^{trans} and v_e in a population of pixels are plotted versus the maximum temperature/thermal dose that was reached in these pixels in Figure S4. All tumor pixels in the center slice were included in this analysis. A slight increase in K^{trans} values could be observed at temperatures around 41-42 °C. Thereafter, the K^{trans} generally seemed to decrease with increasing temperature (Figure S4A). A gradual reduction in v_e values for increasing temperatures was observed (Figure S4B). A similar reduction in K^{trans} and v_e values was observed for increasing thermal dose (Figure S4C and S4D). A similar analysis of maximum temperature/thermal dose vs. parameter value was performed for the endogenous MR contrast parameters. However, no correlation between any of the endogenous MRI contrast parameters and maximum temperature was identified directly after HIFU (data not shown).

Table S1. MR parameter values (mean±SD) in the 240CEM thermal dose area directly after HIFU and in the same tumor area before HIFU. The p-values result from a two-sided paired Student's t-test between the 'Directly after HIFU' and 'Before HIFU' data. K^{trans} and v_e are not shown, since DCE-MRI was only performed after HIFU. The p-values are highlighted bold if there was a significant difference in the MR parameter values between before and directly after HIFU (P<0.05).

Parameter	**Inside 240CEM thermal dose area**		**Outside 240CEM thermal dose area**	
	Before HIFU	**Directly after HIFU**	**Before HIFU**	**Directly after HIFU**
T_1	1679±56	1656±46	1671±27	1672±67
[ms]		(P=0.119)		(P=0.956)
T_2	161±13	149±15	193±25	168±22
[ms]		**(P=0.002)**		**(P=0.001)**
ADC	1.01±0.10	1.00±0.18	1.07±0.14	1.05±0.15
[10^{-3} mm^2/s]		(P=0.901)		(P=0.549)
APT-weighted signal	2.45±1.04	2.81±1.25	2.39±0.71	2.33±0.69
[%]		(P=0.474)		(P=0.866)
$T_{1\rho}$	121±21	121±22	136±13	132±18
[ms]		(P=0.954)		(P=0.505)

1. Graham SJ, Stanisz GJ, Kecojevic A, Bronskill MJ, Henkelman RM. Analysis of changes in MR properties of tissues after heat treatment. Magn Reson Med 1999;42:1061-1071.

2. Hectors SJ, Jacobs I, Strijkers GJ, Nicolay K. Multiparametric MRI analysis for the identification of high intensity focused ultrasound-treated tumor tissue. PLoS One 2014;9:e99936.

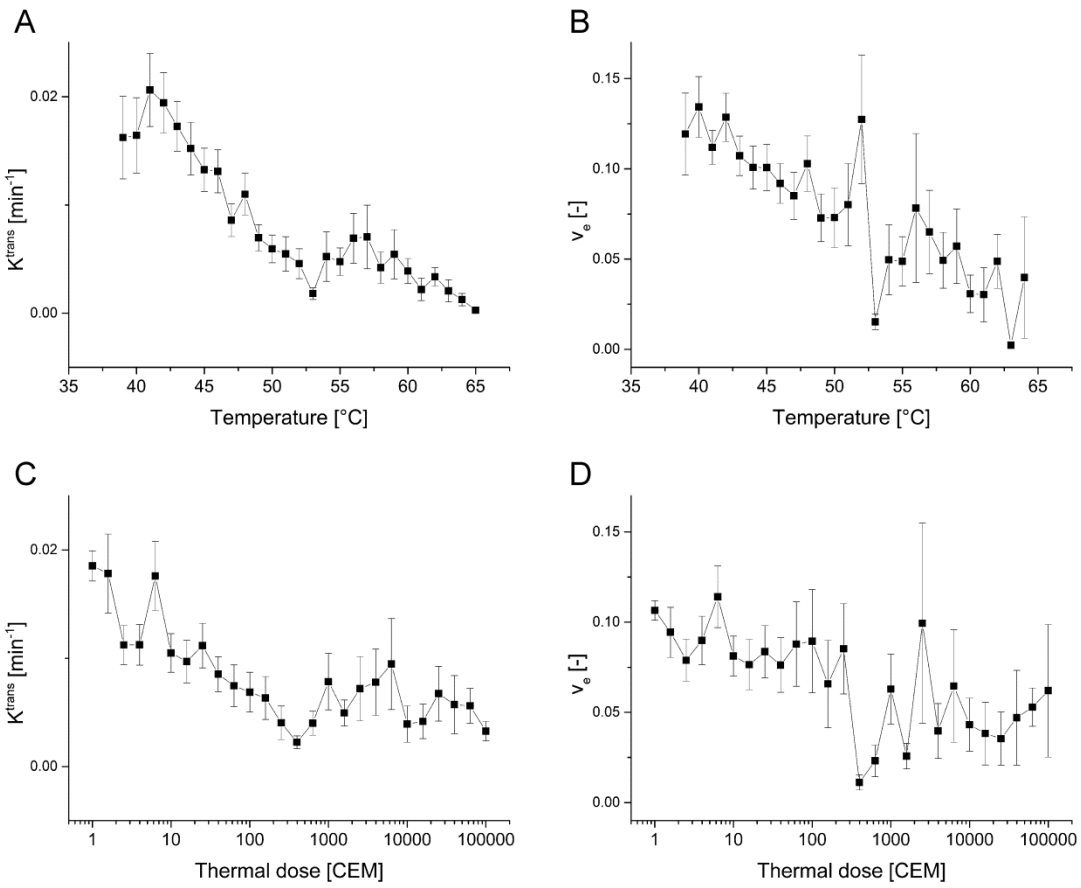

Figure S4. Plot of the relation between pharmacokinetic parameter values (mean±standard error) and ablation temperature/thermal dose. The graph was assembled by determination of the population of pixels in which a certain maximal temperature/thermal dose had been reached and estimation of the mean K^{trans} and v_e values in this population of pixels directly after HIFU.

Supplemental information 5

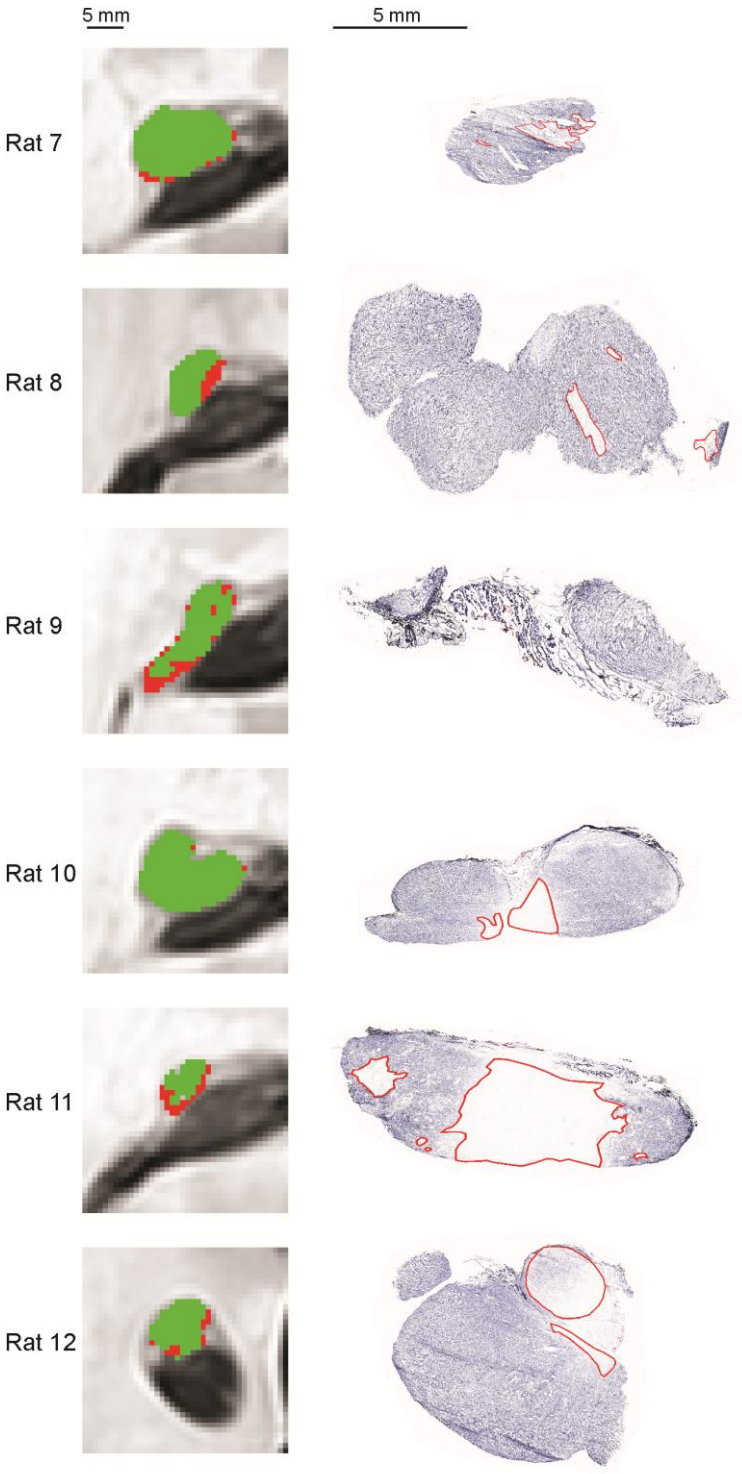

Figure S5. Classification of the tumor pixels as viable (green) or non-viable (red) from clustering with 4 clusters and feature vector {ADC, APTw signal} for all animals in the experimental group 'Directly after HIFU', superimposed on the tumor pixels in the T_2-weighted images. On the right side of the figure, the corresponding NADH-diaphorase-stained tumor sections are shown. The tumor regions that were identified as non-viable on histology is delineated by red contours.

Chapter 8

Discussion and future perspectives

Whereas conventional oncologic imaging is mainly aimed at characterizing the anatomical and morphological tumor features, additional imaging biomarkers have emerged that are potentially more suitable for tumor characterization and early assessment of treatment response. The research presented in this thesis was focused on the development and preclinical evaluation of a variety of endogenous and contrast-enhanced oncologic imaging biomarkers, with applications in evaluation of HIFU therapy. Imaging biomarkers can facilitate discrimination between successfully treated non-viable and untreated viable tumor tissue. In addition, they may provide an improved understanding of treatment effects on the tumor microenvironment. Treatment-induced changes in tumor structure, physiology and metabolism may not only affect tumor progression, but also the efficacy of adjuvant therapies.

The work described in the first part of this thesis was focused on macromolecular DCE-MRI for detailed assessment of tumor microvascular status. The second part describes a number of studies that were aimed at assessment of the suitability of a number of MRI biomarkers for HIFU treatment evaluation. In this chapter, a reflection will be given on the work presented in this thesis. In addition, future perspectives of the different techniques and steps towards clinical translation will be discussed.

8.1. Macromolecular contrast-enhanced MRI

The work in the first chapters of this thesis (**chapter 2, 3 and 4**) was focused on the characterization and in vivo application of a number of dendrimer-based contrast agents for macromolecular contrast-enhanced MRI.

A first main application area of macromolecular contrast agents is MR angiography, which exploits their limited transendothelial diffusion and increased circulation half-lives for detailed imaging of the vasculature. A second application is quantitative macromolecular DCE-MRI, motivated by the fact that high molecular weight agents are more suitable to assess microvascular permeability and blood volume than low molecular weight agents. These two applications provide complementary information on tumor vascular status; whereas MR angiography provides high quality images depicting the tumor vasculature, quantitative macromolecular DCE-MRI enables assessment of physiological parameters that describe microvascular functionality.

In view of these application areas, two types of dendrimer-based contrast agents were evaluated in this research: palmitoylated lower molecular weight albumin-binding dendrimer-based contrast agents (**chapter 2**) and dendrimer-based contrast agents of various molecular weight (**chapter 3**). Since many novel cancer treatment strategies are initially developed and evaluated in a preclinical setting, the albumin-binding dendrimers were specifically designed to possess improved binding to mouse serum albumin compared to the clinically approved gadofosveset trisodium (MS-325). This was realized by functionalization of the dendrimers with a palmitoyl moiety. In vivo application of the dendrimers demonstrated that they possessed long circulation half-lives compared to the low molecular weight non-albumin-binding gadoterate. In

addition, it was demonstrated that these agents were suitable for MR angiography, providing detailed images of the vasculature.

The non-albumin-binding dendrimers of various molecular weight were also characterized by increased circulation half-lives compared to gadoterate, which was most pronounced for the highest molecular weight G5 dendrimer. This agent was also suitable for angiographic imaging purposes. However, the main application area of these contrast agents would be quantitative macromolecular DCE-MRI, to assess tracer-kinetic parameters that are reflective of tumor physiology.

In the multi-agent DCE-MRI approach presented in **chapter 4**, modified dendrimers were used that were better defined and did not possess the fluorescent label rhodamine B. These adaptations were made, since it was found that rhodamine B might introduce albumin-binding properties to the agents and could thereby induce unpredictable in vivo behavior (1). We demonstrated that multi-agent DCE-MRI, using dendrimer-based contrast agents of high and intermediate molecular weight, in conjunction with gadoterate, enabled detailed evaluation of tumor vascular status. It was shown that constrained tracer-kinetic modeling of the multi-agent data facilitated separate assessment of blood flow and microvascular permeability within one imaging session.

8.1.1. Future perspectives

8.1.1.1. Macromolecular DCE-MRI for evaluation of antivascular therapies

As pointed out in **chapter 4** of this thesis, evaluation of antivascular therapies is a field of research for which macromolecular DCE-MRI would be particularly useful. Especially the multi-agent DCE-MRI approach would be a valuable tool, because of its ability to separately determine blood flow and microvascular permeability. This is a major advantage over conventional tracer-kinetic modeling of DCE-MRI data acquired with a low molecular weight contrast agent. A next step in this research would be utilization of this method for detailed evaluation of antiangiogenic and vascular disrupting therapies. Many studies have described that changes in blood flow and permeability induced by such therapies cannot be discriminated with conventional DCE-MRI (2,3). The importance of discrimination between these physiological parameters is widely acknowledged (3-5). This would aid in improved identification of treatment mechanisms, dose selection, more accurate therapy evaluation, and prediction of therapy response. The combination of multiparametric DCE-MRI analysis and advanced image analysis techniques that take into account tumor heterogeneity (e.g. texture analysis) would further enhance the utility of DCE-MRI for cancer imaging and therapy evaluation (3,6,7).

8.1.1.2. Macromolecular DCE-MRI in HIFU treatment evaluation

The macromolecular contrast-enhanced MRI methods can also be considered for evaluation of HIFU treatment. Since ablation of tumor tissue close to large blood vessels may need more energy due to the heat-sink effect caused by perfusion (8), visualization of the vasculature using MR angiography could be valuable. Knowledge of the location of major supplying arteries may also be useful if one would want to perform selective vessel ablation to enhance HIFU treatment effects (9). Furthermore,

MR angiography enables assessment of HIFU-induced vascular alterations, including vasoconstriction, hemorrhage and vessel rupture (10). Knowledge of the dependency of these vascular changes on the applied treatment settings could aid in optimizing the HIFU procedure (10). In addition, changes in vascular integrity affect local tumor perfusion, which has consequences for the tumor microenvironment (11). Besides their use for MR angiography, another possible application of albumin-binding agents in HIFU therapy evaluation is monitoring of tissue coagulation (12). Tissue coagulation induces entrapment of albumin-binding agents and heat-induced protein denaturation alters their affinity to bind to serum albumin (12).

Whereas MR angiography is particularly useful to assess microvascular integrity, the multi-agent DCE-MRI approach can provide detailed physiological information, by assessment of parameters including blood volume, blood flow and microvascular permeability. There are several potential applications for this approach with respect to HIFU, especially in the field of ultrasound-mediated drug delivery. Mild hyperthermia in the periphery of the central ablation zone may result in hyperemia, vasodilation and enhanced microvascular permeability (11). These conditions could temporarily increase tumor oxygenation. On the contrary, temperatures above 42 °C may induce microvascular damage resulting in hypoxic conditions (13). Tumor oxygenation is an important factor for the efficacy of adjuvant radiotherapy, which may be performed in case of an incomplete ablation (11). In addition, hypoxia can promote tumor progression and has been associated with adverse treatment outcome (14). Evaluation of the thermal effects of HIFU on microvascular properties is also important for treatment strategies combining HIFU with chemotherapy (15,16). Besides hyperthermia-induced drug delivery, pulsed HIFU exposures can be employed to enhance drug delivery by mechanical effects on the tumor vasculature (17-20). The multi-agent modeling approach enables detailed evaluation of microvascular function and may therefore be able to determine if treatment conditions were suitable to enhance delivery of chemotherapeutic agents to the tumor tissue.
Zhu et al. have demonstrated that DCE-MRI, using albumin-conjugated Gd-DTPA, enabled both the acquisition of tumor angiograms and determination of functional microvascular parameters (21). This approach facilitated visualization of the tumor vascular supply and evaluation of vascular heterogeneity, as well as combined macroscopic and microscopic assessment of vascular function after antiangiogenic therapy.

A potential limitation of the relatively long circulating albumin-binding and high molecular weight dendrimer-based contrast agents for their use in HIFU treatment evaluation, is that presence of paramagnetic contrast agents during the HIFU procedure can influence the accuracy of MR thermometry (22,23). MR thermometry is most commonly performed using the temperature dependence of the proton resonance frequency (PRF), which is approximately -0.01 ppm/°C (24). However, the PRF is also affected by the presence of gadolinium. The widely used gadopentetic acid has a magnetic susceptibility of 0.32 ppm/mM and therefore a change in gadolinium concentration during temperature mapping will affect the PRF shift (25). Moreover, the magnetic susceptibility effect is temperature dependent, according to $d\Delta X_{Gd\text{-}DTPA}/dT=-$

0.00038 ppm/mM/°C (23). Therefore, presence of paramagnetic contrast agents at the time of HIFU treatment may result in inaccurate temperature mapping and thermal dose calculations. In addition to this aspect, presence of gadolinium in the tumor can affect the measurement of other MR contrast parameters. Since macromolecular contrast agents typically have a long in vivo retention, the use of these agents might be restricted to post-therapy evaluation.

For these reasons, DCE-MRI was performed using low molecular weight contrast agents (**chapter 6 and 7**) or omitted (**chapter 5**) in the studies that were focused on evaluation of HIFU therapy. In **chapter 6**, pre-treatment DCE-MRI was performed one day before HIFU therapy to allow sufficient time for contrast agent washout. In **chapter 7**, DCE-MRI was only performed after HIFU treatment. **Chapter 6** focused on assessment of changes in tumor vascular status after HIFU. It was demonstrated that cluster analysis of DCE-MRI data can identify regional changes in contrast agent uptake-kinetics in tumor regions surrounding the non-perfused volume. It is expected that this method could aid in the evaluation of the effects of HIFU-induced changes in microvascular function, which affects the tumor microenvironment and efficacy of adjuvant chemotherapy and radiotherapy. In this study, we used a literature-based (population-averaged) AIF, whereas the vascular supply could also be affected by the HIFU treatment. Although accurate subject-specific AIF measurement (especially determination of the local tumor AIF) is known to be difficult in mice, it would be interesting to evaluate potential effects of HIFU therapy on the AIF and include this information in the DCE-MRI analysis. Fruytier et al. have demonstrated that phase imaging could be employed to determine the AIF in mice at high field for low molecular weight agents (26) and macromolecular contrast agents (27).

8.1.2. Clinical translation

Dendrimer-based contrast agents have not been clinically approved and their use is currently restricted to preclinical studies. Since many novel cancer therapies are initially evaluated in preclinical studies, the presented methods can be regarded as useful tools for identification of treatment mechanisms, therapy optimization and treatment evaluation. To facilitate clinical translation of the methods, other clinically approved contrast agents may be explored. An obvious alternative to the albumin-binding dendrimer-based contrast agents would be the clinically approved human serum albumin-binding gadofosveset trisodium (MS-325) (28,29). However, the use of MS-325 in a multi-agent approach is complicated by the fact that albumin-bound MS-325 will exist in equilibrium with its unbound form, which has different kinetic properties.

8.2. Multiparametric imaging

Whereas **chapter 6** was aimed at evaluation of regional changes in microvascular function after HIFU treatment, **chapter 5 and 7** were focused on the evaluation of MRI biomarkers for identification of successfully treated tumor after HIFU.

We demonstrated in preclinical tumor models that multiparametric MRI analysis facilitates discrimination between HIFU-treated non-viable tumor and viable non-treated tumor (**chapter 5 and 7**). A number of different MRI methods were evaluated, including quantitative assessment of T_1, T_2, ADC, MTR, APT-weighted signal and $T_{1\rho}$. These parameters were chosen because of their potential sensitivity to a number of tissue changes that were expected upon HIFU treatment, such as cellular and structural disruption, protein denaturation and aggregation, and coagulative necrosis. In addition, it was required that the MRI methods could be incorporated in a multiparametric MRI protocol to provide quantitative parameter maps for cluster analysis. The results of these studies demonstrated the ability of a multiparametric MRI analysis to discriminate between successfully treated non-viable and untreated viable tumor tissue. The best agreement between clustering-derived and histology-derived non-viable tumor fractions was observed at 3 days after HIFU, whereas directly after HIFU the agreement was less. Importantly, it was shown that analysis based on a single MR parameter was less suitable for discrimination between non-viable and viable tumor tissue. This stressed the added value of a multiparametric MRI analysis, in line with other studies that evaluated multiparametric MR imaging for tumor imaging or assessment of tumor treatment response (30-35).

8.2.1. Future perspectives

8.2.1.1. Additional MRI methods

A number of additional MR biomarkers may be considered for inclusion in the multiparametric MRI protocol, to increase its sensitivity for early HIFU therapy effects and to further enhance its accuracy. Chu et al. have reported that one of the acute treatment effects of HIFU is metabolic dysfunction (11). MR spectroscopy could be used to assess these direct changes in tumor metabolism and energy status. Malignant tumors often possess relatively high choline and lactate levels compared to benign tissue. Moreover, their higher energy turnover can result in higher creatine and phosphocreatine levels. After successful therapy, generally lower levels of these metabolites are observed (36), which can be measured with ^{1}H and ^{31}P MRS. Furthermore, reduced ATP levels have been observed with ^{31}P MRS after treatment (37). In addition, it has been reported that treatment-induced apoptosis may result in accumulation of cytoplasmic lipid, which could be monitored with ^{1}H MRS (38,39). An interesting method to assess changes in cellular function has been demonstrated by Jacobs et al. (40), who showed that sodium (^{23}Na) MRI may be a sensitive method to assess changes in cellular integrity after HIFU treatment of uterine fibroids (40). Healthy cells maintain a large sodium and potassium gradient across their cell membrane, which is regulated by the sodium/potassium pump that actively transports these ions across the cell membrane. A loss of membrane integrity leads to influx of sodium from the blood pool and extracellular space into the cells and results in an increased sodium concentration (40). Since the sodium/potassium pump is ATP-dependent, changes in sodium concentration may also be reflective of reduced metabolic function. Whereas MRS is commonly performed with relatively large voxel size, spectroscopic imaging could be employed to obtain spatial information on tumor metabolism and energy status. In order to provide sufficient sensitivity to changes in

metabolite levels within acceptable imaging times, spectroscopic imaging may be accelerated by techniques such as echo-planar imaging, non-uniform undersampling, or compressed sensing (41). This would further facilitate inclusion of these techniques in a multiparametric protocol and promote their clinical application. Another way to increase the sensitivity of MRS to detect changes in cell metabolism is the use of hyperpolarized MRS (42,43). Administration of hyperpolarized ^{13}C-labeled cell substrates facilitates assessment of changes in metabolic fluxes, which are often readily altered after treatment (43). An interesting application of this technique is measurement of early necrosis by administration of hyperpolarized ^{13}C-labeled fumarate. Fumarate is converted to malate within cells, catalyzed by the enzyme fumarase. However, since cellular uptake of fumarate is slow in viable cells, they demonstrate relatively low malate production. In contrast, necrotic cells with a compromised cell membrane display rapid fumarate uptake and conversion to malate (42).

Besides assessment of metabolic function, MR methods that are sensitive to microvascular function could strengthen the multiparametric MRI protocol. We have already shown that DCE-MRI can be employed to characterize tumor vascular status, although a potential drawback of the use of paramagnetic contrast agents is that presence of gadolinium could affect temperature mapping accuracy and quantification of other (endogenous) MRI parameters. ASL enables perfusion imaging without the need for contrast agent administration, which facilitates repeated perfusion assessment. Boss et al. have shown that ASL is a promising technique to assess completeness of radiofrequency ablation of renal cell carcinomas (44).

Another method that could be useful to assess vascular damage and changes in tumor perfusion after HIFU is diffusion-weighted imaging at low b-values. Joo et al. observed a reduction in perfusion-related parameters derived from IVIM analysis at 4 hours after treatment of rabbit liver tumors with a vascular disrupting agent, reflective of drug-induced vascular collapse (45). Further improvements in robust acquisition of multiple low b-value images to reliably extract the perfusion-related parameters (46,47) and establishment of the relation between IVIM-derived perfusion parameters and DCE-MRI derived tracer-kinetic parameters (48) may further promote the use of IVIM-based perfusion-parameters as biomarkers for cancer treatment evaluation.

The above-mentioned methods might be considered to increase the sensitivity of the multiparametric protocol to early HIFU-induced tumor changes. Apart from these techniques, a useful addition to the protocol would be an MR method that is sensitive to tumor oxygenation, as this affects tumor progression and efficacy of adjuvant chemotherapy and radiotherapy. It has been demonstrated that DCE-MRI parameters may be correlated with tumor oxygenation (49,50). However, MOBILE, based on the dependence of the R_1 of lipids on oxygen content, is an interesting method to more directly assess changes in tumor oxygenation (51-53).

8.2.1.2. Multimodality imaging

Combination of MRI with other imaging modalities may further improve evaluation of HIFU therapy (33,43). Especially functional imaging techniques can provide complementary data on tumor response to HIFU treatment. This information may increase sensitivity to early therapy-induced tumor changes. Besides this, it would allow for a more complete characterization of tumor tissue in the transitional zone, which may predict the extent of delayed cell death. Moreover, since HIFU treatment of malignant lesions requires whole tumor coverage, it is important that small amounts of residual or recurrent tumor cells can be detected. Whereas MRS provides functional information on tumor metabolism and energy status, it has a relatively coarse spatial resolution and limited sensitivity to detect small amounts of metabolites. Especially if the extent of residual or recurrent tumor after therapy is small, imaging modalities with a higher sensitivity are required. FDG-PET and FLT-PET are sensitive techniques to measure tumor metabolism and proliferation, respectively. Several studies have demonstrated a decreased uptake of ^{18}F-FDG (54,55) and ^{18}F-FLT (56-59) after tumor therapy. Residual high metabolic and proliferative activity may be reflective of incomplete treatment. A potential advantage of FLT-PET over FDG-PET is that a treatment-induced inflammatory response may also be associated with increased ^{18}F-FDG uptake (43). In addition to these techniques, ^{18}F-MISO PET could be employed to assess tumor oxygenation after therapy (60). HIFU-induced vascular damage can lead to hypoxic conditions in the transitional zone. Tumor hypoxia is associated with poor prognosis and resistance to radiotherapy and chemotherapy (14). Hybrid PET-MRI scanners facilitate simultaneous assessment of a broad range of functional and morphological tissue characteristics (61).

8.2.2. Clinical translation

In the studies presented in this thesis, a number of endogenous and contrast-enhanced oncologic MRI biomarkers were evaluated in a preclinical setting. We demonstrated that (macromolecular) DCE-MRI techniques can be employed to obtain a detailed assessment of tumor microvascular status, which is also valuable information in relation to HIFU therapy. Moreover, we showed that a number of MRI biomarkers enabled identification of successfully treated non-viable tumor tissue after HIFU therapy. Some of these imaging biomarkers may be primarily valuable in a preclinical setting, to aid in development, optimization and evaluation of novel tumor treatment strategies. A number of other biomarkers could be incorporated into clinical protocols for evaluation of HIFU therapy in humans. Clinical introduction of these tools would involve a number of additional steps in imaging biomarker development (62).

8.2.2.1. Time-efficient multiparametric MRI

Clinical introduction of multiparametric MRI analysis poses limitations on the total acquisition time. A high sensitivity and specificity of MRI parameters for identification of successfully treated tumor would decrease the total number of MRI parameters that is needed for accurate assessment of treatment response. In addition, the duration of the multiparametric MRI protocol could be shortened by the use of acceleration techniques, such as parallel imaging and compressed sensing (63). An interesting MRI method for time efficiently measuring multiple MRI parameters is MR fingerprinting

(64). This method is based on continuous variation of pulse sequence parameters during image acquisition to generate unique signal evolutions. These patterns can subsequently be compared to a predefined dictionary of predicted evolutions to provide quantitative MRI parameter maps (64).

8.2.2.2. Imaging biomarker validation: from mice to men

Preclinical tumor models
In our studies, we have used preclinical tumor models to assess the potential of these MRI biomarkers for tumor characterization and treatment response evaluation. These models comprised subcutaneous tumors in mice and rats, which were grown in the hind limb (ectopic). This prevented potential HIFU-induced damage to vital organs or bones. Another advantage of this tumor location was that MRI measurements were not affected by respiratory or cardiac motion. However, a drawback of ectopic tumors may be that they possess different characteristics than tumors grown in the organ of origin (orthotopic). Differences in growth rate and tumor microenvironment, including microvascular properties and interstitial fluid pressure, may affect treatment response (65,66). This may be especially true for chemotherapy or antivascular therapy, since delivery of therapeutic agents will be influenced by microvascular status. We expect the influence of the tumor microenvironment on the suitability of the presented imaging methods for HIFU therapy evaluation to be less pronounced. As an example, in agreement with our findings at 3 days after HIFU, several preclinical and clinical studies have demonstrated a decrease in ADC after a variety of treatments of different tumor types (67-69). In addition, protein degradation and aggregation is expected to be a ubiquitous effect of HIFU, not specific to a particular tumor type. As a consequence, treatment effects on some biomarkers can be expected to be relatively consistent, whereas other imaging biomarkers might be influenced by a complex combination of different treatment effects. Subcutaneous preclinical tumors in murine models of the disease are also known to be more homogeneous in comparison with tumors in humans (66).

Because of these aspects, evaluation of the pre-treatment variation in the different biomarkers, the precise extent of change upon treatment, and the time at which these changes occur is important for further clinical introduction of the MRI biomarkers for therapy evaluation. Characterization of pre-treatment variation would involve evaluation of natural variation between and within different clinical tumor types and assessment of the repeatability and reproducibility of the imaging method in a clinical setting (36,62).

Histological validation
The ability of the different MRI biomarkers and multiparametric analysis to identify successfully treated tumor was evaluated by quantitative comparison between MRI and histology. By evaluation of the correlation between MRI-derived and histology-derived non-viable tumor fractions, the most promising set of MRI parameters to assess successfully treated tumor was identified. In the study presented in **chapter 7**, we attempted to improve the spatial correspondence between MRI and histology by

the use of tissue marking dyes. Whereas MRI-derived and histology-derived non-viable tumor fractions were generally in good visual agreement, clinical biomarker validation would benefit from further improving the spatial agreement between MRI and histology. This could be established by the use of MRI- and histology-visible fiducial markers and tissue marking dyes (70,71). The efficacy of MR-HIFU treatment is often initially investigated in treat-and-resect studies, which are aimed at assessment of treatment margins and evaluation of treatment efficacy using gold-standard histopathological analysis (72). These studies would enable further validation of the multiparametric MRI approach by correlation of MRI findings with histopathological indices.

8.2.2.3. Imaging biomarker qualification and utilization

Further clinical translation of the MRI biomarkers would involve large multi-center studies, in which imaging techniques are standardized and in which their suitability for assessment of early tumor response to HIFU therapy is evaluated and compared to established clinical end-points for treatment response (62,73). This would involve assessment if early imaging biomarker changes are predictive of an eventual reduction in tumor size and a favorable treatment outcome. Our preclinical studies were focused at early assessment of treatment response and MRI follow-up was limited to 3 days after HIFU. It would be interesting to evaluate the presented methods for long-term follow-up after HIFU, during which a further inflammatory response and repair processes are expected (74,75).

Based on the pre-treatment variation in the imaging biomarkers and the extent of change in response to treatment, threshold values or image features could be selected that indicate when a change in a biomarker can be regarded as a significant treatment effect. Such information, derived from pre- and post-treatment multiparametric MRI data acquired in clinical trials could be utilized to establish computer aided-diagnosis systems (76). These systems can be employed in a clinical setting for patient-specific tissue classification, before and after treatment. Multiparametric MRI parameter values, but also tumor texture could facilitate machine-based decision making (76,77).

An interesting approach to making patient-specific predictions about treatment outcome is the integration of multimodality imaging data into mathematical models of tumor growth (78). Whereas the clinical use of these models needs to be further established, the combination of different imaging techniques offers unique opportunities to noninvasively and longitudinally acquire quantitative data related to tumor cellularity, vascularity, glucose consumption and oxygenation status (33). This allows patient-specific model predictions to be directly compared with actual treatment response and outcome.

8.3. Conclusion

The studies presented in this thesis demonstrated that macromolecular contrast-enhanced MRI facilitates detailed evaluation of tumor microvascular function. Albumin-binding and high molecular weight dendrimer-based contrast agents proved to be suitable for MR angiography. In addition, it was shown that a novel constrained multi-agent tracer-kinetic modeling approach for DCE-MRI enabled robust characterization of tumor microvascular status. This information can improve pre-treatment tumor characterization and treatment evaluation. In addition, we have evaluated a number of MRI biomarkers with respect to their suitability for identification of successfully treated tumor after HIFU therapy. Cluster analysis of DCE-MRI data was able to identify regional tracer-kinetic changes after HIFU. Besides this, multiparametric MRI, especially through clustering analysis of the ADC and APT-weighted signal, enabled discrimination between successfully treated non-viable tumor and untreated viable tumor after HIFU treatment.

8.4. References

1. Cai HH, Zhong X, Yang PH, Wei W, Chen JN, Cai JY. Probing site-selective binding of rhodamine B to bovine serum albumin. Colloid Surface A 2010;372(1-3):35-40.
2. Nielsen T, Wittenborn T, Horsman MR. Dynamic Contrast-Enhanced Magnetic Resonance Imaging (DCE-MRI) in Preclinical Studies of Antivascular Treatments. Pharmaceutics 2012;4(4):563-589.
3. O'Connor JP, Jackson A, Parker GJ, Roberts C, Jayson GC. Dynamic contrast-enhanced MRI in clinical trials of antivascular therapies. Nat Rev Clin Oncol 2012;9(3):167-177.
4. O'Connor JP, Jackson A, Parker GJ, Jayson GC. DCE-MRI biomarkers in the clinical evaluation of antiangiogenic and vascular disrupting agents. Br J Cancer 2007;96(2):189-195.
5. Zweifel M, Padhani AR. Perfusion MRI in the early clinical development of antivascular drugs: decorations or decision making tools? Eur J Nucl Med Mol Imaging 2010;37 Suppl 1:S164-182.
6. Jackson A, O'Connor JP, Parker GJ, Jayson GC. Imaging tumor vascular heterogeneity and angiogenesis using dynamic contrast-enhanced magnetic resonance imaging. Clin Cancer Res 2007;13(12):3449-3459.
7. Rose CJ, Mills SJ, O'Connor JP, Buonaccorsi GA, Roberts C, Watson Y, Cheung S, Zhao S, Whitcher B, Jackson A, Parker GJ. Quantifying spatial heterogeneity in dynamic contrast-enhanced MRI parameter maps. Magn Reson Med 2009;62(2):488-499.
8. Jiang F, He M, Liu YJ, Wang ZB, Zhang L, Bai J. High intensity focused ultrasound ablation of goat liver in vivo: Pathologic changes of portal vein and the "heat-sink" effect. Ultrasonics 2013;53(1):77-83.
9. Voogt MJ, Trillaud H, Kim YS, Mali WP, Barkhausen J, Bartels LW, Deckers R, Frulio N, Rhim H, Lim HK, Eckey T, Nieminen HJ, Mougenot C, Keserci B, Soini J, Vaara T, Kohler MO, Sokka S, van den Bosch MA. Volumetric feedback ablation of uterine

fibroids using magnetic resonance-guided high intensity focused ultrasound therapy. Eur Radiol 2012;22(2):411-417.
10. Hynynen K, Chung AH, Colucci V, Jolesz FA. Potential adverse effects of high-intensity focused ultrasound exposure on blood vessels in vivo. Ultrasound Med Biol 1996;22(2):193-201.
11. Chu KF, Dupuy DE. Thermal ablation of tumours: biological mechanisms and advances in therapy. Nat Rev Cancer 2014;14(3):199-208.
12. Vogel MW, Entius CA, Pattynama PM. Monitoring tissue coagulation during thermoablative treatment by using a novel magnetic resonance imaging contrast agent. Invest Radiol 2004;39(11):661-665.
13. Kong G, Braun RD, Dewhirst MW. Characterization of the effect of hyperthermia on nanoparticle extravasation from tumor vasculature. Cancer Res 2001;61(7):3027-3032.
14. Walsh JC, Lebedev A, Aten E, Madsen K, Marciano L, Kolb HC. The clinical importance of assessing tumor hypoxia: relationship of tumor hypoxia to prognosis and therapeutic opportunities. Antioxid Redox Signal 2014;21(10):1516-1554.
15. Hijnen N, Langereis S, Grull H. Magnetic resonance guided high-intensity focused ultrasound for image-guided temperature-induced drug delivery. Adv Drug Deliv Rev 2014;72:65-81.
16. Chen Q, Krol A, Wright A, Needham D, Dewhirst MW, Yuan F. Tumor microvascular permeability is a key determinant for antivascular effects of doxorubicin encapsulated in a temperature sensitive liposome. Int J Hyperthermia 2008;24(6):475-482.
17. Frenkel V. Ultrasound mediated delivery of drugs and genes to solid tumors. Adv Drug Deliv Rev 2008;60(10):1193-1208.
18. Frenkel V, Etherington A, Greene M, Quijano J, Xie J, Hunter F, Dromi S, Li KC. Delivery of liposomal doxorubicin (Doxil) in a breast cancer tumor model: investigation of potential enhancement by pulsed-high intensity focused ultrasound exposure. Acad Radiol 2006;13(4):469-479.
19. Hundt W, Yuh EL, Steinbach S, Bednarski MD, Guccione S. Comparison of continuous vs. pulsed focused ultrasound in treated muscle tissue as evaluated by magnetic resonance imaging, histological analysis, and microarray analysis. Eur Radiol 2008;18(5):993-1004.
20. Hancock HA, Smith LH, Cuesta J, Durrani AK, Angstadt M, Palmeri ML, Kimmel E, Frenkel V. Investigations into pulsed high-intensity focused ultrasound-enhanced delivery: preliminary evidence for a novel mechanism. Ultrasound Med Biol 2009;35(10):1722-1736.
21. Zhu W, Kato Y, Artemov D. Heterogeneity of tumor vasculature and antiangiogenic intervention: insights from MR angiography and DCE-MRI. PLoS One 2014;9(1):e86583.
22. Hijnen NM, Elevelt A, Grull H. Stability and trapping of magnetic resonance imaging contrast agents during high-intensity focused ultrasound ablation therapy. Invest Radiol 2013;48(7):517-524.
23. Hijnen NM, Elevelt A, Pikkemaat J, Bos C, Bartels LW, Grull H. The magnetic susceptibility effect of gadolinium-based contrast agents on PRFS-based MR thermometry during thermal interventions. J Ther Ultrasound 2013;1:8.

24. McDannold N. Quantitative MRI-based temperature mapping based on the proton resonant frequency shift: review of validation studies. Int J Hyperthermia 2005;21(6):533-546.
25. van Osch MJ, Vonken EJ, Viergever MA, van der Grond J, Bakker CJ. Measuring the arterial input function with gradient echo sequences. Magn Reson Med 2003;49(6):1067-1076.
26. Fruytier AC, Magat J, Colliez F, Jordan B, Cron G, Gallez B. Dynamic contrast-enhanced MRI in mice at high field: Estimation of the arterial input function can be achieved by phase imaging. Magn Reson Med 2013.
27. Fruytier AC, Magat J, Neveu MA, Karroum O, Bouzin C, Feron O, Jordan B, Cron GO, Gallez B. Dynamic contrast-enhanced MRI in mouse tumors at 11.7 T: comparison of three contrast agents with different molecular weights to assess the early effects of combretastatin A4. NMR Biomed 2014;27(11):1403-1412.
28. Lauffer RB, Parmelee DJ, Dunham SU, Ouellet HS, Dolan RP, Witte S, McMurry TJ, Walovitch RC. MS-325: albumin-targeted contrast agent for MR angiography. Radiology 1998;207(2):529-538.
29. Lauffer RB, Parmelee DJ, Ouellet HS, Dolan RP, Sajiki H, Scott DM, Bernard PJ, Buchanan EM, Ong KY, Tyeklar Z, Midelfort KS, McMurry TJ, Walovitch RC. MS-325: a small-molecule vascular imaging agent for magnetic resonance imaging. Acad Radiol 1996;3 Suppl 2:S356-358.
30. Hoeks CM, Barentsz JO, Hambrock T, Yakar D, Somford DM, Heijmink SW, Scheenen TW, Vos PC, Huisman H, van Oort IM, Witjes JA, Heerschap A, Futterer JJ. Prostate cancer: multiparametric MR imaging for detection, localization, and staging. Radiology 2011;261(1):46-66.
31. Jacobs MA. Multiparametric magnetic resonance imaging of breast cancer. J Am Coll Radiol 2009;6(7):523-526.
32. Padhani AR, Miles KA. Multiparametric imaging of tumor response to therapy. Radiology 2010;256(2):348-364.
33. Yankeelov TE, Abramson RG, Quarles CC. Quantitative multimodality imaging in cancer research and therapy. Nat Rev Clin Oncol 2014;11(11):670-680.
34. Muller BG, Futterer JJ, Gupta RT, Katz A, Kirkham A, Kurhanewicz J, Moul JW, Pinto PA, Rastinehad AR, Robertson C, de la Rosette J, Sanchez-Salas R, Jones JS, Ukimura O, Verma S, Wijkstra H, Marberger M. The role of magnetic resonance imaging (MRI) in focal therapy for prostate cancer: recommendations from a consensus panel. BJU Int 2014;113(2):218-227.
35. Dominietto M, Rudin M. Could magnetic resonance provide in vivo histology? Front Genet 2014;4:298.
36. Marcus CD, Ladam-Marcus V, Cucu C, Bouche O, Lucas L, Hoeffel C. Imaging techniques to evaluate the response to treatment in oncology: current standards and perspectives. Crit Rev Oncol Hematol 2009;72(3):217-238.
37. Hilf R. Mitochondria are targets of photodynamic therapy. J Bioenerg Biomembr 2007;39(1):85-89.
38. Lee SC, Poptani H, Pickup S, Jenkins WT, Kim S, Koch CJ, Delikatny EJ, Glickson JD. Early detection of radiation therapy response in non-Hodgkin's lymphoma xenografts by in vivo 1H magnetic resonance spectroscopy and imaging. NMR Biomed 2010;23(6):624-632.

39. Liimatainen T, Hakumaki JM, Kauppinen RA, Ala-Korpela M. Monitoring of gliomas in vivo by diffusion MRI and 1H MRS during gene therapy-induced apoptosis: interrelationships between water diffusion and mobile lipids. NMR Biomed 2009;22(3):272-279.
40. Jacobs MA, Ouwerkerk R, Kamel I, Bottomley PA, Bluemke DA, Kim HS. Proton, diffusion-weighted imaging, and sodium (23Na) MRI of uterine leiomyomata after MR-guided high-intensity focused ultrasound: a preliminary study. J Magn Reson Imaging 2009;29(3):649-656.
41. Thomas MA, Nagarajan R, Huda A, Margolis D, Sarma MK, Sheng K, Reiter RE, Raman SS. Multidimensional MR spectroscopic imaging of prostate cancer in vivo. NMR Biomed 2014;27(1):53-66.
42. Brindle KM, Bohndiek SE, Gallagher FA, Kettunen MI. Tumor imaging using hyperpolarized 13C magnetic resonance spectroscopy. Magn Reson Med 2011;66(2):505-519.
43. Brindle K. New approaches for imaging tumour responses to treatment. Nat Rev Cancer 2008;8(2):94-107.
44. Boss A, Martirosian P, Schraml C, Clasen S, Fenchel M, Anastasiadis A, Claussen CD, Pereira PL, Schick F. Morphological, contrast-enhanced and spin labeling perfusion imaging for monitoring of relapse after RF ablation of renal cell carcinomas. Eur Radiol 2006;16(6):1226-1236.
45. Joo I, Lee JM, Han JK, Choi BI. Intravoxel incoherent motion diffusion-weighted MR imaging for monitoring the therapeutic efficacy of the vascular disrupting agent CKD-516 in rabbit VX2 liver tumors. Radiology 2014;272(2):417-426.
46. Le Bihan D, Turner R, Moonen CT, Pekar J. Imaging of diffusion and microcirculation with gradient sensitization: design, strategy, and significance. J Magn Reson Imaging 1991;1(1):7-28.
47. Andreou A, Koh DM, Collins DJ, Blackledge M, Wallace T, Leach MO, Orton MR. Measurement reproducibility of perfusion fraction and pseudodiffusion coefficient derived by intravoxel incoherent motion diffusion-weighted MR imaging in normal liver and metastases. Eur Radiol 2013;23(2):428-434.
48. Bisdas S, Braun C, Skardelly M, Schittenhelm J, Teo TH, Thng CH, Klose U, Koh TS. Correlative assessment of tumor microcirculation using contrast-enhanced perfusion MRI and intravoxel incoherent motion diffusion-weighted MRI: is there a link between them? NMR Biomed 2014;27(10):1184-1191.
49. Zahra MA, Hollingsworth KG, Sala E, Lomas DJ, Tan LT. Dynamic contrast-enhanced MRI as a predictor of tumour response to radiotherapy. Lancet Oncology 2007;8(1):63-74.
50. Jensen RL, Mumert ML, Gillespie DL, Kinney AY, Schabel MC, Salzman KL. Preoperative dynamic contrast-enhanced MRI correlates with molecular markers of hypoxia and vascularity in specific areas of intratumoral microenvironment and is predictive of patient outcome. Neuro Oncol 2014;16(2):280-291.
51. Jordan BF, Magat J, Colliez F, Ozel E, Fruytier AC, Marchand V, Mignion L, Bouzin C, Cani PD, Vandeputte C, Feron O, Delzenne N, Himmelreich U, Denolin V, Duprez T, Gallez B. Mapping of oxygen by imaging lipids relaxation enhancement: A potential sensitive endogenous MRI contrast to map variations in tissue oxygenation. Magn Reson Med 2012.

52. Jordan BF, Magat J, Colliez F, Ozel E, Fruytier AC, Marchand V, Mignion L, Gallez B. Application of MOBILE (mapping of oxygen by imaging lipids relaxation enhancement) to study variations in tumor oxygenation. Adv Exp Med Biol 2013;789:281-288.
53. Colliez F, Neveu MA, Magat J, Cao Pham TT, Gallez B, Jordan BF. Qualification of a noninvasive magnetic resonance imaging biomarker to assess tumor oxygenation. Clin Cancer Res 2014;20(21):5403-5411.
54. Ohira T, Okuma T, Matsuoka T, Wada Y, Nakamura K, Watanabe Y, Inoue Y. FDG-MicroPET and diffusion-weighted MR image evaluation of early changes after radiofrequency ablation in implanted VX2 tumors in rabbits. Cardiovasc Intervent Radiol 2009;32(1):114-120.
55. Vera P, Dubray B, Palie O, Buvat I, Hapdey S, Modzelewski R, Benyoucef A, Rousseau C, Meyer ME, Bardet S, Gardin I, Fiore FD, Michel P. Monitoring tumour response during chemo-radiotherapy: a parametric method using FDG-PET/CT images in patients with oesophageal cancer. EJNMMI Res 2014;4(1):12.
56. Trigonis I, Koh PK, Taylor B, Tamal M, Ryder D, Earl M, Anton-Rodriguez J, Haslett K, Young H, Faivre-Finn C, Blackhall F, Jackson A, Asselin MC. Early reduction in tumour [18F]fluorothymidine (FLT) uptake in patients with non-small cell lung cancer (NSCLC) treated with radiotherapy alone. Eur J Nucl Med Mol Imaging 2014;41(4):682-693.
57. Sugiyama M, Sakahara H, Sato K, Harada N, Fukumoto D, Kakiuchi T, Hirano T, Kohno E, Tsukada H. Evaluation of 3'-deoxy-3'-18F-fluorothymidine for monitoring tumor response to radiotherapy and photodynamic therapy in mice. J Nucl Med 2004;45(10):1754-1758.
58. Yang YJ, Ryu JS, Kim SY, Oh SJ, Im KC, Lee H, Lee SW, Cho KJ, Cheon GJ, Moon DH. Use of 3'-deoxy-3'-[18F]fluorothymidine PET to monitor early responses to radiation therapy in murine SCCVII tumors. Eur J Nucl Med Mol Imaging 2006;33(4):412-419.
59. Pan MH, Huang SC, Liao YP, Schaue D, Wang CC, Stout DB, Barrio JR, McBride WH. FLT-PET imaging of radiation responses in murine tumors. Mol Imaging Biol 2008;10(6):325-334.
60. Lopci E, Grassi I, Chiti A, Nanni C, Cicoria G, Toschi L, Fonti C, Lodi F, Mattioli S, Fanti S. PET radiopharmaceuticals for imaging of tumor hypoxia: a review of the evidence. Am J Nucl Med Mol Imaging 2014;4(4):365-384.
61. Judenhofer MS, Wehrl HF, Newport DF, Catana C, Siegel SB, Becker M, Thielscher A, Kneilling M, Lichy MP, Eichner M, Klingel K, Reischl G, Widmaier S, Rocken M, Nutt RE, Machulla HJ, Uludag K, Cherry SR, Claussen CD, Pichler BJ. Simultaneous PET-MRI: a new approach for functional and morphological imaging. Nat Med 2008;14(4):459-465.
62. Abramson RG, Burton KR, Yu JP, Scalzetti EM, Yankeelov TE, Rosenkrantz AB, Mendiratta-Lala M, Bartholmai BJ, Ganeshan D, Lenchik L, Subramaniam RM. Methods and Challenges in Quantitative Imaging Biomarker Development. Acad Radiol 2015;22(1):25-32.
63. Tsao J, Kozerke S. MRI temporal acceleration techniques. J Magn Reson Imaging 2012;36(3):543-560.

64. Ma D, Gulani V, Seiberlich N, Liu K, Sunshine JL, Duerk JL, Griswold MA. Magnetic resonance fingerprinting. Nature 2013;495(7440):187-192.
65. Ho KS, Poon PC, Owen SC, Shoichet MS. Blood vessel hyperpermeability and pathophysiology in human tumour xenograft models of breast cancer: a comparison of ectopic and orthotopic tumours. BMC Cancer 2012;12:579.
66. Ruggeri BA, Camp F, Miknyoczki S. Animal models of disease: pre-clinical animal models of cancer and their applications and utility in drug discovery. Biochem Pharmacol 2014;87(1):150-161.
67. Patterson DM, Padhani AR, Collins DJ. Technology insight: water diffusion MRI--a potential new biomarker of response to cancer therapy. Nat Clin Pract Oncol 2008;5(4):220-233.
68. Moffat BA, Hall DE, Stojanovska J, McConville PJ, Moody JB, Chenevert TL, Rehemtulla A, Ross BD. Diffusion imaging for evaluation of tumor therapies in preclinical animal models. MAGMA 2004;17(3-6):249-259.
69. Ross BD, Moffat BA, Lawrence TS, Mukherji SK, Gebarski SS, Quint DJ, Johnson TD, Junck L, Robertson PL, Muraszko KM, Dong Q, Meyer CR, Bland PH, McConville P, Geng HR, Rehemtulla A, Chenevert TL. Evaluation of cancer therapy using diffusion magnetic resonance imaging. Mol Cancer Ther 2003;2(6):581-587.
70. Schmitz AC, van den Bosch MA, Loo CE, Mali WP, Bartelink H, Gertenbach M, Holland R, Peterse JL, Rutgers EJ, Gilhuijs KG. Precise correlation between MRI and histopathology - exploring treatment margins for MRI-guided localized breast cancer therapy. Radiother Oncol 2010;97(2):225-232.
71. McGrath DM, Vlad RM, Foltz WD, Brock KK. Technical note: fiducial markers for correlation of whole-specimen histopathology with MR imaging at 7 tesla. Med Phys 2010;37(5):2321-2328.
72. Huisman M, van den Bosch MA. MR-guided high-intensity focused ultrasound for noninvasive cancer treatment. Cancer Imaging 2011;11:S161-166.
73. Padhani AR, Liu G, Koh DM, Chenevert TL, Thoeny HC, Takahara T, Dzik-Jurasz A, Ross BD, Van Cauteren M, Collins D, Hammoud DA, Rustin GJ, Taouli B, Choyke PL. Diffusion-weighted magnetic resonance imaging as a cancer biomarker: consensus and recommendations. Neoplasia 2009;11(2):102-125.
74. Cheng HL, Purcell CM, Bilbao JM, Plewes DB. Usefulness of contrast kinetics for predicting and monitoring tissue changes in muscle following thermal therapy in long survival studies. J Magn Reson Imaging 2004;19(3):329-341.
75. Wijlemans JW, Deckers R, van den Bosch MA, Seinstra BA, van Stralen M, van Diest PJ, Moonen CT, Bartels LW. Evolution of the ablation region after magnetic resonance-guided high-intensity focused ultrasound ablation in a Vx2 tumor model. Invest Radiol 2013;48(6):381-386.
76. Wang S, Burtt K, Turkbey B, Choyke P, Summers RM. Computer Aided-Diagnosis of Prostate Cancer on Multiparametric MRI: A Technical Review of Current Research. Biomed Res Int 2014;2014:789561.
77. Mouthuy N, Cosnard G, Abarca-Quinones J, Michoux N. Multiparametric magnetic resonance imaging to differentiate high-grade gliomas and brain metastases. J Neuroradiol 2012;39(5):301-307.

78. Yankeelov TE, Atuegwu N, Hormuth D, Weis JA, Barnes SL, Miga MI, Rericha EC, Quaranta V. Clinically relevant modeling of tumor growth and treatment response. Sci Transl Med 2013;5(187):187ps189.

Summary

Magnetic Resonance Imaging Biomarkers of Cancer

with applications in High Intensity Focused Ultrasound treatment evaluation

The work presented in this thesis was aimed at the development and evaluation of magnetic resonance imaging (MRI) methods for tumor imaging and therapy evaluation, with a specific focus on High Intensity Focused Ultrasound (HIFU). To this aim, various studies were performed in tumor-bearing mice. An overview of oncologic imaging methods and the potential suitability of MRI for HIFU therapy evaluation was given in **chapter 1**.

The first part (**chapter 2, 3 and 4**) of this thesis was focused on macromolecular contrast-enhanced MRI for assessment of tumor vascular status.
Chapter 2 demonstrated the characterization and in vivo evaluation of blood-kinetics and biodistribution of different lower generations of dendrimer-based MRI contrast agents, functionalized with a palmitoyl moiety to facilitate reversible binding to mouse serum albumin (MSA). Differences in structure between the agents affected their relaxometric properties, aggregation behavior and affinity for MSA. The agents possessed prolonged circulation times compared to the low molecular weight Gd-DOTA and proved to be suitable for blood pool imaging, as shown with MR angiography.
In **chapter 3**, the characterization and in vivo evaluation of dendrimer-based MRI contrast agents of various molecular weight was described. The dendrimers possessed an increased relaxivity compared to Gd-DOTA. The circulation half-lives of the agents increased with their molecular weight and the elimination half-life of the highest molecular weight G5 dendrimer was 5 times higher than of Gd-DOTA.
Differences in blood-kinetics and tumor accumulation between the agents implied that they possess a range of tumor wash-in and wash-out rates. Therefore, these agents are suitable candidates for macromolecular DCE-MRI. MR angiography demonstrated the utility of the highest molecular weight G5 dendrimer for blood pool imaging.
In **chapter 4**, a novel tracer-kinetic modeling approach for macromolecular dynamic contrast-enhanced MRI (DCE-MRI) was demonstrated. The approach was based on sequential injection of multiple contrast agents of various molecular weight within one imaging session and simultaneous modeling of the multi-agent DCE-MRI data. Simulations demonstrated that multi-agent tracer-kinetic modeling reduced bias and uncertainty in tracer-kinetic parameter estimation, compared to single-bolus modeling. The method was applied in a mouse tumor model, using dendrimer-based contrast agents of various molecular weight and Gd-DOTA. Simultaneous fitting of the multi-agent data enabled separate estimation of parameters characterizing blood flow and microvascular permeability. Significant differences in the extraction fraction and washout rate constant between the agents, dependent on their molecular weight, were consistently observed. This demonstrated the suitability of the constrained multi-agent modeling approach to obtain a detailed assessment of tumor vascular status.

The remaining part of this thesis was focused on the identification of MRI biomarkers for evaluation of HIFU treatment. Two of these studies (**chapter 5 and 6**) involved tumor ablation using a preclinical therapeutic transducer outside of the MRI scanner and treatment evaluation using a high-field MRI scanner.

Chapter 5 described the evaluation of HIFU treatment using a multiparametric MRI protocol, consisting of quantitative assessment of the T_1, T_2, apparent diffusion coefficient (ADC) and magnetization transfer ratio (MTR). Tumor-bearing mice underwent MRI before, directly after and 3 days after HIFU. A cluster analysis was employed on different feature vectors (i.e. combinations of MRI parameters), to assess the optimal set of MRI parameters for identification of successfully treated non-viable tumor tissue. Clusters were classified as non-viable if the fraction of clusters significantly increased after HIFU. Clustering-derived and histology-derived non-viable tumor fractions were quantitatively compared. The highest correlation between these fractions was observed for feature vector {T_1, T_2, ADC} at 3 days after HIFU. Directly after HIFU the agreement was less. These results demonstrated that a multiparametric MRI protocol enables identification of successfully treated tumor after HIFU.
Chapter 6 was focused on DCE-MRI evaluation of HIFU therapy. DCE-MRI was performed on tumor-bearing mice before, directly after and 3 days after HIFU. Non-perfused tumor fractions were quantitatively compared with histology-derived non-viable tumor fractions. The best agreement between these fractions was observed at 3 days after HIFU, whereas directly after HIFU the non-perfused tumor fraction was higher than the non-viable fraction. Cluster analysis of tracer-kinetic parameters K^{trans} and v_e was employed to interrogate the changes in contrast agent uptake-kinetics in tumor regions outside the non-perfused volume. After HIFU, the fraction of pixels in two clusters, exhibiting a low K^{trans} and either a low or high v_e, was significantly increased. Histological analysis suggested that HIFU-induced changes in these clusters were a consequence of structural disruption and hemorrhage, resulting in reduced microvascular function as also implied by vascular endothelium and hypoxia staining.
A step towards clinical translation of multiparametric MRI analysis for evaluation of HIFU therapy was demonstrated in **chapter 7**. This study was aimed at the evaluation of HIFU treatment using a quantitative MRI analysis consisting of T_1, T_2, ADC, $T_{1\rho}$, amide proton transfer (APT) and DCE-MRI measurements. HIFU-treatment was performed on tumor-bearing rats, using a clinical 3T MR-HIFU system which facilitated real-time treatment monitoring using MR thermometry. Multiparametric MRI was performed before, directly after and 3 days after HIFU. Cluster analysis of all combinations of endogenous MRI parameters was performed. The optimal set of MRI parameters to identify successfully treated tumor tissue was assessed by quantitative comparison between clustering-derived and histology-derived non-viable tumor fractions. The best agreement between these fractions was observed after clustering with feature vector {ADC, APT-weighted signal}, at 3 days after HIFU. The suitability of the multiparametric cluster analysis for evaluation of HIFU therapy was found to be higher than of thermal dose mapping and contrast-enhanced MRI, which are conventional methods for HIFU-therapy monitoring and evaluation, respectively.
In **chapter 8**, a reflection was given on the work presented in this thesis. Moreover, future perspectives and steps towards clinical translation were discussed.

In conclusion, this thesis describes a number of contrast-enhanced and endogenous MRI biomarkers for cancer imaging and treatment evaluation. It was demonstrated that macromolecular DCE-MRI enables detailed evaluation of tumor vascular status and multiparametric MRI enables identification of successfully HIFU-treated tumor.

List of publications

Published

1. **Jacobs I**, Strijkers GJ, Nicolay K, Schabel MC. A novel approach to tracer-kinetic modeling for (macromolecular) dynamic contrast-enhanced magnetic resonance imaging. Magn Reson Med 2015; DOI 10.1002/mrm.25704.
2. Hectors SJ, **Jacobs I**, Strijkers GJ, Nicolay K. Automatic segmentation of subcutaneous mouse tumors by multiparametric MR analysis based on endogenous contrast. MAGMA 2014; DOI 10.1007/s10334-014-0472-1.
3. Hectors SJ, **Jacobs I**, Strijkers GJ, Nicolay K. Amide proton transfer imaging of high intensity focused ultrasound-treated tumor tissue. Magn Reson Med 2014;72(4):1113-1122.
4. **Jacobs I***, Hectors SJCG*, Strijkers GJ, Nicolay K. Multiparametric MRI analysis for the identification of high intensity focused ultrasound-treated tumor tissue. PloS one 2014;9(6):e99936.
5. Paulis LE, **Jacobs I**, van den Akker NM, Geelen T, Molin DG, Starmans LW, Nicolay K, Strijkers GJ. Targeting of ICAM-1 on vascular endothelium under static and shear stress conditions using a liposomal Gd-based MRI contrast agent. J Nanobiotechnology 2012;10:25.
6. Kluza E, **Jacobs I**, Hectors SJ, Mayo KH, Griffioen AW, Strijkers GJ, Nicolay K. Dual-targeting of alphavbeta3 and galectin-1 improves the specificity of paramagnetic/fluorescent liposomes to tumor endothelium in vivo. J Control Release 2012;158(2):207-214.
7. Onuki Y, **Jacobs I**, Artemov D, Kato Y. Noninvasive visualization of in vivo release and intratumoral distribution of surrogate MR contrast agent using the dual MR contrast technique. Biomaterials 2010;31(27):7132-7138.

Submitted / In preparation

8. **Jacobs I***, Hectors SJCG*, Schabel MC, Grüll H, Strijkers GJ, Nicolay K. Cluster analysis of DCE-MRI data identifies regional tracer-kinetic changes after tumor treatment with High Intensity Focused Ultrasound. Submitted.
9. **Jacobs I***, Hectors SJCG*, Heijman E, Keupp J, Berben M, Strijkers GJ, Grüll H, Nicolay K. Multiparametric MRI analysis for the evaluation of Magnetic Resonance-guided High Intensity Focused Ultrasound treatment. Submitted.
10. Hectors SJCG, **Jacobs I**, Moonen CTW, Strijkers GJ, Nicolay K. MRI methods for the evaluation of High Intensity Focused Ultrasound tumor treatment – current status and future needs. Submitted.
11. **Jacobs I**, Wouters SJ , Keizer HM, Janssen HM, Gianolio E, Arena F, Aime S, Strijkers GJ, Nicolay K. Synthesis and characterization of palmitoylated poly(propylene imine) dendrimer-based albumin-binding magnetic resonance imaging contrast agents. In preparation.
12. **Jacobs I**, Wouters SJ , Keizer HM, Janssen HM, Gianolio E, Arena F, Aime S, Strijkers GJ, Nicolay K. Synthesis and characterization of poly(propylene imine) dendrimer-based magnetic resonance imaging contrast agents of various molecular weight. In preparation.

13. **Jacobs I**, Strijkers GJ, Kobayashi H, Nicolay K. Concepts in Diagnostic Probe Design. Book chapter: Small Animal Imaging, 2nd edition. Kiessling F, Hauff P, Pichler BJ (eds.). Springer-Verlag, Berlin Heidelberg.

* These authors contributed equally.

Refereed conference proceedings (1st author only)

Jacobs I, Hectors SJCG**,** Strijkers GJ**,** Nicolay K, Schabel MC. Constrained multi-agent tracer-kinetic modeling to assess tumor vascular changes induced by DMXAA treatment. International Society for Magnetic Resonance in Medicine (ISMRM) annual meeting, 2015, Toronto, Canada.

Jacobs I, Hectors SJCG, Heijman E, Keupp J, Berben M, Strijkers GJ, Grüll H, Nicolay K. Multiparametric MRI cluster analysis for evaluation of MR-guided High Intensity Focused Ultrasound tumor treatment. European Molecular Imaging Meeting (EMIM), 2015, Tübingen, Germany. *(Awarded with an ESMI 2015 Excellence Award for Young Researchers)*.

Jacobs I, Hectors SJCG**,** Strijkers GJ**,** Schabel MC, Nicolay K. Constrained multi-agent tracer-kinetic modeling for evaluation of antivascular tumor therapy. European Molecular Imaging Meeting (EMIM), 2015, Tübingen, Germany. *(Awarded with the EMIM 2015 poster award in the category "Tumour vascularization and hypoxia")*.

Jacobs I, Hectors SJCG, Heijman E, Keupp J, Berben M, Strijkers GJ, Grüll H, Nicolay K. Multiparametric MRI analysis for the evaluation of MR-guided High Intensity Focused Ultrasound treatment. 7th ISMRM Benelux Chapter Meeting, 2015, Ghent, Belgium. *(Awarded with best poster presentation)*.

Jacobs I, Strijkers GJ, Keizer H, Janssen H, Nicolay K, Schabel MC. A novel approach to tracer-kinetic modeling of (macromolecular) multi-bolus DCE-MRI data, applied in a murine tumor model. International Society for Magnetic Resonance in Medicine (ISMRM) annual meeting, 2014, Milan, Italy. *(Awarded with a certificate of merit; summa cum laude)*.

Jacobs, I., Hectors, S.J.C.G., Strijkers, G.J., Nicolay, K. Cluster analysis of DCE-MRI derived pharmacokinetic parameters to assess vascular effects of tumor ablation with HIFU. International Symposium for Therapeutic Ultrasound (ISTU), 2014, Las Vegas, USA.

Jacobs I, Wouters SJ, Keizer H, Gianolio E, Strijkers GJ, Nicolay K. In vitro and in vivo characterization of (albumin-binding) dendritic MRI contrast agents for dynamic contrast-enhanced MRI. International Society for Magnetic Resonance in Medicine (ISMRM) annual meeting, 2013, Salt Lake City, USA.

Jacobs, I., Hectors, S.J.C.G., Strijkers, G.J., Nicolay, K. High temporal resolution DCE-MRI with T2* compensation for evaluation of the effects of HIFU treatment. ESMRMB 29th Annual scientific meeting, 2012, Lisbon, Portugal.

Jacobs, I., Hectors, S.J.C.G., Strijkers, G.J., Nicolay, K. High temporal resolution DCE-MRI with T2* compensation for evaluation of the effects of HIFU treatment. 4th ISMRM Benelux Chapter Meeting, 2012, Leuven, Belgium.

Jacobs, I., Paulis, L., Castermans, K., Coolen, B., Geelen, T., Strijkers, G.J., Nicolay, K. In vivo molecular MRI of ICAM-1 expression after cardiac ischemia-reperfusion injury in mice. 2nd ISMRM Benelux Chapter Meeting, 2010, Utrecht, The Netherlands.

Acknowledgements / Dankwoord

Net als dat er meer achter het plaatje op de voorkant van dit proefschrift zit dan je op het eerste oog ziet, geldt dat ook voor de inhoud van dit proefschrift. Achter de schermen zijn veel mensen heel belangrijk geweest bij het tot stand komen van dit werk. Ik ben blij dat ik nu uitgebreid stil kan staan bij wat velen van jullie de afgelopen jaren voor me betekend hebben.

Klaas, ik kan me het moment nog goed herinneren dat ik voor het eerst bij u op gesprek kwam om te informeren naar de mogelijkheden om een master binnen de Biomedical NMR groep te doen. U nam alle tijd om me alle verschillende projecten binnen de groep uit te leggen en na de afsluitende rondleiding had ik ongeveer alle hoekjes van n-laag gezien. Dit zorgde ervoor dat ik me direct thuis en gewaardeerd voelde. Tot op heden is dat gevoel alleen nog maar sterker geworden. Uw deur staat altijd open om dingen te bediscussiëren en u bent altijd bereid om op korte termijn manuscripten, abstracts, presentaties etc. te bekijken. Als dingen even niet zoals gepland gingen bleef u vertrouwen houden in een goede afloop en kreeg ik alle mogelijkheden om samenwerkingen met andere onderzoeksgroepen te zoeken. Heel hartelijk dank voor het vertrouwen en de jarenlange prettige begeleiding.

Gustav, ook jou wil ik bedanken voor de fijne begeleiding en het vertrouwen gedurende mijn promotie. Ook al had ik zelf soms het idee dat dingen niet liepen zoals hoorde, gaf je aan dat je zelf vaak dacht: 'Igor en Stefanie, dat komt wel goed'... En als ik het idee had dat ik er echt even niet uitkwam bracht jouw pragmatische kijk op zaken uitkomst. Na een gesprek met jou waren sommige problemen geen problemen meer, en zo toch dan werden die getackeld door eerst maar eens het eerste sub-probleem te bekijken. Zelfs in het weekend schoot je te hulp als er iets met de scanner was, waardoor het onderzoek weer gewoon door kon gaan. Ik wens je veel succes in Amsterdam!

I would also like to thank the other members of my PhD committee; dr. ir. M. Mischi, prof. dr. Chrit Moonen, prof. dr. Bernard Gallez, dr. Jurger Fütterer and dr. Matthias Schabel. Thank you for reviewing my thesis and taking part in the committee. With some of you I have collaborated more extensively, on which I will come back later.

Stefanie, met jou heb ik tijdens mijn promotie nauw samen mogen werken en dat was me een groot genoegen. Voor de buitenwereld leek die hele promotie je maar gemakkelijk af te gaan, en ik moet eerlijk zeggen, voor mij leek dat soms ook. Maar ik maakte ook van dichtbij je ontzettende drive en werklust mee. Het gevoel dat we er samen helemaal voor gingen werkte erg motiverend. We konden samen niet alleen heel goed flessen ontgast water open maken, maar waren in veel andere opzichten ook een goed team. Ik heb veel geleerd van de vele discussies over onze gezamenlijke studies. Ook was je altijd bereid om mee te denken over dingen en me te helpen toen ik met mijn pols in het gips zat, tot grote hilariteit van anderen. Daarnaast werden door de leuke samenwerking met jou de scansessies in het weekend minder saai en de congressen nog leuker. We hadden het geluk samen veel congressen te mogen bezoeken, wat dan mooi gecombineerd kon worden met wat toeristische activiteiten, zoals het ~~vallen~~ skiën in Les Houches en ~~geld weggooien~~ cashen in Las Vegas. Ik wens je veel succes in New York en een mooie tijd daar samen met Ralf.

During my PhD, I had the opportunity to collaborate with a number of external research groups, which has been very valuable for my PhD:

Matthias, the collaboration with you was invaluable for my PhD. It started with our interest in using the MCBE blind AIF estimation algorithm, but in the end your expertise in tracer-kinetic modeling and your novel ideas brought much more to the table. We had great benefit from your advice and help. I'm pleased that our study on multi-agent tracer-kinetic modeling has led to a nice publication and hopefully another one to follow.

I would also like to thank prof. dr. Silvio Aime, dr. Eliana Gianolio and dr. Francesca Arena from the University of Turin for the pleasant collaboration. We have learned a lot from your expertise in characterization of MRI contrast agents. Thank you for giving us the opportunity of doing experiments in your lab, for many valuable discussions and for doing some extra experiments that have been a nice contribution to chapter 2 and 3.

Bernard Gallez and Anne-Catherine Fruytier, thank you for demonstrating the AIF measurements at your institution and the valuable discussions on this matter.

Rolf, thank you for the effort you put in implementing the MCBE AIF estimation algorithm in Mathematica. It appeared to be easier said than done, but I enjoyed working on this project together with you and I have learned a lot from this.

Naast deze externe groepen waren een aantal samenwerkingen dichter bij huis ook erg waardevol:

Henk Keizer en Henk Janssen van SyMO-Chem, bedankt voor de synthese van de dendrimeren, jullie mooie bijdrage aan hoofdstuk 2-4 en de vele waardevolle discussies. Jullie waren altijd zeer bereid om mee te denken over de resultaten of de weg daar naartoe en hadden vaak goede ideeën over hoe bepaalde resultaten het best gepresenteerd konden worden. Ik ben blij dat we dit nu hebben kunnen bekronen met de publicatie van het multi-agent artikel en hopelijk volgen hoofdstuk 2 en 3 ook nog.

Door onze verhuizing naar de High Tech Campus kregen we de mogelijkheid om een studie te doen met het 3T MR-HIFU systeem, wat een mooie afsluiter was van onze promoties. Gelukkig konden we in dit werk gebruik maken van de preklinische opstelling die Nicole heeft opgezet. Edwin, het was erg fijn dat we een beroep konden doen op jouw kennis van het MR-HIFU systeem. Het was erg prettig om met je samen te werken en leuk dat je net zo gedreven was als wij om er een mooie studie van te maken. Ik ben trots op het eindresultaat van deze studie. Monique, ook jij hebt hier een belangrijke rol in gespeeld, door je waardevolle hulp bij de histologische validatie. Ook wil ik graag Caren, Marije, Carlijn en Marleen bedanken voor jullie goede biotechnische ondersteuning. Jochen, I would like to thank you for the valuable discussions about the APT measurements. Holger, bedankt voor je kritische blik op onze manuscripten. Vaak kwam je met goede punten waar wij zelf nog niet zo goed bij stilgestaan hadden en zorgde je er zo voor dat de manuscripten beter en duidelijker werden. Daarnaast vind ik het altijd erg interessant om jouw visie te horen op het translationele aspect van het soort studies dat wij doen.

Ik wil ook alle andere partners binnen het VOLTA consortium van CTMM hartelijk danken voor de nuttige discussies.

Tijdens mijn promotie heb ik het genoegen gehad een aantal studenten te begeleiden die allen veel nuttig werk verzet hebben:

Siem, je hebt tijdens jouw afstuderen nogal wat epjes en NMR buizen verslonden. Als je nagaat dat die ook nog allemaal gemeten moesten worden is het nauwelijks voor te stellen dat je daarnaast ook nog tijd wist te vinden om me op de nieuwste hits van Fabrizio te wijzen. Je hebt een berg werk gezet, wat allemaal terug te vinden is in hoofdstuk 2 en 3 en hopelijk binnenkort ook gepubliceerd gaat worden. Je werkte met veel enthousiasme aan je project (zo ontving ik wel eens papers van je met als neventitel 'HALLELUJA_DIT_IS_EM_FUCK_YEAH') en ook al was de iëleng soms nog zo bitter, dan liet je je niet uit het veld slaan en ging je onvermoeibaar door. Zo hebben we ook mooie metingen kunnen doen in Turijn en zijn de resultaten toch nog sjiek geworden.
Ik wil ook graag alle bachelor studenten bedanken die vol enthousiasme hebben gewerkt aan de karakterisatie van de dendritische contrastmiddelen. Robbert, Ronald, Evi, Marina, Lisanne, Josiane en Tom, jullie werk is niet direct terug te vinden in deze thesis, maar stond aan de basis van hoofdstuk 2 en 3, of heeft geleid tot extra begrip van de in deze hoofdstukken beschreven contrastmiddelen.

Naast de al genoemde personen, die vaak zichtbaar waren op onze publicaties, zijn er ook veel mensen achter de schermen erg belangrijk geweest:

David, Leonie en Jo, bedankt voor jullie goede biotechnische ondersteuning. Het was fijn om altijd te kunnen rekenen op wat extra handen of jullie kunde als ons bepaalde biotechnische handelingen niet lukten. Jullie toonden je bovendien altijd zeer betrokken bij het welzijn van de dieren. Graag wil ik ook alle CPV medewerkers en DEC medewerkers bedanken.

Larry, vaak als ik beneden door de scanner ruimte loop denk ik 'wat hebben we het toch eigenlijk goed voor elkaar hier', en dat is aan jou te danken. In een ruimte waarin de faciliteiten goed in elkaar zitten en waarin je je geen zorgen hoeft te maken over of de apparatuur wel werkt is het prettig werken.

Floortje, je zorgt er altijd voor dat alles soepel loopt binnen de groep en dingen snel en goed geregeld worden. Daarnaast heb je als zonnetje in huis en gangmaker binnen onze groep ook een belangrijke verbindende rol. Het spijt me dat ik je toch regelmatig teleur heb moeten stellen als je weer eens deelnemers zocht voor een leuke activiteit. Ik ben vol vertrouwen dat ik dit jaar wel mee kan helpen om de meerkamp titel binnen te slepen.
Ik wil graag ook Hedwig bedanken voor de hulp bij praktische zaken in mijn eerste jaren bij de Biomedical NMR groep.

Ik wil ook nog wat mensen bedanken die een belangrijke rol achter de schermen op de HTC hebben gespeeld. Jeannette en Bas van Philips Innovation Services, bedankt voor de vele ICP analyses. Dirk, Mario, Frans, Christ, Gerry, Frenk, Christa en Suzanne, bedankt voor het draaiende houden van de labs en alles wat daarbij komt kijken.

Ook mijn collega PhD studenten en overige groepsgenoten hebben allemaal wel met het een of ander geholpen en uiteraard bijgedragen aan de leuke sfeer binnen de groep.

Ten eerste mijn kamergenoten:

Rik, het was erg leuk om jou tijdens mijn afstuderen en promotie als kamergenoot en later ook als buurman te hebben. Naast alle leuke gesprekken op het werk zorgde je er ook voor dat ik af en toe met wat buitenlucht in aanraking kwam en wist je me te wijzen op de wonderen der natuur die zich vlakbij ons raam afspeelden. Ik heb veel plezier beleefd aan samen hardlopen en fietsen en hopelijk gaan we dat in de toekomst nog regelmatig doen. Veel succes in Maastricht!

Tom, je was naast een waardevol lid van team tumor ook een leuke kamergenoot, lid van de boulderkoningen en lid van de sportaholics. Naast wetenschappelijke discussies, waren er dus ook genoeg luchtigere discussies onder het genot van een TGVke of andere (minder lekkere) drankjes.

Valentina, it was very nice to have you as my office neighbor during the last couple of years. I really liked your company and how you can talk about things in a funny and enthusiastic way, as well as how you could be so amazed about that some really stupid studies could get published in good journals. I'm sure that your articles will be a lot better!

Jo, ik vond het een genoegen om met jou op een kantoor te zitten. Je bemiddelde als we op het laatste moment nog een protocol goedgekeurd moesten zien te krijgen en daarnaast genoot ik altijd van je mooie verhalen.

Naast mijn kamergenoten zijn er natuurlijk nog alle andere fijne (ex)groepsgenoten:

Bart, wetenschappelijk gezien hadden we weinig met elkaar van doen, maar daarbuiten des te meer. Je was een gangmaker en altijd in om even een drankje te doen, fitness goeroe te spelen, en je was zelfs een van de meest fanatieke boulderaars. En als ik het even druk had op het werk en weinig tijd had om te koken wist je heel goed wat een mens dan het hardste nodig had; jouw überkip. Misschien ben ik je daar nog wel het meest dankbaar voor…

Sharon, bedankt voor je hulp bij de statistiek. Ik ben behoorlijk wat wijzer geworden van de ervaring die je hierin al had.

Luc, ik heb genoten van onze avonturen samen in Baltimore. Je had een geweldige two-step en football worp in huis en zorgde daarnaast vooral voor veel gezelligheid.

Nilske, jij bent misschien wel de trouwste boulderkoning en altijd in voor mooie avonturen. Ik ben ervan overtuigd dat we nog ooit een 7C gaan klimmen en de geocache op gaan halen.

Miranda en Marloes, jullie ook bedankt voor de gezelligheid en sportieve uitspattingen.

Ot, bedankt voor de mooie tijd op Pukkelpop en tijdens het wakeboarden. Het is altijd leuk om je weer te zien.

Verder wil ik nog een aantal begeleiders bedanken die me vóór mijn promotie wegwijs gemaakt hebben in het onderzoek. Leonie, ik heb veel geleerd van je begeleiding en vind het leuk dat we elkaar nog regelmatig spreken. Erik, bedankt voor je goede begeleiding tijdens mijn eerste stage binnen de groep. Ewelina, thank you for giving us the first experience with in vivo measurements in tumor-bearing mice.

En dan zijn er nog een hoop groepsgenoten of ex-groepsgenoten met wie ik vele leuke

gesprekken en ervaringen heb gehad en die me allemaal wel met iets geholpen hebben. Jeanine, Katrien, Abdallah, Bram, Wolter, Jules, Tessa, Martijn, Richard, Bastiaan, Roel, Glenda, Maarten, Mariska, Steffie, Nicole, Esther, René, Laura, Tiemen, Sin Yuin, Pedro, Sander, Anke, Desiree, Bernard, Prashant, Jolita, Jeroen, Glenda, alle studenten en iedereen die ik nu vergeten ben… ik kan helaas niet bij elk van jullie uitgebreid stilstaan, maar ik wil jullie allemaal heel hartelijk bedanken voor de mooie tijd en leuke sfeer binnen de groep en daarbuiten.

I would also like to thank my former supervisors that were not part of the Biomedical NMR group; Yoshinori Kato, Dmitri Artemov and Zaver Bhujwalla, thank you for supervising me during my internship at the *In vivo* Cellular and Molecular Imaging Center at Johns Hopkins University. I learned a lot from this project and it was a great experience.

Naast alle werk gerelateerde personen, die vaak ook vrienden te noemen zijn, wil ik nog stil staan bij mijn vriendengroep. Ik ga jullie niet allemaal bij naam noemen, maar ik wil jullie wel allemaal bedanken voor alle leuke momenten samen en de mooie vriendschap, die bij velen zelfs terug gaat tot aan de kleuterklas. Hoewel jullie altijd geïnteresseerd waren in hoe het met mijn promotie ging, kwamen jullie ook vaak niet verder dan ‘hoe is het met de muizen?’ en dat was eigenlijk ook wel prettig. Zo was er bij jullie vooral veel ruimte voor plezier en ontspanning en dat was na het werk toch meestal het hardste nodig. Ik ben er trots op dat we zo’n mooie groep hebben en hoop dat we dat nog lang zo kunnen houden.

Ik wil ook mijn familie bedanken voor de interesse in hoe het ging gedurende de afgelopen jaren. John, jij ook bedankt voor je hulp bij het drukken van mijn thesis!

En dan een aantal personen die misschien wel het belangrijkste voor me zijn geweest:

Elco, het is heel fijn om een tweelingbroer te hebben zoals jij. Ik weet niet hoe ik dat moet omschrijven, maar het is als een soort van beste vriend die je dan zelfs nog extra goed begrijpt. Al zijn we vrij verschillend is dat verschil denk ik niet zo groot als het voor de buitenwereld lijkt en hebben we veel dezelfde interesses en gedachten. Zo kan ik met jou zowel over hele serieuze als hele onserieuze zaken praten, samen sporten, gezellig samen eten, etc. Als er een deel van het onderzoek niet vlotte kon ik altijd bij terecht en nam je zonder problemen de hele avond de tijd om met mij na te gaan waar het probleem precies zat en hoe daar verandering in gebracht kon worden. Ook als bijvoorbeeld een stuk code niet werkte nam je uitgebreid de tijd om dit met mij te fixen. Ik heb heel veel bewondering voor wat je met BrewPi voor elkaar hebt weten te boksen en hoe je in je eentje zo’n breed scala aan vaak ook nog heel ingewikkelde taken weet te volbrengen. Mooi om te zien hoe goed je bedrijf zich aan het ontwikkelen is. Xandra, ik ben ook heel blij met jou als überschoonzus. Ik vind het altijd heel gezellig om met je buurten en daarnaast is het heel relaxed dat ik altijd bij jullie aan kan schuiven om een hapje mee te eten of gewoon een gezellig avondje te chillen.

Sigrid, doordat je nu in Den Haag woont zie ik je wat minder vaak maar ik denk dat we altijd die speciale band zullen houden. Je was niet alleen heel sociaal, geïnteresseerd en behulpzaam in huis, maar we konden vooral altijd veel plezier hebben over van alles en nog wat. Dit geldt ook voor Bram en ik kan er altijd erg van genieten als we weer eens met zijn allen thuis zijn. Jullie hebben een mooi leven

opgebouwd in Den Haag en ik vind het heel leuk dat jullie nu binnenkort gaan trouwen. Veel geluk samen!

Pap en mam, bij alles wat ik doe kan ik rekenen op jullie onvoorwaardelijke steun. Jullie hebben me geleerd om hard te werken en ergens vol voor te gaan, maar dat het ook niet erg is als iets een keer niet lukt. Als dingen even tegen zaten tijdens mijn promotie kon ik altijd bij jullie terecht om te kijken hoe we die om konden buigen en het geheel weer op de rails te krijgen. Bovenal bleven jullie altijd het volste vertrouwen hebben op een goede afloop.

Mede dankzij de hulp en steun van iedereen die ik hierboven genoemd heb (of vergeten ben) kan ik deze mooie periode nu afsluiten en beginnen aan een volgend avontuur. Bedankt!

Cover description

‘By inspecting the tumor tissue in a special way, information can be obtained that would remain invisible otherwise’.

The image is a 3D stereogram; an object is hidden inside the image which appears in 3D only when viewed correctly.

This is a reference to the MRI methods and image analysis techniques that are presented in this thesis, such as the multiparametric MRI analysis and multi-agent tracer-kinetic modeling approach. With these techniques, valuable information about the tumor tissue could be extracted that could not be obtained with conventional MR imaging techniques.

Instruction: hold the image at approximately 40 cm from your eyes. Now instead of focusing on the image itself, relax your eyes as if you were looking at a point at some distance behind the image. With some practice, the hidden object may show up. This way of looking can be practiced by staring at the two zeros below. By relaxing your eyes and looking through the page, gradually 3 zeros will appear.

0 0

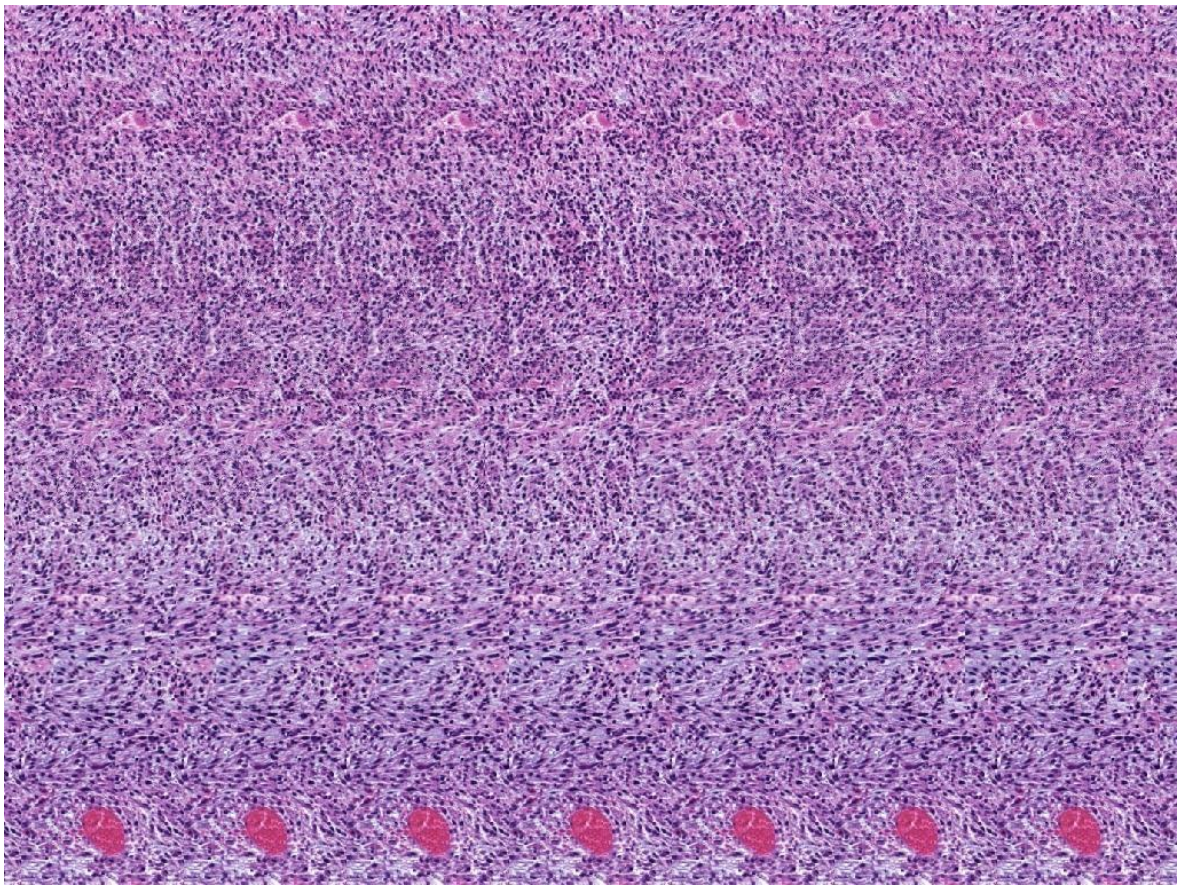

The background pattern of the image is based on a histopathological image of a tumor at 3 days after High Intensity Focused Ultrasound treatment. The depth mask, displaying the hidden object (a Philips Achieva 3.0 T MRI scanner) is shown below.

In the occasion you would see multiple, slightly overlapping MRI scanners, try to change your focus point (by practicing with the zeros on the previous page or focusing at slightly different distances behind the page).

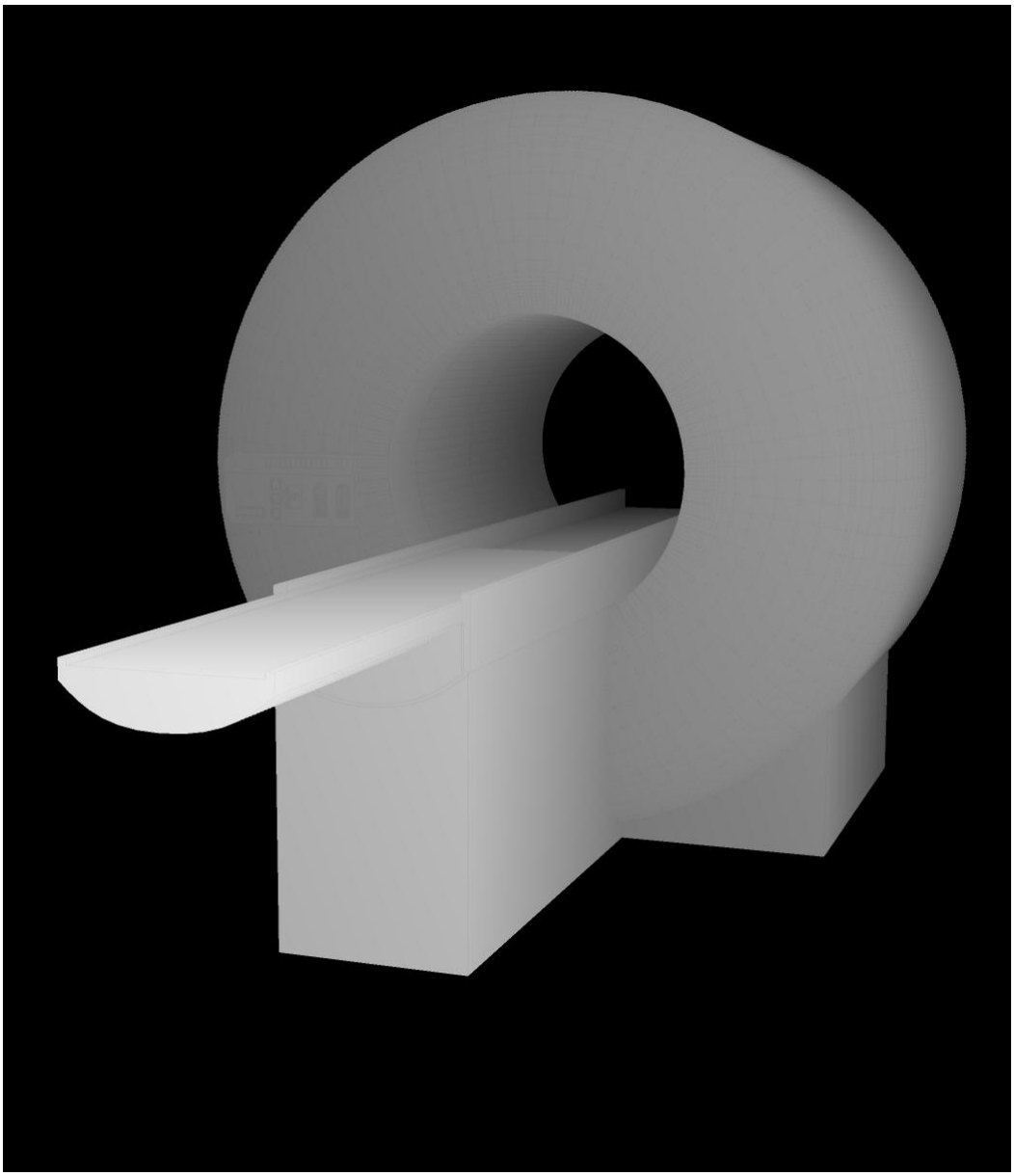

About the author

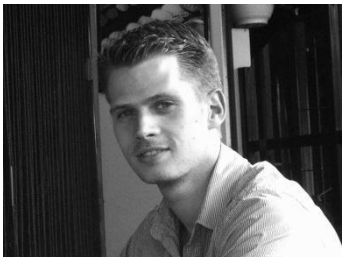

Igor Jacobs was born on November 15th, 1985, in Geldrop, the Netherlands. He finished his pre-university education at the Varendonck-College in Asten in 2004 and continued his education at the Eindhoven University of Technology (TU/e), where he studied Biomedical Engineering. After obtaining his Bachelor of Science degree in 2007, he followed the master track of Molecular Bioengineering and Molecular Imaging with a specialization in Biomedical NMR. During his master studies, he did an internship in the Biomedical NMR group of Prof. Dr. Klaas Nicolay at the TU/e on the topic of iron oxide-based MRI contrast agents. Following this project, he performed an internship at the *In Vivo* Cellular and Molecular Imaging Center (ICMIC) of the Johns Hopkins University School of Medicine in Baltimore, United States, in the group of Prof. Dr. Zaver M. Bhujwalla and under supervision of Dr. Yoshinori Kato and Dr. Dmitri Artemov. The topic of this internship was dual contrast nanocarriers for non-invasive monitoring of drug release. His graduation project was performed in the Biomedical NMR group at the TU/e and focused on molecular MR imaging of myocardial infarction. After obtaining his master's degree in 2010, he started his PhD research in the Biomedical NMR group in 2010, entitled 'Magnetic Resonance Imaging biomarkers of cancer', with a specific focus on application of these biomarkers for evaluation of High Intensity Focused Ultrasound treatment. This project was performed within the framework of the Center for Translational Molecular Medicine (project VOLTA). In 2014, he started as a post-doctoral fellow in the Biomedical NMR group at the TU/e. His project is performed within the framework of NanoNextNL and focuses on efficient tumor drug delivery systems.